CUMULATIVE DISSERTATION

Towards unifying approaches in exposure modelling for scenario-based multi-hazard risk assessments

by

Juan Camilo Gómez Zapata

Univ.-Diss.

zur Erlangung des akademischen Grades

"doctor rerum naturalium"

(Dr. rer. nat.)

in der Wissenschaftsdisziplin "Georisks"

eingereicht an der

Mathematisch-Naturwissenschaftlichen Fakultät

Institut für Geowissenschaften

der Universität Potsdam

und

vorbereiten in der Sektion Erdbebengefährdung und dynamische Risiken der Helmholtz-Zentrum Potsdam
Deutsches GeoForshungsZentrum GFZ

Submitted on August 26, 2022

Ort und Tag der Disputation:
Campus Golm, Building 27, Room 1.10, Universität Potsdam; Monday, 23 January 2023, 2 p.m.

Supervisors:
Prof. Dr. Fabrice COTTON
Dr. Massimiliano PITTORE

External Reviewer:
Prof. Dr. Carmine GALASSO

Examination Board:
Prof. Dr. Fabrice COTTON
Prof. Dr. Carmine GALASSO
PD Dr. Heidi KREIBICH
Prof. Dr. Frank KRÜGER
Prof. Dr. Bruno MERZ

Published online on the
Publication Server of the University of Potsdam:
https://doi.org/10.25932/publishup-58614
https://nbn-resolving.org/urn:nbn:de:kobv:517-opus4-586140

Declaration of Authorship

I, Juan Camilo Gomez Zapata, hereby declare that this thesis titled, '**Towards unifying approaches in exposure modelling for scenario-based multi-hazard risk assessments** and the work presented in it are my own. I confirm that:

- I have fully acknowledged and referenced the ideas and work of others, whether published or unpublished, in my thesis.
- This dissertation was not submitted for the award of any other degree or diploma in any other institution.

Signed:

Place, Date:

Abstract

This cumulative thesis presents a stepwise investigation of the exposure modelling process for risk assessment due to natural hazards while highlighting its, to date, not much-discussed importance and associated uncertainties. Although "exposure" refers to a very broad concept of everything (and everyone) that is susceptible to damage, in this thesis it is narrowed down to the modelling of large-area residential building stocks. Classical building exposure models for risk applications have been constructed fully relying on unverified expert elicitation over data sources (e.g., outdated census datasets), and hence have been implicitly assumed to be static in time and in space. Moreover, their spatial representation has also typically been simplified by geographically aggregating the inferred composition onto coarse administrative units whose boundaries do not always capture the spatial variability of the hazard intensities required for accurate risk assessments. These two shortcomings and the related epistemic uncertainties embedded within exposure models are tackled in the first three chapters of the thesis. The exposure composition of large-area residential building stocks is studied on the scope of scenario-based earthquake loss models. Then, the proposal of optimal spatial aggregation areas of exposure models for various hazard-related vulnerabilities is presented, focusing on ground-shaking and tsunami risks. Subsequently, once the experience is gained in the study of the composition and spatial aggregation of exposure for various hazards, this thesis moves towards a multi-hazard context while addressing cumulative damage and losses due to consecutive hazard scenarios. This is achieved by proposing a novel method to account for the pre-existing damage descriptions on building portfolios as a key input to account for scenario-based multi-risk assessment. Finally, this thesis shows how the integration of the aforementioned elements can be used in risk communication practices. This is done through a modular architecture based on the exploration of quantitative risk scenarios that are contrasted with social risk perceptions of the directly exposed communities to natural hazards.

In Chapter 1, a Bayesian approach is proposed to update the prior assumptions on such composition (i.e., proportions per building typology). This is achieved by integrating high-quality real observations and then capturing the intrinsic probabilistic nature of the exposure model. Such observations are accounted as real evidence from both: field inspections (Chapter 2) and freely available data sources to update existing (but outdated) exposure models (Chapter 3). In these two chapters, earthquake scenarios with parametrised ground motion fields were transversally used to investigate the role of such epistemic uncertainties related to the exposure composition through sensitivity analyses. Parametrised scenarios of seismic ground shaking were the hazard input utilised to study the physical vulnerability of building portfolios. The second issue that was investigated, which refers to the spatial aggregation of building exposure models, was investigated within two decoupled vulnerability contexts: due to seismic ground shaking through the integration of remote sensing techniques (Chapter 3); and within a multi-hazard context by integrating the occurrence of associated tsunamis (Chapter 4). Therein, a careful selection of the spatial aggregation entities while pursuing computational efficiency and accuracy in the risk estimates due to such independent hazard scenarios (i.e., earthquake and tsunami) are discussed. Therefore, in this thesis, the physical vulnerability of large-area building portfolios due to tsunamis is considered through two main frames: considering and disregarding the interaction at the vulnerability level, through consecutive and decoupled hazard scenarios respectively, which were then contrasted.

Contrary to Chapter 4, where no cumulative damages are addressed, in Chapter 5, data and approaches, which were already generated in former sections, are integrated with a novel modular method to ultimately study the likely interactions at the vulnerability level on building portfolios. This is tested by evaluating cumulative damages and losses after earthquakes with increasing magnitude followed by their respective tsunamis. Such a novel method is grounded on the possibility of re-using existing fragility models within a probabilistic framework. The same approach is followed in Chapter 6 to forecast the likely cumulative damages to be experienced by a building stock located in a volcanic multi-hazard setting (ash-fall and lahars). In that section, special focus was made on the manner the forecasted loss metrics are communicated to locally exposed communities. Co-existing quantitative scientific approaches (i.e., comprehensive exposure models; explorative risk scenarios involving single and multiple hazards) and semi-qualitative social risk perception (i.e., level of understanding that the exposed communities have about their own risk) were jointly considered. Such an integration ultimately allowed this thesis to also contribute to enhancing preparedness, science divulgation at the local level as well as technology transfer initiatives.

Finally, a synthesis of this thesis along with some perspectives for improvement and future work are presented.

Zusammenfassung

Diese kumulative Diplomarbeit stellt eine schrittweise Untersuchung des Expositionsmodellierungsprozesses für die Risikobewertung durch Naturgefahren dar und weist auf seine bisher wenig diskutierte Bedeutung und die damit verbundenen Unsicherheiten hin. Obwohl sich „Exposition“ auf einen sehr weiten Begriff von allem (und jedem) bezieht, der für Schäden anfällig ist, wird er in dieser Arbeit auf die Modellierung von großräumigen Wohngebäudebeständen eingeengt. Klassische Gebäudeexpositionsmodelle für Risikoanwendungen wurden vollständig auf der Grundlage unbestätigter Expertenerhebungen über Datenquellen (z. B. veraltete Volkszählungsdatensätze) erstellt und wurden daher implizit als zeitlich und räumlich statisch angenommen. Darüber hinaus wurde ihre räumliche Darstellung typischerweise auch vereinfacht, indem die abgeleitete Zusammensetzung geografisch auf grobe Verwaltungseinheiten aggregiert wurde, deren Grenzen nicht immer die räumliche Variabilität der Gefahrenintensitäten erfassen, die für genaue Risikobewertungen erforderlich sind. Diese beiden Mängel und die damit verbundenen epistemischen Unsicherheiten, die in Expositionsmodellen eingebettet sind, werden in den ersten drei Kapiteln der Dissertation verfolgt. Die Exposure-Zusammensetzung von großflächigen Wohngebäudebeständen wird im Rahmen szenariobasierter Erdbebenschadenmodelle untersucht. Anschließend wird der Vorschlag optimaler räumlicher Aggregationsbereiche von Expositionsmodellen für verschiedene gefahrenbezogene Anfälligkeiten präsentiert, wobei der Schwerpunkt auf Bodenerschütterungs- und Tsunami-Risiken liegt. Anschließend, sobald die Erfahrung in der Untersuchung der Zusammensetzung und räumlichen Aggregation der Exposition für verschiedene Gefahren gesammelt wurde, bewegt sich diese Arbeit in Richtung eines Kontextes mit mehreren Gefahren, während sie sich mit kumulativen Schäden und Verlusten aufgrund aufeinanderfolgender Gefahrenszenarien befasst. Dies wird erreicht, indem eine neuartige Methode vorgeschlagen wird, um die bereits bestehenden Schadensbeschreibungen an Gebäudeportfolios als Schlüsseleingabe für die Berücksichtigung einer szenariobasierten Multi-Risiko-Bewertung zu berücksichtigen. Abschließend zeigt diese Arbeit, wie die Integration der oben genannten Elemente in der Risikokommunikation genutzt werden kann. Dies erfolgt durch eine modulare Architektur, die auf der Untersuchung quantitativer Risikoszenarien basiert, die mit der sozialen Risikowahrnehmung der direkt von Naturgefahren betroffenen Gemeinschaften kontrastiert werden.

In Kapitel 1 wird ein bayesianischer Ansatz vorgeschlagen, um die früheren Annahmen zu einer solchen Zusammensetzung (d. h. Anteile pro Gebäudetypologie) zu aktualisieren. Dies wird erreicht, indem hochwertige reale Beobachtungen integriert und dann die intrinsische Wahrscheinlichkeitsnatur des Expositionsmodells erfasst wird. Solche Beobachtungen werden sowohl aus Feldbegehungen (Kapitel 2) als auch aus frei verfügbaren Datenquellen zur Aktualisierung bestehender (aber veralteter) Expositionsmodelle (Kapitel 3) als echte Beweise gewertet. In diesen beiden Kapiteln wurden Erdbebenszenarien mit parametrisierten Bodenbewegungsfeldern transversal verwendet, um die Rolle solcher epistemischen Unsicherheiten in Bezug auf die Expositionszusammensetzung durch Sensitivitätsanalysen zu untersuchen. Parametrisierte Szenarien seismischer Bodenerschütterungen waren der Gefahreneingang, der verwendet wurde, um die physische Anfälligkeit von Gebäudeportfolios zu untersuchen. Das zweite untersuchte Problem, das sich auf die räumliche Aggregation von Gebäudeexpositionsmodellen bezieht, wurde in zwei entkoppelten Vulnerabilitätskontexten untersucht: durch seismische Bodenerschütterungen durch die Integration von Fernerkundungstechniken (Kapitel 3); und innerhalb eines Multi-Hazard-Kontextes durch Einbeziehung des Auftretens assoziierter Tsunamis (Kapitel 4). Darin wird eine sorgfältige Auswahl der räumlichen Aggregationseinheiten bei gleichzeitigem Streben nach Recheneffizienz und Genauigkeit bei den Risikoschätzungen aufgrund solcher unabhängiger Gefahrenszenarien (d. h. Erdbeben und Tsunami) diskutiert. Daher wird in dieser Arbeit die physische Vulnerabilität von großen Gebäudeportfolios durch Tsunamis durch zwei Hauptrahmen betrachtet: Berücksichtigung und Nichtberücksichtigung der Wechselwirkung auf der Vulnerabilitätsebene, durch aufeinanderfolgende bzw. entkoppelte Gefahrenszenarien, die dann gegenübergestellt wurden.

Im Gegensatz zu Kapitel 4, wo keine kumulativen Schäden angesprochen werden, werden in Kapitel 5 Daten und Ansätze, die bereits in früheren Abschnitten generiert wurden, mit einer neuartigen modularen Methode integriert, um letztendlich die wahrscheinlichen Wechselwirkungen auf der Schwachstellenebene beim Aufbau von Portfolios zu untersuchen. Dies wird getestet, indem kumulative Schäden und Verluste nach Erdbeben mit zunehmender Magnitude gefolgt von den jeweiligen Tsunamis bewertet werden. Eine solche neuartige Methode basiert auf der Möglichkeit, bestehende Fragilitätsmodelle innerhalb eines probabilistischen Rahmens wiederzuverwenden. Derselbe Ansatz wird in Kapitel 6 verfolgt, um die wahrscheinlichen kumulativen Schäden zu prognostizieren, denen ein Gebäudebestand ausgesetzt sein wird, der sich in einer vulkanischen Umgebung mit mehreren Gefahren (Aschefall und Lahare) befindet. In diesem Abschnitt wurde besonderes Augenmerk auf die Art und Weise gelegt, wie die prognostizierten Verlustmetriken an lokal exponierte Gemeinden kommuniziert werden. Koexistierende quantitative wissenschaftliche Ansätze (d. h. umfassende Expositionsmodelle; explorative Risikoszenarien mit Einzel- und

Mehrfachgefahren) und semiqualitative soziale Risikowahrnehmung (d. h. Grad des Verständnisses, das die exponierten Gemeinschaften über ihr eigenes Risiko haben) wurden gemeinsam berücksichtigt. Eine solche Integration ermöglichte es dieser Arbeit schließlich auch, zur Verbesserung der Bereitschaft, der wissenschaftlichen Verbreitung auf lokaler Ebene sowie zu Technologietransferinitiativen beizutragen.

Abschließend wird eine Zusammenfassung dieser These zusammen mit einigen Perspektiven für Verbesserungen und zukünftige Arbeiten präsentiert.

Acknowledgments

First, I would like to sincerely thank my supervisors Fabrice Cotton and Massimiliano Pittore for their unconditional support during the years that we have worked together. I am forever grateful for having trusted in me, and for having spent your time guiding my research process and shaping my crazy ideas. Likewise, I would like to thank my mentor, Pierre-Yves Bard, from whom I received the passion for research since we met in Grenoble in 2017 during my master's studies. You three have been beyond inspiring in science and in human values.

I would like to deeply thank several colleagues at the GFZ for their valuable advice and supported during the elaboration of this study: Nils Brinkmann, Matthias Rüster, Elif Türker, Kevin Fleming, Jörn Lauterjung, Andrey Babeyko, Cecilia Nievas, Graeme Weatherill, Henning Lilienkamp, Jose Bayona, Ugur Öztürk, Sebastian Specht, Sriram Reedy, Dino Bindi, Raquel Zafrir, Simantini Shinde, Carla Valenzuela, Angela Gomez, Dorina Kroll, Solveig Strütze, Susanne Köster, Kirsten Elger, Uwe Lemgo, and many others. Each one of you contributed to many activities in your own special manner, either scientifically, administratively, or with a generous smile, for which I am beyond grateful. Without your support, this work would not have been possible.

Thanks also go to the many people in Colombia, Chile, Peru, Ecuador and Germany who supported the elaboration of Journal, Conference or Data papers during the last few years: Orlando Arroyo, Roberto Torres-Corredor, Juan Lizarazo, Sergio Medina, Paula Aguirre, Hernan Santa Maria, Yvonne Merino, Nicola Tarque, Cristian Parrado, Fernando Barragán-Ochoa, Camilo Zapata, Elisabeth Schöpfer, Michael Langbein, Patrick Aravena, Christian Geiß, Sven Harig, Alireza Mahdavi Hugo Rosero, Theresa Frimberger, Michael Krautblatter, Daniel Straub, Fabio Brill, Kerstin Büche, and Harald Spahn. Likewise, I would like to thank the members of South American institutions with whom I have been in contact during the last years (i.e., SENESCYT, SYNGER, CENEPRED, INDECI, COFOPRI, PREDES, ONEMI, SHOA) for the co-organization of the workshops held either virtually or in person. I would also like to thank several people that kindly supported my research initiatives by providing data sources, critical feedback, or by sharing some ideas during interesting meetings: Esteban Sáez, Rodrigo Cienfuegos, Luis Ceferino, Glendy Linares, Waldor Arevalo, Sandra Santa-Cruz, Benjamin Bernard, Daniel Andrade, Diego Molina, Hugo Yepes, Pablo Palacios, Jose Marrero, Juan Carlos Singaucho, Bonifacius Adiguna Yogatama, Roger Machacca, Luis Chasi, Angela Blanco-Voigt, Tiziana Rossetto, Ingrid Charvet, Dina D'Ayala, Carmine Galasso, Felipe Rivera, Juan Palomino, Anawat Suppasri, Hellen Crowley, Ricardo Monteiro, and Vitor Silva. I am glad and humbled that many nice people were on board with me during this adventure.

I would like to thank the German Federal Ministry of Education and Research (BMBF) that have funded my research within the programme CLIENT II—International Partnerships for Sustainable Innovations in the frame of the RIESGOS project, a truly inspiring project that allowed me to learn every day.

Lastly, but most importantly, I would like to thank my family, Eucaris, Susana, and Daniel. You three, with your unconditional love have been the heart, soul, and muscle that has kept me strong and motivated. I love you.

List of Contents

1. Introduction 1

1.1. Scope of the thesis 2

1.2. Presentation of the study 3

1.3. Author's Publications and Contributions 3

1.3.1. Publications in the frame of the thesis 3

1.3.2. Publications not associated with the thesis 4

1.3.3. Contributions to open software 5

1.3.4. Contributions to data repositories: 5

2. Epistemic uncertainty of probabilistic building exposure compositions in scenario-based earthquake loss models 7

2.1. Introduction 8

2.2. Current state of the art in building- exposure modelling for seismic risk assessment 9

2.2.1. The use of taxonomies for building exposure modelling 9

2.2.1.1. Risk-oriented taxonomies: Schemes 9

2.2.1.2. Faceted taxonomies: taxonomic attributes 9

2.2.2. Exposure modelling methods for large area spatially distributed buildings 10

2.2.2.1. Top-down approach: building class from the analysis of aggregated data 10

2.2.2.2. Bottom-up approach: individual building observations 10

2.2.2.3. Dynamic building exposure modelling based on data collection and statistical analyses 10

2.3. Methodology 11

2.3.1. Probabilistic - exposure models: a Bayesian formulation 11

2.3.1.1. The definition of the likelihood function: The intra-scheme compatibility levels 11

2.3.1.2. Prior and posterior distributions 11

2.3.1.3. Synthetic building portfolios for a logic tree construction and spatial allocation 12

2.3.2. Probabilistic inter-scheme compatibility matrix 12

2.3.3. Scenario-based earthquake risk assessment with spatially distributed ground motion fields 13

2.3.4. Epistemic uncertainty of the building exposure definition in earthquake loss models 13

2.4. Application 13

2.4.1. Context of the study area: Valparaíso 13

2.4.2. Probabilistic exposure model construction for Valparaíso 14

2.4.2.1. The definition of the likelihood function: The intra-scheme compatibility levels 14

2.4.2.2. Prior and posterior distributions 17

2.4.2.3. Synthetic building portfolios for a logic tree construction and spatial allocation 19

2.4.2.4. Scenario-based earthquake risk assessment with spatially distributed ground motion fields 21

2.4.3. Results: epistemic uncertainty of exposure compositions in seismic risk scenario 23

2.4.3.1. The role of the concentration factor α_0 24

2.4.3.2. The role of the identification of buildings attributes (evidence) in the likelihood term. 24

2.4.3.3. The role of the selection of the prior distribution type 25

2.4.3.4. The role of the spatially cross-correlated ground motion residuals 26

2.5. Discussion and future outlook 28

2.6. Conclusions and recommendations 29

Declarations 31

3. Towards a Sensitivity Analysis in Seismic Risk with Probabilistic Building Exposure Models: An Application in Valparaíso, Chile Using Ancillary Open-Source Data and Parametric Ground Motion 32

3.1. Introduction 33

3.2. Context of the study area. 34
3.3. Materials and Methods 35
3.3.1. Delimitation of the urban area and some initial features 36
3.3.2. Building exposure and vulnerability models for Valparaíso 36
3.3.2.1. The initial commune-based SARA exposure model with merged classes 36
3.3.2.2. Preliminary model: a simple downscaling using spatial disaggregation of population 41
3.3.2.3. Ancillary data available for Valparaíso 44
3.3.2.4. Bayesian exposure model for Valparaíso 44
3.3.2.5. Comparison of exposure models available for Valparaíso 45
3.3.3. Generation of seismic ground motion fields for an earthquake scenario 48
3.3.3.1. Ground motion prediction equation (GMPE) 49
3.3.3.2. Site term (spatial distribution of Vs_{30}) 49
3.3.3.3. Spatial correlation model 49
3.4. Sensitivity analyses on scenario-based seismic risk assessment 51
3.5. Discussion 52
3.6. Conclusions 54
Appendix A: Spatial delimitation of the urban area and available data sources for building exposure modelling 55
Appendix B: Assumptions followed in the preliminary model (Sect. 3.3.2.2) to obtain building counts from population and footprint areas 56
Appendix C: Data collection of building attributes in Valparaíso and their classification 57
Appendix D: Basic Overview of the Probabilistic Exposure Modelling Approach 59
4. Variable-resolution building exposure modelling for earthquake and tsunami scenario-based risk assessment. An application case in Lima, Peru 62
4.1. Introduction 63
4.2. Methodology 65
4.2.1. Simulation of scenario-based hazards with spatially distributed intensities 65
4.2.2. Construction of focus maps 66
4.2.3. Generation of CVT-based exposure models 66
4.2.4. Condition tree for multi-hazard exposure modelling 66
4.2.5. The classification of the building stock into vulnerability classes and aggregation 67
4.2.6. Scenario-based risk assessment 67
4.3. Application example 67
4.3.1. Context of the study area: Metropolitan Lima, Peru 67
4.3.2. Construction of earthquake and tsunami scenarios for Lima 68
4.3.3. Construction of focus maps for Lima 71
4.3.4. Generation of CVT-based exposure aggregation boundaries. 72
4.3.5. Classification of the building stock of Lima into vulnerability classes and aggregation 74
4.3.6. Comparisons of the obtained aggregation areas for exposure modelling 76
4.3.7. Results: scenario-based risk assessment 77
4.3.7.1. Seismic risk 77
4.3.7.2. Tsunami risk 78
4.3.8. Comparison between earthquake and tsunami scenario-based induced losses 82
4.4. Discussion 83
4.5. Conclusions 84

5. Scenario-based multi-risk assessment from existing single-hazard building fragility-models. An application for consecutive earthquakes and tsunamis in Lima, Peru 86

5.1. Introduction 87

5.2. Proposed Method 89

5.2.1. Exposure modelling: taxonomic description, inter-scheme conversion and spatial aggregation of building classes 90

5.2.2. The probabilistic description and compatibility of inter-scheme damage states 91

5.2.3. State-dependent fragility functions 92

5.2.4. Loss assessment for sequences of cascading hazards scenarios 94

5.3. Application example 94

5.3.1. Context of the study area: Metropolitan Lima, Peru 94

5.3.2. Scenarios of earthquake and tsunami for Lima 94

5.3.3. Exposure modelling: taxonomic description, inter-scheme conversion and spatial aggregation of building classes for Lima 95

5.3.4. Inter-scheme damage states for the models adopted for Lima 98

5.3.5. Tsunami state-dependent fragility functions for Lima 99

5.3.6. Cumulative damage from consecutive ground shaking and tsunami scenarios in Lima 102

5.4. Results 102

5.5. Discussion 106

5.6. Conclusions 108

6. Community Perception and Communication of Volcanic Risk from the Cotopaxi Volcano in Latacunga, Ecuador 110

6.1. Introduction 111

6.2. Framework and objectives 112

6.2.1. Description of the study area 113

6.2.2. Objectives 115

6.3. Materials and Methods 116

6.3.1. The CIS programme: the creation of a local laboratory to evaluate the social perception of risk and resilience 116

6.3.1.1. Comparative analysis of the social risk perception factors to natural hazards and the spatial distribution of volcanic-related risk factors 116

6.3.2. The RIESGOS project: iterative simulation improvement and enhanced communication 118

6.3.2.1. The RIESGOS demonstrator tool for quantitative multi-risk analysis 118

6.4. Results 120

6.4.1. The recognition of the Latacunga local laboratory by the local actors of the community 120

6.4.1.1. Comparative analysis of the social risk perception factors to natural hazards and the spatial distribution of volcanic-related risk factors 120

6.4.2. The communication of the scenario-based risk assessment concept with local stakeholders 123

6.5. Discussion 124

6.6. Conclusion 126

6.7. Appendix A 127

7. Synthesis 133

Bibliography 137

List of Figures

Figure 2-1. Location of the study area within (a) Chile, (b) the communes of Valparaíso and Viña del Mar (red) within the Valparaíso Region, and (c) the locations of the 604 surveyed buildings. Map data: ©Google Earth 2021. 15

Figure 2-2. Graphical representation of the (a) SARA and (b) HAZUS building classes. The colours encode the compatibility value with extremes in red and blue, representing high and low compatibilities, respectively. Grey indicates neutral and white refers to no explicit compatibility value being assigned. 16

Figure 2-3. Pictures of some selected buildings' façades surveyed in Valparaíso. Their classifications in terms of the SARA and HAZUS schemes are displayed considering the two weighting arrangements presented in Table 2-3. ©Google Street View, 2021. 17

Figure 2-4. Distributions of the most likely vulnerability classes of the 604 buildings surveyed in Valparaíso. This was achieved by evaluating the compatibility levels between the observed taxonomic building attributes and the typologies within each scheme: (a) SARA and (b) HAZUS. For each scheme we consider the two weighting arrangements (W.A-1, W.A-2) shown in Table 2-3. 17

Figure 2-5. Inter-scheme compatibility matrices for SARA (source) and HAZUS (target) for the residential building stock of Valparaíso. They are obtained from the weighting arrangements (a) W.A-1 and (b) W.A-2 for their common attributes (Table 2-3). 18

Figure 2-6. Posterior distributions obtained for the (a) SARA and (b) HAZUS schemes for the 604 inspected building surveyed in Valparaíso while considering different weighting arrangements (W.A.) and flat and informative priors. 19

Figure 2-7. Logic tree with four levels constructed to explore the impact of the building exposure composition modelling in Valparaíso. The twelve branches result from every considered scheme. The entire one is shown only for SARA, however, the same procedure has been carried out for HAZUS. 20

Figure 2-8. Dependency between the portfolio composition and the estimated total building counts (from dasymetric disaggregation of the population and occupancy). The subplots on the first column (top-down approach) comprises a single value of expected building counts either equally composed (i.e., with equal proportions) or as defined by the SARA model (GEM, 2014) and the respective weightings. The distributions in the other subplots correspond to every case of the logic tree of Figure 2-7. 21

Figure 2-9. Left: distribution of the slope-based Vs_{30} values in Central Chile (Allen and Wald, 2007) as provided by the USGS. Right: refined values within the study area using the former and the seismic microzonation reported in Mendoza et al. (2018). .. 22

Figure 2-10. First row: median values of the Mw 8.2 earthquake rupture for three IMs (a) PGA, (b) S.A. (0.3 s), and (c) S.A. (1.0 s) using the Montalva et al. (2017) GMPE. The earthquake hypocentre is depicted by a white square. The rupture plane is displayed by a green rectangle. The study area is shown by a yellow square. Second row: details of the study area with a single realisation of the cross-correlated seismic GMF for their corresponding spectral periods using the Markhvida et al. (2018) model. 22

Figure 2-11. Comparison of the scenario-based direct financial losses (USD) on the residential building stock in Valparaíso considering SARA and HAZUS (moderate code) using the 1,000 GMF for each case: with a spatially cross-correlation model (Corr.) and spatially uncorrelated (No Corr.). Different portfolio compositions are considered: top-down vision and expert elicitation (first column), equally composed portfolios (second one), and the customized posterior distributions of Figure 2-6. .. 23

Figure 2-12. Normalized loss exceedance curves (LEC) for different exposure compositions as depicted in the logic tree (Figure 2-7) for the SARA scheme. Curves are displayed in blue if the ground motion cross-correlation model was addressed and in yellow with spatially uncorrelated ground motions. LEC from their respective customized posterior distributions are displayed in non-continuous white curves. The single composition vision as informative priors (as defined by GEM) are depicted in purple when the spatially cross-correlated GMF were addressed and in red with spatially uncorrelated GMF. Black curves represent the losses of a portfolio whose composition is assumed to have equal proportions. 25

Figure 2-13. Normalized loss exceedance curves (LEC) for different exposure compositions as depicted in the logic tree (Figure 2-7) for the HAZUS scheme. Curves are displayed in blue if the ground motion cross-correlation model was addressed and in yellow with spatially uncorrelated ground motions. LEC from their respective customized posterior distributions are displayed in non-continuous white curves. The single composition vision as informative priors (from the inter-scheme conversion matrices in Figure 2-5) are depicted in purple when the spatially cross-correlated GMF were addressed and in red with spatially uncorrelated GMF. In every plot, the LEC values from their respective posterior distributions are displayed in non-continuous white curves. Black curves represent the losses of a portfolio whose class composition is assumed to have equal proportions. 26

Figure 2-14. Normalized losses (a, b) SARA and (c, d) HAZUS schemes for the exposure compositions in Valparaíso for two selected $\alpha 0$ values. The loss curve from the top-down assumption (from expert-based priors) is used as benchmark. 27

Figure 2-15. Normalized losses for the earthquake scenario in Valparaiso for SARA and HAZUS schemes. Plots show sensitivity on (a) the selection of the weighting arrangement (wj), and (b) the portfolio composition, either from a top-down vision (Prior) or including surveyed evidence (Post.). The normalization nomenclature (i.e., $||\ ||$) is used to distinguish the benchmarks 28

Figure 3-1. Location of the study area within (a) Chile, (b) Valparaíso Region (grey) and Valparaíso Province (red) (c) Communes of Valparaíso and Viña del Mar, (d) a detail of the two communes showing Sentinel-2 images for September 21st, 2019 (downloaded from the Copernicus Open Access Hub of the European Space Agency (ESA). Map data: ©Google Earth 2019. Edited from Zafrir, (2020) and Gómez Zapata et al., (2022b). 35

Figure 3-2. Flowchart outlining the input data gathered, the processes and the three resulting residential building exposure model for Valparaíso (Chile) we will be presenting. These exposure models, together with the parametric ground motions, are used as inputs for the sensitivity scenario-based seismic risk in the last stage of this study. 36

Figure 3-3. Building counts at the commune level. For 15 SARA building classes (after having combined similar typologies (Sect. 3.3.2.1)). the colour scale represents the material type (green: wooden; orange: masonry; blue: reinforced concrete). 39

Figure 3-4. Fragility functions for 15 SARA building classes as reported by Villar-Vega et al., (2017) describing their differential seismic vulnerabilities. The curves are presented in a similar order as in Figure 3-3..... 40

Figure 3-5. Inferred ranges of residential building counts in the study area. This outcome is obtained from the spatial disaggregation of night-time residents at the block level as reported by the official 2017 Chilean census. 41

Figure 3-6. Spatial distributions of the building counts for the six subcategories in the range A-F obtained from the preliminary model. The latter involves a simple downscaling using the dasymetric disaggregation of the population based on of use of night-time residents at the block level as reported by the official 2017 Chilean census..... 42

Figure 3-7. Spatial distributions of the building counts for the SARA typologies obtained from the preliminary downscaled model. The colour scale reflects the material type (green: wooden; orange: masonry; blue: reinforced concrete). 43

Figure 3-8. Building footprints for a certain area in Valparaíso (© OpenStreetMap contributors 2021. Distributed under the Open Data Commons Open Database License (ODbL) v1.0). Map data: ©Google Earth 2020. Figure reprinted from Zafrir, (2020).. 44

Figure 3-9. Spatial distributions of the building counts for the subcategories in the range A-F obtained from the probabilistic model in Valparaíso. 45

Figure 3-10. Spatial distributions of the building counts for the SARA typologies obtained from the probabilistic model in Valparaíso. The colour scale is selected in terms of the material type (green: wooden; orange: masonry; blue: reinforced concrete). 46

Figure 3-11. Comparison of the building counts per SARA typology for the three exposure models considered for Valparaíso: Initial commune-based model with merged classes, the preliminary model (simple downscaling), and the Bayesian model. 47

Figure 3-12. Distribution of the Vs_{30} values in Valparaíso and Viña del Mar (a) considering 600 m/s uniformly distributed all through; (b) as proposed by the USGS (Heath et al., 2020); and (c) its combination with the seismic microzonation (Mendoza et al., 2018). 50

Figure 3-13. Median values of the Mw 9.1 earthquake for three IMs (a) PGA, (b) S.A. (0.3 s) and (c) S.A. (1.0 s) using the (Montalva et al., 2017) GMPE. The earthquake hypocentre is shown as a white dot. The rupture plane is represented as a green rectangle. 50

Figure 3-14. Single realisation of a GMF with these conditions:(a) PGA uncorrelated; spatially correlated (JB) (Jayaram and Baker, 2009) for (b) PGA, (c) S.a(0.3 s), (d) S.a(1.0 s); and cross-correlated (MK) (Markhvida et al., 2018) for (e) PGA, (f) S.a(0.3 s), (g) S.a(1.0 s). 50

Figure 3-15. Normalised loss for the earthquake scenario in Valparaíso for the three exposure models (in each subplot) and 27 ground motions assemblages using the set of uncorrelated ground motions with Vs_{30} (Topogr.), and the Abrahams, 2015 GMPE as benchmark..... 51

Figure 3-16. Similar information as shown in Figure 3-15 showing the normalised loss differences between each exposure model. 52

Figure 3-17. Land use classification for the study area. Map data: ©Google Earth 2020. Figure modified from Zafrir, (2020) 55

Figure 3-18. Categories according to the available input data in the study area. 136 grid cells represented by green colour have information of build-up height according to Zafrir, (2020) as well as the OSM footprint area (Sect. 3.3.2.3.1), 51 grid cells represented with blue colour have information about the build-up height and density from remote sensing data products (as studied by Zafrir, (2020)), 158 grid cells represented by orange colour have a complete information only about the footprint area from OSM, and 39 grid cells represented by pink colour have no input information. Map data: ©Google Earth 2020. Figure modified from Zafrir, (2020)..... 55

Figure 3-19. Building façade of an inspected building, with ID=599 in Merino-Peña et al., (2021)..... 57

Figure 3-20. Distribution of attributes values within the GEM V.2.0 taxonomy for 604 inspected buildings in Valparaíso for: (a) material type, (b) material technology, (c) non- structural exterior walls, and (d) lateral load-resisting system..... 57

Figure 3-21. Resulting fuzzy compatibility scores for the building in Figure 3-19 with respect to the SARA typologies. The solid and dashed segment represent the equivalent defuzzified values according to the mode, median or mean value of the triangular fuzzy numbers. 59

Figure 3-22. Distribution of the SARA typologies for the sample constituted by 604 surveyed buildings randomly distributed throughout Valparaíso..... 59

Figure 3-23. (a) Footprint area distribution for a given grid cell, with a mean ~81 m^2. (b) The posterior distribution obtained for that grid cell after having maximised the likelihood function which, in this case, was for low rise buildings. Adapted from Zafrir et al., (2020). 61

Figure 4-1. Median seismic ground motion for a single realisation using the Montalva et al., (2017) GMPE for peak ground acceleration (PGA) and spectral acceleration (SA) for periods 0.3 s and 1.0 s, and for three scenarios (Mw 8.6, 8.8 and 9.0) along the Peruvian subduction zone. Green rectangles represent the rupture planes. Hypocentres are shown by white dots. The study area (Metropolitan Lima) is enclosed within a yellow rectangle. For this area, and for the Mw 8.8 scenario, there is shown one realisation of spatially cross-correlated ground motion field per spectral acceleration. Tsunami inundation heights for the three selected scenarios are displayed for the study area. The northern "La Punta" sector (Callao district) and the southern Chorrillos district are indicated by white rectangles. Map data: ©Google Earth 2021. 69

Figure 4-2. Section of the triangular mesh used for the TsunAWI simulations in the La Punta sector (Callao district). The mean resolution in the pilot area is approximately 20 m, whereas the shortest edge length measures about 7 m. The basemap and data are from © OpenStreetMap 2021. Distributed under the Open Data Commons Open Database License (ODbL) v1.0). 70

Figure 4-3. Section of the triangular mesh together with the inundation data product (10 m raster) for the tsunami scenario involving a magnitude 8.8 event in the Callao Harbour area. The basemap is from © OpenStreetMap contributors 2021. Distributed under the ODbL v1.0 License..... 70

Figure 4-4. Expected tsunami inundation height (m) for two local areas within Lima for six tsunami scenarios (with locations in Figure 4-1). Map data: ©Google Earth 2021. 71

Figure 4-5. Example of the construction of focus maps for Lima. (a) 5,000 weighted seeding points sample a focus map through a Poisson point process. The normalised focus map is constructed from a log-linear pooling algorithm of the combined layers (population density (PD) and tsunami inundation height (TI) with a selection of 30% and 70% weights respectively). Map data: ©Google Earth 2021. 72

Figure 4-6. The resultant CVT geocells from the focus maps shown above. The common exposed area to a Mw 9.0 earthquake and tsunami is coloured in pink whilst the area only exposed to seismic risk is coloured in grey. Map data: ©Google Earth 2021. 73

Figure 4-7. Spatial distribution of Vs_{30} values in Lima/Callao as reported by Ceferino et al. (2018b) enclosed within the CVT-based model PD30_TI70_5,000. 73

Figure 4-8. Flowchart outlining the process for constructing the building exposure model for Metropolitan Lima, including the condition tree used for the construction of CVT-based exposure models for the aggregation of earthquake and tsunami vulnerability building classes. (*District-based aggregation entities are only used for seismic risk to compare absolute loss values). 74

Figure 4-9. Inter-scheme compatibility matrices for Lima showing the compatibility level between the seismic-oriented reference scheme SARA and the tsunami-oriented target schemes: Left: Suppasri et al., (2013) and Right: De Risi et al., (2017). 75

Figure 4-10. Example of the building class frequency distribution in "La Punta" (Callao) mapped using the seismic oriented- SARA scheme (Yepes-Estrada et al., 2017) (a) At the block level, (b) at the CVT based model PD30_TI70_5,000. The latter model is used to aggregate the tsunami vulnerability oriented building classes: (c) Suppasri et al. (2013) and (d) De Risi et al. (2017). Map data: ©Google Earth 2021. 76

Figure 4-11. Variability in the area (in meters square) of the geocells of every aggregation area for exposure modelling, for (a) the entire urban area of Lima, and (b) for the area for which tsunami-induced loss values were obtained for the Mw 9.0 scenario. Seven models are evaluated: the administrative block-based model and six CVT. The percentages assigned to the two focus maps' components (PD= Population density, and TI= tsunami inundation height) are written, and are followed by the sampling seeding points. 76

Figure 4-12. Computed loss distributions from a Mw 8.8 scenario for the residential building stock of Lima classified in terms of the SARA vulnerability classes aggregated into eight geographical entities. Two ground motion field conditions are analysed in every case, namely with the selected cross-correlation model (Corr.) and with uncorrelated ground motion fields (No Corr.)..... 78

Figure 4-13. Spatially distributed losses in the "La Punta" sector (Callao) induced by seismic ground-shaking of a Mw 8.8 earthquake scenario. They are mapped over six aggregation areas of the building portfolio classified in terms of the SARA vulnerability classes. This is done for two randomly selected realisations with uncorrelated ground motion fields and cross-correlated ground motion fields using the Markhvida et al., (2018) for the periods PGA, 0.3 s and 1.0 s. Map data: ©Google Earth 2021..... 79

Figure 4-14. Losses induced by six tsunamis for the six CVT models normalised with respect to the ones at the block level. Tsunami vulnerability has been computed using the set of building classes proposed in (a) Suppasri et al. (2013) and (b) De Risi et al. (2017). 80

Figure 4-15. Absolute losses (USD) for six tsunami scenarios for the residential building portfolio of Lima classified in terms of two reference schemes and aggregated at the block-based model. 80

Figure 4-16. Discrepancy between the tsunami-induced losses between each CVT-based model and the block model for the six scenarios. The values obtained from the Suppasri et al., (2013) and De Risi et al., (2017) schemes are denoted by stars and circles respectively. 80

Figure 4-17. Spatial distribution of tsunami-induced normalized losses (Mw 8.8 scenario) for the La Punta sector (Callao district). Map data: ©Google Earth 2021. 81

Figure 4-18. Spatial distribution of tsunami-induced normalized losses (Mw 8.8 scenario) for the Chorrillos district (Lima) using two tsunami reference schemes (a) Suppasri et al., 2013 and (b). De Risi et al., 2017. Map data: ©Google Earth 2021. 82

Figure 4-19. Comparison of the independent earthquake-induced losses (EQ) for two conditions (using the 1,000 GMF for each case: with a spatially cross-correlation model (Corr.) and spatially uncorrelated (No Corr.); and the tsunami-induced losses (TS) under two TS reference schemes for six magnitude scenarios over every common area exposed to both perils. 83

Figure 5-1. (a) Example of the principle proposed for classifying the same building class into two hazard-dependent reference schemes with associated fragility models. (b) Schematic representation of the proposed method to calculate cumulative damage from the case of earthquake-tsunami that is developed afterward. 90

Figure 5-2. Scale to assess the damage level on buildings as proposed by the AeDES form. Reprinted from Baggio et al, (2007). 91

Figure 5-3. Example of a set of damage state-dependent fragility functions for several single hazard fragility functions comprising progressive transition probabilities. Figure modified from Gómez Zapata et al., (2020). 93

Figure 5-4. Expected tsunami inundation heights for three out of the six considered scenarios per moment magnitude (Mw). These raster products are available from Harig and Rakowsky, (2021). Two densely populated areas are depicted by white rectangles: in the north the "La Punta" (Callao) and Chorrillos in the south. Updated figure from Gómez Zapata et al., (2021e). Map data: ©Google Earth 2021. 95

Figure 5-5. Spatial distribution of the percentage of the main structural material of the residential buildings in Metropolitan Lima in each CVT (Central Voronoi Tessellation) geocell using the dataset of Gómez Zapata et al., (2021b). The colour scale represents the material type: (a) masonry and earthen (red); (b) reinforced concrete, RC and Unknown, UNK (blue); (c) wooden types (green). Only CVT that intersected the census-based blocks (INEI, 2017) are shown. 97

Figure 5-6. Classification of the buildings in the maximum exposed area to both perils (Mw 9.0 scenario) in terms of the (a) seismic-vulnerability oriented SARA classes (used as a source scheme) and (b) the inter-scheme conversion matrix. The former two models are used as inputs to obtain the (c) proportions for the tsunami-oriented building classes of Medina (2019). 98

Figure 5-7. Examples of the AeDES-based heuristics (see original AeDES form (Baggio et al., (2007) on Figure 5-2)) that describe the expected observable damage onto the four selected building components listed in Eq. 5-5 (vertical structure (VS); floor (FL); roof (RF); infills and partitions (IP)) using the scale from I-A (i.e., I=0 (null) to A=9 (>2/3 extension within the "very heavy" damage level). This is done per damage state per building class within two hazard-dependent vulnerability schemes. 99

Figure 5-8. Predicted likelihood probabilities of classifying each damage state of two building types that belong to the earthquake-oriented (EQ) vulnerability scheme SARA (***DkzA*** (with building types k and sets of damage states z)) and two building types that belong to the tsunami-oriented (TS) scheme Medina (***DjyB***, with building types j and sets of damage states y). These features comes from having scored the likely observable damage $\{\boldsymbol{OD}\}\boldsymbol{n}$ onto the building components listed in Eq. 5-5 in terms of the AeDES scale (i.e., 0=L - 9=A (e.g., as shown in Figure 7). The predicted likelihood probabilities on the figure are only shown for the building components VS (vertical structure) and IP (infills and partitions) for masonry buildings (subplots a, c) and wooden buildings (subplots b, d). 100

Figure 5-9. Probabilistic inter-scheme damage compatibility matrices for three pairs of building classes: (a) Masonry, (b) Wooden, and (c) Reinforced concrete (RC). The pairs of building typologies shown had the greatest compatibility in Figure 5-6b. Their respective fragility functions are comprised within the source earthquake-oriented (EQ) vulnerability scheme SARA (***DkzA***, with building types k and sets of damage states z) and the target tsunami-oriented (TS) scheme Medina (***DjyB***, with building types j and sets of damage states y). 101

Figure 5-10. Analytical tsunami fragility functions with initial undamaged state as proposed by Medina, (2019) (continuous lines) and derived state-dependent fragility curves (non-continuous lines) in terms of flow depth (m) as IM for six building classes: (a) M-MP (masonry), (b) M-PN (wooden), (c) M-PCP1-T1 (framed reinforced concrete (RC), one storey with similar length-width ratio), (d) M-PCP1-T2 (framed RC, one storey, with a higher length to width ratio), (e) M-PCP2 (framed RC, 2 storeys, (f) M-PCP3 (framed RC, 3 or more storeys). 101

Figure 5-11. Proposed workflow for multi-risk assessment in Lima from each pair of consecutive earthquake and tsunami scenarios. A Mw 8.8 event is displayed as an example (subplot a). The processes regarding the natural hazardous events are highlighted in green. Blue and orange indicate the exposure and vulnerability processes, respectively. The spatially cross-correlated ground motion fields (subplot b) and an initial exposure model (with earthquake-oriented classes, in subplot d) are inputs for the seismic vulnerability process using analytical fragility functions for ground-shaking (subplot c), which provides the damage-updated exposure models (subplot f). The reference scheme conversion processes (building classes and damage states shown in subplot g) that generate the sets of damaged-exposure models are, together with the tsunami inundation models (subplot e) the inputs used by the state-dependent tsunami fragility functions (subplot h) to finally obtain the distribution of cumulative damages and losses (red box in subplot i) 103

Figure 5-12. Five loss exceedance curves for the residential building portfolio of Lima are presented in six subplots per earthquake magnitude scenario (M_w (8.5-9.0). Three out of the five curves represent the disaggregated losses per hazard event: shaking-induced losses only (blue); far-field tsunami-induced losses (initial undamaged state, purple); state-dependent tsunami-induced losses (with pre-existing shaking induced damage, orange). The green curves represent the losses expected from the cascading sequence. The red ones show the losses derived solely using empirical tsunami fragility functions (implying that they have an implicit contribution by the earthquake phase) 104

Figure 6-1. Location of the main volcanic systems in the Ecuadorian Andes highlighting the location of the Cotopaxi volcano and Latacunga. Modified after Andrade et al., (2005). 113

Figure 6-2. Left picture: Channel of the Cutuchi River in the city centre of Latacunga. An old textile factory is visible, which has been buried up to the fourth story by the 1877 lahar. Right picture: Thick sequence of lahar deposits, scoria flow deposits and tephra beds exposed in a quarry along the Rio Saquimala close to Mulalo. (Photos: Theresa Frimberger, 2018)..... 114

Figure 6-3. (a) Location of the Cotopaxi volcano and the main drainages and populated centres. (b) Estimated lahar footprints in the southern drainage system from three scenarios as function of the VEI (Volcanic Explosivity Index). (c) Brief description of the eruption scenarios expected at Cotopaxi in terms of the VEI. Modified after (Andrade et al., 2005; Frimberger et al., 2020). 115

Figure 6-4. (a) Population qualified for the survey to evaluate the social risk perception in the urban centre of Latacunga (b) Sites to survey within the residential buildings. Modified after (Grupo FARO et al., 2020). 117

Figure 6-5. Graphical scale and correspondence between the pre-index value and the reduced index. 118

Figure 6-6. Example of the graphical representation of loss distribution due to ash fall scenario in the RIESGOS demonstrator (as of December 2020) from a previously selected VEI. Reddish and greenish aggregation areas representing higher and lower values respectively. On top of these results, the lahar model (with the same VEI) is displayed as input to calculate the cumulative damage over the same geo-cells exposed to both perils. 120

Figure 6-7. Spatial representation of the perception of volcanic hazards in the urban centre of Latacunga in terms of (a) recurrence; (b) exposure level; (c) vulnerability; (d) resilience; (e) subjective risk; (f) risk index calculated using the former components as inputs. Modified after (Grupo FARO et al., 2020). 123

Figure 6-8. Example of the graphical representation of the spatially distributed ash fall intensities as isolines in the RIESGOS demonstrator (as of December 2020) from a previously selected VEI. The thickness values are displayed. Once a point within the isolines is clicked, the expected load (kPa) value is also shown. 129

Figure 6-9. Example of the graphical representation of the footprint and intensities of the lahars in the RIESGOS demonstrator (as of December 2020) from a previously selected VEI. On the top-right side of the window, the outputs of the lahar simulation are listed (i.e. lahar flow velocity, flow depth, pressure, erosion and deposition) 129

Figure 6-10. Example of the graphical representation of the residential building exposure model in the RIESGOS demonstrator (as of December 2020). It is represented into aggregation areas based on the official rural and urban administrative divisions of Latacunga. There are displayed the quantities of every ash fall risk oriented building class proposed in Torres-Corredor et al., (2017) within a selected area. 130

Figure 6-11. Example of the graphical representation of damage state distribution due to the combined effect of ash falls and lahar scenarios in the RIESGOS demonstrator (as of December 2020) calculated using the method proposed in Gómez Zapata et al., 2020; Langbein et al., (2020). 130

Figure 6-12. Example of the visualization of the expected interruption probabilities in the RIESGOS demonstrator (as of December 2020) of the electrical power network due to the action of a lahar scenario. 131

List of Tables

Table 2-1. Building classes in terms of the SARA scheme proposed for Valparaíso with the respective intensity measure of their associated fragility functions (as reported in Villar-Vega et al. 2017). Prior proportions per building class, average night-time residents (Res. /bdg), and replacement cost (Repl. Cost (USD/bdg)) are reported as in Yepes-Estrada et al. (2017). 15

Table 2-2. Building classes and short description of the HAZUS scheme (FEMA, 2012) proposed for Valparaíso. 15

Table 2-3. Sets of weighting arrangements that score the common attribute types of the SARA and HAZUS schemes. 16

Table 2-4. HAZUS Building classes for Valparaíso together with two sets of their prior proportions, average night-time residents (Res /bdg.) and replacement cost (Repl. Cost (USD/bdg.). They are assumed to be the same as the highest compatibility score with respect to a class of SARA from every inter-scheme compatibility matrix displayed in Figure 2-5. 18

Table 3-1. SARA building classes proposed for the study area along with short descriptions. Average number of dwellings (Dwel./ bdg), night-time residents (Res. /bdg) and replacement cost (Repl. Cost (USD)) are reported as in Yepes-Estrada et al., (2017). Average footprint area (Ft./bdg m^2) values are derived from the construction quality categories per dwelling as suggested by Yepes-Estrada et al. (2017) and the mean range of storeys and dwellings per class (see Table 3-4). A new typology in the range A- F is proposed in terms of the similarities of their footprint areas. 38

Table 3-2. Average footprint areas and heights derived for the six subcategories in the range A-F for Viña del Mar and Valparaíso 38

Table 3-3. Comparison between the counts and frequencies for each building typology of the three considered exposure models. 47

Table 3-4. Procedure followed in deriving the building footprint area values for each SARA typology in Valparaíso according to the description provided in Sect. 3.3.2.1. 56

Table 3-5. Data collection for the building in Figure 3-19. 57

Table 3-6. Short description of observed attribute values incorporated into the four attribute types in Figure 3-20. 58

Table 4-1. Summary of TsunAWI model parameters used in the tsunami simulations. 68

Table 4-2. Variability of area (km^2) and file-size (MB) across the exposure models proposed for (a) the entire urban area of Metropolitan Lima, and (b) for the area exposed to the tsunami from the Mw 9.0 scenario event. Only geocells with an urban land use are considered. 77

Table 5-1. SARA building classes proposed for the residential building stock of Metropolitan Lima and Callao, with their respective replacement costs per building unit (Repl. Cost (USD/bdg.) as reported in Yepes-Estrada et al., (2017) in the frame of the SARA model released by GEM (Global Earthquake Model) in 2015, which was based on official census data reported by INEI, (2007). The intensity measures (IM) of the associated seismic fragility functions to each building class, as reported in Villar-Vega et al., (2017), are also provided. 96

Table 6-1. Hazard matrix and perception of risk factors towards natural hazards in the urban area of Latacunga. 121

Table 6-2. Example of the procedure for calculating the risk perception pre-index. 127

Table 6-3. Questionnaire within the survey to assess the social risk perception to volcanic risk in the urban area of Latacunga. The mean values of the entire survey are reported. Adapted after Grupo FARO et al., (2020). 128

Chapter 1

1. Introduction

The risk of communities being exposed to single and multiple natural hazards has been increasing in the last decades. Although the occurrence of independent hazards has not changed much during human history, there are nowadays more complex interactions between hazards, either acting simultaneously or in close succession, that have been affecting more communities around the world with sometimes devastating effects. Moreover, urban areas with susceptible infrastructure and rapidly growing populations have been expanding to territories where they are nowadays more exposed to hazardous events than ever before. To anticipate the likely consequences that these hazards might cause to the exposed assets and people, practitioners, engineers, and scientists have proposed several types of risk assessment over the years (i.e., index-based, probabilistic methods, and scenario-based models).

Classical probabilistic and scenario-based risk models for large-area residential building portfolios comprise three components (i.e., hazard, exposure, and vulnerability). While some researchers have made significant efforts to study the causes, and likely spatial distribution of the potential hazards to occur in specific regions, others have focused on studying the different physical vulnerability of various types of assets subjected to hazard intensities that are usually addressed independently. Notably, within these three components, the exposure module has comparatively received less research attention. Conventional exposure models localise assets of interest within a region (e.g., large-area residential building portfolios) over administrative areas that are beforehand categorised as a function of their susceptibility to single or multiple hazards into mutually exclusive and collectively exhaustive building typologies. For risk assessment, these classes are assigned to vulnerability models which comprise fragility functions and the so-called consequence model (e.g., replacement costs). These predefined classes are the so-called "risk-oriented taxonomies" (Pittore et al., 2018) and are not always unequivocally used to classify heterogeneous building stocks and are often linked to vulnerability functions calibrated elsewhere (not for the specific area of application).

Therefore, there can be several epistemic uncertainties associated with the exposure definition (composition and spatial aggregation), that are in turn correlated with the variance in the risk estimates. As the degree of knowledge of the building portfolio increases, i.e., through high-quality observation; through the integration of freely available crowdsourced data and statistical analysis; or through the careful selection of the spatial aggregation entities, these epistemic uncertainties on risk models can be successively explored and reduced. A logical pathway is to first evaluate how tuning these exposure sub-components may modify the risk outcomes if one considers only the action of single hazards, and then, increase the complexity by performing such an investigation in a multi-hazard context.

Methodological shortcomings and uncertainties entailed by the exposure subcomponents can be more pronounced in a multi-hazard context. Classical multi-hazard risk models for buildings that make use of empirical fragility models derived from field reconnaissance after a sequence of hazards, implicitly comprised the observation of the damage caused by compound or cascading events. However, they are usually local models designed for specific construction practices and geographical settings. Likewise, these fragility functions mostly depend upon a single observed hazard intensity measure (typically the lastly acting one during the sequence of hazards). Hence, their extrapolation in other geographical contexts is not straightforward nor always trustful for risk assessment. Besides, in multi-hazard risk, there is still the necessity of standardizing the descriptions of observable damage features after the occurrence of any type of

hazardous event through harmonising scales. This standardisation is relevant because it can allow to include and update the information related to the damage within the exposure modelling process. If a probabilistically-sound method can be proposed for such a harmonisation, alternative methods that allow reusing existing vulnerability models (that were individually calibrated by experts) can be proposed for a multi-risk context. This setting could also contribute to assessing the cumulative damage on the exposed assets from various hazards intensities of different nature acting in close succession and pave the way towards the disaggregation of the losses per hazard scenario.

Thereby, this thesis contributes to filling out some of the gaps in the state of the art related to three subcomponents entailed to the exposure modelling, i.e., (1) composition (proportions assigned to each typology); (2) spatial aggregation (selection of boundaries to represent building stocks); (3) and pre-existing damage (observable damage onto buildings before the occurrence of a hazardous event). This is done to understanding their respective and individual roles in scenario-based risk assessment of single and multiple hazards. The study of these subcomponents has been done through the adoption of fixed risk scenarios. A risk scenario, as stated in Li et al., (2016), is considered a situation picture in which a hazardous event with a certain probability would occur and cause some damage. Such an adoption allows isolating the study of the exposure sub-component of interest while reducing the degrees of freedom and investigating how their individual uncertainties are propagated throughout the risk chain. Thus, optimally designed exposure models can contribute to obtaining comprehensive outcomes from scenario-based risk models. In this sense, risk scenarios are not only important for research and insurance purposes, but also for risk communication practices. The use of risk scenarios has been increasingly shown to be beneficial for risk communication initiatives due to its more intuitive presentation to stakeholders in comparison with probabilistic hazard approaches. Thereby, the related outcomes of the risk models due to single and multiple natural hazards might be of interest to stakeholders for decision making, i.e., to propose mitigation strategies, landscape planning, response planning, design of evacuation routes, and enhancing overall preparedness to future hazardous events.

1.1. Scope of the thesis

Deterministic scenarios (either single or multi-hazard) were used throughout the development of this thesis. First, the importance of constraining various subcomponents of the exposure modelling process into a single scenario-based hazard vulnerability (i.e., ground shaking) is presented. Then, this thesis moves towards its application to multi-hazard risk and risk communication activities. Reducible epistemic and thematic uncertainties linked to those modelling processes are implicitly addressed throughout such a piece-wise analysis.

Several research questions are tackled through the development of this thesis:

- Can we identify the sources of epistemic uncertainties embedded within probabilistic exposure models and propagate them to assess their role in earthquake loss models?
- Can we make use of freely open data from volunteering geo-information activities to probabilistically update and continuously refine the composition and resolution of exposure?
- Can we find optimal geographical units for exposure aggregation and risk assessment that are compatible with the spatial variability of the hazard intensities or exposure proxies (e.g. population)?
- Can single-hazard vulnerability models that have been already individually calibrated be harmonised and reused within a holistic framework that allows multi-hazard risk assessment in residential building portfolios?
- Can we assess the cumulated damage and losses that are expected from residential building stocks affected by cascading hazards?
- Can we contribute improving the forecasting of direct economic losses induced by hazard scenarios on real important urban areas exposed to single and multiple (sometimes consecutive) hazards?
- Can we effectively communicate risk to directly exposed communities while considering their own risk perception?
- Can we work on an interdisciplinary and modular approach that facilitates risk communication and enhances the preparedness of communities?

1.2. Presentation of the study

Having in mind the aforementioned shortcomings and the need of improving the current practices entailed in exposure modelling activities, ***Chapter 2*** contributes to the implementation of a Bayesian approach to probabilistically model stochastic building portfolios and update its composition through the integration of prior distributions with field observations. The adoption of this approach allowed the investigation of various epistemic uncertainties embedded in exposure models as well as their differential impact on scenario-based seismic risk models. The description of buildings in terms of taxonomic attributes is remarked herein to classify portfolios into other sets of classes as well as for transparent data collection.

Although field inspections of building attributes are great input to constrain the composition of probabilistic building exposure models, it could be the case, that the number of sampled assets is not statistically representative of the total number of buildings within the area of interest. Completing the visual inspection of such a sample, especially for large urban areas, might be unfeasible. To tackle that shortcoming, ***Chapter 3*** shows how the increasing availability of Volunteered Geo-Information (VGI) data can be useful to generate and update probabilistic building exposure models. Through a simple land-use land-cover classification from remote sensing imagery, this chapter also highlights the importance of accurately constraining the spatial aggregation areas of the exposure models.

Traditional exposure models for building portfolios for risk estimations have been spatially aggregated onto coarse administrative areas that are not correctly capturing the spatial variability of the hazard intensity of interest. If the same building stock is exposed to multiple hazards (often with contrasting spatial variabilities), one can realise that finding an optimal exposure aggregation area that can be simultaneously compatible with such hazard intensities is a problem with increasing complexity. To track that objective, ***Chapter 4*** presents and compares decoupled estimations of the scenario-based earthquake and tsunami loss assessment while raising awareness about the efficiency and uncertainties related to the selection of spatial aggregation entities for the mapping of the risk metric. Two sets of tsunami-oriented sets of building classes with existing empirical tsunami fragility models (constructed by others after in-situ damage reconnaissance) are used during the loss estimates. This chapter concludes that as the earthquake magnitude increases, the expected losses might be controlled by ground shaking. This result is not particularly surprising because empirical tsunami fragility models were derived from buildings that suffered cumulative damage due to the joint effect of the tsunami-generating earthquake and the tsunami itself.

To calculate the cumulative damage and losses that a building stock exposed to cascading hazards may experience, ***Chapter 5*** presents a novel and integrative method that reuses and probabilistically harmonise existing fragility/ vulnerability models available in the literature. A set of analytically derived state-dependent tsunami fragility functions that capture the previous damage due to ground shaking replace the traditional empirical ones. Taxonomic building attributes are an important input to characterise the observable damage across the different hazard-related vulnerabilities. This aspect relies on some of the ideas presented in Chapter 1 about the importance of standardized vulnerability-independent taxonomies, which combined with sound probabilistic modelling are instrumental for more robust risk assessment practices.

Chapter 6 presents the integration between exposure models constructed for another multi-hazard setting (i.e., a volcanic environment) and carefully chosen multi-hazard risk scenarios into an explorative tool designed for risk communication initiatives. This is a proven application that was presented to a directly exposed community while studying their own risk perception.

1.3. Author's Publications and Contributions

1.3.1. Publications in the frame of the thesis

1. **Chapter 2:**
   Published as: Gómez Zapata, J.C., Pittore, M., Cotton, F., Lilienkamp, H., Simantini, S., Aguirre, P., Hernan, S.M., 2022b. Epistemic uncertainty of probabilistic building exposure compositions in scenario-based earthquake loss models. *Bulletin of Earthquake Engineering.* https://doi.org/10.1007/s10518-021-01312-9
   J.C.G.Z and M.P conceived the study. J.C.G.Z wrote the manuscript. J.C.G.Z and S.S conducted the data processing based on surveys supervised

by P.A and H.S. F.C and M.P supervised the study and reviewed the manuscript.

2. **Chapter 3:**
Published as: Gómez Zapata, J.C.; Zafrir, R.; Pittore, M.; Merino, Y. Towards a Sensitivity Analysis in Seismic Risk with Probabilistic Building Exposure Models: An Application in Valparaíso, Chile Using Ancillary Open-Source Data and Parametric Ground Motions, *ISPRS International Journal of Geo-Information* 11, no. 2: 113. https://doi.org/10.3390/ijgi11020113.
Conceptualization, M.P, J.C.G.Z. and Raquel Zafrir; methodology, M.P; investigation, R.Z, J.C.G.Z. and Y.M; writing—original draft preparation, J.C.G.Z and R.Z; writing—review and editing J.C.G.Z; supervision, M.P. All authors read and agreed to the published version of the manuscript.

3. **Chapter 4:**
Published as: Gómez Zapata, J.C., Brinckmann, N., Harig, S., Zafrir, R., Pittore, M., Cotton, F., Babeyko, A., 2021. Variable-resolution building exposure modelling for earthquake and tsunami scenario-based risk assessment. An application case in Lima, Peru. *Natural Hazards and Earth System Sciences* 21, 3599–3628. https://doi.org/10.5194/nhess-21-3599-2021
J.C.G.Z and M.P conceived the study. J.C.G.Z wrote the manuscript. N.B contributed to software development. S.H carried out the tsunami simulations. R.Z contributed to visualisation, and H.S. M.P, F.C, and A.B supervised the study and reviewed the manuscript.

4. **Chapter 5:**
Published as: Gómez Zapata, J.C., Pittore, M., Brinckmann, N., Lizarazo, J., Medina, S., Tarque, N., Cotton, F., 2022. Scenario-based multi-risk assessment from existing single-hazard building fragility-models. An application for consecutive earthquakes and tsunamis in Lima, Peru. *Natural Hazards and Earth System Sciences*. Discuss. [preprint], https://doi.org/10.5194/nhess-2022-183
J.C.G.Z and M.P conceived the study. J.C.G.Z wrote the manuscript. J.C.G.Z conducted the data processing and formal analysis. N.B contributed to software development. J.L and S.M developed analytical tsunami fragility functions. N.T provided input to the synthetic scorings of observable damage per building typology. M.P and F.C supervised the study and reviewed the manuscript.

5. **Chapter 6:**
Published as: Gómez Zapata, J.C; Parrado, C.; Frimberger, T.; Barragán-Ochoa, F.; Brill, F.; Büche, K.; Krautblatter, M.; Langbein, M.; Pittore, M.; Rosero-Velásquez, H.; Schöpfer, E.; Spahn, H.; Zapata-Tapia, C. 2021, Community Perception and Communication of Volcanic Risk from the Cotopaxi Volcano in Latacunga, Ecuador. *Sustainability,* 13, 1714. https://doi.org/10.3390/su13041714
Conceptualization, J.C.G.Z., M.P., C.P.; methodology, M.P., C.P., E.S., F.B-O., H.S.; software, M.L.; validation, T.F., C.Z.-T., C.P.; formal analysis, J.C.G.Z., F. B-O., C.P.; investigation, T.F., F.B., K.B., M.K.; resources, C.Z.-T.; data curation, J.C.G.Z., M.L, H.R.; writing—original draft preparation, J.C.G.Z., M.L., C.P.; writing—review and editing, T.F., F.B., J.C.G.Z.; visualization, T.F., F.B-O., M.L.; supervision, H.S.; project management, E.S.

1.3.2. Publications not associated with the thesis

1. Aristizábal, C., Bard, P.-Y., Beauval, C., Gómez, J.C., 2018. Integration of Site Effects into Probabilistic Seismic Hazard Assessment (PSHA): A Comparison between Two Fully Probabilistic Methods on the Euroseistest Site. *Geosciences* 8. https://doi.org/10.3390/geosciences8080285

2. Feliciano, D., Arroyo, O., Cabrera, T., Contreras, D., Valcárcel Torres, J.A., Gómez Zapata, J.C., 2022. Seismic risk scenarios for the residential buildings in the Sabana Centro province in Colombia. *Natural Hazards and Earth System Sciences Discussions* 2022, 1–33. [preprint], https://doi.org/10.5194/nhess-2022-73

3. Geiß, C., Aravena Pelizari, P., Calderon, A.R.S., Schöpfer, E., Langbein, M., Riedlinger, T., Villar Vega, M., Santa María, H., Gómez Zapata, J.C., Pittore, M., So, E., Fekete, A., Taubenböck, H., 2022. Benefits of Global Earth Observation Missions for Exposure Estimation and Earthquake Loss Modelling – Evidence from

Santiago de Chile, Chile. *Natural Hazards.* https://doi.org/10.1007/s11069-022-05672-6

4. Nicodemo, G., Digrisolo, A., Masi, A., Gómez Zapata, J.C., An integrated approach for collecting exposure data of residential buildings. An application for Calvello (Southern Italy) *(in preparation).*

5. Öztürk, U., Gómez Zapata, J.C., Wagener, T., Aristizabal Giraldo, E.V., Motivating urban poor to live on landslide-prone areas. *(In preparation).*

6. Rosero-Velásquez, H., Gómez Zapata, J.C., Monsalve M., Ferrario E., Straub, D., Determining representative seismic Hazard scenarios, with application to Valparaiso, Chile. *(In preparation).*

1.3.3. Contributions to open software

1. Brinckmann, N., Gomez-Zapata, J.C., Pittore, M., Rüster, M., 2021. DEUS: Damage-Exposure-Update-Service. V. 1.0. GFZ Data Services. https://doi.org/10.5880/riesgos.2021.011

2. Gómez Zapata, J.C., Shinde, S., Pittore, M., Merino-Peña, Y., 2021. Scripts to generate (1) attribute-based fuzzy scores for SARA and HAZUS building classes, and (2) probabilistic inter-scheme compatibility matrices. An application on the residential building stock of Valparaiso (Chile) for seismic risk applications. GFZ Data Services. https://doi.org/10.5880/riesgos.2021.002

3. Pittore, M., Gomez-Zapata, J.C., Brinckmann, N., Rüster, M., 2021. Assetmaster and Modelprop: web services to serve building exposure models and fragility functions for physical vulnerability to natural-hazards. V. 1.0. GFZ Data Services. https://doi.org/10.5880/riesgos.2021.005

4. Pittore, M., Haas, M., Gomez-Zapata, J.C., Brinckmann, N., Rüster, M., Proß, B., 2021. Quakeledger: a web service to serve earthquake scenarios. V. 1.0. GFZ Data Services. GFZ Data Services. https://doi.org/10.5880/riesgos.2021.003

5. Weatherill, G., Pittore, M., Haas, M., Brinckmann, N., Rüster, M., Gomez-Zapata, J.C., 2021. Shakyground: a web service to serve GMPE-based ground motion fields. V. 1.0. GFZ Data Services. https://doi.org/10.5880/riesgos.2021.004

1.3.4. Contributions to data repositories:

1. Gómez Zapata, J. C., Zafrir, R., Harig, S., and Pittore, M., 2021. Customised focus maps and resultant CVT-based aggregation entities for Lima and Callao (Peru). V. 1.0., GFZ Data Serv., https://doi.org/10.5880/riesgos.2021.006/

2. Gómez Zapata, J. C., Zafrir, R., Brinckmann, N., and Pittore, M., 2021. Residential building exposure and physical vulnerability models for ground-shaking and tsunami risk in Lima and Callao (Peru). V. 1.0., GFZ Data Serv., https://doi.org/10.5880/riesgos.2021.007/

3. Gómez Zapata, J. C., Brinckmann, N., Pittore, M., and Cotton, F.: 2021. Seismic ground motion fields for six deterministic earthquake scenarios (Mw 8.5-9.0) for Lima (Peru), GFZ Data Serv., https://doi.org/10.5880/riesgos.2021.008/

4. Gómez Zapata, J. C., Brinckmann, N., Pittore, M., and Cotton, F. 2021. Spatial representation of direct loss estimates on the residential building stock of Lima (Peru) from decoupled earthquake and tsunami scenarios on variable resolutions exposure models., GFZ Data Serv., https://doi.org/10.5880/riesgos.2021.009/

5. Gómez Zapata, J. C., Medina, S., and Lizarazo-Marriaga, J.: Creation of simplified state-dependent fragility functions through ad-hoc scaling factors to account for previous damage in a multi-hazard risk context. An application to flow-depth-based analytical tsunami fragility functions for the Pacific coast of South America, GFZ Data Serv. https://doi.org/10.5880/riesgos.2022.002/ Review link: https://dataservices.gfz-potsdam.de/panmetaworks/review/b1e611344f04b57fa73d31e48f5b482cda74afa8254c5685ad0fe4f97d3f8c6c/

6. Gómez Zapata, J. C., Pittore, M., Probabilistic inter-scheme compatibility matrices for multi-

hazard exposure modeling. An application using existing vulnerability models for earthquakes and tsunami from synthetic datasets constructed using the AeDEs form through expert-based heuristics, GFZ Data Serv., https://doi.org/10.5880/riesgos.2022.003/ Review link https://dataservices.gfz-potsdam.de/panmetaworks/review/6355f1be60969620c71b09b4ff4595d9f3d2247b30260a49cce816c9f5f41e0d/

7. Arroyo, O., Feliciano, D., Gomez Zapata, J.C., Shinde, S., Brinckmann, N., 2022. RRVS Building survey for building exposure modelling in Chua (Colombia) Status. GFZ Data Services. https://doi.org/10.5880/riesgos.2022.001

8. Merino-Peña, Y., Pittore, M., Gomez-Zapata, J.C., 2021. RRVS Building survey for building exposure modelling in Valparaiso and Viña del Mar (Chile). V. 1.0. GFZ Data Services. https://doi.org/10.5880/riesgos.2021.001

Chapter 2

2. Epistemic uncertainty of probabilistic building exposure compositions in scenario-based earthquake loss models

Abstract

In seismic risk assessment, the sources of uncertainty associated with building exposure modelling have not received as much attention as other components related to hazard and vulnerability. Conventional practices such as assuming absolute portfolio compositions (i.e., proportions per building class) from expert-based assumptions over aggregated data crudely disregard the contribution of uncertainty of the exposure upon earthquake loss models. In this work, we introduce the concept that the degree of knowledge of a building stock can be described within a Bayesian probabilistic approach that integrates both expert-based prior distributions and data collection on individual buildings. We investigate the impact of the epistemic uncertainty in the portfolio composition on scenario-based earthquake loss models through an exposure-oriented logic tree arrangement based on synthetic building portfolios. For illustrative purposes, we consider the residential building stock of Valparaíso (Chile) subjected to seismic ground-shaking from one subduction earthquake. We have found that building class reconnaissance, either from prior assumptions by desktop studies with aggregated data (top-down approach), or from building-by-building data collection (bottom-up approach), plays a fundamental role in the statistical modelling of exposure. To model the vulnerability of such a heterogeneous building stock, we require that their associated set of structural fragility functions handle multiple spectral periods. Thereby, we also discuss the relevance and specific uncertainty upon generating either uncorrelated or spatially cross-correlated ground motion fields within this framework. We successively show how various epistemic uncertainties embedded within these probabilistic exposure models are differently propagated throughout the computed direct financial losses. This work calls for further efforts to redesign desktop exposure studies, while also highlighting the importance of exposure data collection with standardized and iterative approaches [a].

[a] published as: Gómez Zapata, J.C., Pittore, M., Cotton, F., Lilienkamp, H., Simantini, S., Aguirre, P., Santa Maria H., 2022. Epistemic uncertainty of probabilistic building exposure compositions in scenario-based earthquake loss models. Bulletin of Earthquake Engineering. https://doi.org/10.1007/s10518-021-01312-9

2.1. Introduction

Epistemic uncertainties stem from the incomplete knowledge of the actual problem and its parameters, or simply from, often unavoidable, modelling and methodology errors (e.g., Vamvatsikos et al. 2010). The performance of earthquake loss models for large-scale residential building portfolios under the influence of such epistemic uncertainties, which are related to the lack of data describing the exposure composition, is the central aspect of this work. Exposure refers to the number, type, and monetary value of the elements (e.g., buildings) that are under threat from natural hazards and are subjected to potential loss (e.g., UNISDR, 2009). Together with the hazard and vulnerability components, the exposure contributes to most quantitative risk assessment applications. In such studies, the degree of knowledge of the hazard and exposure components plays a fundamental role since their associated uncertainties are propagated to the final loss estimates. Therefore, accurate estimates of the expected spatial distribution of seismic ground-shaking intensities for an earthquake scenario, together with increasingly consistent classifications of the building stock into suitable building vulnerability classes, will provide more accurate central metrics and minimize the variance of the final loss estimates over an area of interest. Being able to track and disaggregate the influence of the hazard and exposure is a crucial factor for decision making, urban planning, and finance (e.g., the insurance industry). In the latter, the smaller the variation in the mean loss values, the lower the risk is perceived (Wesson and Perkins, 2001).

In exposure modelling, the buildings are classified into vulnerability classes which ultimately describe their expected susceptibility to damage. The vulnerability-class definition, therefore, links the hazard intensities to the expected damage based on a clear understanding of the building's structural and non-structural characteristics (e.g., Calvi et al. 2006). Porter et al. (2002) showed that the influence of uncertainties in ground shaking on the overall uncertainty in the seismic performance of individual buildings (repair cost) is similar to the influence of uncertainty in the capacity of a building to resist the damage. However, for large-scale seismic risk, it has been conventionally assumed that the relative uncertainty associated with the definition of building classes and their relative proportions contributes much less to the final loss estimates than the aleatory components of the risk processing chain (i.e., ground motion variability in seismic hazard). This has led to the general practice of assuming that the collection of building exposure data is not as worthwhile compared to the more detailed assessment of the hazard component (Crowley and Bommer, 2006). This practice implies further community-accepted assumptions, such as supposing fixed proportions over aggregated data (i.e., census-based desktop studies), without exploring their underlying uncertainties. Only in recent times have a few studies pointed out the exposure uncertainty is an area that would particularly benefit from further assessment (Crowley, 2014; Corbane et al. 2017; Silva et al. 2019). Under this framework, there are several components of epistemic uncertainty that need further exploration, such as the basic reconnaissance of the building classes and their location while gathering their attributes, as well as exploring sensitivities in loss outcomes if more than a single set of building classes is used. Therefore, the assessment of a selected set of taxonomic attributes within a statistical exposure model while investigating the uncertainty in the class assignment and their effects on the loss estimates is a pathway worth exploring within a seismic risk framework.

This work describes how the epistemic uncertainty associated with defining a building exposure model is correlated with the variance in the loss estimates in earthquake scenarios. First, we briefly describe the current practices and limitations in the current state of the art in building exposure modelling for seismic risk (Sect. 2.2). Subsequently, we present a method for exploring the epistemic uncertainty of the building exposure models in earthquake loss models (Sect. 2.3). As a premise, in this work the building exposure model is visualized under the scope of compositional theory within a Bayesian framework in three stages: (1) statistical modelling based on the collection of data about a building's attributes and the configuration of synthetic building portfolios; (2) a novel method for obtaining the probabilistic compatibility-levels between two sets of building classifications; (3) the novel proposal of an exposure-oriented logic-tree that propagates and disaggregates some of the components that contribute to uncertainty in the loss estimates. These steps are exemplified for the residential building stock of Valparaíso, Chile (Sect. 2.4), to investigate how their associated variability impacts upon estimates of direct financial losses arising from a subduction earthquake scenario, while also considering both uncorrelated and spatially cross-correlated ground motion fields (GMF).

2.2. Current state of the art in building-exposure modelling for seismic risk assessment

In classical exposure models for large-scale seismic risk assessment, only some basic attributes are used to classify a building stock (e.g., the material of the lateral load resistance system (LLRS), height, and age). To date, few efforts to explore the associated uncertainties in the exposure composition have been made. For instance, Crowley and Pinho (2004) considered the spatial variation in the individual attributes as being random and less than the uncertainty induced by grouping different individual buildings into a single typology. Crowley et al. (2005) later showed that there is a great variability in the damage loss ratios imposed by grouping certain typologies in terms of storey ranges over a portfolio, even when the buildings are assumed to have other homogenous attributes (e.g., in terms of material of the LLRS). These simplifications have led to the practice of representing the epistemic uncertainty in the classification of buildings into predefined typologies as aleatory uncertainty. However, the same study also pointed out that detailed inspections to collect attributes of all the buildings in a study area would allow this uncertainty to be treated as epistemic. This is relevant considering that the location of specific building attributes are, in reality, not aleatory within a building stock (e.g., Dell'Acqua, et al. 2013; Martínez-Cuevas et al. 2017) and can affect their seismic vulnerability (Lagomarsino and Giovinazzi, 2006). Unfortunately, considering the extent and the evolution of the built environment, a full enumeration of the taxonomic features of the assets is a highly time and resource-intensive task, and often simply unfeasible (Pittore et al. 2017). Furthermore, the associated complexity in the building classification would increase and will lead to a more extensive set of classes in comparison to the available set of fragility functions (Haas, 2018; Martins and Silva, 2020). However, if only a sample of the building structures within the entire stock is inspected, the epistemic uncertainly associated with the class assignment in exposure models could be accounted for, allowing then the investigation of their impact upon earthquake loss models. For this aim, the use of taxonomies is a conventional practice to describe the built environment.

2.2.1. The use of taxonomies for building exposure modelling

2.2.1.1. Risk-oriented taxonomies: Schemes

Buildings are grouped into categories with expected similar performance when subjected to ground shaking. These categories are actually *risk-oriented taxonomies* which describe vulnerability classes with respect to a specific natural hazard and are described by a set of mutually exclusive, collectively exhaustive, building classes. To refer to such a set of building classes, we will be using the word "*scheme*". Some of the most common schemes include the European Macroseismic Scale 1998 (EMS-98, Grünthal, 1998), the USA specific HAZUS model (FEMA, 2003), and PAGER-STR (Jaiswal et al. 2010). These schemes classify large-scale exposure models often based on census information and are spatially aggregated over specific administrative units. Given the lack of local models, these taxonomies have been applied outside their original geographical scope. This is the case for HAZUS, which has been used to classify building stocks and to estimate losses in other geographical contexts (e.g., in Chile, Aguirre et al. 2018). Similar practices have been reported using the EMS-98 risk-oriented taxonomy in Central Asia (e.g., Bindi et al. 2011; Pilz et al. 2013).

2.2.1.2. Faceted taxonomies: taxonomic attributes

Faceted taxonomies, by contrast, provide an exhaustive and structured sets of mutually exclusive and well-described attributes. These taxonomies allow the description of individual structures in a standard way and are largely independent of specific fragility or vulnerability models. The most widely used and well-established example is the GEM Building Taxonomy (GEM v.2.0, Brzev et al. 2013). This taxonomy has been adapted for a multi-hazard-risk initiative (GED4ALL, Silva et al. 2018) and for classifying structures with special occupancies, such as schools, to assess their seismic vulnerability within the Global Library of School Infrastructure project (GLOSI) outlined in D'Ayala et al. (2020). Every building class within a given *risk-oriented taxonomy* can be disaggregated into attributes within a *faceted taxonomy*. This has been described in (Pittore et al., 2018b) and has been noted in Pavić et al. (2020).

2.2.2. Exposure modelling methods for large area spatially distributed buildings

Regardless of the type of taxonomy (either risk-oriented or faceted), there are two conventional methods for the exposure modelling of large-scale spatially distributed buildings: (1) *a top-down* approach, which involves the analysis of aggregated data (e.g., census data) through expert elicitation, and (2) *a bottom-up* approach, which uses individual observations. These two approaches classify the building stock by addressing a double expert elicitation process:

(1) To classify the building inventory into assumed building classes within a given study area.
(2) To obtain the building exposure composition (i.e., proportions in every building class).

These approaches are briefly explained hereafter. An innovative approach that dynamically combines these through statistical analyses will be introduced and discussed later in this work.

2.2.2.1. Top-down approach: building class from the analysis of aggregated data.

Recently, the implementation of the GEM *"mapping schemes"* for the analysis of aggregated data has been outlined in Yepes-Estrada et al. (2017) and further implemented in the European exposure model (Crowley et al. 2020) and the Global Seismic Risk model (Silva et al. 2020). These mapping schemes classify a building stock through desktop studies and expert elicitation with respect to earthquake vulnerability classes. Each class is described by selected attributes from the GEM v2.0 faceted taxonomy. They rely on available regionally aggregated data (e.g., region-specific census data) while addressing socioeconomic characteristics for *dwellings* and not at the building level (Crowley, 2014). Since there might be only a few very useful attributes for physical vulnerability assessment, these mapping-schemas have been customized to include other attributes by defining covariate relations between census descriptors and expected proportions per building class to ultimately use a single set of typologies to represent a building stock (e.g., Acevedo et al., 2020; Dabbeek and Silva, 2020). Therefore, the variation of taxonomic attributes is still being treated as being random within an aleatory uncertainty framework instead of a reducible and trackable epistemic uncertainty. Moreover, exposure models derived from purely top-down desktop studies neglect the temporal evolution of the ancillary data. Since census data are neither standard across regions nor in time (including possible changing data formats), once the mapping schema is used, the resultant exposure model would remain static until new census information is generated (Silva et al. 2019). Recent discussions about epistemic uncertainties in regional exposure models have been presented by Kalakonas et al. (2020). These authors observed negligible differences in the loss estimates when alternative exposure compositions were compared within a sensitivity analysis for probabilistic risk assessment. Notably, recent studies have highlighted the importance of the statistical nature of the exposure models by forecasting its dynamic spatiotemporal evolution (Rivera et al., 2020; Calderón and Silva, 2021) as well as counting with efficient techniques for their spatial aggregation (Dabbeek et al., 2021).

2.2.2.2. Bottom-up approach: individual building observations

When the composition of the portfolio is expected to be heterogeneous, data collection of attributes over a selected sample of individual buildings is required to constrain and validate the underlying assumptions imposed by a top-down vision. Freely available data products such as OpenStreetMap (OSM) may offer some descriptors (occupancy or footprint shape) that have been proved to be useful for constructing large scale exposure models with particular occupancies (e.g., Sousa et al. 2017). However, due to the lack of standardized data formats, including vulnerability drivers' attributes within harmonized data formats is still required by volunteer mapping initiatives to describe more robust schemes. This harmonization has been addressed by data standards with taxonomic attributes. This is the case for FEMA 154, (2002), the SASPARM 2.0 project (Grigoratos et al. 2016), CARTIS (Polese et al. 2020); and initiatives for data collection of post-earthquake damage such as AeDES (Baggio et al. 2007; Nicodemo et al. 2020). Recently, Kechidi et al. (2021) presented a comprehensive comparison between census-based (using mapping schemes) and survey-based (inspecting a sample) exposure models for risk assessment. The authors highlighted that the accuracy of the risk estimates is directly correlated with the number of surveys within a given region.

2.2.2.3. Dynamic building exposure modelling based on data collection and statistical analyses

Some studies have proposed the association between building characteristics (dynamically collected) and

their related vulnerability classes through statistical modelling. These type of approaches were first exemplified by Pittore and Wieland (2013) who employed Bayesian networks, and by Riedel et al. (2015) who made use of machine learning techniques. Moreover, a dynamic building exposure modelling method with a probabilistic nature has been recently suggested by Pittore et al. (2020), where it was proposed to define the portfolio's vulnerability classes in a top-down manner, while the expected frequency of the related classes was constrained through a bottom-up approach by integrating attribute-based data collection. To the best of the authors' knowledge, these statistical models have not yet been exploited to investigate the epistemic uncertainties in building exposure model composition, nor its impact on loss estimates. A detailed exploration of the epistemic uncertainty carried by statistical building exposure models upon scenario-based loss estimates is introduced hereafter.

2.3. Methodology

2.3.1. Probabilistic - exposure models: a Bayesian formulation

The building portfolio configuration is conceptualized by *compositional theory* within a fully probabilistic Bayesian framework, as initially suggested by Pittore et al. (2020). First, we introduce the concept of the likelihood function, followed by the assumptions on the prior and the posterior distributions within this context. This formulation considers risk-oriented schemes that contain a finite set of building classes and their associated fragility functions.

2.3.1.1. The definition of the likelihood function: The intra-scheme compatibility levels

A suitable scheme containing k risk-oriented building classes is selected for the area of interest, where we assume some data has also been collected through surveying (evidence). Following the proposal of Pittore et al. (2020), we assume that a sample of $n = \{n_1, \dots, n_k\}$, $\sum_k n_i = N$ building types are observed, where n_i is the number of specimens of building type i. We assume that the statistical population of buildings from which the observed sample is drawn is characterized by k typologies, whose frequencies are characterised by a proportion $\theta = \{\theta_1, \dots, \theta_k\}$, $\theta_i > 0$ $\forall i$ and $\sum_k \theta_k = 1$. Assuming a Multinomial sampling model, the probability of observing n conditionals on θ is given by:

$$p(n|\theta) = Mul(n|\theta)\frac{N!}{\prod_{i=1}^{k} n_i!}\prod_{i=1}^{k}\theta_k^{n_i} \qquad \text{Eq. 2-1}$$

We assume that the set of observations given their proportions is the likelihood distribution of the Bayesian formulation for building exposure modelling. This emerges naturally considering the bottom-up data collection of individual attributes. Subsequently, every risk-oriented building class (k within a given scheme (e.g.,T_k^A) is translated into basic taxonomic attribute values $\{F\}_m$ offered by a faceted building taxonomy. This is expressed by Eq. 2-2.

$$\sum_m p(T_k^A|\{F\}_m) \qquad \text{Eq. 2-2}$$

Triangular fuzzy values are assigned through expert criteria to score the compatibility degree between the observed attribute values and every building class, as formulated in (Pittore et al., 2018b), to constrain the actual proportion of every class within the exposure model. Subsequently, the data collection over individual buildings are used in the class assignment. Every attribute type j has an associated numerical weight, w_j, that acknowledges their relevance to the vulnerability assessment as well as their ability to be satisfactorily identified during the survey. By evaluating the compatibility degree between the observed building attributes and the building class, a transparent assignment of the most likely class within a fully probabilistic framework is achieved.

2.3.1.2. Prior and posterior distributions

As formulated in Pittore et al. (2020), the expected proportion θ_i for every building class is treated as a Dirichlet-distributed random variable:

$$Dir(\alpha) = \frac{\Gamma(\sum_{i=1}^{k}\alpha_i)}{\prod_{i=1}^{k}\Gamma(\alpha_i)}\prod_{i=1}^{k}\theta_i^{\alpha_i - 1} \qquad \text{Eq. 2-3}$$

where $\alpha = \{\alpha_1, \dots, \alpha_k\}$, $\alpha_i > 0$ $\forall i$ with $\alpha_0 = \sum_{i=1}^{k}\alpha_i$ being termed the concentration factor. The Dirichlet hyperparameter α_i is factorized as a product of a proportion (θ_k) and a common concentration factor such as:

$$\alpha_i = \theta_k \alpha_o \qquad \text{Eq. 2-4}$$

where α_0 increases the virtual counts for the category k. By Bayes theorem, and since the prior Dirichlet is the conjugate prior for the Multinomial likelihood, the posterior probability distribution of θ_i will also be a

Dirichlet distribution that can be described in terms of the likelihood $p(\boldsymbol{n}|\boldsymbol{\theta})$ and prior $p(\boldsymbol{\theta})$:

$$(\theta|n) \propto p(n|\theta)p(\theta) \qquad \text{Eq. 2-5}$$

When the number of observations increases, the probability estimate is dominated by the Multinomial likelihood. Therefore, the expert-based priors will be increasingly superseded by real data as it is continuously captured during surveys.

2.3.1.3. Synthetic building portfolios for a logic tree construction and spatial allocation

We propose to further characterise the prior and likelihood terms to obtain customized posterior distributions with proportions that represent the building stock composition. This is done through a logic tree. A similar approach was suggested by Riga et al. (2017) to highlight the uncertainties at the vulnerability level. Within our scope, we propose it as a tool for exploring the epistemic uncertainty in the portfolio composition. It has four complexity levels, namely:

(1) The selection of the building class scheme (group of building classes).
(2) The selection of the numerical weight, w_j (per attribute type j), which scores and ranks the relevance of every attribute type in the vulnerability assessment and their ability for assessment during surveys. The set of w_j is called the 'weighting arrangement" (W.A).
(3) The definition of a prior distribution which describes the initial guess about the composition of the building portfolio in the form of a Dirichlet distribution. This composition describes the representability of every building class in the area and is driven by data collection, expert criteria, or aggregated data (e.g., census).
(4) The selection of the hyper-parameter α_0 (concentration factor(s)) of the conjugate posterior Dirichlet distribution obtained from Eq. 2-5. This selection acknowledges the degree of trust in the former assumptions. Larger values ($\alpha_0 \sim 50$) represents a higher level of knowledge give similar compositions (almost unanimous consensus) whilst smaller ones ($\alpha_0 \sim 1$) means low information content and hence low knowledge of the portfolio composition that result in sparser distributions (Hastie et al. 2015). For each selected α_0, a number of samples must be selected to represent stochastic compositions within synthetic building portfolios.

With this formulation, we retain the statistical nature of the exposure modelling while overcoming the top-down vision of having a fixed composition. To spatially distribute every synthetic building portfolio, a dasymetric disaggregation from population counts is followed as proposed in Pittore et al. (2020). This approach is suitable for a differential spatial allocation of the synthetic building portfolios whose composition is being reconfigured with every sample. Population counts reported in any aggregated data source (e.g., LandScan; WorldPop; GPWv4) can be used.

It should be noted that the former steps regard the use of a single group of building classes (scheme T_k^A). However, for the exposure modeller, there might be more than one suitable scheme to describe the building stock of a given area (e.g., T_j^B). Although subjective compatibility relations between building classes contained in two different schemes have been already proposed (e.g., between HAZUS and EMS-98 in Hancilar et al. 2010), there is still the question of how to obtain some of the basic metrics for this alternative exposure model T_j^B (i.e., their proportions, average night-time residents, and replacement costs). This is not a trivial task since this information might be only available in terms of one reference scheme. Thereby, we propose to obtain these metrics for other suitable schemes through the formulation of probabilistic inter-scheme compatibility matrices. This method is described in the following.

2.3.2. Probabilistic inter-scheme compatibility matrix

As presented in Eq. 2-2, we assume that each building class k within a given scheme (T_k^A) can be disaggregated into observable taxonomic features of a faceted taxonomy $\{F\}_m$. This procedure is also followed for the target scheme (T_j^B) of interest. A straightforward application of the total probability theorem and a probabilistic description of the building type in taxonomic features allow us to define Eq. 2-6. This formulation allows us to obtain their probabilistic compatibility degree $p(T_k^A|T_j^B)$ as a matrix.

$$p(T_k^A|T_j^B) = \sum_m p(T_k^A|\{F\}_m \cap T_j^B)p(\{F\}_m|T_j^B) \qquad \text{Eq. 2-6}$$

Since we assume that the representations of a building within the two considered schemes are conditionally independent ($\perp\!\!\!\perp$) given the information on taxonomical features, we can describe the source scheme (T_k^A) as being modelled in terms of the taxonomic attributes that also compose the target-scheme (T_j^B: T_k^A) $\perp\!\!\!\perp$ $T_j^B|\{F\}_m$, the former equation can also be expressed as a product, as expressed in Eq. 2-7.

$$p(T_k^A|T_j^B) = \sum_m p(T_k^A|\{F\}_m)p(T_j^B|\{F\}_m)\frac{p(\{F\}_m)}{p(T_j^B)} \quad \text{Eq. 2-7}$$
$$(since\ T_k^A \perp\!\!\!\perp T_j^B|\{F\}_m)$$

We obtain a probabilistic representation of the compatibility degree across the two considered building classes in an alternative Bayesian formulation, as presented in Eq. 2-8.

$$p(T_k^A|T_j^B) = \sum_m p(T_k^A|\{F\}_m)p(T_j^B|\{F\}_m)\frac{p(\{F\}_m)}{p(T_j^B)} \quad \text{Eq. 2-8}$$

Synthetic surveys based on the possible combinations of attributes that may describe every building class are input to solve the compatibility scores and are integrated through the selection of the weighting arrangement for every commonly considered attribute. (w_j, see Sect. 2.3.1.1). Using this matrix, we can obtain the missing normalized values (i.e., distribution of prior proportions) of the target scheme ($\{R\}_{T_j^B}$) by simply applying a dot product between the obtained matrix and the equivalent quantities of the source scheme ($\{R\}_{T_k^A}$), as per Eq. 2-9.

$$\{R\}_{T_j^B} = p(T_k^A|T_j^B) \,.\{R\}_{T_k^A} \quad \text{Eq. 2-9}$$

For non-normalized metrics (e.g., average night-time residents and replacement cost of every class), the associated value with the most compatible class of the source scheme (T_k^A) is proposed to be selected. Examples of this procedure have been recently reported in Gomez-Zapata et al. (2021a, 2021c). Once we have the number of residents and prior compositions of the alternative portfolio, we can once again perform the formerly described dasymetric disaggregation procedure from population counts (end of Sect. 2.3.1.3) to obtain an exposure model for T_j^B.

2.3.3. Scenario-based earthquake risk assessment with spatially distributed ground motion fields

An earthquake scenario is selected for the construction of a seismic rupture and the simulation of spatially distributed ground motion from suitable ground motion prediction equation(s) (GMPE). At least 1,000 ground motion simulations must be computed for the considered earthquake rupture scenario to address its aleatory uncertainty (Silva 2016). Each realisation generates a spatially and inter-period cross-correlated GMF that is estimated based upon the GMPE-based intra-event variance. The actual selection of the cross-correlation model (among the currently available ones) is naturally also subject to epistemic uncertainties and its study is beyond the scope of this work. It is important to generate spatially cross-correlated ground motion fields for the same intensity measures that are required by the fragility functions and its use is transversal to all the logic tree levels (Sect. 2.3.1.3). To complement the vulnerability analysis, a consequence model that includes the total replacement cost for the building class and their loss ratios for every damage state must be selected.

2.3.4. Epistemic uncertainty of the building exposure definition in earthquake loss models

Once all of the aforementioned components are gathered, each synthetic portfolio customised within the logic tree (Sect. section 2.3.1.3) is used to investigate the impact of the differential building exposure composition on scenario-based earthquake loss models through Monte Carlo simulations. This allows us to differentially propagate and disaggregate the influence of each of the four components listed in Sect. section 2.3.1.3. Sensitivity analyses are done to compare their respective loss estimates (replacement cost values) with each other and to explore their related individual uncertainties.

2.4. Application

2.4.1. Context of the study area: Valparaíso

The study area comprises the communes of Valparaíso and Viña del Mar in Chile (see Figure 2-1). Hereafter, for simplicity, both communes will be called 'Valparaíso'. It is the second-largest Chilean urban centre, with its port being the main container

and passenger port in Chile and hence, is vital for the country's economy. As described by Indirli et al. (2011), Valparaíso shows a very heterogeneous building inventory, with its historic district being declared a World Heritage Site by UNESCO in 2003 after recognizing its diverse urban layout and architecture (Jiménez, et al. 2018). Geiß et al. (2017) investigated the usefulness of training segments from OSM data for exposure data modelling from satellite imagery for Valparaíso.

The Central Chile area, and in particular Valparaíso, have been hit by powerful historical earthquakes. One of the few with a description is the 1906 earthquake, with an inferred magnitude of Mw 8.0 - 8.2 (Carvajal et al. 2017), which caused widespread damage (Montessus de Ballore, 1914). In 1985, a Mw 8.0 event with an epicentre located just 120 km west of the city destroyed 70.000 houses and damaged an additional 140,000 dwellings, leaving 950,000 persons homeless, and caused losses of about $1.8 billion (Comte et al. 1986). The 2010 Mw 8.8 earthquake caused structural damage to some buildings in Viña del Mar (de la Llera et al. 2017) and impacted the labour market recovery and the overall economy (Jiménez Martínez et al. 2020). Furthermore, recent seismic activity was noticed in the region during the 2017 Mw 6.9 event, which was triggered by a slow slip event and led to an important clustered aftershock sequence (Ruiz et al. 2017). It is notable that the MARVASTO project (Indirli et al. 2011) developed earthquake scenarios to obtain the expected seismic ground motions and the structural performance of three churches in the city. To the best of the authors' knowledge, no scenario describing seismic risk for the residential building stock of Valparaíso has been reported in the scientific literature.

2.4.2. Probabilistic exposure model construction for Valparaíso

2.4.2.1. The definition of the likelihood function: The intra-scheme compatibility levels

Two earthquake-oriented schemes, namely SARA and HAZUS, have been considered to represent the building portfolio in Valparaíso. Both schemes have already been proposed for exposure modelling at the third administrative division, "commune", in Chile in earlier works. SARA constitutes an effort to harmonize and define all the building types in the South American Andes region (GEM, 2014), through expert judgment that carefully designed local mapping-schemas at the country level (Yepes-Estrada et al. 2017). Thus, on the one hand, we can infer 17 SARA building classes for Valparaíso, combining the storey ranges when it was possible (Table 2-1). On the other hand, according to Aguirre et al. (2018), HAZUS addresses 11 residential classes for another Chilean city with similar construction practices as Valparaíso (see Table 2-2). Short descriptions of the typologies enclosed in both schemes are provided in these two tables. Notably, SARA implies the assumption that the residential buildings in Chile can only comprise up to 19 storeys, does not include steel types, and only considers wall structure for reinforced concrete structures.

604 randomly distributed buildings in the urban area of Valparaíso (Figure 2-1) were inspected by local structural engineers from the Chilean Research Centre for Integrated Disaster Risk Management (CIGIDEN) to test the actual plausibility of the selected schemes in the study area. To construct the customized likelihood terms that regard the building proportions of the surveyed sample, as presented in Sec. 2.3.1.1, the building stock is assumed to follow a Multinomial distribution. This data collection of their attribute values was done in terms of the GEM v.2.0 taxonomy through the RRVS web-platform (Haas et al. 2016) and is available in Merino-Peña et al. (2021).

Every building class in the two schemes is disaggregated into attribute types and values of the GEM v.2.0 taxonomy. The corresponding fuzzy compatibility levels between the attribute values and building classes are assigned through expert elicitation (see Sect. 2.3.1.1as proposed in Pittore et al., 2018b). Their graphical representation is depicted in Figure 2-2. The complete description of these taxonomic attributes can be found in the web version of the Glossary for GEM taxonomy (https://taxonomy.openquake.org/). A python code to generate these schemes in JSON format along with these figures has been made available in Gomez-Zapata et al. (2021b).

The observed attribute values are classified using the two selected weighting arrangements. This process leads to different building typology distributions, as shown in Figure 2-4. This is because the LLRS ductility was, in most of the cases, not correctly assigned during the surveys (i.e. unreinforced (W.A-1) and reinforced structures (W.A-2).

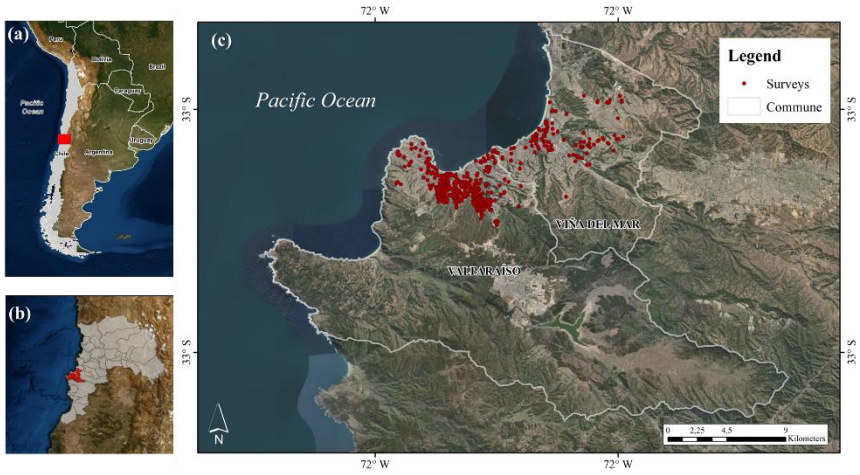

Figure 2-1. Location of the study area within (a) Chile, (b) the communes of Valparaíso and Viña del Mar (red) within the Valparaíso Region, and (c) the locations of the 604 surveyed buildings. Map data: ©Google Earth 2021.

Table 2-1. Building classes in terms of the SARA scheme proposed for Valparaíso with the respective intensity measure of their associated fragility functions (as reported in Villar-Vega et al. 2017). Prior proportions per building class, average night-time residents (Res. /bdg), and replacement cost (Repl. Cost (USD/bdg)) are reported as in Yepes-Estrada et al. (2017).

SARA building class	Description	IM	Prior Prop	Res. /bdg	Repl. Cost USD/bdg
CR-PC-LWAL-H1-3	Precast (PC), reinforced concrete (RC) wall system (LWAL), height (H) between 1–3 stories	PGA	0.005	18	360,000
CR-LWAL-DNO-H1-3	RC wall system, non-ductile (DNO), 1–3 stories	PGA	0.032	14	288,000
CR-LWAL-DNO-H4-7	RC wall system, non-ductile, 4–7 stories	S.A at 1.0s	0.010	54	1080,000
CR-LWAL-DUC-H1-3	RC wall system, ductile (DUC), 1–3 stories	PGA	0.011	15	336,000
CR-LWAL-DUC-H4-7	RC wall system, ductile, 4–7 stories	S.A at 1.0s	0.006	54	1,260,000
CR-LWAL-DUC-H8-19	RC wall system, ductile, 8–19 stories	S.A at 1.0s	0.002	173	4,032,000
ER-ETR-H1-2	Reinforced (ETR) rammed earth (ER), 1–2 stories	PGA	0.029	4	43,750
MCF-DNO-H1-3	Confined masonry (MCF), non-ductile, 1–3 stories	PGA	0.152	5	94,500
MCF-DUC-H1-3	Confined masonry, ductile, 1–3 stories	PGA	0.034	14	288,000
MR-DNO-H1-3	Reinforced masonry (MR), non-ductile, 1–3 stories	PGA	0.029	18	360,000
MR-DUC-H1-3	Reinforced masonry, ductile, 1–3 stories	PGA	0.012	18	360,000
MUR-ADO-H1-2	Unreinforced masonry with adobe, 1–2 stories	PGA	0.111	4	43,750
MUR-STDRE-H1-2	Dressed stone (STDRE) unreinforced masonry, 1–2 stories	PGA	0.006	5	43,750
MUR-H1-3	Unreinforced masonry, between 1–3 stories	PGA	0.060	6	52,500
UNK	Unknown	S.A at 0.3s	0.108	4	35,000
W-WLI-H1-3	Wood (W), LLRS: Light wood (WLI), 1–3 stories	S.A at 0.3s	0.273	5	108,000
W-WS-H1-2	Wood, LLRS: Solid wood (WS), 1–2 stories	S.A at 0.3s	0.121	4	43,750
			∑ 1.0		

Table 2-2. Building classes and short description of the HAZUS scheme (FEMA, 2012) proposed for Valparaíso.

HAZUS building class	Description
W1	Wood, light frame < 5000 sq. ft². (~ 465 m²), between 1–2 stories
S2L	Steel braced frame, between 1–3 stories
S3	Steel light frame. Does not specify a storey range
S5H	Steel frame, unreinforced masonry infill walls, high rise
C2L	RC shear walls, between 1–3 stories
C2M	RC shear walls, between 4–7 stories
C2H	RC shear walls, high rise
C3L	RC frame buildings, unreinforced masonry infill walls, between 1–3 stories
RM1L	Reinforced masonry walls; wood or metal deck diaphragms, 1–3 stories
RM1M	Reinforced masonry walls; wood or metal deck diaphragms, 4–7 stories
URML	Unreinforced masonry bearing walls, between 1–3 stories

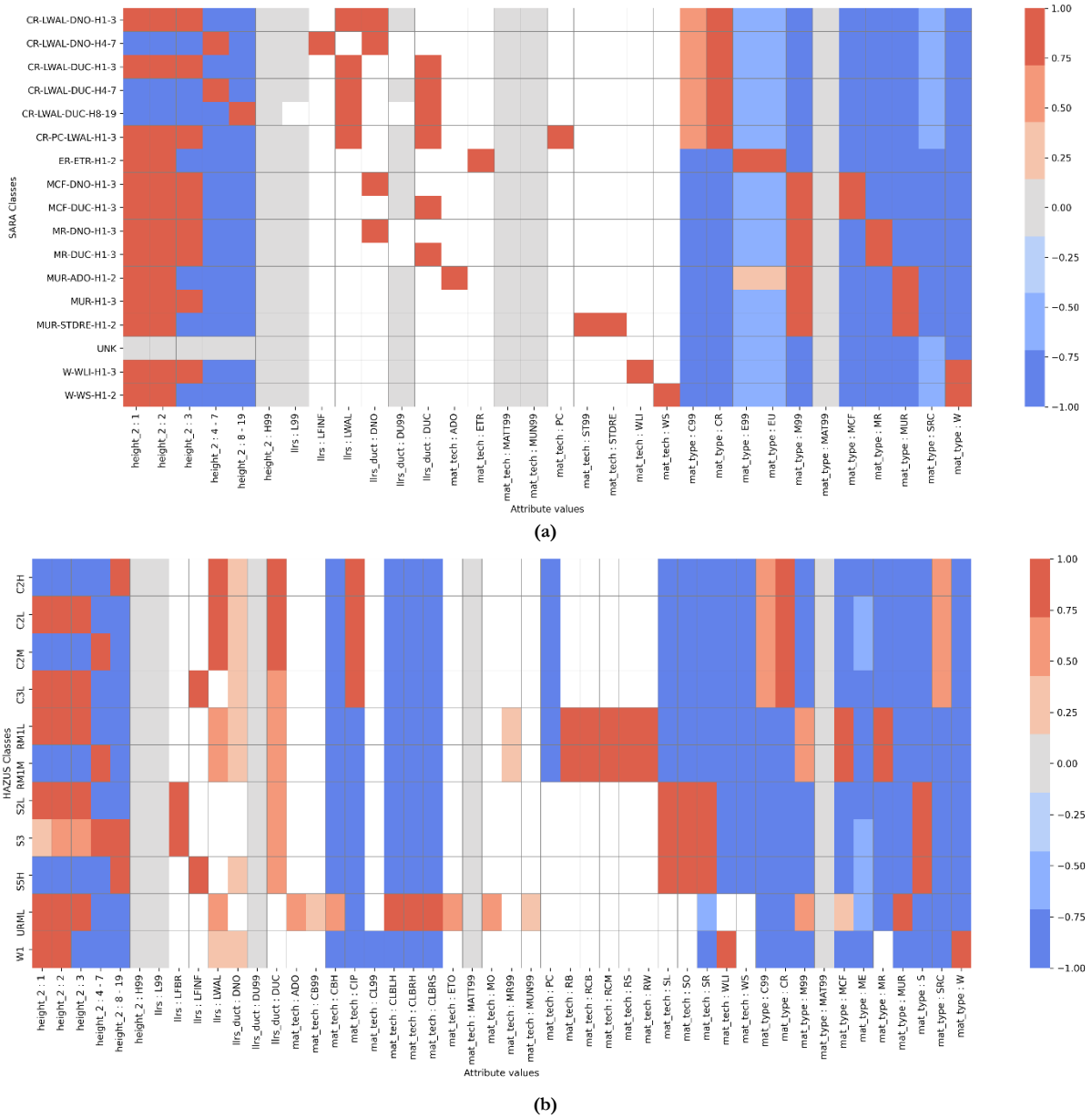

Figure 2-2. Graphical representation of the (a) SARA and (b) HAZUS building classes. The colours encode the compatibility value with extremes in red and blue, representing high and low compatibilities, respectively. Grey indicates neutral and white refers to no explicit compatibility value being assigned.

Table 2-3. Sets of weighting arrangements that score the common attribute types of the SARA and HAZUS schemes.

Taxonomic Attribute	W.A-1	W.A-2
Material type	0.40	0.30
Material technology	0.10	0.10
LLRS (lateral load resistance system)	0.15	0.20
LLRS ductility	0.25	0.10
Storey range	0.10	0.30

SARA	W-WLI-H1	CR-LWAL-DUC-H8-19	CR-LWAL-DUC-H4-7
HAZUS	W1	C2H	RM1M

SARA	UNK	MUR-STDRE-H1-2 (*W.A-1*); MUR-H1-3 (*W.A-2*)	UNK (*W.A-1; W.A-2*)	MCF-DNO-H1-3 (*W.A-1*); MCF-DUC-H1-3 (*W.A.2*)	MR-DNO-H1-3 (*W.A-1*); MR-DUC-H1-3 (*W.A.2*)
HAZUS	C2H	URML	S3	RM1L	RM1L

Figure 2-3. Pictures of some selected buildings' façades surveyed in Valparaíso. Their classifications in terms of the SARA and HAZUS schemes are displayed considering the two weighting arrangements presented in Table 2-3. ©Google Street View, 2021.

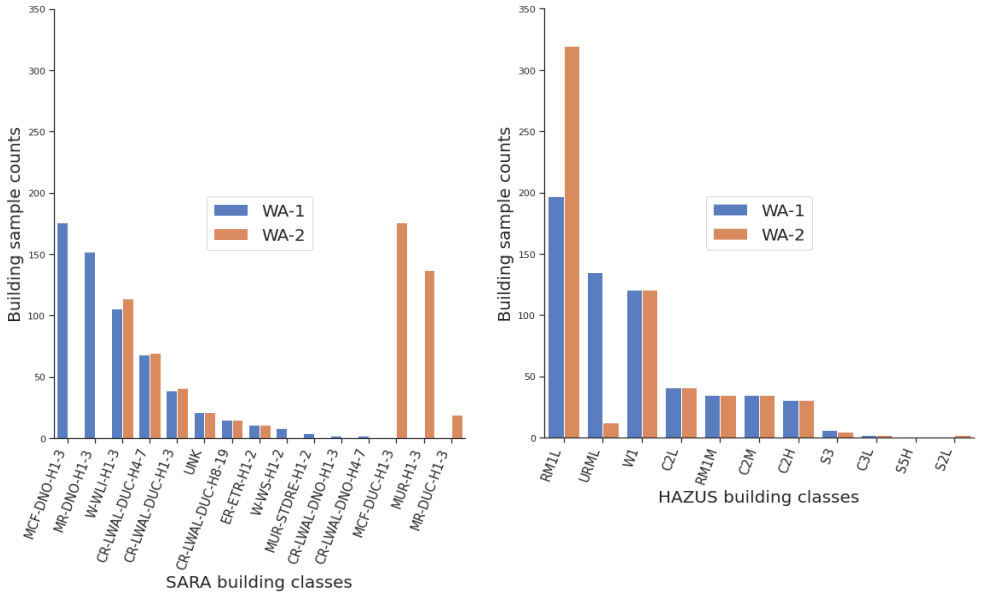

Figure 2-4. Distributions of the most likely vulnerability classes of the 604 buildings surveyed in Valparaíso. This was achieved by evaluating the compatibility levels between the observed taxonomic building attributes and the typologies within each scheme: (a) SARA and (b) HAZUS. For each scheme we consider the two weighting arrangements (W.A-1, W.A-2) shown in Table 2-3.

2.4.2.2. Prior and posterior distributions

Priors have been considered as (1) informative if the portfolio composition is derived from expert elicitation (GEM, 2014) and (2) uninformative if the portfolio has equal proportions per class. Since informative prior proportions, average night-time occupancy, and replacement costs are only known for the source scheme SARA (Table 2-1), we follow the method presented in Section 2.3.2 (inter-scheme compatibility matrix) to obtain these quantities for HAZUS (target scheme). This is obtained by generating all possible combinations of attribute values per scheme (see the horizontal axis of Figure 2-2). The two sets of weights reported in Table 2-3 are used to obtain the inter-scheme compatibility matrices presented in Figure 2-5. The scripts and related inputs to produce these two matrices are provided in Gómez Zapata et al., (2021d). The application of Eq. 2-9 allows us to obtain the two sets of informative priors' proportions for the HAZUS building classes that are reported in Table 2-4.

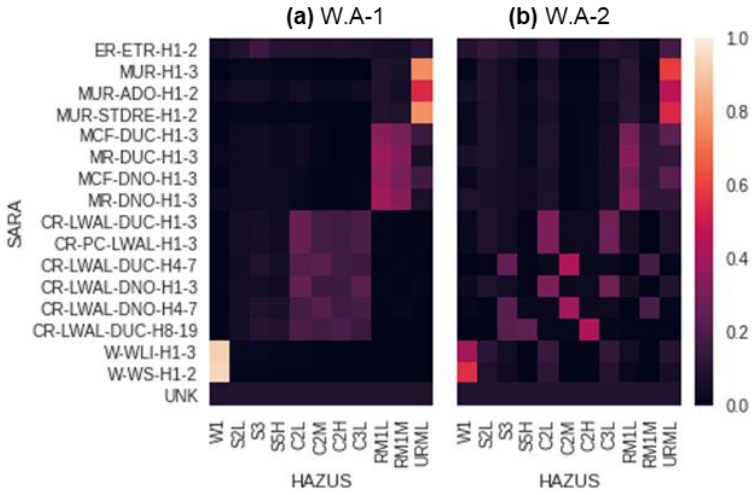

Figure 2-5. Inter-scheme compatibility matrices for SARA (source) and HAZUS (target) for the residential building stock of Valparaíso. They are obtained from the weighting arrangements (a) W.A-1 and (b) W.A-2 for their common attributes (Table 2-3).

Table 2-4. HAZUS Building classes for Valparaíso together with two sets of their prior proportions, average night-time residents (Res /bdg.) and replacement cost (Repl. Cost (USD/bdg.). They are assumed to be the same as the highest compatibility score with respect to a class of SARA from every inter-scheme compatibility matrix displayed in Figure 2-5.

	W.A-1			W.A-2		
HAZUS building class	**Prior prop.**	**Res. /bdg.**	**Repl. Cost (USD/bdg)**	**Prior prop.**	**Res. /bdg.**	**Repl. Cost (USD/bdg.)**
W1	0.384	4	43,750	0.204	4	43,750
S2L	0.039	15	336,000	0.091	15	336,000
S3	0.044	54	1,260,000	0.061	54	1,260,000
S5H	0.033	173	4032000	0.026	173	4,032,000
C2L	0.046	18	336,000	0.114	18	336,000
C2M	0.028	54	1,260,000	0.022	54	1,260,000
C2H	0.027	173	4,032,000	0.021	173	4,032,000
C3L	0.033	14	288,000	0.100	15	336,000
RM1L	0.112	18	360,000	0.120	18	420,000
RM1M	0.094	18	360,000	0.046	54	1,080,000
URML	0.160	5	43,750	0.196	6	52,500
	$\sum$ 1.0			**$\sum$ 1.0**		

Table 2-4 also reports the replacement costs and night-time residents for each of the HAZUS target classes. These quantities are assigned from the SARA source class with the largest compatibility in the inter-scheme compatibility matrices. Therefore, identical values of replacement costs and night-time residents are obtained across the HAZUS scheme for both W.A-1 and W.A-2, except for the classes C3L, RM1L, RM1M, and URML. Once we have obtained the prior and likelihood terms for every building class, the posterior distributions are constructed following Eq. 2-5 and are shown in Figure 2-6. Since the assignment of priors through expert elicitation has been at the commune level (GEM, 2014), the obtained posterior distributions are up-scaled to represent different exposure models with various building compositions in Valparaíso.

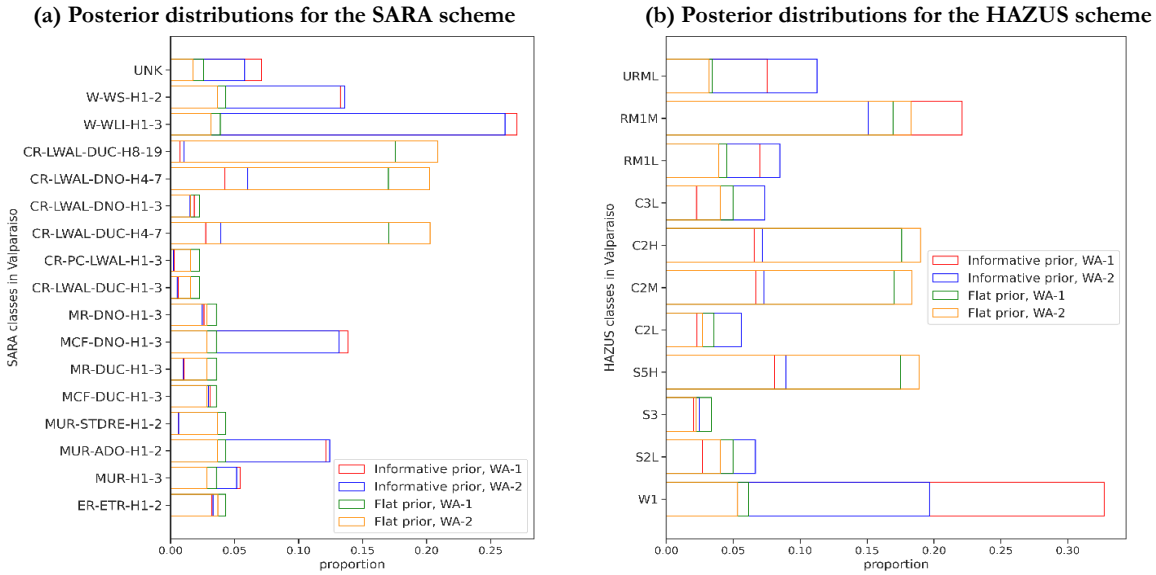

Figure 2-6. Posterior distributions obtained for the (a) SARA and (b) HAZUS schemes for the 604 inspected building surveyed in Valparaíso while considering different weighting arrangements (W.A.) and flat and informative priors.

2.4.2.3. Synthetic building portfolios for a logic tree construction and spatial allocation

Each of the four types of posterior distributions per considered scheme are explored by considering three concentration factors (α_o), namely: α_{0_1} = 1.0; α_{0_2} = 15, and α_{0_3} = 50 (see Eq. 2-4). They describe three different degrees of confidence in the assumptions beneath the construction of the posterior distribution: very low, moderate, and very high, respectively. Since we assume conjugacy (Eq. 2-5), we generate 300 random samples from the twelve Dirichlet posterior distributions per scheme. Each of these samples represents a synthetic building portfolio. They can also be interpreted as 300 different criteria (e.g., a pool of virtual experts) regarding the portfolio composition: very divergent opinions, moderately similar, and very similar, with respect to the average proportions in the posteriors. A logic tree with four branches was ultimately constructed, as shown in Figure 2-7.

Dasymetric disaggregation of the gridded population product GPWv4, with a 30 arc-second grid resolution model and population projections for 2020 (CIESIN, 2018) was carried out to obtain the spatial distribution of the building counts per synthetic buildings portfolio. For this process, we have used the occupancy (residents per building class) of the SARA (Table 2-1) and HAZUS schemes (Table 2-4).

The corresponding expected total building counts in terms of SARA and HAZUS schemes assuming equally composed portfolios, as well as expert-based are shown in the first column of Figure 2-8. Since the number of residents in every HAZUS building class is different for W.A-1 and W.A-2, the building counts vary accordingly. It can be seen that in the top-down approach, the total building counts in Valparaíso are almost identical, regardless of the scheme implemented. The plots in the other four columns of Figure 2-8 display the associated variabilities in the estimations of the total number of buildings for the synthetic portfolios constructed from the 300 samples. Regardless of the scheme used, it is evident that the total building counts from synthetic portfolios obtained from posterior distributions with flat priors present a much lower variability than their counterparts with informative priors. Of course, results assuming equally composed portfolios from prior distributions are not realistic for the study area. These related subplots are only shown to raise awareness that a careful first assumption on the prior is vital, otherwise the next step (defining α_0) may lead to very different building proportions with respect to the ones based on informative assumptions (e.g., expert-based).

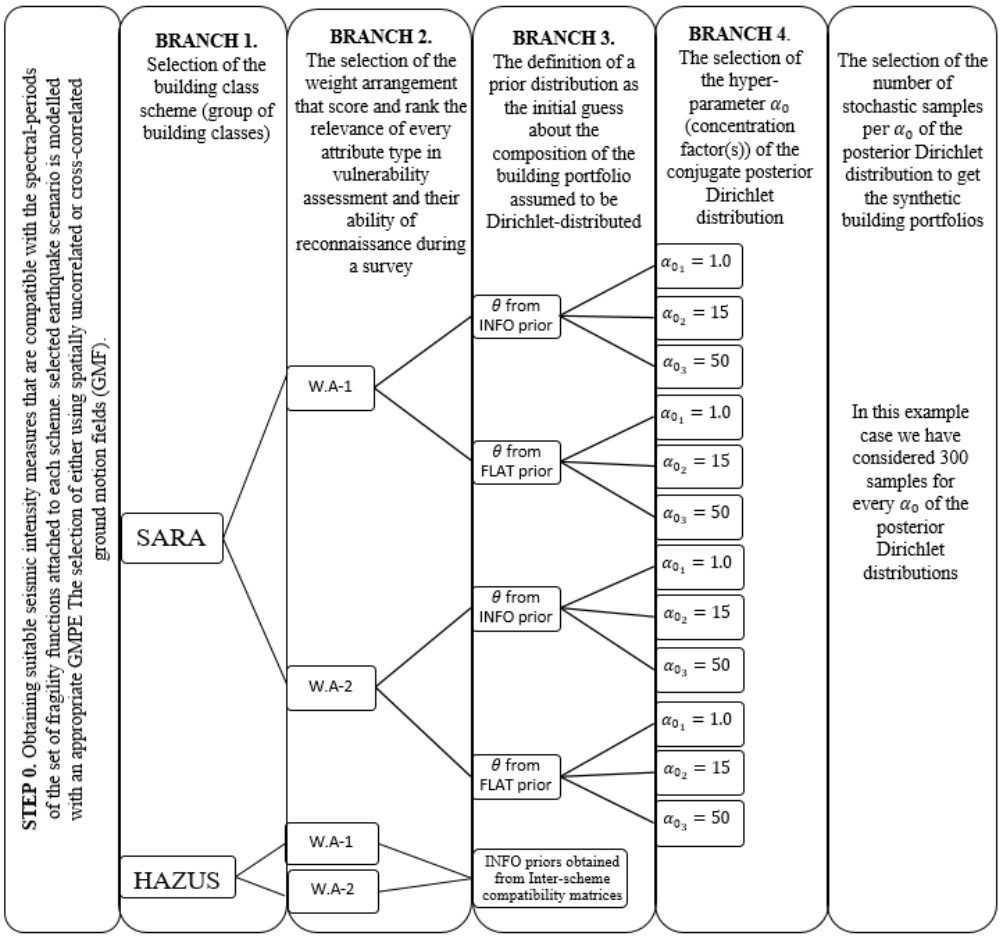

Figure 2-7. Logic tree with four levels constructed to explore the impact of the building exposure composition modelling in Valparaíso. The twelve branches result from every considered scheme. The entire one is shown only for SARA, however, the same procedure has been carried out for HAZUS.

Moreover, it is interesting that when both informative priors and $\alpha_0 = 50$ (high degree of confidence) are jointly addressed, the resultant variability in the building counts provide a range that contains the value of the unique composition that was assigned by the top-down approach. This type of similarity is more evident in the HAZUS scheme, whilst a larger variability appears in the SARA scheme. This might be due to the comparatively larger sensitivity of SARA to the individual building assessment during the surveys (in terms of the weighting arrangement, see Figure 2-4) which also impacted upon the construction of their respective likelihood distributions. Also, for both schemes, we observe that the selection of W.A-2 imposes a larger number of observations of ductile buildings (with a larger number of residents, see Table 2-1 and Table 2-4). Therefore, there is a consequent reduction in the variance of building counts when these distributions are obtained from W.A-2 in comparison to when they are generated using W.A-1. The reduction in this variability does not necessarily mean that the third boxplot in Figure 2-8-j better represents the entire building counts for the exposure model of Valparaíso than its counterpart in Figure 2-8-h. Rather, it is pointing to the underlying assumptions in deriving total building counts from dasymetric disaggregation, fully relying on top-down approaches (without integrating any evidence). Instead of having a fixed total buildings count (Figure 2-8-a, f), we are obtaining a range of total building count values whose variation is consistent with prior assumptions and observations (third boxplots in Figure 2-8- c, e, j, and h). These ranges are also consistent with the variations observed in Geiß et al. (2017), that assessed the likely range of building counts for Valparaíso (i.e., 64,803 – 72,412 building units) by combining remote sensing data products and OpenStreetMap building footprints.

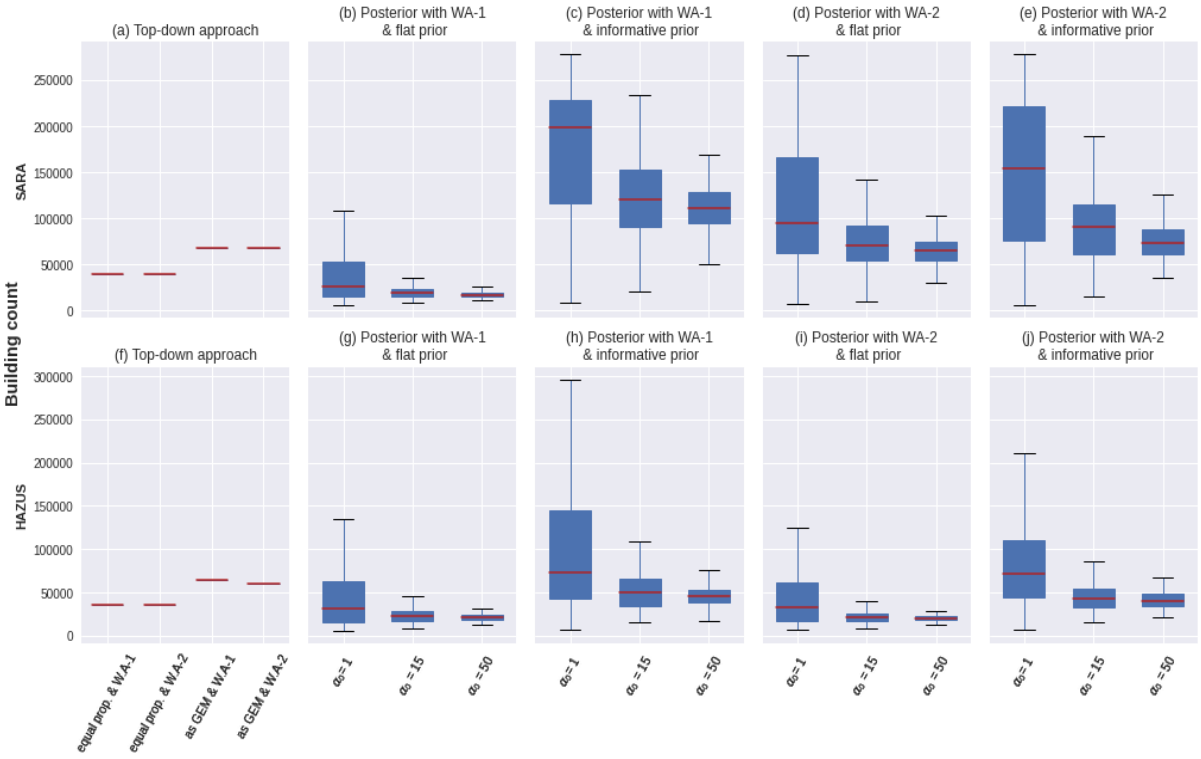

Figure 2-8. Dependency between the portfolio composition and the estimated total building counts (from dasymetric disaggregation of the population and occupancy). The subplots on the first column (top-down approach) comprises a single value of expected building counts either equally composed (i.e., with equal proportions) or as defined by the SARA model (GEM, 2014) and the respective weightings. The distributions in the other subplots correspond to every case of the logic tree of Figure 2-7.

2.4.2.4. Scenario-based earthquake risk assessment with spatially distributed ground motion fields

An earthquake scenario with a magnitude Mw 8.2, similar to the 1906 Valparaíso event, is used throughout this example. Given the lack of instrumentation at that time, its exact location and other parameters are uncertain. A finite fault model was generated making use of the OpenQuake Engine (Pagani et al. 2014). The basic parameters used in the simulations are: hypocentral location (longitude = -72.25°; latitude = -33.88°; depth = 28 km), strike = 9°, dip = 18°, and rake = 90°. The ground motion values were modelled using the Montalva et al. (2017) GMPE developed for the Chilean inter-plate subduction area. This GMPE considers in the "site" term the shear wave velocity in the uppermost 30 meters depth (Vs_{30}). We used the topography-based Vs_{30} values (Allen and Wald, 2007) and replaced them when possible with the seismic microzonation study reported in Mendoza et al. (2018). The final Vs_{30} gridded values are displayed in Figure 2-9.

As a first step, we generate the GMPE-based median ground motion fields (GMF) for PGA; S.A. (0.3 s); S.A. (1.0 s) for the selected earthquake scenario. They are shown in Figure 2-10 a-c, respectively. To account for spatial variability, we follow two approaches where we generate these fields: (1) uncorrelated random fields (No Corr) and (2) spatially and inter-period cross-correlated random fields using the Markhvida et al. (2018) cross-correlation model (Corr). The aleatory uncertainty in the simulated ground motion has been addressed by generating 1,000 realisations in every case. Figure 2-10d-f shows single realisations of cross-correlated GMF per spectral acceleration for the study area.

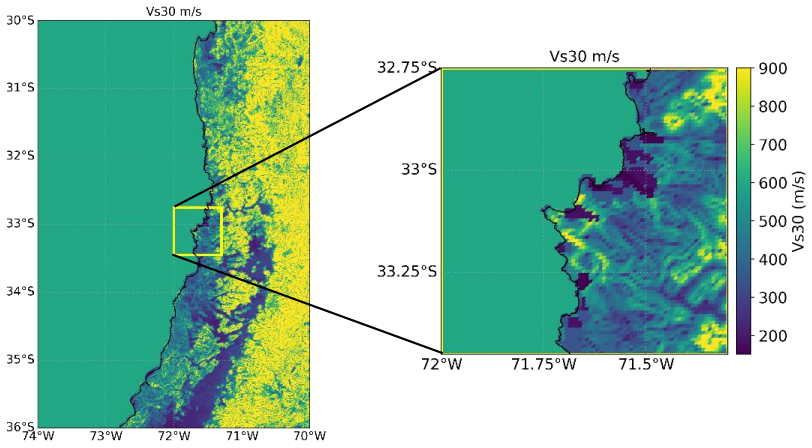

Figure 2-9. Left: distribution of the slope-based Vs_{30} values in Central Chile (Allen and Wald, 2007) as provided by the USGS. Right: refined values within the study area using the former and the seismic microzonation reported in Mendoza et al. (2018).

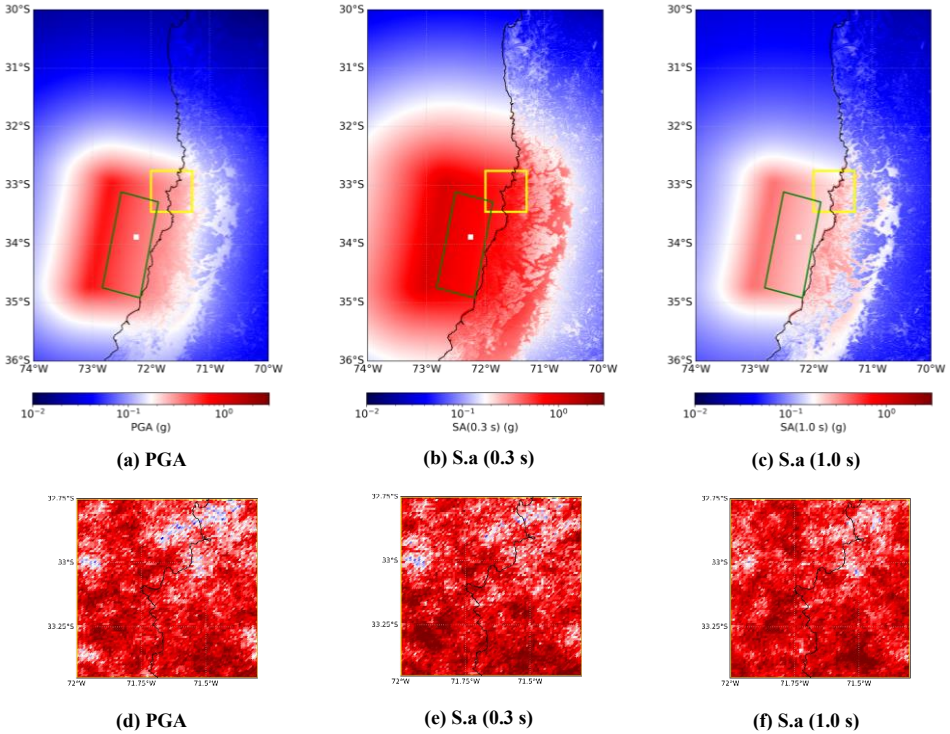

Figure 2-10. First row: median values of the Mw 8.2 earthquake rupture for three IMs (a) PGA, (b) S.A. (0.3 s), and (c) S.A. (1.0 s) using the Montalva et al. (2017) GMPE. The earthquake hypocentre is depicted by a white square. The rupture plane is displayed by a green rectangle. The study area is shown by a yellow square. Second row: details of the study area with a single realisation of the cross-correlated seismic GMF for their corresponding spectral periods using the Markhvida et al. (2018) model.

The selection of the aforementioned GMFs is related to the IM required by the SARA fragility functions (Villar-Vega et al. (2017). It should be noted that, although HAZUS (FEMA, 2012) provides fragility functions at the fundamental period of the structure, using PGA as the only IM for the entire set of curves. The seismic design standard for moderate-code (MC) is selected for the HAZUS classes for which this category is available (i.e., 8 types out of 11) and low-code (LC) is assumed for the remaining 3 types (S5H, C3L, and URML). This decision stems from the fact that the construction of most of the currently inhabitable residential buildings in Valparaíso took place between the establishment of two major Chilean seismic codes (NCh433 Of.72, INITN, 1972, and NCh433 Of.96, INN, 1996). Their development was motivated by the 1960 Mw 9.5 Valdivia earthquake and the 1985 Mw 8.0 Valparaíso earthquake

respectively. The consequence model for vulnerability assessment is complemented with the selection of loss ratios. For the four damage states considered by these two sets of fragility models, we assume ratios of 2%, 10%, 50%, and 100% of their replacement costs (Table 2-1, Table 2-4). Similar loss ratios were recently suggested (e.g., Martins and Silva, 2020).

2.4.3. Results: epistemic uncertainty of exposure compositions in seismic risk scenario

The influence of the epistemic uncertainty in the residential building portfolio composition of Valparaíso to loss assessment is carried out while performing a sensitivity analysis for the selected earthquake scenario (Mw 8.2) and the various exposure compositions considered. Two comparisons are presented:

(1) The direct financial losses are computed only for the portfolios whose composition is given by the posterior distributions (Figure 2-6), and whose median building counts are given by the value in red on the boxplots when $\alpha_0 \sim 50$ in Figure 2-8). These results are reported in Figure 2-11.

(2) The direct financial losses for every complete distribution of Figure 2-8 are computed, and their results are presented in the form of normalized loss exceedance curves (LEC).

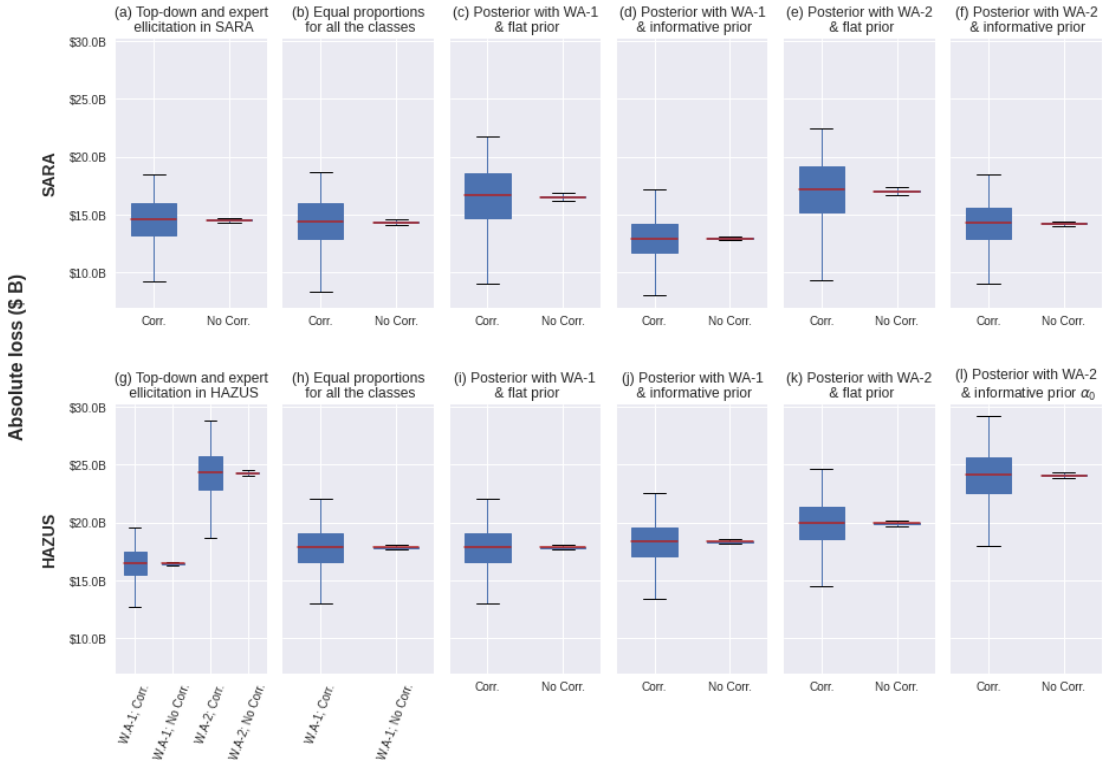

Figure 2-11. Comparison of the scenario-based direct financial losses (USD) on the residential building stock in Valparaíso considering SARA and HAZUS (moderate code) using the 1,000 GMF for each case: with a spatially cross-correlation model (Corr.) and spatially uncorrelated (No Corr.). Different portfolio compositions are considered: top-down vision and expert elicitation (first column), equally composed portfolios (second one), and the customized posterior distributions of Figure 2-6.

Figure 2-11 shows the overall variability in the losses imposed by the epistemic uncertainty related to the consideration of using or not spatially cross-correlated GMF. There is a very low variability in the resulting losses when 1,000 uncorrelated GMF were generated (No Corr). In fact, for such a dense, spatially aggregated building portfolio, the effect of spatially uncorrelated variations in the ground motion will eventually average out, leading to very little dispersion in the loss estimates. Similar evidence on the impact of correlation models and the size of the building portfolios have been noted by others (i.e., Bazzurro and Luco, 2005; Sousa et al. 2018; Silva, 2019).

Figure 2-11 also shows that, for a single composition, using either cross-correlated GMF (for SARA) or only spatially correlated GMF (for HAZUS), similar uncertainty ranges are expected. A similar feature was noted by Michel et al. (2017) performing sensitivity analyses to the IM of the fragility functions for various

spatially correlated GMF. Subsequently, we present loss exceedance curves (LEC) from the earthquake scenario considering the SARA and HAZUS schemes for the complete distribution of building counts presented in Figure 2-8. They are illustrated in Figure 2-12 and Figure 2-13, respectively. They are obtained considering the 300 synthetic portfolios for each of the 12 posteriors distributions as presented in Figure 2-7. LEC are displayed in blue if cross-correlated GMF were addressed and in yellow considering spatially uncorrelated GMF. There are another three sets of LEC included in each subplot:

(1) A pair of curves that represent the direct losses obtained from a unique composition according to the joint expert elicitation at the Commune level (GEM, 2014) and the use of mapping-schemas over census data (Yepes-Estrada et al. 2017). They are coloured in purple when cross-correlated GMF are accounted for and in red when spatially uncorrelated GMFs were not addressed.
(2) A pair of curves generated considering the portfolio composition, as described by the posterior distributions (Figure 2-6), are represented by non-continuous white curves.
(3) A pair of curves while foreseeing the portfolio with equally composed proportions are shown by black curves.

The white and black curves have not been distinguished by colours on whether spatially cross-correlated GMF are or not included. Nonetheless, when they were addressed, these two sets of curves are always within the range of the blue and the purple curves (i.e., smoother shape and shorter initial plateau). Similarly, when spatially uncorrelated GMF are accounted for, they fall within the range of the yellow and red curves (sharper shapes). A decision to normalise the direct financial losses (repair cost) in all LEC results with respect to the maximum loss values obtained from the use of GMF with spatially uncorrelated residuals has been taken. Then, the metric in these two plots is the "normalized number of losses". This decision is supported by Vamvatsikos et al. (2010) who argued that, due to continuously evolving exposure over time and location, erroneous physical damage predictions can arise if the losses are shown as absolute instead of normalized. This procedure is useful to compare the uncertainties that arise from the different synthetic building portfolios.

The axes are not identical for the SARA (Figure 2-12) and HAZUS (Figure 2-13) results. For the latter, the horizontal axis starts at 0.7 to graphically highlight some differences. These curves are the joint result of the epistemic uncertainty in the selection of the basic scheme (set of buildings), its degree of confidence, the IM of the fragility functions and whether using a correlation model or not. The role of these involved components is discussed separately hereafter.

2.4.3.1. The role of the concentration factor a_0

The plots in the first column of Figure 2-12 (SARA) and Figure 2-13 (HAZUS) show a greater dispersion (and therefore uncertainty in the results) when α_{0_1}=1.0 is addressed. This represents a lower degree of confidence in the portfolio compositions which is perceived as an "increased spread" around the mean value. This variability decreases for $\alpha_{0_2} = 15$ (intermediate degree of confidence) in the second column, being the lowest when $\alpha_{0_3} = 50$ is considered (third column), which simulates an almost unanimous consensus on the portfolio composition as defined by the posterior distributions.

2.4.3.2. The role of the identification of buildings attributes (evidence) in the likelihood term.

The selection of the numerical weight, w_j, which score and integrate the taxonomic attribute types, and that together with the collected data evidence construct the likelihood term (see Sect. 2.3.1.1), does not show a relatively large impact on the resultant LEC for the SARA scheme. This could be inferred from Figure 2-6 where the weighting arrangement did not impose such a large difference upon the construction of posterior distributions as the prior definition did. Nonetheless, these weights did heavily impact upon the construction of the inter-scheme compatibility matrices for HAZUS (Figure 2-5). The former ones are used to obtain the informative prior and replacement costs for HAZUS (see Table 2-4), and hence also impacted upon their respective loss estimates. This feature is evident in the different importance assigned to the ductility level (Table 2-3) which led to the assignment of a larger proportion of non-ductile building classes for W.A-1 (Figure 2-4). This is also linked to the fact that the fragility functions of W.A-1 driven classes (non-ductile: DNO), require lower acceleration values to reach the same damage state than the W.A-2 driven classes (ductile: DUC) (e.g., MCF-DNO-H1-3 vs. MCF-DUC-H1-3 in SARA; and URML vs. RM1L in HAZUS).

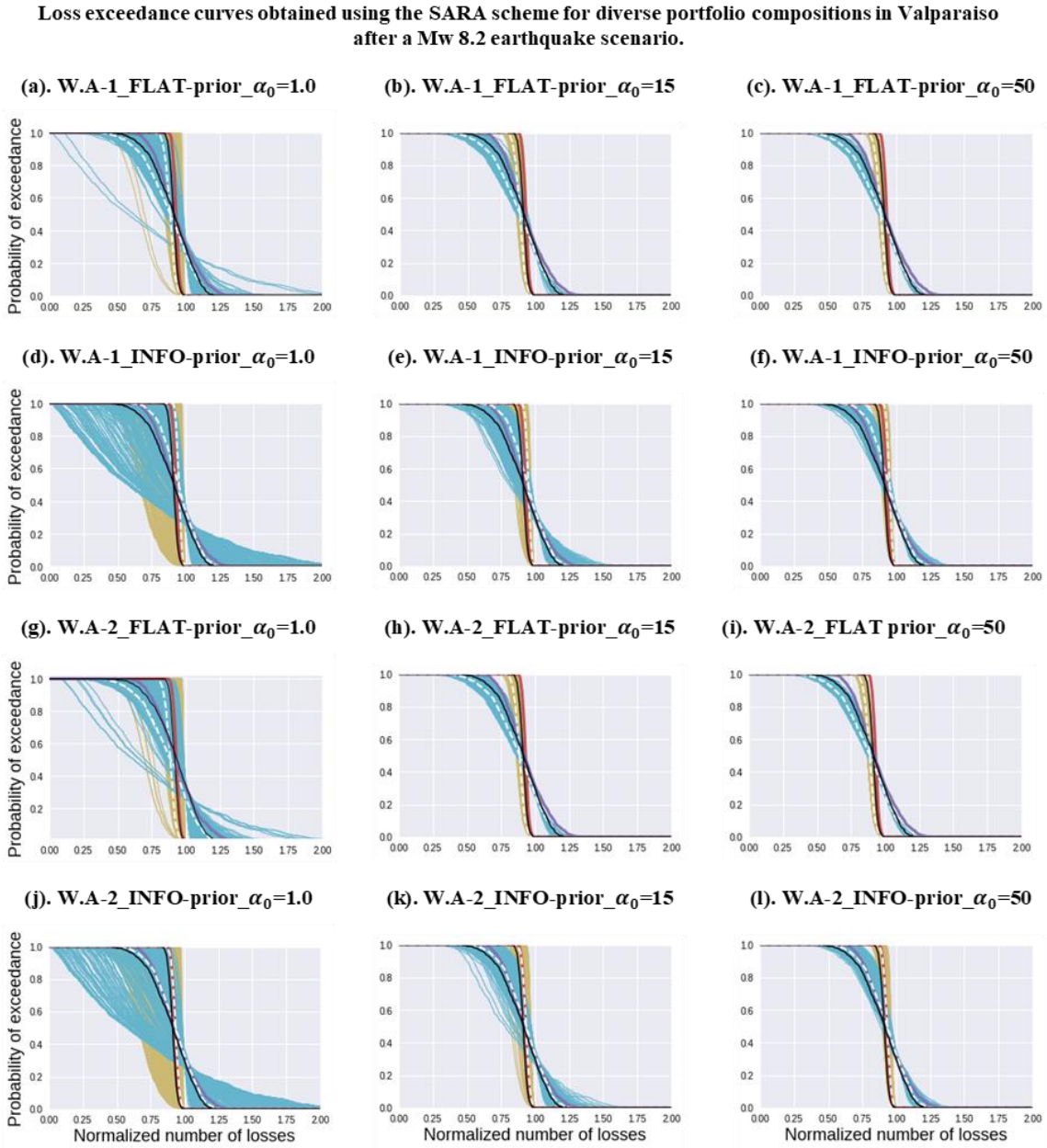

Figure 2-12. Normalized loss exceedance curves (LEC) for different exposure compositions as depicted in the logic tree (Figure 2-7) for the SARA scheme. Curves are displayed in blue if the ground motion cross-correlation model was addressed and in yellow with spatially uncorrelated ground motions. LEC from their respective customized posterior distributions are displayed in non-continuous white curves. The single composition vision as informative priors (as defined by GEM) are depicted in purple when the spatially cross-correlated GMF were addressed and in red with spatially uncorrelated GMF. Black curves represent the losses of a portfolio whose composition is assumed to have equal proportions.

2.4.3.3. The role of the selection of the prior distribution type

LEC obtained from posterior distributions which were constrained using a flat prior (non-continuous white curves in the first and third rows) always led to lower values than assuming equally composed portfolios (respective black curves) and assuming unique top-down vision using the GEM mapping-schemes (purple and red curves). Posteriors created with flat priors tend to concentrate lower loss values at the lowest probabilities of exceedance (p.o.e). The opposite is observed when informative priors are addressed. Since for both types of posteriors there was an incorporation of evidence (surveys) into the construction of the likelihood term, these differences come from the selection of the type of prior (uninformative vs. informative). Similar features could be observed in Figure 2-6 where flat priors largely

impacted upon the creation of the posterior distributions. We recall once again that flat priors are only introduced herein for illustrative purposes and their use is never recommended. The greater dispersion in SARA's LEC might be due to the joint effect of the prior definition and the variability induced by using the cross-correlation model for the GMF generated for the three spectral periods required by SARA. This aspect is discussed hereafter.

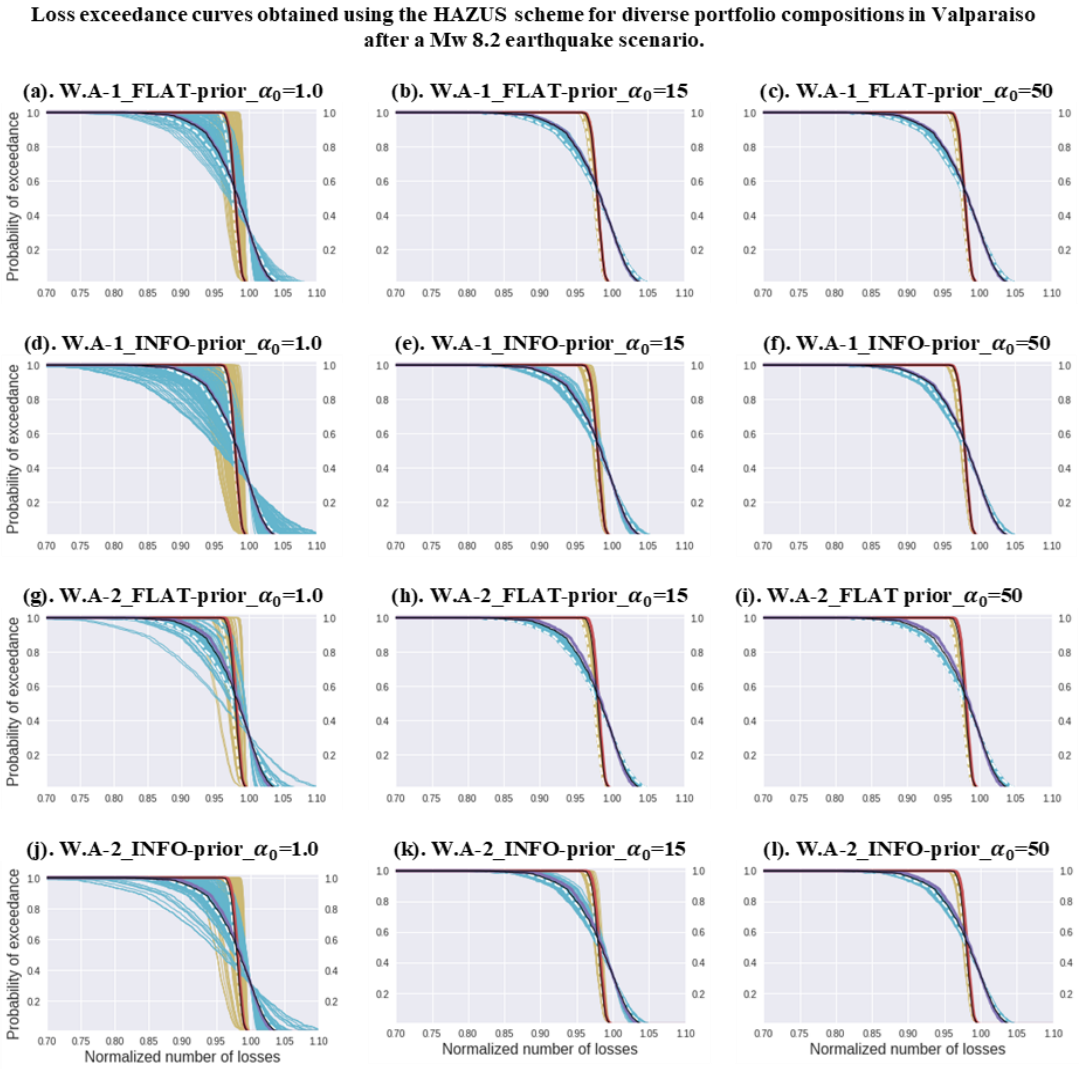

Figure 2-13. Normalized loss exceedance curves (LEC) for different exposure compositions as depicted in the logic tree (Figure 2-7) for the HAZUS scheme. Curves are displayed in blue if the ground motion cross-correlation model was addressed and in yellow with spatially uncorrelated ground motions. LEC from their respective customized posterior distributions are displayed in non-continuous white curves. The single composition vision as informative priors (from the inter-scheme conversion matrices in Figure 2-5) are depicted in purple when the spatially cross-correlated GMF were addressed and in red with spatially uncorrelated GMF. In every plot, the LEC values from their respective posterior distributions are displayed in non-continuous white curves. Black curves represent the losses of a portfolio whose class composition is assumed to have equal proportions.

2.4.3.4. The role of the spatially cross-correlated ground motion residuals

Regardless of the building portfolio composition, when the cross-correlation model is considered, their corresponding LEC shows a greater variability. Moreover, considering that the spatial correlation of ground motion IMs decreases rapidly with distance (e.g., Schiappapietra and Douglas, 2020), its effect on loss-estimations is maximized when it is applied to a dense and large exposure model such as ours (aggregated building portfolio on a 1 km x 1 km grid), since buildings within a grid cell are treated as if the inter-station distance was zero. Additionally, because we have utilised the HAZUS fragility functions only using PGA, the spatially cross-correlated GMFs are not needed. This leads to a lower variability in the HAZUS' LEC that only starts to be perceptible, for

greater p.o.e, at larger values of their normalized metric (i.e., 0.7). Interestingly, whether we decide to use spatially uncorrelated or cross-correlated GMF, when we employ a single IM in the vulnerability analyses, as assumed for HAZUS, we observe that as the level of knowledge in the exposure composition increases (with increasing α_0), the bias in the LEC (made up of the stochastic portfolios) is accordingly reduced. Contrary, this point of convergence with respect to the composition of each posterior distribution is never reached by the SARA's LEC. Considering that PGA alone is not a sufficient IM to model the various structural fragility functions that a real heterogeneous building portfolio requires (Luco and Cornell, 2007), when we decide to use more realistic fragility functions for the heterogeneous portfolio, the spatial variation in the ground motion places a lower limit on the uncertainty in the loss estimates that cannot be entirely reduced (Bal et al. 2010; Michel et al. 2017). This remaining embedded uncertainty in the loss estimations will be present even when the composition of the building portfolio is well known (i.e., $\alpha_{0_3} = 50$).

Complementary, in Figure 2-14 we present normalized loss curves using the results obtained from the top-down assumption (single exposure composition) and without correlation per scheme. Only posterior distributions designed with informative priors and with W.A-2 (ductile structures in the surveys) are used and are shown by purple lines. Blue lines represent the stochastic portfolios either with $\alpha_{0_2} = 15$ or $\alpha_{0_3} = 50$. As expected, it can also be seen that as α_0 increases, there is a continuous reduction in the biases. For similar α_0, we see the larger variability in the normalized loss given by the posterior proportions of SARA in comparison with HAZUS. This once again shows the impact of the cross-correlated GMF.

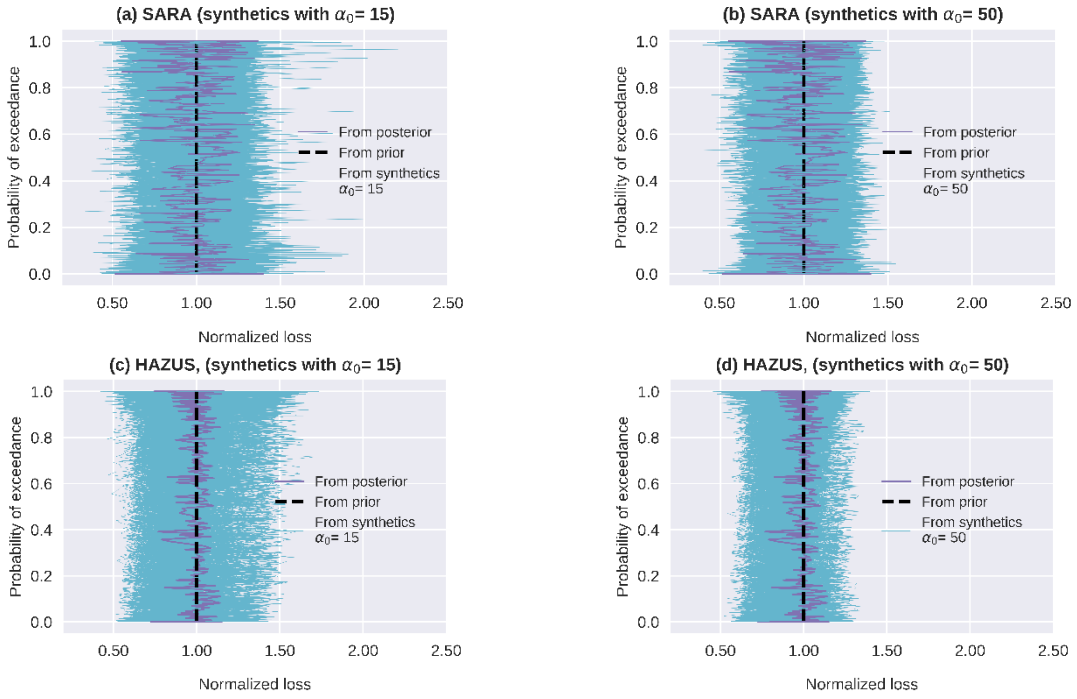

Figure 2-14. Normalized losses (a, b) SARA and (c, d) HAZUS schemes for the exposure compositions in Valparaíso for two selected α_0 values. The loss curve from the top-down assumption (from expert-based priors) is used as benchmark.

Figure 2-15-a displays the sensitivity resulting from the selection of the weighting arrangement (w_j) for both schemes. Its benchmark is the HAZUS loss curve which was obtained by assuming the portfolio composition as the posterior proportion for W.A-1 (Figure 2-6) and with spatially cross-correlated GMF. Similarly, as shown in Figure 2-11, the largest values are obtained for HAZUS with W.A-2. Figure 2-15-b shows the impact of foreseeing the portfolio composition either exclusively from a top-down vision (Prior) or when the evidence from surveys is included (Post.). Its benchmark is the HAZUS loss curve assuming a portfolio that is entirely composed as the prior proportion for W.A-1 (Table 2-4) and with spatially cross-correlated GMF. Although the posterior always led to larger losses, it is noted that

such differences are comparative lower for SARA than for HAZUS. Interestingly, in both figures, we observe that for the HAZUS model, the spatially correlated GMF for PGA used by its fragility functions led to certain variations around the same value with respect to the benchmark, but still considerably lower than using uncorrelated random residuals.

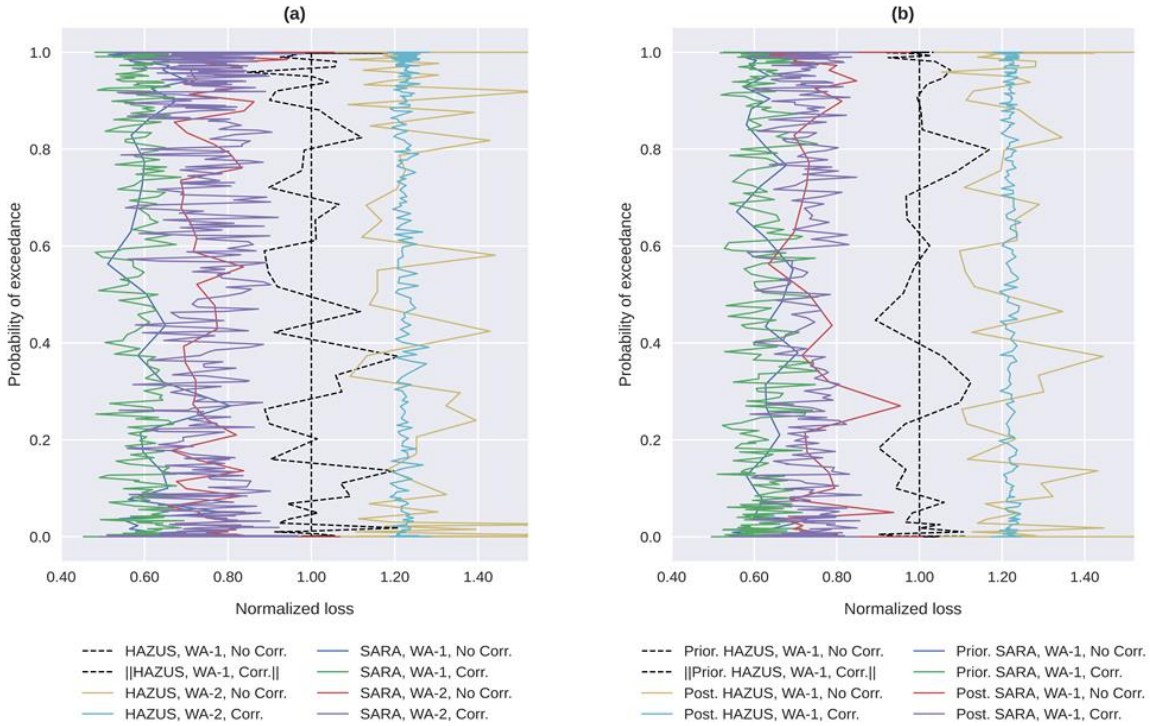

Figure 2-15. Normalized losses for the earthquake scenario in Valparaiso for SARA and HAZUS schemes. Plots show sensitivity on (a) the selection of the weighting arrangement (w_j), and (b) the portfolio composition, either from a top-down vision (Prior) or including surveyed evidence (Post.). The normalization nomenclature (i.e., $||\ ||$) is used to distinguish the benchmarks

2.5. Discussion and future outlook

In this study we have considered that, within a Bayesian approach for exposure modelling, the Dirichlet distribution is suitable for representing the composition (i.e., the relative proportions) of spatially distributed residential building portfolios. To consider the integration of empirical (e.g., field-based) observations into the model, we have assumed the likelihood term to follow a multinomial distribution. Due to conjugacy of multinomial and Dirichlet distributions, prior and posterior are both Dirichlet distributions that differ only by the empirical contribution inferred from the frequency observed in the field. It is also worth noting that this data collection does not need to be exclusively derived from surveys, but complementary exploiting remote sensing and image reconnaissance (e.g., (Liuzzi et al., 2019). Furthermore, we have proposed to factorize the Dirichlet hyperparameter α_i through the so-called concentration factor, α_0, that "weights" and adjusts the prior proportions to the observed frequencies. This parameter is useful for describing the extent of confidence in the building portfolio's initial assumptions while still lacking a consistent number of empirical observations. With the increase of observations, the influence of the concentration factor on the posterior distribution will promptly decrease.

We have proposed to arrange the components involved into a logic tree approach (Figure 7). It has allowed us to explore individually how the related uncertainty to their individual components are propagated throughout scenario-based seismic risk and ultimately be reflected in the biases of the direct loss estimates (replacement cost). For the sake of simplicity in illustrating the proposed approach, we have considered only some uncertainties in the parameters employed throughout its development. Thus, the application part of this work has several limitations that are beyond its scope. However, they could be addressed in future research. We list some of them hereafter.

- The fixed number of population counts projected for 2020 reported by GPWv4 (CIESIN, 2018) was spatially disaggregated to estimate the distribution of total building counts per stochastic exposure model (Figure 2-8). This was based on the average number of night-time residents (for each building class) that we have assumed to be statistical values. However, accounting population projections as well as the number of inhabitants per building as random variables that may follow local distributions (e.g., Calderón and Silva, 2021).
- A larger set of prior distributions could also be obtained in future studies by knowledge-elicitation. This process could be done more rigorously to constrain the prior assumptions for smaller sectors within a large study area.
- The choice of GMPE(s) influences the resulting cross-correlated ground motion fields for earthquake scenarios. This comes from the manner in which the residuals and soil nonlinearity are accounted for in the functional form of the selected attenuation model (Weatherill et al. 2015). Hence, it is worth conducting sensitivity analyses in the future that provide us a more complete picture about their differential impact within the proposed method (e.g., Kotha et al. 2018). However, for the subduction regime upon which Valparaíso is located, there are few adequate GMPE models available (i.e., Abrahamson et al. 2016; Montalva et al. 2017). In fact, Hussain et al. (2020) found negligible differences in direct loss estimates for the residential building stock of another Chilean city after using these GMPE to simulate associated GMF from subduction earthquake scenarios.
- The subjective selection of the type of spatial cross-correlation model used to generate the GMF carries epistemic uncertainties (Weatherill et al. 2015). Although the selected model proposed by Markhvida et al. (2018) has been already implemented for subduction earthquakes for the South American context by Markhvida et al. (2017), more rigorous practices could include the incorporation of a locally constrained spatial correlation model (Candia et al. 2020, study published after the elaboration of our work). Furthermore, it is important to have in mind the simplifications induced by applying generic correlation models. These assumptions might induce overestimations in the risk estimates as observed in Abbasnejadfard et al., (2021).

We emphasize that the test site we have selected (Valparaíso, Chile) has been only presented to discuss the role of uncertainty in the exposure model definition on scenario-based earthquake loss models using the methodology herein presented. Likewise, it should be noted that the resulting direct loss estimates that we obtained from flat-prior, as well as those from spatially uncorrelated GMF, are unrealistic and have been presented only as a part of the sensitivity analyses included in the methodology. The study presented does not argue whether one scheme (SARA or HAZUS) is better suited for representing the residential building stock of the city. Although the use of the set of SARA building classes is not completely validated from the surveyed data (Figure 2-3) and is more sensitive to the non-identification of certain attributes (Figure 2-4), their associated fragility functions (Villar-Vega et al. 2017), unlike HAZUS (FEMA, 2012), provide some advantages for risk assessment. For instance, they were derived from the analysis of some regional records within the tectonic setting of the study area and also provided a clearer link between GMF with spatially and inter-period cross-correlated IM required to model the seismic vulnerability of heterogeneous building stocks.

Furthermore, the differences in the loss estimates after using the two schemas call for caution when using exposure and vulnerability models originally developed for other regions (e.g., HAZUS for the US), rather than choosing more local ones (SARA). However, considering that that set of fragility functions was derived using a regional database of records, they lack hazard-consistent ground motions records as recently discussed by Hoyos and Hernández, (2021). Interestingly, these authors also agreed on the possibility of implementing logic trees for various stages within the derivation of vulnerability functions. Such advice emerged as a justification after they found large differences in the risk metrics for a local (city-scale) building portfolio imposed by using the regionally derived SARA fragility functions compared to their subsequent parametrisation (i.e., accounting for local structural characteristics and a locally-consistent record selection).

2.6. Conclusions and recommendations

This study argues that most large-area portfolios within an exposure model are affected by epistemic uncertainties, resulting in a range of possible total building counts and class compositions. Expert-

elicited models used by top-down approaches, even when carefully crafted may often provide only a partial perspective of the real composition of the building stock, while bottom-up approaches based on field-surveys are usually resource-intensive and are seldom carried out systematically.

To tackle these limitations, an exploratory Bayesian framework to study the epistemic uncertainty in seismic risk estimates associated with the probabilistic nature of the building exposure model has been presented. This approach allows the seamless integration of desktop-based and expert-elicited approaches (Sect. 2.2.1.1) with empirical field-based (and remote) observations 2.2.1.2). In the proposed Bayesian formulation, these uncertainties can decrease by improving the number of observations and the quality of prior assumptions. The influence of the epistemic uncertainties to the resulting loss estimation has been explored through a logic tree approach with four hierarchical components:

(1) Considering the selection of risk-oriented building class schemes with associated sets of seismic fragility functions.
(2) The selection of the weighting arrangement (w_j) that rank relevance of taxonomic building attributes upon vulnerability assessment, as well as their ability of reconnaissance by the surveyor. They are used to probabilistically assign the building classes (Figure 2-4) and to configure the likelihood terms to update the proportions of building compositions.
(3) The selection of prior distributions about the composition of the building portfolio from expert-based knowledge (e.g., conventional top-down desktop studies). This is assumed to follow a Dirichlet distribution.
(4) The selection of the concentration factor α_0 of the resultant posterior Dirichlet distribution. This parameter represents the degree of confidence in the underlying assumptions when little empirical evidence is available.

While valuable information can be retrieved from aggregated data sources (e.g., census data) and mapping schemes in order to gather expert-based priors, they should not be used to represent a given building stock (Sect. 2.2.2.1) without exploring the underlying uncertainties. Moreover, such top-down approaches, including the expert-based elicitation of the prior distributions, should be integrated by empirical observations whenever possible. Within this framework, the expert-based priors will be increasingly superseded by real data in the statistical exposure models. An iterative process can thus be envisaged which aims at continuously updating the model rather than employing static modelling.

The description of building classes in terms of taxonomic attribute types has been shown to be instrumental in identifying the most likely classes of a selected observed sample (within a predefined scheme). Considering the presence of certain taxonomic attributes within a probabilistic exposure model as part of a reducible epistemic uncertainty framework allows better links between the observed structural features of buildings with their most likely vulnerability classes. Such data collections, in terms of a faceted taxonomy, allows us to assess the degree of compatibility of each surveyed building with respect to a set of risk-oriented building classes (Sect. 2.3.1.1). Furthermore, this description is also an input for a novel probabilistic inter-scheme conversion (Sect. 2.3.2). That approach is useful for obtaining exposure descriptors (i.e., number of buildings belonging to a certain class, night-time residents, and replacement costs) under another reference (target) scheme in large-area exposure modelling applications. This can be done in terms of vulnerability descriptors for other hazard-reference schemes (e.g., Gomez-Zapata et al. 2021a), thus extending its application beyond the field of seismic risk.

The findings suggest that the direct losses (repair costs) for the residential building stock of Valparaíso subjected to the considered earthquake scenario (Mw 8.2) largely depend upon the decisions made when modelling the building stock under one preferred scheme, as well as upon the range of variation in the total buildings count. This is then a reducible uncertainty that is still accordingly propagated throughout the vulnerability assessment. The blue LEC (accounting spatially cross-correlated GMF) shown in subplots Figure 2-12f,l and Figure 2-13f,l display the ideal, yet hypothetical results, that might be obtained in the case of high quality expert-based priors assumptions, along with taxonomic data collection (at the individual building level) embedded within the proposed statistical modelling approach. Finally, well-structured standards for continuous exposure data collection, based on vulnerability-independent standard taxonomies, combined with sound probabilistic modelling, are instrumental for more robust risk assessment practices.

Acknowledgements

We would like to thank the structural engineers from CIGIDEN for having carried out the RRVS building surveys and to Yvonne Merino (PUC) and Patrick Aravena (DLR) for supervising it. We thank Catalina Yepes (GEM) for providing the SARA model. Thanks to Esteban Sáez (PUC) for providing the seismic microzonation of Valparaíso. Our gratitude to Graeme Weatherill, Nils Brinckmann, Matthias Rüster, and Jörn Lauterjung (GFZ) for their advice and support. We also thank two anonymous reviewers who provided constructive feedback to significantly improve this work. Thanks also goes to Kevin Fleming for the careful proofreading.

Funding The authors disclose the receipt of the following financial support for the research, authorship, and/or publication of this article: J.C. Gomez-Zapata, M. Pittore, and S. Shinde from the RIESGOS and RIESGOS 2.0 projects, funded by the German Federal Ministry of Education and Research (BMBF), with Grant No. 03G0876A-J and 03G0905A-H respectively. These projects are part of the funding programme CLIENT II – International Partner-ships for Sustainable Innovations'. H. Lilienkamp was funded by the Helmholtz Einstein International Berlin Research School in Data Science (HEIBRiDS). P. Aguirre and H. Santa Maria have been funded by the Research Center for Integrated Disaster Risk Management (CIGIDEN), ANID/FONDAP/15110017 and ANID-FONDECYT 1191543.

Availability of data and materials

are available in these repositories: Gomez-Zapata et al. (2021b); Merino-Peña et al. (2021).

Declarations

Conflict of interest. The authors declared no potential conflicts of interest with respect to the research, authorship, and/ or publication of this article.

Chapter 3

3. Towards a Sensitivity Analysis in Seismic Risk with Probabilistic Building Exposure Models: An Application in Valparaíso, Chile Using Ancillary Open-Source Data and Parametric Ground Motion

Abstract

Efforts have been made in the past to enhance building exposure models on a regional scale with increasing spatial resolutions by integrating different data sources. This work follows a similar path and focuses on the downscaling of the existing SARA exposure model that was proposed for the residential building stock of the communes of Valparaíso and Viña del Mar (Chile). Although this model allowed great progress in harmonising building classes and characterising their differential physical vulnerabilities, it is now outdated, and in any case, it is spatially aggregated over large administrative units. Hence, to more accurately consider the impact of future earthquakes on these cities, it is necessary to employ more reliable exposure models. For such a purpose, we propose updating this existing model through a Bayesian approach by integrating ancillary data that has been made increasingly available from Volunteering Geo-Information (VGI) activities. Its spatial representation is also optimised in higher resolution aggregation units that avoid the inconvenience of having incomplete building-by-building footprints. A worst-case earthquake scenario is presented to calculate direct economic losses and highlight the degree of uncertainty imposed by exposure models in comparison with other parameters used to generate the seismic ground motions within a sensitivity analysis. This example study shows the great potential of using increasingly available VGI to update worldwide building exposure models as well as its importance in scenario-based seismic risk assessment [b].

---

[b] published as: Gómez Zapata, J.C.; Zafrir, R.; Pittore, M.; Merino, Y. Towards a Sensitivity Analysis in Seismic Risk with Probabilistic Building Exposure Models: An Application in Valparaíso, Chile Using Ancillary Open-Source Data and Parametric Ground Motions. ISPRS Int. J. Geo-Inf. 2022, 11, 113. https://doi.org/10.3390/ijgi11020113

3.1. Introduction

Exposure refers to the presence of people, livelihoods, species or ecosystems, services, infrastructure, or economic and social assets in places and settings that could be adversely affected by a hazardous events (UNISDR, 2009). Therefore, to describe their differential levels of propensity or predisposition to be affected, various methodologies are used to assess specific types of vulnerabilities (i.e., social, physical, systemic, etc.). In the case of evaluating the physical vulnerability of a building stock exposed to earthquakes (i.e., forecasting the likely distributions of damages and direct financial losses), it is necessary, among other actions, to investigate the expected seismic ground motions as well as the composition of the building portfolio. The latter involves classifying buildings into mutually exclusive collective-exhaustive building classes to form the so-called building exposure model. Each class describes a distinctive physical vulnerability to ground-shaking depending on its physical properties or attributes (Calvi et al., 2006). Typically, the uncertainty in the exposure component has received less attention than other parts of the seismic risk chain (i.e., hazard, vulnerability) (Crowley and Bommer, 2006). Notably, only a few recent studies have indicated that its investigation would benefit from increased research (Crowley, 2014; Corbane et al., 2017). In this context, the concepts of intra-building and inter-building-variabilities were formally introduced by Silva et al., (2019). The first involves the variations at the individual level, whilst the second refers to the differences between various units belonging to the same class. Both types of variabilities are embedded in the problem of classifying a building stock (sometimes very heterogeneous) into a limited set of subjectively proposed typologies. Nonetheless, it is important to consider that, due to the scope of using the exposure model as input for risk estimations, the complexity in the classification of buildings should not increase beyond the available set of fragility functions for generic typologies designed for specific areas (Haas, 2018; Martins and Silva, 2021).

Top-down studies (i.e., desktop studies) that rely on expert-based assumptions and census data analyses are to date the most widely used approaches to represent the composition of large-scale exposure models over administrative boundaries. These activities foresee the exposure model as it was a screenshot for a fixed time and with a unique composition while establishing both: the classes and their respective proportions. Following that approach, global exposure models have been proposed (Jaiswal et al., 2010; Gunasekera et al., 2015; Silva et al., 2020). Some of them have made use of census co-variants to infer building classes through so-called "mapping-schemes" (e.g. Rao et al., 2020). However, since census data are available for dwellings and not buildings, further assumptions on the dwelling-to-buildings ratios are employed by that method (e.g. Crowley et al., 2020). Consequently, distinct expert-based assumptions can lead to contrasting models for the same study area (e.g. Ma et al., 2021; Xin et al., 2021). Furthermore, recent paradigms in exposure modelling have increasingly demonstrated the relevance of counting with spatial and temporal projections to track the evolution and dynamics of the built environment (e.g. Rivera et al., 2020; Calderón and Silva, 2021b) as well as counting with efficient spatial aggregation techniques (Dabbeek et al., 2021).

In order to validate the assumptions of the aforementioned top-down approaches about the portfolio composition and to identify zones with similar or contrasting physical vulnerabilities, it is required to consider with bottom-up perspectives (i.e., in-situ or remote data collection) (Wieland and Pittore, 2017). This is especially relevant when some building attributes that drive their seismic vulnerability, such as structural irregularities (Lagomarsino and Giovinazzi, 2006) are neither randomly nor homogenously spatially distributed throughout the area of interest (Wieland et al., 2012). In this framework, emerging technologies have been proved to be useful to classify large-scale building stocks. For instance, we can mention the use of machine learning techniques over local datasets (Riedel et al., 2015); feature extraction from remote sensing (e.g. Liuzzi et al., 2019; Torres et al., 2019); façade image reconnaissance analyses (e.g. Aravena Pelizari et al., 2021; Rueda-Plata et al., 2021); integrating multi-source information from remote sensing and surveys (Geiß et al., 2017b); and downscaling existing models based on remote sensing products being used as ancillary data (e.g., Zafrir et al., 2020; Geiß et al., 2021). Moreover, methods to design focused surveys for data collection were also proposed (e.g., Pittore et al., 2015). These types of survey designs are useful when the full enumeration of entire building stocks is a highly resource-intensive task (Pittore et al. 2017). During such inspections, instead of "labelling" buildings as certain typologies, their attributes can also be collected in terms of well-known

taxonomies (e.g., Brzev et al., 2013). Based on the former idea, (Pittore et al., 2018b) proposed to assess the degree of compatibility between predefined building classes and inspected building attributes. This procedure offered not only a more transparent classification system (e.g. Nicodemo et al., 2020), but also the ability to configure other hazard-oriented vulnerability schemes (i.e., they are applied not only to earthquakes, e.g. Shinde et al., 2020).

Some recent studies have shown that carefully inspecting a smaller sample (representative subset) is instrumental to inferring the seismic vulnerability of a larger area (e.g., Polese et al., 2019; Kechidi et al., 2021; Tocchi et al., 2021). However, the integration of such bottom-up data collection within a robust statistical framework is a relatively new type of approach that was first considered in (Pittore et al., 2020b). That study proposed a Bayesian method to probabilistically forecast the composition of the building stock of a given area through expert-based priors (about the expected proportions per class) that are increasingly superseded by the real data that is continuously captured during surveys and used to configure the likelihood term. Then, the resulting posterior distribution was assumed to provide the exposure composition (i.e., proportions per class). It is worth exploring the capabilities of integrating freely available crowdsourcing data-sources (e.g., OpenStreetMap, OSM) into such probabilistic exposure models. Although this type of volunteer-acquired data lacks standardised formats and completeness (Hecht et al., 2013; Wang et al., 2020), they offer valuable information on the spatial location of certain attributes without necessary performing time consuming in-situ data collection. They have proved useful to get socio-economic indicators (Feldmeyer et al., 2020); assessing the physical vulnerability of local buildings to earthquakes (e.g., Sousa et al., 2017; Tumurbaatar et al., 2022; Nievas et al., 2022) and floods (e.g., Figueiredo and Martina, 2016; Cerri et al., 2021); and in global exposure initiatives (Soman et al., 2020; Schorlemmer et al., 2020).

Throughout this work, we rely on the results first outlined in Zafrir, 2020; Zafrir et al., (2020) that formally presented a Bayesian approach for building exposure modelling to then achieve the following specific objectives:

- Presenting the capabilities of integrating a freely available dataset gathered from VGI (without having to inspect individual buildings) to derive a probabilistic exposure model for residential buildings in Valparaíso and Viña del Mar (Chile) based on the inferred building footprint area for certain typologies.
- In addition to better characterising the building composition, this approach has improved its spatial representation by downscaling a coarser existing exposure model onto higher resolution regular grids. Define a large magnitude earthquake scenario and construct a related set of exhaustive seismic ground motion fields through the variation of some of its driving parameters.
- Use the former set of ground motions along with the three exposure models as inputs to independently calculate the direct economic losses that are expected from the building portfolio subjected to such a worst-case earthquake scenario. This vulnerability assessment allows us to propagate and compare the uncertainties embedded in the exposure models with respect the parameters used to constrain the seismic ground motions.

3.2. Context of the study area.

The study area includes the communes of Valparaíso and Viña del Mar (Chile) which have 295,113 and 326,759 inhabitants respectively (2017) (INE, 2018), forming the second-largest urban area of the country after Santiago de Chile. The area also houses the main port of the country, and therefore its physical security is vital for the national economy. For simplicity, both communes are referred to as 'Valparaíso' hereafter. In Figure 3-1 we show the location of the study area within central Chile, as well as within the first, second, and third administrative divisions (i.e., region, province, and communes, respectively).

Valparaíso has been afflicted by powerful historical earthquakes. The 1730 event with an inferred magnitude of Mw 9.1 - 9.3 is recognised as one of the largest earthquakes occurred in Chile in written history (Carvajal et al., 2017). Another destructive earthquake with an inferred moment magnitude Mw 8.0 - 8.2 occurred in 1906 and caused significant damage (Montessus de Ballore, 1914). Since then, 12 earthquakes with a macroseismic intensity greater than VII (Mercalli scale) have affected this area (Indirli et al., 2011). It is remarkable the 1985 Mw 7.8 event that destroyed 140.000 dwellings, left 950.000 persons homeless, and caused losses of about $1.8 billion (Comte et al., 1986). The last one out of those 12 events was the 2010 Mw 8.8 earthquake, which caused structural damages to buildings in Viña del Mar (de la

Llera et al., 2017) and impacted upon labour markets (Jiménez Martínez et al., 2020). More recently, the 2017 Mw 6.9 event was felt in the city, although with a lower intensity (Nealy et al., 2017). To forecast the expected damage distributions and losses resulting from future earthquake scenarios affecting the area of interest, in addition to investigating the likely seismic ground motions, it is also necessary to constrain the spatial distribution and composition of the exposed building stock and their associated physical vulnerabilities.

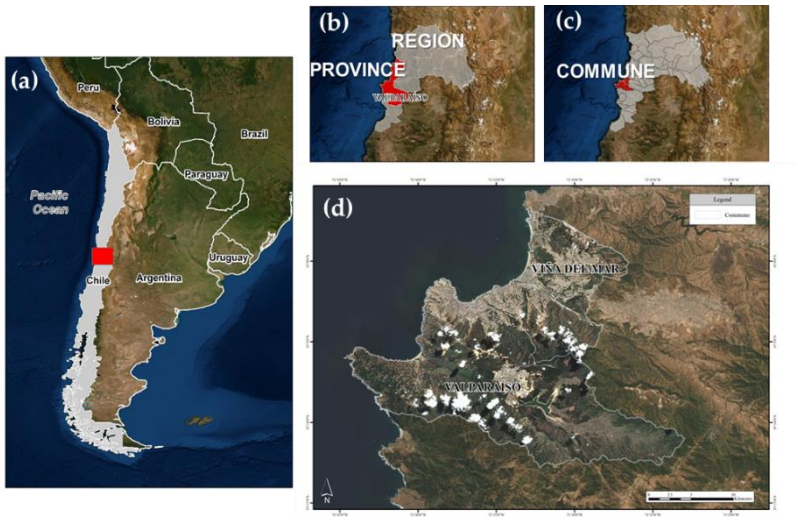

Figure 3-1. Location of the study area within (a) Chile, (b) Valparaíso Region (grey) and Valparaíso Province (red) (c) Communes of Valparaíso and Viña del Mar, (d) a detail of the two communes showing Sentinel-2 images for September 21st, 2019 (downloaded from the Copernicus Open Access Hub of the European Space Agency (ESA). Map data: ©Google Earth 2019. Edited from Zafrir, (2020) and Gómez Zapata et al., (2022b).

Valparaíso has a very diverse building portfolio (Indirli et al., 2011) and notably, its historic quarter was declared World Heritage Site by UNESCO in 2003 after distinguishing its varied urban fabric (Jiménez et al., 2018). Few studies have reported on building exposure models for Valparaíso. The South American Risk Assessment (SARA) project harmonized the residential building through a top-down approach (GEM, 2014). It reached its highest spatial resolution at their third administrative division (i.e., commune in Chile). This means that, for the area of our interest, this dataset was aggregated onto two large geocells. On the other hand, (Geiß et al., 2017a) investigated the use of bottom-up approaches, such as the integration between OSM training segments and remote sensing satellite imagery for exposure modelling in Valparaíso. That study provided a land-use map and a possible range of building units.

More recently, and following the Bayesian method outlined by Pittore et al., (2020b), residential building exposure models of Valparaíso were modelled in Gómez Zapata et al., (2022b). These authors made use of existing expert-based prior assumptions along with only a few (~600) remote building-by-building surveys to ultimately create various posterior distributions that emulated synthetic building portfolios whose variable composition depended on the relative degree of knowledge of the true proportions associated with each class. Thereby, the 2020-based population counts from remote sensing data (Documentation for the Gridded Population of the World, Version 4 (GPWv4), Revision 11 Data Sets) were used to spatially allocate each synthetic portfolio according to the night-time residents assumed for each class. The latter was done over the same resolution (i.e., ~ 1 km regular grid) through dasymetric disaggregation. The latter study did not provide a unique or better estimate of the exposure composition, but it rather presented how the range of variations of building counts and class proportions can be successfully diminished to consequently reduce the epistemic uncertainty in scenario-based loss estimates.

3.3. Materials and Methods

We first present the derivation of a land-use map recently available for the study area. Later, we introduce some generalities of the building exposure model along with certain assumptions over the composition of the residential building stock of Valparaíso. We then recall a Bayesian method to

update the initial assumptions through the integration of the available OSM building footprints to ultimately derive a probabilistic exposure model along with two intermediate exposure models. Finally, the physical vulnerability of the residential building stock and its associated direct economic losses stock are calculated for a selected earthquake scenario. This allows us to explore some differences and epistemic uncertainties imposed by the exposure models available for Valparaíso in earthquake loss models.

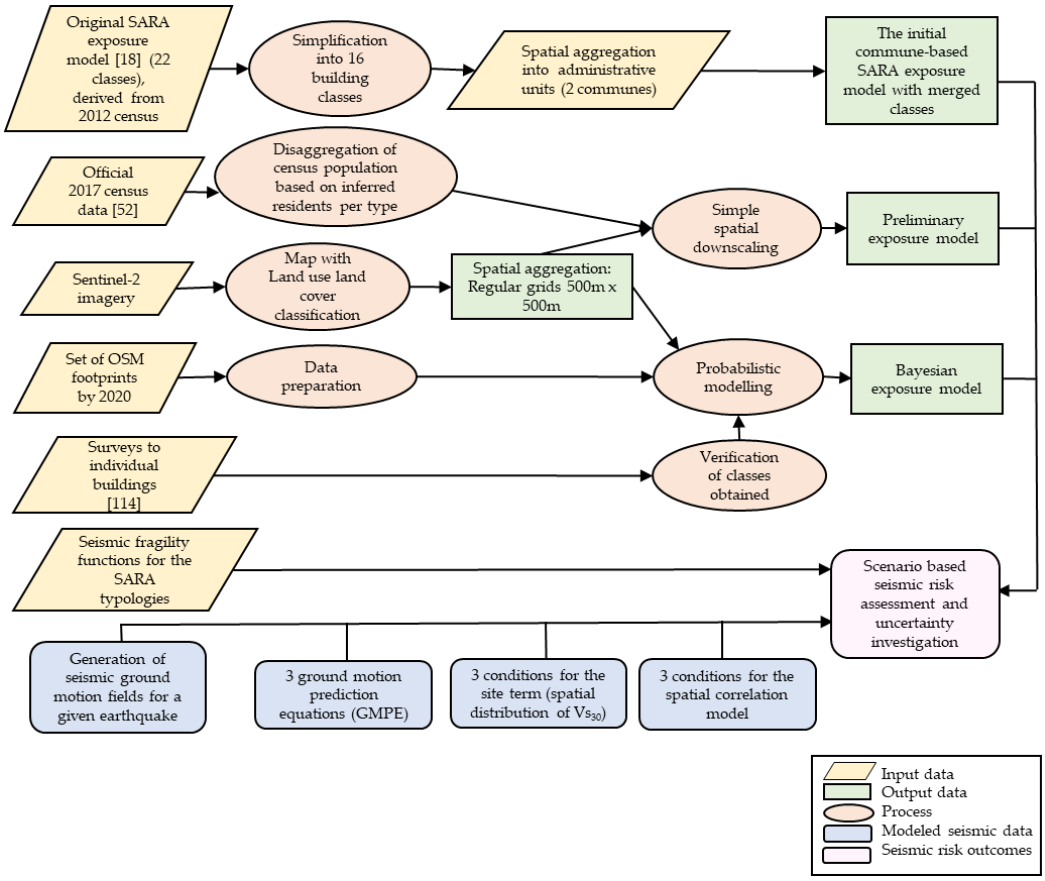

Figure 3-2. Flowchart outlining the input data gathered, the processes and the three resulting residential building exposure model for Valparaíso (Chile) we will be presenting. These exposure models, together with the parametric ground motions, are used as inputs for the sensitivity scenario-based seismic risk in the last stage of this study.

3.3.1. Delimitation of the urban area and some initial features

A supervised classification using Sentinel-2 imagery (September 21, 2019 (Figure 3-1d) at level tier C1 (ESA, 2018)) was carried out in Zafrir, (2020) for the study area. It derived a land-use classification making use of the ERDAS software (ERDAS, 2014) to have a clearer delimitation of the built-up area in Valparaíso. The resultant land use classification is presented in Figure 3-17 (Appendix A). Although this product has not had as many signatures as other more exhaustive models (e.g., (Mohammadi et al., 2020)), it has still allowed us to better relate the built-up area for a continuous urban extent to meaningful geographical entities.

3.3.2. Building exposure and vulnerability models for Valparaíso

Three exposure models for residential buildings are presented hereafter along with a brief description of some available ancillary data used to constrain the third (Bayesian) one.

3.3.2.1. The initial commune-based SARA exposure model with merged classes

We assume that the residential building stock of Valparaíso and Viña del Mar can be fully represented in terms of the typologies originally proposed by the SARA project Yepes-Estrada et al. (2017). That project established the composition of the residential building stocks of the Andean countries based on expert elicitation to design "mapping-schemes".

These schemes define the relationship between a few country-specific census descriptors (i.e., façades and floor material) and certain vulnerability classes for dwellings. Notably, the Chilean census employed by the authors dates from 2002 (INE, 2002). Therefore, the original SARA exposure model presented the composition of the residential building stock of Valparaíso for that year. Although the typologies might not drastically change, it is highly likely that their associated building counts will considerably differ from the current context of the city.

The SARA building classes are described in terms of certain attributes contained in the GEM v.2.0 building taxonomy (Brzev et al., 2013), i.e., type and material of the lateral load-resisting system (LLRS), height, and rarely, ductility type and material technology. Descriptions of these attributes are provided in https://taxonomy.openquake.org/. For each dwelling class, the authors proposed "dwelling fractions" (i.e., dwellings per building type) to obtain the number of buildings. For Valparaíso, the SARA project proposed 22 classes (Yepes-Estrada et al. 2017) while we have reduced this to 16. The assumptions considered to reduce the number of typologies are:

- We do not consider the class "UNK" (unknown) because it lacks observable attributes. Its proportion (~10%) was redistributed to the other classes.
- We have combined five pairs of classes into a more generic enclosing typology that have a similar taxonomic description and only differ in their storey range. These are: ER-ETR-H1 within ER-ETR-H1-2, MCF-DNO-H1 within MCF-DNO-H1-3, MUR-ADO-H1 within MUR-ADO-H1-2, W-WLI-H1 within W-WLI-H1-3, W-WS-H1 within W-WS-H1-2.

The 16 resulting classes have differential seismic vulnerabilities as expressed by their corresponding fragility functions reported by Villar-Vega et al., (2017) (Figure 3-4). Table 3-1 provides further information per typology. The average footprint areas per class (Ft./bdg. (m^2)) were derived from the "reference average area per dwelling" values as a function of the construction quality reported in Yepes-Estrada et al., (2017) for Chile. They are: 70 m^2, 80 m^2, and 70 m^2 for upper, middle, and lower construction quality respectively. Aligned with the construction practices in Valparaíso and with the last two Chilean seismic codes (NCh433 Of.72, (INITN, 1972), and NCh433 Of.96,(INN, 1996), earthen, masonry and non-ductile (excluding RC) types were assumed to have a lower construction quality; wooden and non-ductile RC classes to have a middle one; and ductile RC classes to have an upper quality. The values of such categorization are multiplied by the number of dwellings per class; and then divided by their respective average number of storeys. Finally, they are divided by the number of buildings per class to obtain the inferred building footprint area per typology. This procedure is illustrated in Table 3-4.

Table 3-1 also reports a new categorization (i.e., A, B, C, D, E, F) of the SARA classes as a function of the similarities between their average footprint areas that was conceived initially by Zafrir, (2020). Although this assemblage is consistent with the number of storeys for the lowest (A: 1-2 storeys) and largest values (E: 4-7; and F: 8-19), the grouping for the classes ranging from 1 to 3 storeys (B, C, D) was made in terms of the similarities in their average footprint area values and not any other attribute (e.g. material type). This new categorization, along with the footprint, is used later in this study. A summary of the average height and footprint area (m^2) values of the reclassified typologies are reported in Table 3-2.

It is worth noting that the building counts of the original SARA model over administrative spatial boundaries were obtained through the dasymetric disaggregation of population counts reported in remote-sensing products over resolutions of ~ 1 km^2. This type of procedure is comprehensively described in Dell'Acqua et al., (2013). The disaggregation assumed a fixed number of night-time residents per building typology. The highest spatial resolution of the aggregated exposure model of the original SARA model was made available at the third administrative division of Chile (commune). This means that our area of interest (Valparaíso and Viña del Mar) is only composed of two large geocells (Figure 3-3). Hence, one of the shortcomings of the SARA model is that the spatial distribution of buildings is unknown because all of the exposure information is provided at the centroid of each geocell. Thus, this assumption disregards the outcomes from land-use classifications, which is particularly relevant for Valparaíso as can be seen from Figure 3-17. Although this resolution could be sufficient regional seismic risk estimates (Bal et al., 2010), it will not be adequate for more detailed analysis using local ground motions, nor when aiming for future urban requalification (e.g. Senouci et al., 2018). Thus, a direct downscaling of such information into a more detailed resolution was needed. It was initially carried out by Zafrir, (2020). This process is explained in the following section.

Table 3-1. SARA building classes proposed for the study area along with short descriptions. Average number of dwellings (Dwel./ bdg), night-time residents (Res. /bdg) and replacement cost (Repl. Cost (USD)) are reported as in Yepes-Estrada et al., (2017). Average footprint area (Ft./bdg m²) values are derived from the construction quality categories per dwelling as suggested by Yepes-Estrada et al. (2017) and the mean range of storeys and dwellings per class (see Table 3-4). A new typology in the range A- F is proposed in terms of the similarities of their footprint areas.

Typologies	Description	Dwel / bdg.	Ft/ bdg. (m²)	Res/ bdg.	Repl. Cost (USD)	New type
ER+ETR/H:1,2	Rammed earth, 1-2 stories	1.25	78.79	4	43,750	A
MUR+ADO/H:1,2	Unreinforced masonry with adobe blocks, 1-2 stories	1.25	66.84	4	43,750	
MUR+STDRE/H:1,2	Unreinforced masonry, dressed stone, 1-3 stories	1.25	65.32	5	43,750	
W+WS/H:1,2	Solid wood, between 1-2 stories	1.25	80.00	4	108,000	
MCF/DNO/H:1,3	Confined masonry non ductile, 1-3 stories	4	46.67	5	94,500	B
MUR/H:1,3	Unreinforced masonry, 1-3 stories	1.5	70.00	6	52,500	
W+WLI/H:1,3	Light wood members, 1-3 stories	1.5	80.00	5	108,000	
CR/LWAL/DNO/H:1,3	Reinforced Concrete wall system, non-ductile, 1-3 stories	4	160.00	14	288,000	C
CR/LWAL/DUC/H:1,3	Reinforced concrete wall system, ductile, 1-3 stories	4	140.00	15	336,000	
MCF/DUC/H:1,3	Confined masonry ductile, 1-3 stories	4	160.00	5	288,000	
CR+PC/LWAL/H:1,3	Precast reinforced concrete wall system, 1-3 stories	5	160.00	18	360,000	D
MR/DNO/H:1,3	Reinforced masonry non ductile, 1-3 stories	5	160.00	18	360,000	
MR/DUC/H:1,3	Reinforced masonry ductile, 1-3 stories	5	140.00	18	360,000	
CR/LWAL/DNO/H:4,7	Reinforced concrete wall system, non-ductile, 4-7 stories	15	240.00	54	1,080,000	E
CR/LWAL/DUC/H:4,7	Reinforced concrete wall system, ductile, 4-7 stories	15	210.00	54	1,260,000	
CR/LWAL/DUC/H:8,19	Reinforced concrete wall system, ductile, 8-19 stories	48	218.15	173	4,032,000	F

Table 3-2. Average footprint areas and heights derived for the six subcategories in the range A-F for Viña del Mar and Valparaíso

Typology	Average height (m)	In Viña del Mar		In Valparaíso	
		Average footprint area (m2)	Proportion	Average footprint area (m2)	Proportion
A	**3.75**	**67.5**	**21%**	**73**	**38%**
B	**4.5**	**71**	**59%**	**66**	**50%**
C	**6**	**153**	**11%**	**153**	**7%**
D	**7.5**	**115**	**5%**	**153**	**3%**
E	**15**	**225**	**3%**	**225**	**1%**
F	**36**	**280**	**1%**	**280**	**1%**

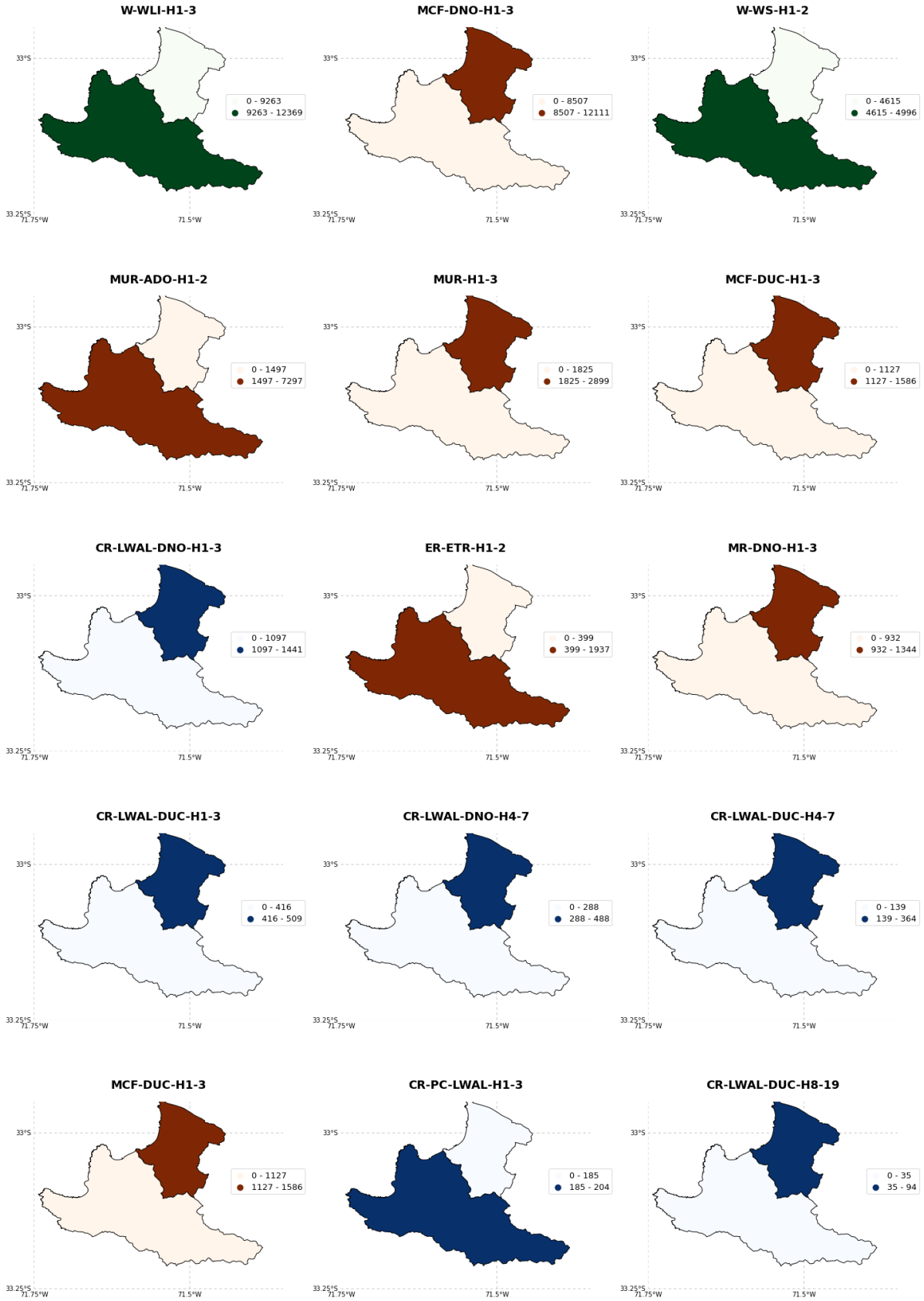

Figure 3-3. Building counts at the commune level. For 15 SARA building classes (after having combined similar typologies (Sect. 3.3.2.1)). the colour scale represents the material type (green: wooden; orange: masonry; blue: reinforced concrete).

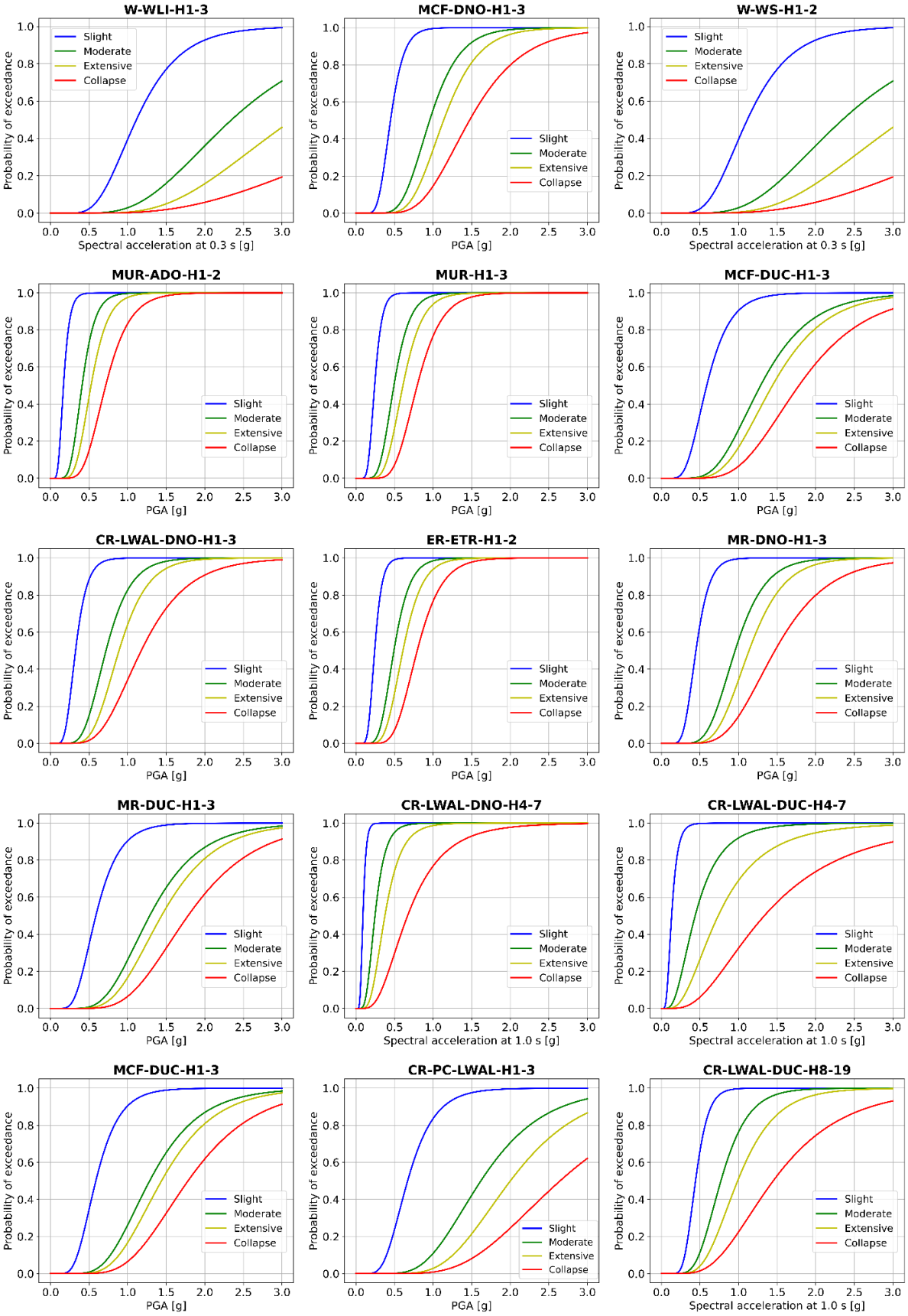

Figure 3-4. Fragility functions for 15 SARA building classes as reported by Villar-Vega et al., (2017) describing their differential seismic vulnerabilities. The curves are presented in a similar order as in Figure 3-3.

3.3.2.2. Preliminary model: a simple downscaling using spatial disaggregation of population

This model constitutes a downscaling of the model at the commune level that spatially aggregates the building counts over a regular 500 x 500m resolution grid. It was originally reported in Zafrir, (2020). Achieving higher resolutions was discarded because that would require further assumptions that would increase the uncertainties of such models. Moreover, since the resulting exposure models are input for seismic risk analyses, the use of higher resolution models would lead to important and unnecessary computational problems (e.g. Scheingraber and Käser, 2020; Gómez Zapata et al., 2021a) that we prefer to reduce at this stage. This stems from the need to address the aleatory uncertainties implicit in a stochastic process, such as by generating thousands of realisations of spatially correlated ground motion fields (Gómez Zapata et al., 2021f).

Contrary to the original SARA model that derived the number of buildings for Chile while using large-scale aggregated population counts and a nationwide mapping scheme based on the 2002 census, such metrics were rather obtained only for the specific study area. First, the urban area mapped from the land-use land cover analysis (Sect. 3.3.1, Figure 3-17) was used as the external boundary of the grid. Then, the population reported in the official 2017 census data (INE, 2018) was used to obtain the number of buildings of every typology based on their associated night-time residents. This census data provides this type of information for various aggregation boundaries, ranging from small urban blocks up to large rural areas with few structures and inhabitants. Such population counts were redistributed throughout the 384 geo-cells cells that make up the 500 x 500m resolution grid. This redistribution was done according to the ratio of enclosed urban blocks with a residential occupancy. Then, the number of buildings for each grid cell was estimated through the disaggregation of the redistributed population. This was done employing equation Eq. 3-1 in Appendix B as proposed by Pittore et al., (2020b). Figure 3-5 shows the resulting ranges of building counts obtained for this model.

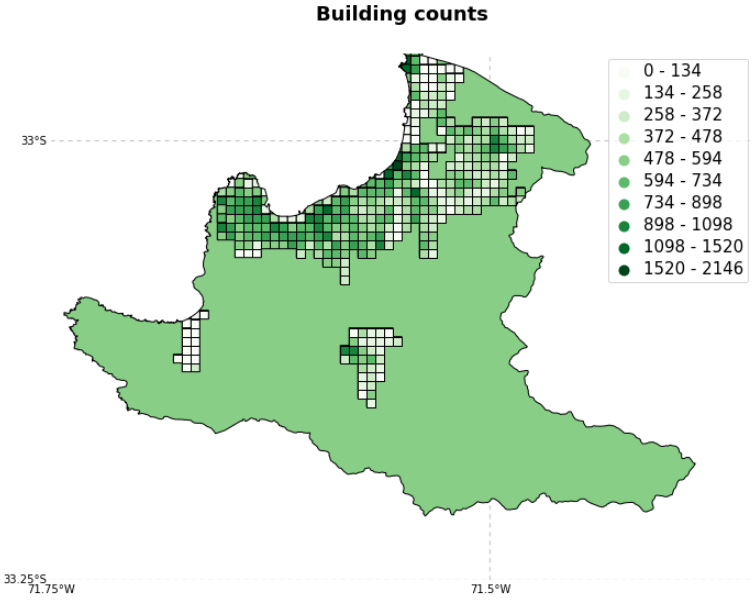

Figure 3-5. Inferred ranges of residential building counts in the study area. This outcome is obtained from the spatial disaggregation of night-time residents at the block level as reported by the official 2017 Chilean census.

Considering the relations proposed in Table 3-1 and Table 3-2, for the subcategories in the range A-F and the SARA typologies, their spatial distributions was obtained as displayed in Figure 3-6 and Figure 3-7 respectively. Note that in these three figures, the background areas (that is not subdivided into regular grids) have intermediate values of buildings counts. That feature corresponds to the spatial redistribution of the UNK class throughout the entire study area (Sect. 3.3.2.1) as well as a contribution of some residential blocks of the census dataset that were not contained within the grid.

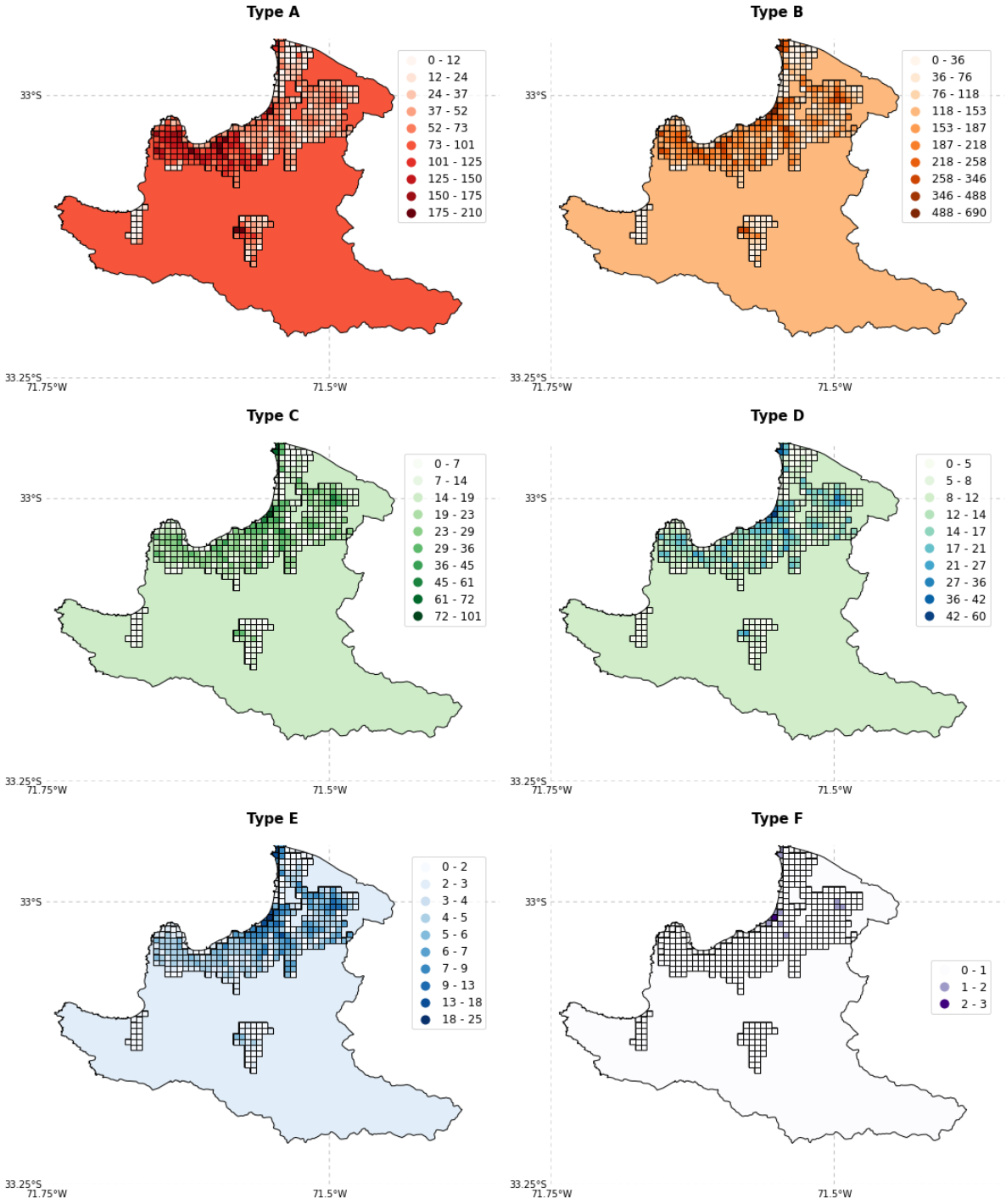

Figure 3-6. Spatial distributions of the building counts for the six subcategories in the range A-F obtained from the preliminary model. The latter involves a simple downscaling using the dasymetric disaggregation of the population based on of use of night-time residents at the block level as reported by the official 2017 Chilean census.

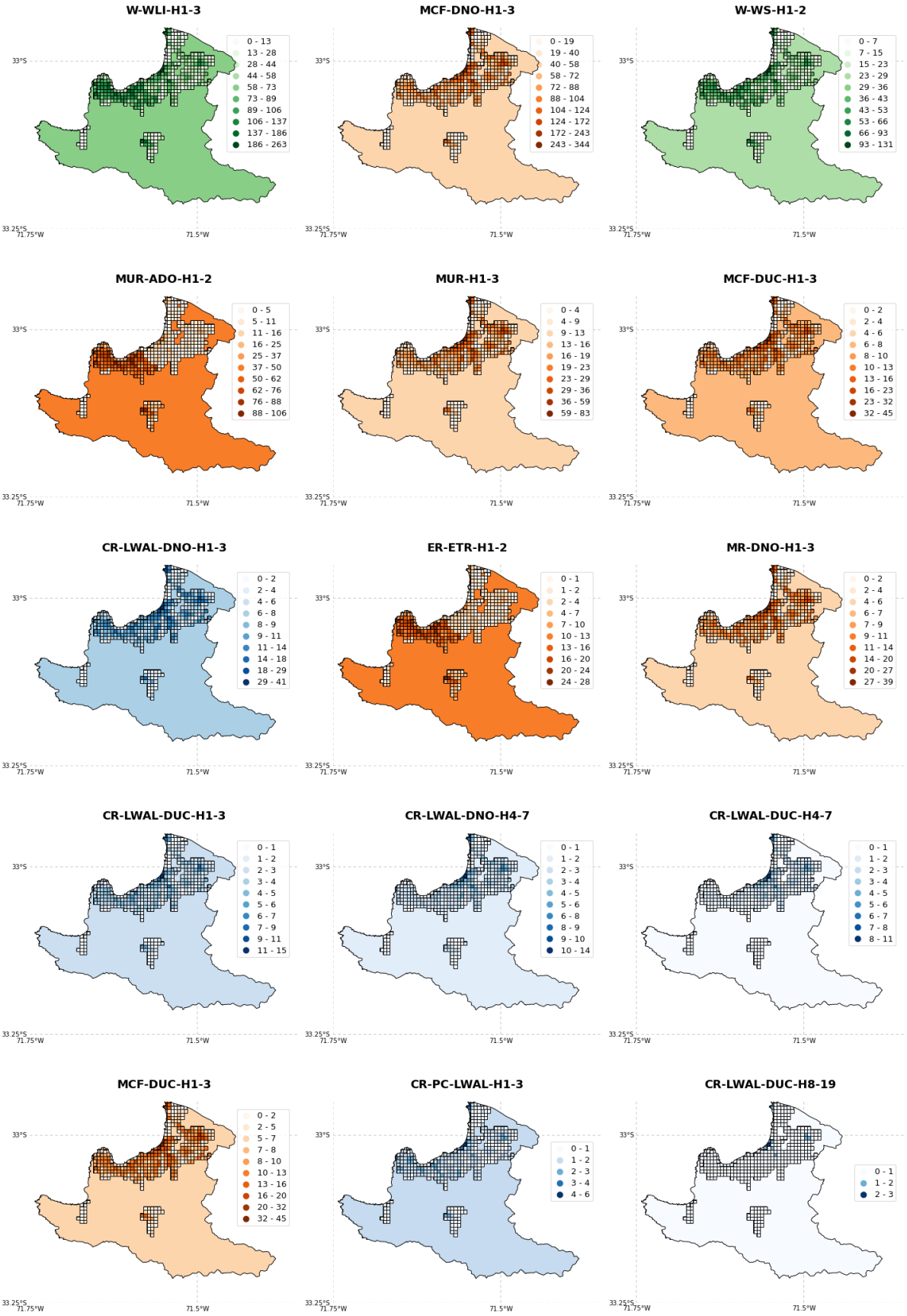

Figure 3-7. Spatial distributions of the building counts for the SARA typologies obtained from the preliminary downscaled model. The colour scale reflects the material type (green: wooden; orange: masonry; blue: reinforced concrete).

3.3.2.3. Ancillary data available for Valparaíso

3.3.2.3.1. OpenStreetMap (OSM)

A large collection of building geometries for the study area has been available since the Humanitarian *OpenStreetMap team task* mapped the affected and surrounding areas by the Great 2014 Valparaíso Fire to support damage assessment and first response (OSM Task Manager, 2014a, b). That event destroyed over 2,900 homes and burned over 1,000 ha. in 5 days (Reszka and Fuentes, 2015). Since then, the availability of this type of crowdsourcing data has been on the rise. Examples of the OSM building footprints for a selected area of Valparaíso are shown in Figure 3-8. The types of available input data for the 384 grid cells that contain residential buildings in the study area are displayed in Figure 3-18 (Appendix A).

Figure 3-8. Building footprints for a certain area in Valparaíso (© OpenStreetMap contributors 2021. Distributed under the Open Data Commons Open Database License (ODbL) v1.0. Map data: ©Google Earth 2020. Figure reprinted from Zafrir, (2020).

3.3.2.3.2. Data collection of taxonomic attributes in Valparaíso and building classification

604 randomly distributed buildings throughout the study area (see Appendix C) were inspected by expert civil engineers from the Pontificia Universidad Católica de Chile (Merino-Peña et al., (2021). Their attributes were collected in terms of the GEM V.2.0 taxonomy (Brzev et al., 2013) while making use of the RRVS (Rapid Remote Visual Screening) web-platform (DEMO: Remote Rapid Visual Screening (RRVS)). This tool makes use of Google Street View and OSM footprints. The resulting dataset is available in Merino-Peña et al., (2021). A summary of some of the observed taxonomic features as well as the method utilised in the classification of this building sample are provided in Appendix C. It is worth noting that, contrary to the approach of Gómez Zapata et al., (2022b), the data collection from the RRVS surveys was not directly integrate within the Bayesian model. Instead, this information is used to compare the plausibility of the generated exposure model, as will be presented afterward.

3.3.2.4. Bayesian exposure model for Valparaíso

The theoretical conceptualisation and assumptions of this model initially proposed in Zafrir, (2020) that relied on former approaches (Pittore et al., 2020b; Gómez Zapata et al., 2022b) is presented in the Appendix D. Out of a total of 384 grid cells, 294 grid cells, for which OSM footprint area was available Figure 3-18 were updated using the Bayesian approach. The resultant probabilistic exposure model gives to each geo-cell the total number of buildings classified into the six subcategories in the range from A to F. In order to complete the exposure information for the remaining 90 grid cells (~23% of the model), a hybrid model was generated by combining the generated information from the Bayesian approach

along with the preliminary model that comprised a simple spatial downscaling (Sect. 3.3.2.1). During this procedure, the individually surveyed buildings using the RRVS platform and their classifications (Appendix C) were used to cross-check the spatial distributions of the predominant building classes for seismic vulnerability within the grid cells. Figure 3-9 displays the spatial distributions of the building counts for such subcategories in the range from A to F. Once the posterior distributions for the six subcategories in the range A-F were obtained for each grid cell, the resulting quantities are expanded to the corresponding set of 16 SARA building classes using their relative proportions (Table 3-1, Table 3-2). Figure 3-10 does the same for 15 selected SARA building classes.

3.3.2.5. Comparison of exposure models available for Valparaíso

Figure 3-11 and Table 3-3 illustrate the number of buildings obtained from the three exposure models considered. Bearing in mind that the simplest model (initial commune-based) was generated using the oldest data, it is not surprising that it gives the lowest building counts. The preliminary model (simple downscaling) which was generated inferring the building counts from the population at the block level produces only slightly larger counts. However, the results obtained from the probabilistic approach leads to important differences for the four most common types, as well as for CR-LWAL-DNO/ (DUC)-H4-7. Although the respective proportions per type do not significantly vary, the Bayesian approach leads to an increase of ~34% and ~40% in the total number of buildings in comparison with the commune-based and the simple downscaling models, respectively.

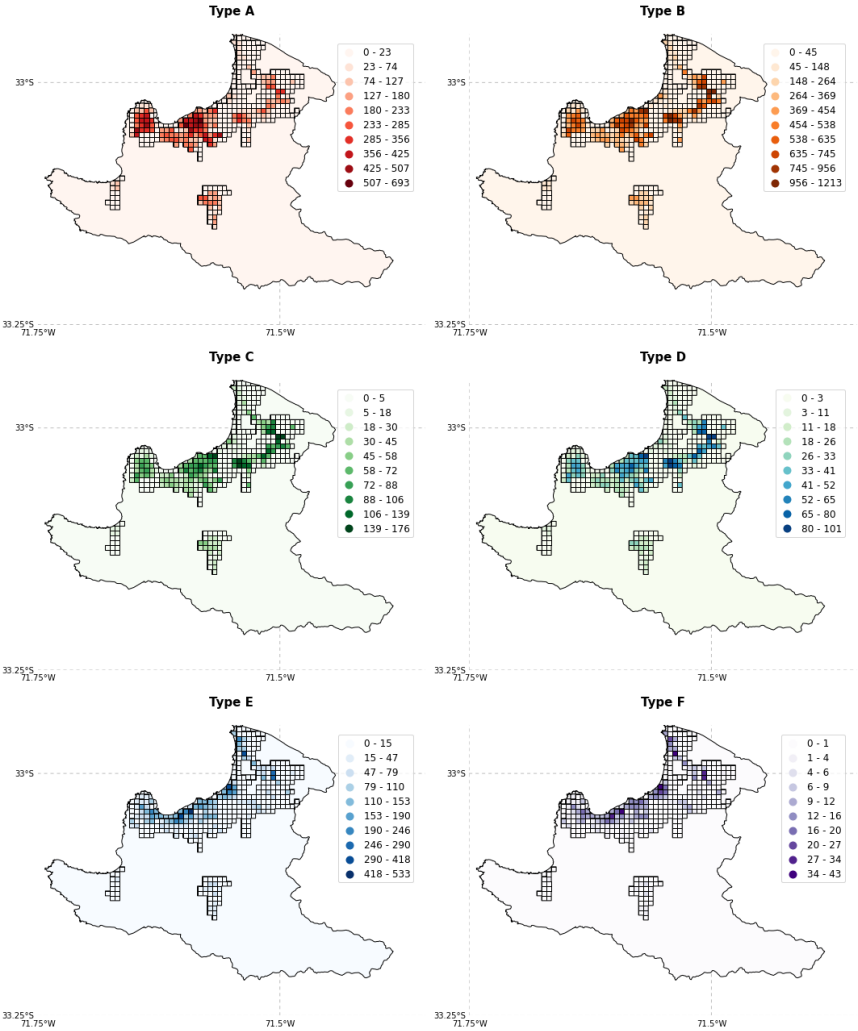

Figure 3-9. Spatial distributions of the building counts for the subcategories in the range A-F obtained from the probabilistic model in Valparaíso.

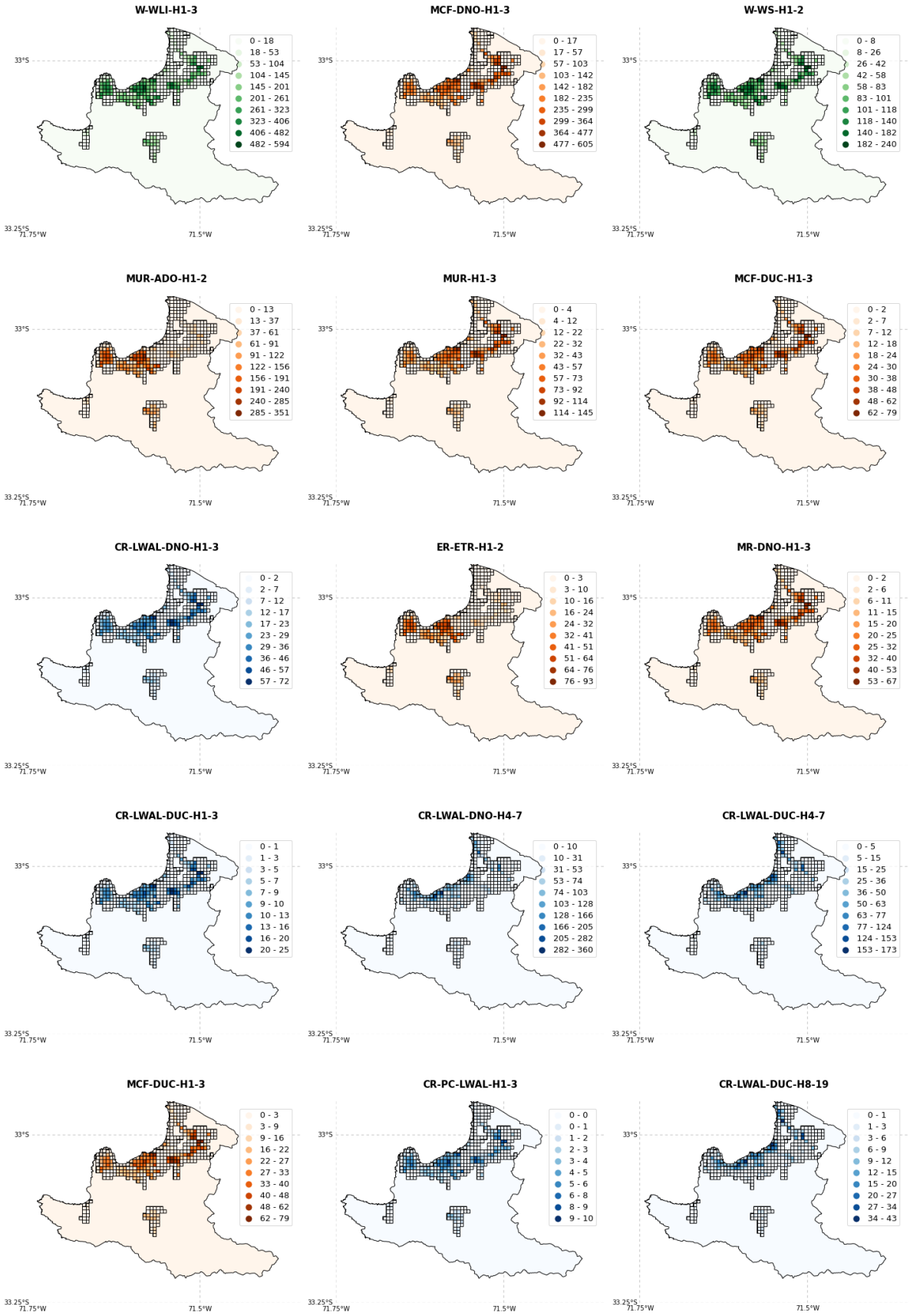

Figure 3-10. Spatial distributions of the building counts for the SARA typologies obtained from the probabilistic model in Valparaíso. The colour scale is selected in terms of the material type (green: wooden; orange: masonry; blue: reinforced concrete).

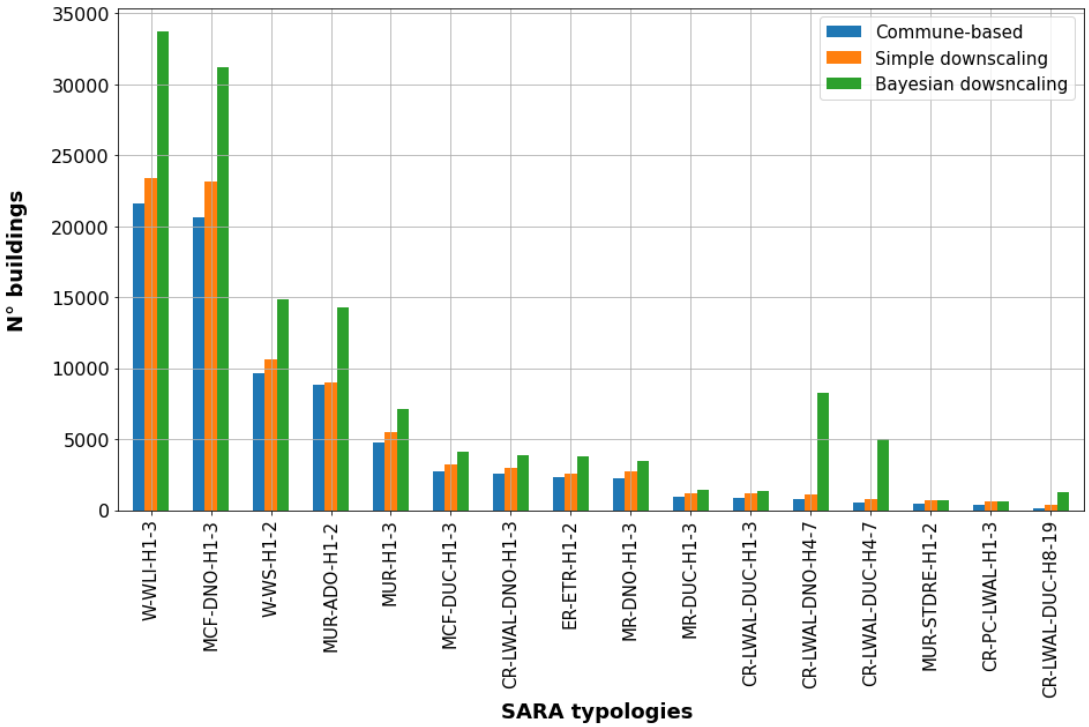

Figure 3-11. Comparison of the building counts per SARA typology for the three exposure models considered for Valparaíso: Initial commune-based model with merged classes, the preliminary model (simple downscaling), and the Bayesian model.

Table 3-3. Comparison between the counts and frequencies for each building typology of the three considered exposure models.

	Initial model (Commune-based with merged classes, Sect. 3.3.2.1)	Freq. (%)	Preliminary model (Simple downscaling, Sect. 3.3.2.2)	Freq. (%)	Probabilistic model (Bayesian downscaling, Sect. 3.3.2.4)	Freq. (%)
W-WLI-H1-3	21631	27.29	23374	26.22	33695	24.97
MCF-DNO-H1-3	20617	26.01	23146	25.97	31244	23.15
W-WS-H1-2	9610	12.12	10619	11.91	14835	10.99
MUR-ADO-H1-2	8793	11.09	9013	10.11	14298	10.59
MUR-H1-3	4723	5.96	5494	6.16	7128	5.28
MCF-DUC-H1-3	2712	3.42	3216	3.61	4111	3.05
CR-LWAL-DNO-H1-3	2537	3.2	3006	3.37	3854	2.86
ER-ETR-H1-2	2335	2.95	2542	2.85	3801	2.82
MR-DNO-H1-3	2274	2.87	2728	3.06	3449	2.56
MR-DUC-H1-3	924	1.17	1222	1.37	1407	1.04
CR-LWAL-DUC-H1-3	865	1.09	1166	1.31	1311	0.97
CR-LWAL-DNO-H4-7	775	0.98	1065	1.19	8293	6.14
CR-LWAL-DUC-H4-7	502	0.63	792	0.89	4980	3.69
MUR-STDRE-H1-2	452	0.57	723	0.81	689	0.51
CR-PC-LWAL-H1-3	388	0.49	633	0.71	603	0.45
CR-LWAL-DUC-H8-19	129	0.16	398	0.45	1265	0.94
∑ total	79267	100	89137	100	134963	100

We remark some of the particularities obtained for the two intermediate and more simplified exposure models for the study area:

- The first model (Sect. 3.3.2.1) is quite similar to such original SARA model since it maintains its spatial representation over administrative units. Its composition is made from the combination of similar classes in terms of their height.
- The second one (preliminary downscaled model, Sect. 3.3.2.2) constitutes the spatial disaggregation of the former onto higher resolutions regular grid cells (500m x 500m). The total number of buildings was estimated by disaggregating the population at the block-level from the 2017 official Chilean census.

The former two models consider that all the geo-cells have the same proportions for the six subcategories A-F within Viña del Mar and Valparaíso (Table 3-2) as proposed by the original exposure model SARA. Conversely, as formerly stated, the third and definitive model (Sect. 3.3.2.4) was derived using a Bayesian approach. It estimated the building counts directly from the existing OSM footprints of residential buildings (Sect. 3.3.2.3.1). The exposure composition within every geo-cell was modelled as a posterior Dirichlet distribution which is assumed to be proportional to the maximum likelihood estimation of the inferred footprint areas per building typology (Equations Eq. 3-8 and Eq. 3-11). Moreover, it has the same spatial resolution adopted by the second model.

Regarding the composition of the three aforementioned models, we can observe a general trend of transversally maintaining similar proportions in their building classes (Table 3-3). This might mean that the construction practices for residential buildings along the study area have been maintained at least from 2002 until 2020. However, certain differences can be highlighted within that general trend. Interestingly, the Bayesian-derived model led to much larger quantities for two typologies: CR-LWAL-DNO/ (DUC)-H4-7 (Figure 3-11) that are mostly grouped in Viña del Mar and in the vicinity of the coastline. This feature might either reflect the increasing tendency of constructing higher building rises, or possible artifacts which could have been induced by incorrectly associating relatively larger building footprints to these types of moderate rise buildings. Considering the recent practices of incrementally constructing higher-rise buildings, the first hypothesis might be plausible.

The comparison of the spatial distribution of the building classes for the second (preliminary downscaling) against the third (Bayesian-based), either for the A-F subcategories (Figure 3-6 and Figure 3-9) or for the SARA classes (Figure 3-7 and Figure 3-10), allow us to identify some differences. As formerly described, the maps of the second model show non-zero values on the background area. Notably, these quantities are larger for earthen building and unreinforced masonry types (the most common types in the study area according to the original SARA model as well as to the three models herein presented). Both typologies could represent the presence of more informally constructed buildings outside the urban perimeter. A clearer spatial delimitation of these typologies is still pending and relevant since they can be especially vulnerable to seismic actions (Acevedo et al., 2017).

Furthermore, it is interesting to see that the second model displays quite small and unrealistic counts for the buildings characterised as walled reinforced concrete and moderate to high rise (blue colours in Figure 3-7). This contrasts with the Bayesian model that reported larger and well-focused areas where the presence of these typologies is expected. The presence of comparatively larger building footprints for which we associate these building types occurs in focused zones close to the coast and in Viña del Mar. These areas are typically characterised to host medium- and high-rise buildings (Jiménez et al., 2018), thus, confirming the predictive Bayesian model. However, in the absence of robust alternatives to validate these results, the epistemic uncertainty of the estimated proportions for these walled reinforced concrete and moderate to high rise classes would be comparatively higher. It is worth noting that better constraining the spatial distribution of these types of structures is still necessary because, besides the differences in the expected counts, their associated uncertainties in the reconnaissance of their ductility levels and construction quality could significantly and differentially drive their seismic vulnerabilities (Arroyo et al., 2021; Vásquez et al., 2021).

3.3.3. Generation of seismic ground motion fields for an earthquake scenario

A worst-case mega-thrust earthquake scenario with a moment magnitude of Mw 9.1, similar to the one that hit Valparaíso in 1730 is considered (Carvajal et al., 2017). We simulate a finite fault model and obtain their respective spatially distributed spectral accelerations using Shakyground 1.0 (Weatherill et al.,

2021), a script that relies on the OpenQuake Engine (Pagani et al., 2014). The basic parameters used in the simulations are: hypocentre location (longitude = −71.5°; latitude = −32.5°; depth = 25 km), strike = 3°, dip = 15°, and rake = 117°. Seismic ground motion fields are generated following a sensitivity analysis selecting various alternative parameters, namely: (1) the GMPE selection, (2) the Vs_{30} model, (3) the spatial correlation model.

3.3.3.1. Ground motion prediction equation (GMPE)

The selection of the GMPE has been proved to be largely relevant in probabilistic seismic risk (e.g. Kalakonas et al., 2020; Kotha et al., 2018) as well as in scenario-based risk (e.g. Hussain et al., 2020) for building stocks. We make use of three ground motion prediction equations (GMPE) formerly proposed for inter-plate subduction tectonic regions to generate seismic ground motion fields for PGA, S.A(0.3 s), and S.A(1.0 s). They are namely:

- Ghofrani & Atkinsonm, (2014) (Ghofrani and Atkinson, 2014)
- Abrahamson et al, (2015) (Abrahamson et al., 2016) ("BC Hydro" Model)
- Montalva et al. (2017) (Montalva et al., 2017): adaptation of the former GMPE, calibrated to Chile.

3.3.3.2. Site term (spatial distribution of Vs_{30})

Local site conditions, such as soft soils can heavily impact direct loss estimates for building stocks exposed to earthquakes (Peyghaleh et al., 2018). The "site" term of the selected GMPE considers the shear wave velocity for the 30 uppermost meters (Vs_{30} values) as the only proxy. Sensitivity on this term was performed considering three Vs_{30} conditions:

- Assuming Vs_{30} values of 600 m/s uniformly distributed throughout the study area. This emulates the presence of a moderately homogenous weathered rock with similar values assumed for the seabed rocks (Figure 3-12-a).
- Derived from slope-proxy as proposed by the USGS (Heath et al., 2020). (Figure 3-12-b).
- The combination between the former model and, when available, the derived values from a local seismic microzonation reported in Mendoza et al., (2018) (Figure 3-12-c).

3.3.3.3. Spatial correlation model

The impact of either accounting spatial uncorrelated, correlated or cross-correlated ground motion fields in earthquake loss models for large-scale building portfolios has been found to be highly relevant in former studies (e.g. Weatherill et al., 2015). We present as an example a single realisation of the ground motion field while considering the Vs_{30} values from microzonation (Figure 3-12-c) and the Montalva et al. (2017) GMPE for three considered conditions:

- Uncorrelated ground motion fields (Figure 3-14-a)
- A spatial correlation model (Jayaram and Baker, 2009) (Jayaram and Baker, 2009) (Figure 3-14-b,c,d).
- The cross-correlation model proposed by Markhvida et al. (2018) (Markhvida et al., 2018) (Figure 3-14-e,f,g). It is useful when various intensity measures (IM), such as spectral accelerations at different periods are used by the set of fragility functions.

In order to account for the aleatoric uncertainty of the GMPE-based ground motions, we follow the advice of (Silva, 2016) and compute 1,000 realisations per each configuration of GMPE, Vs_{30}, and spatial correlation. The three exposure models formerly presented are addressed as the fourth element within this sensitivity analysis to calculate their seismic vulnerability. These models along with their fragility functions are assembled in order to fulfil the data formats required by the software Assetmaster and Modelprop (Pittore et al., 2021). They produce inputs, that together with the ground motions provided by Shakyground are used by the engine DEUS (Brinckmann et al., 2021) to estimate the damage and losses. The replacement cost values suggested in Villar-Vega et al., (2017) and loss ratios per damage state (i.e., 2%, 10%, 50%, and 100%) are used. Therefore, 81 parametric combinations for risk assessment are generated per ground motion realisation.

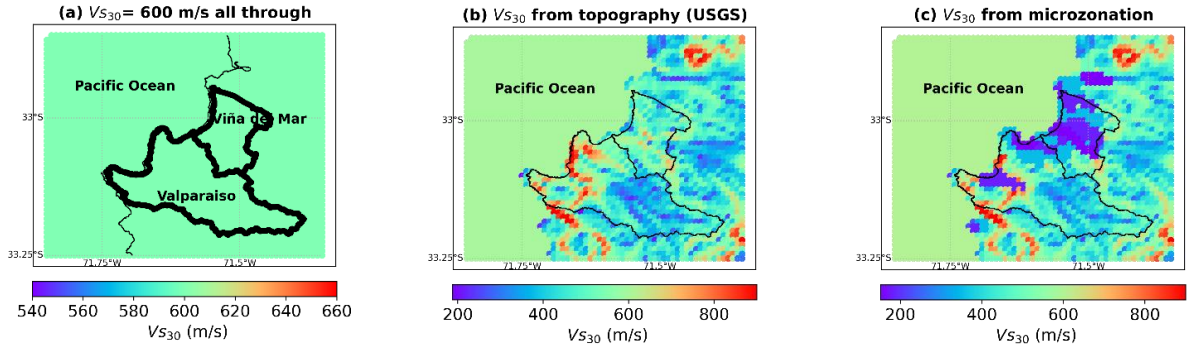

Figure 3-12. Distribution of the Vs_{30} values in Valparaíso and Viña del Mar (a) considering 600 m/s uniformly distributed all through; (b) as proposed by the USGS (Heath et al., 2020); and (c) its combination with the seismic microzonation (Mendoza et al., 2018).

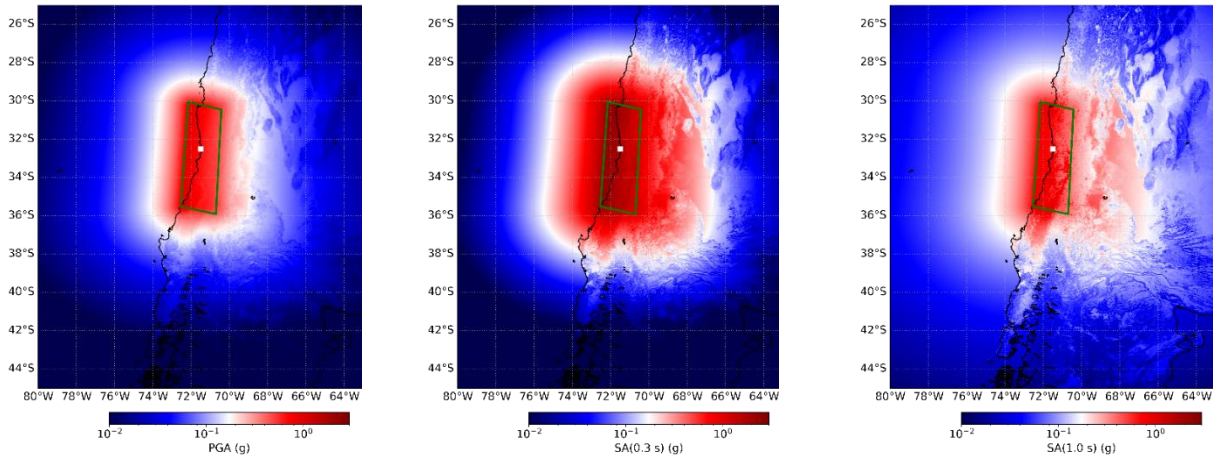

Figure 3-13. Median values of the Mw 9.1 earthquake for three IMs (a) PGA, (b) S.A. (0.3 s) and (c) S.A. (1.0 s) using the (Montalva et al., 2017) GMPE. The earthquake hypocentre is shown as a white dot. The rupture plane is represented as a green rectangle.

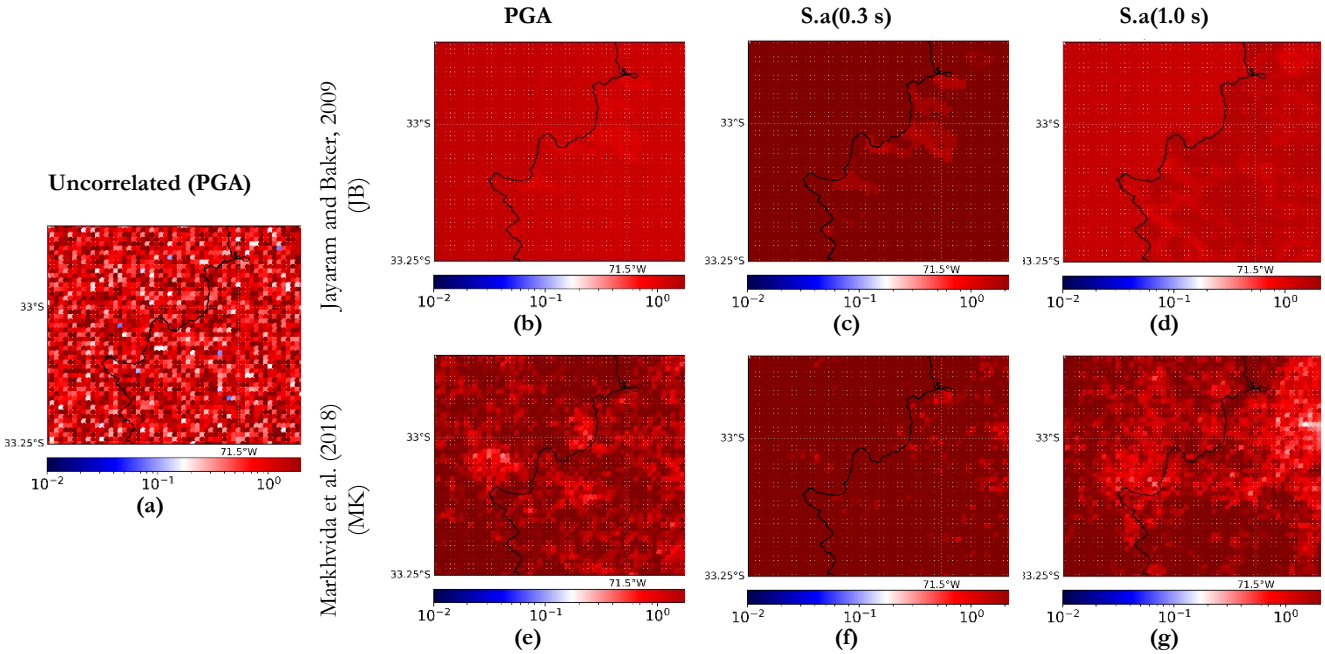

Figure 3-14. Single realisation of a GMF with these conditions:(a) PGA uncorrelated; spatially correlated (JB) (Jayaram and Baker, 2009) for (b) PGA, (c) S.a(0.3 s), (d) S.a(1.0 s); and cross-correlated (MK) (Markhvida et al., 2018) for (e) PGA, (f) S.a(0.3 s), (g) S.a(1.0 s).

3.4. Sensitivity analyses on scenario-based seismic risk assessment

This systematic investigation describes a condition tree that allows us to compare the impact of individual parameters on the risk estimates and their epistemic uncertainties (Beven et al., 2018). To avoid possible misinterpretations of absolute economic loss values, we have made the decision of providing these results in terms of normalised loss values. They were normalised with respect to the maximum loss value (among the 1000 realisations) obtained for the initial commune-based model along with the assemblage of uncorrelated ground motion fields, slope-based Vs_{30} values, and the Abrahamson et al, (2015) GMPE. This decision of providing normalised results is supported by the suggestions made by Gomez-Zapata et al., (2022); Vamvatsikos et al., (2010) who discussed that, because of the continuously spatio-temporal changing exposure, erroneous damage forecasts can appear if the losses are shown as absolute. Moreover, normalised values allow us to easily highlight the scale in the differences between the various models. Because of the differences in the buildings counts of the three exposure models, we have also added a second normalisation coefficient to the normalisation of the building counts across all the models to account for the role of the exposure composition.

Figure 3-15 displays the comparison between the normalised losses obtained for the three building exposure model subjected to the assembled ground motion fields shown in the vertical axis per GMPE. Figure 3-16 reports the same information in a collapsed and hierarchical manner for the three exposure models.

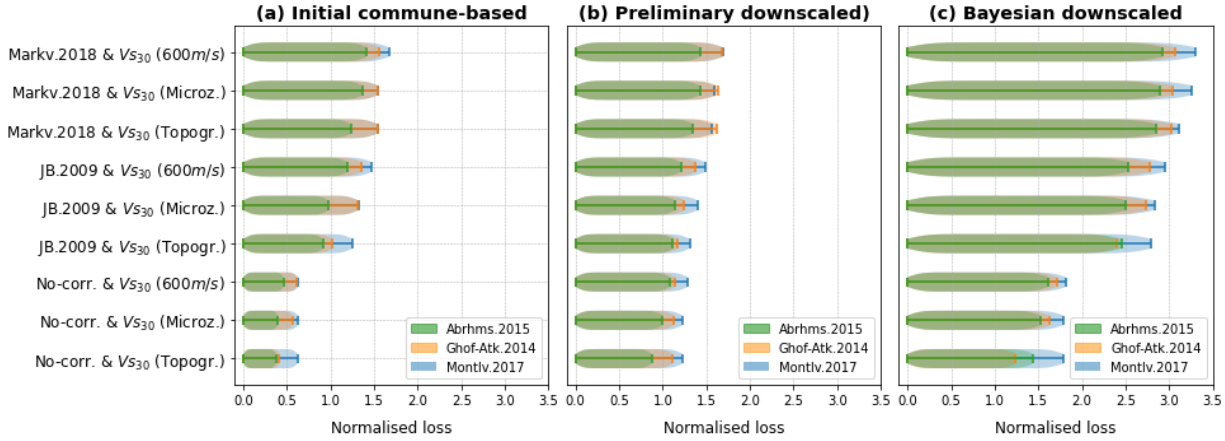

Figure 3-15. Normalised loss for the earthquake scenario in Valparaíso for the three exposure models (in each subplot) and 27 ground motions assemblages using the set of uncorrelated ground motions with Vs_{30} (Topogr.), and the Abrahams, 2015 GMPE as benchmark

Figure 3-15 and Figure 3-16 show the comparative lower impact that carries the selection of the GMPE upon the normalised losses across all of the evaluated cases. This might be due to the fact that they follow very similar functional forms (Montalva et al., 2017). We still can identify that generally, the GMPE proposed by Abrahamson et al, 2015 induced the lowest estimates whilst the Montalva et al, 2017 one induced the largest variability. As reported in Weatherill et al., (2015), the implementation of an inter-period cross-correlation model imposes the largest variations regardless of the exposure model used. This condition, combined with the unrealistic case of having homogenous Vs_{30} values imposes the largest values. The normalised metric is diminished when the simpler spatial correlation model and the uncorrelated ground motions are adopted. This is especially evident for the commune-based model (Figure 3-15-b) for which, the use of spatially uncorrelated ground motions led to a general underestimation of the results (values < 1.0 with respect to the normalising model). This low-resolution model along with having neglected the inter-period dependency of the fragility functions and correlated ground motions lead to unrealistic underestimations. This feature was already noted by Stafford, (2012). Notably, the differences between the preliminary downscaled model and the commune-based one are very low for the case of using uncorrelated GMF regardless the GMPE and Vs_{30} parametrisations. Moreover, the arrangement of the normalised risk metrics of the preliminary downscaled model (Figure 3-15-b) presents a smoother shape in contrast with the

other two exposure models. This feature is a contribution of having a more spread-out aggregation (Figure 3-7) made of unrealistic portfolio composition (very few walled high-rise reinforced concrete buildings). Finally, the Bayesian-derived exposure model (Figure 3-15-c) produces the highest estimated losses due to its comparative larger building counts. It might appear that the difference in these counts induced a linear increment of the losses with respect to the preliminary exposure model. However, this trend is not entirely linear. This is due to the different spatial distribution of the buildings (Figure 3-10) and having larger proportions of walled medium-rise RC buildings (Figure 3-11) which despite being are more resistant to ground shaking (Figure 3-4), have higher replacement costs (Table 3-1).

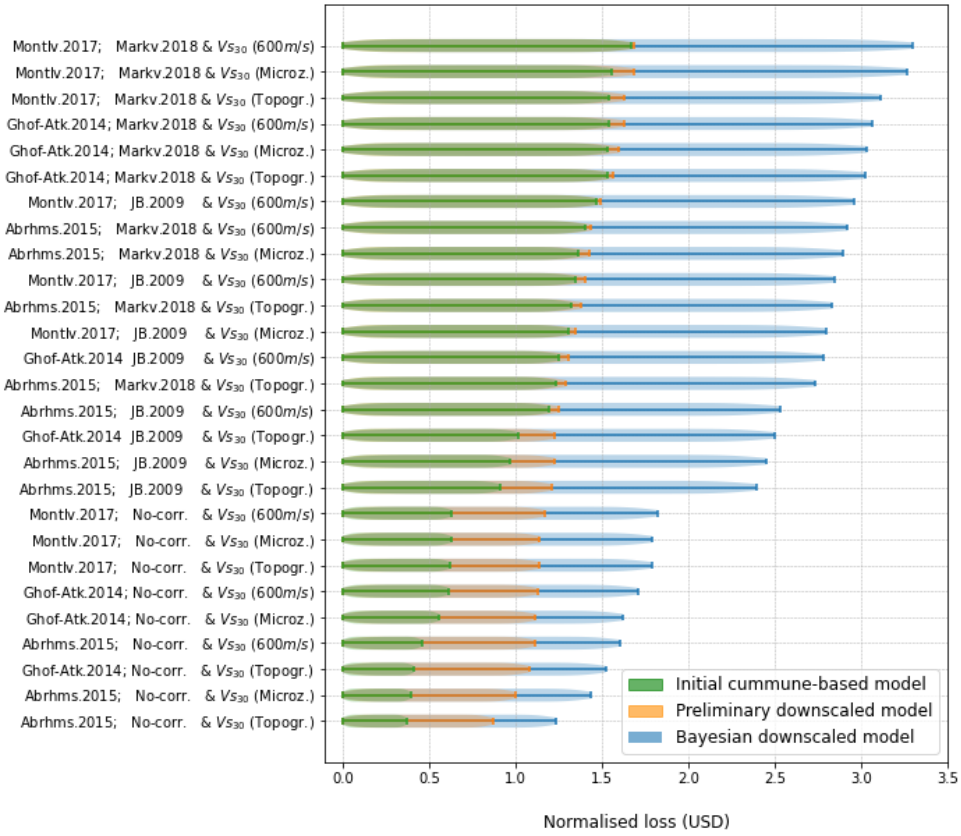

Figure 3-16. Similar information as shown in Figure 3-15 showing the normalised loss differences between each exposure model.

3.5. Discussion

This work is based on the assumption that the residential building stock of Valparaíso and Viña del Mar (Chile) can be entirely characterised by a set of typologies proposed by the SARA project Yepes-Estrada et al. (2017). However, exposure models could have been designed for other schemes, as proposed by Aguirre et al., (2018) for the Chilean context. The SARA typologies were constrained by expert-elicitation over the official 2002 Chilean census while being spatially aggregated onto two large-size administrative units. Some classes were merged to present the initial model (Sect. 3.3.2.1). Thereafter, in order to refine the spatial representation, another preliminary exposure model was also presented employing data from 2017 (Sect. 3.3.2.2). Then, a probabilistic model that was initially presented in Zafrir, (2020) through a Bayesian approach is recalled. Its development comprised the exploitation of recent and freely available datasets while updating its composition based on up-to-date observations.

Due to the various data sources with contrasting vintages used in deriving these three exposure models, their total building counts vary. The Bayesian model led to quantities that are ~34% and ~40% larger with respect to the first and second models respectively (Table 3-3). Complementarily, the building counts obtained for the three models can be compared with the study of (Geiß et al., 2017a) that, after integrating remote sensing data products with OpenStreetMap footprints,

reported a range between 64,803 – 72,412 building units for the Valparaíso commune (excluding Viña del Mar). The mean value of that range is ~40% larger than the 41,722 building counts reported by the first commune-based SARA model (Figure 3-3) whilst the values obtained by the second and third models are consistent and within the cited range.

Among the three exposure models presented, we consider that the probabilistic model provides a better representation of the updated composition of the residential building portfolio in the study area. However, this approach has several limitations and uncertainties. For instance, the posterior distribution that represents the proportions of each class was configured making use of uninformative priors (Appendix D). Informative priors could have been obtained either if we counted with more complete OSM data about other building attributes or if we counted with expert-based prior assumptions for similar spatial units used to aggregate the model. Hence, although in Gomez-Zapata et al., (2022) expert-based priors at the commune level were utilised to derive probabilistic exposure models, their resulting model was still generated at the same resolution. Therefore, it would not be wise generalising prior distributions that were initially assumed for coarser resolutions than the one we aimed for.

It is worth testing in future studies how the increasing availability of ancillary data from OSM (that might also provide other taxonomic attributes) or from other sources (i.e. surveys, feature extraction from remote sensing) could be integrated within probabilistic exposure models. In this regard, recently reported exposure models constructed with ancillary data (e.g. Aravena Pelizari et al., 2021; Cerri et al., 2021) are worth being continuously updated with Bayesian approaches to acknowledge their statistical nature and forecast their spatiotemporal dynamics.

Although probabilistic exposure models could have been satisfactorily obtained for higher resolutions, we have considered since an early stage that such resulting models are input for seismic risk assessment. Therefore, the selected resolution for the exposure models satisfies that the heterogeneities of the building stock are identifiable, while at the same time ensuring that risk estimates from earthquake scenarios maintain a meaningful mapping resolution in concordance with the spatial variation of the intensities of the seismic ground motions (Zuccaro et al., 2018). Moreover, this resolution avoids unnecessarily computational efforts when thousands of seismic ground motion fields (stochastically constructed) are used to assess the physical vulnerability of the exposed buildings (Bal et al., 2010; Gómez Zapata et al., 2021f).

The three aforementioned exposure models are utilised to perform a sensitivity analysis in scenario-based seismic risk along with other three components that partly parametrise the seismic ground motion fields for a single megathrust earthquake. They are the selection of the types of GMPE, Vs_{30} proxy, and spatial correlation model. We have observed the significant and higher importance of the exposure model than these evaluated parameters. This sensitivity study relies on the vague and generalised assumption of using of Vs30 proxy to address seismic site effects (Pilz and Cotton, 2019). Thus, addressing wave propagation studies that were out of the scope of our work would in the future profit the quality of the resultant loss estimates herein presented. Complementary, but also out of our scope, it is worth recognising, that even if we had used local correlation models for the Chilean subduction zone (i.e., Candia et al., 2020) published after this study), the use of generic and isotropic correlation models without having performed local wave-form analyses in the vicinity of the study area might anyway induce overestimations in the risk estimates (Abbasnejadfard et al., 2021).

It is worth noting that we are not claiming that the scenario-based economic losses for the residential building stock of Valparaíso and Viña del Mar are exhaustive. Instead, this sensitivity analysis allowed us to explore certain epistemic and aleatoric uncertainties embedded in the exposure and ground motion models. Therefore, the aforementioned observations should neither be generalised for any type of probabilistic risk assessment nor for other earthquake scenarios. Although Kalakonas et al., (2020) recently reported negligible differences between two alternative country-sized exposure models in sensitivity analyses for probabilistic risk, their composition was defined through top-down approaches and not integrating ancillary data into probabilistic models as herein presented. Moreover, it is worth noting that there are other components within the seismic risk chain that we did not address in this sensitivity study. For instance, it is worth exploring in future studies the role of other parameters on the final loss estimates, such as the definition of replacement costs, loss ratios per damage, the method used in deriving more local vulnerability functions explicitly for the Chilean context (e.g. Cabrera et al., 2020) as well as their dependency with hazard intensities (Sousa et al., 2018). Consequently, more

rigorous analyses, but also beyond our scope, would comprise feature importance assessment through machine learning techniques along with macroseismic intensities calibrated through Bayesian approaches (e.g. Pittore et al., 2018a) and available datasets of damage reconnaissance after real earthquakes (Contreras et al., 2021).

3.6.Conclusions

A method to spatially downscale the residential building exposure model of Valparaíso and Viña del Mar (Chile) is recalled relying on a Bayesian formulation. As a result, a probabilistic model is generated through the integration of recent OSM data. Other two intermediate exposure models are generated making use of out-of-date ancillary data. When we compare the three models we observe important differences with respect to their composition and spatial distributions. The current construction practices in the study area as well as observations from surveys confirm that the probabilistic model provides a better representation of the composition of the residential building portfolio of interest. This type of probabilistic exposure modelling highlights the dynamic spatiotemporal evolution of the built environment. Depending on the ancillary data utilised, building exposure models may have different building counts and uncertain compositions. In order to minimise such uncertainties, high-quality data should be continuously integrated into probabilistic models.

This study has provided a partial understanding of the importance of counting with incrementally updated exposure models (i.e. when their composition is probabilistically constructed) and their crucial role in earthquake loss models. Through a sensitivity analysis in scenario-based seismic risk, we remark the importance of constantly constraining the seismic ground motions along with a good level of knowledge of the building stock. Although we do not provide absolute numbers of direct economic losses, the presented results can be used to improve the knowledge of individual parts of the seismic risk chain through future studies.

Author Contributions: Conceptualization, M.P., J.C.G.-Z., and R.Z.; methodology, M.P.; investigation, R.Z, J.C.G.-Z., and Y.M.; writing—original draft preparation, J.C.G.-Z., and R.Z.; writing—review and editing, J.C.G.-Z.; supervision, M.P. This study presents the initial results shown at the EGU-2020 conference (Zafrir et al., 2020) and the study elaborated by R.Z (Zafrir, 2020). The latter was submitted to the Stuttgart Technology University of Applied Sciences as a requirement for the Master Photogrammetry and Geoinformatics in 2020. All authors have read and agreed to the published version of the manuscript.

Data Availability Statement: The data regarding the building surveys has been made available in these repositories: (Gómez Zapata et al., 2021c; Merino-Peña et al., 2021). The software utilized in this study are freely available in (Weatherill et al., 2021; Pittore et al., 2021; Brinckmann et al., 2021). The data and codes related to the Bayesian exposure models presented in this study are available on request from the corresponding author.

Acknowledgments: We would like to also thank Paula Aguirre, Tamara Cabrera, Rosita Jünemann (PUC, CIGIDEN), Javiera Yáñez Sánchez, and Mercedes Eva Parada (MVUC) for having discussed with us exposure modelling, physical vulnerability, and risk in Valparaíso and Viña del Mar. We thank Catalina Yepes (GEM) for having provided the SARA model. Our gratitude also goes to Fabrice Cotton, Jörn Lauterjung (GFZ), Patrick Aravena, and Christian Geiß (DLR) for their support during the elaboration of this study. We thank Kevin Fleming for the careful proofreading. We thank the editors and three anonymous reviewers who provided constructive feedback.

Funding: This research was funded by the RIESGOS and RIESGOS 2.0 projects, funded by the German Federal Ministry of Education and Research (BMBF) with Grant No. 03G0876A-J and 03G0905A-H, respectively. These projects are part of the funding programme CLIENT II—International Partnerships for Sustainable Innovations'. Yvonne Merino was funded by the Research Center for Integrated Disaster Risk Management (CIGIDEN), ANID/FONDAP/15110017.

Conflicts of Interest: The authors declare no conflict of interest.

Appendix A: Spatial delimitation of the urban area and available data sources for building exposure modelling

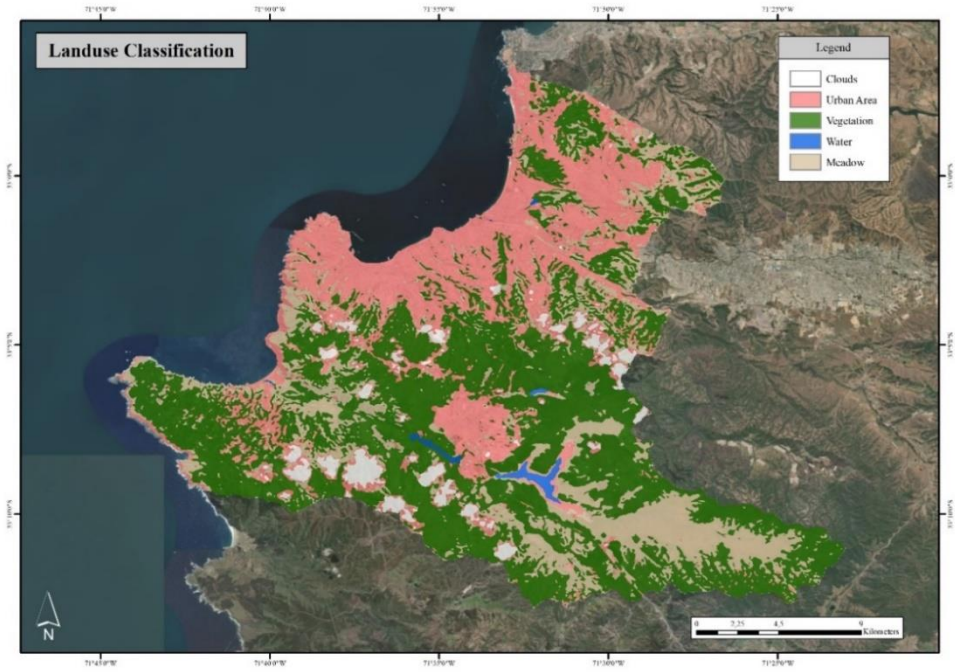

Figure 3-17. Land use classification for the study area. Map data: ©Google Earth 2020. Figure modified from Zafrir, (2020) .

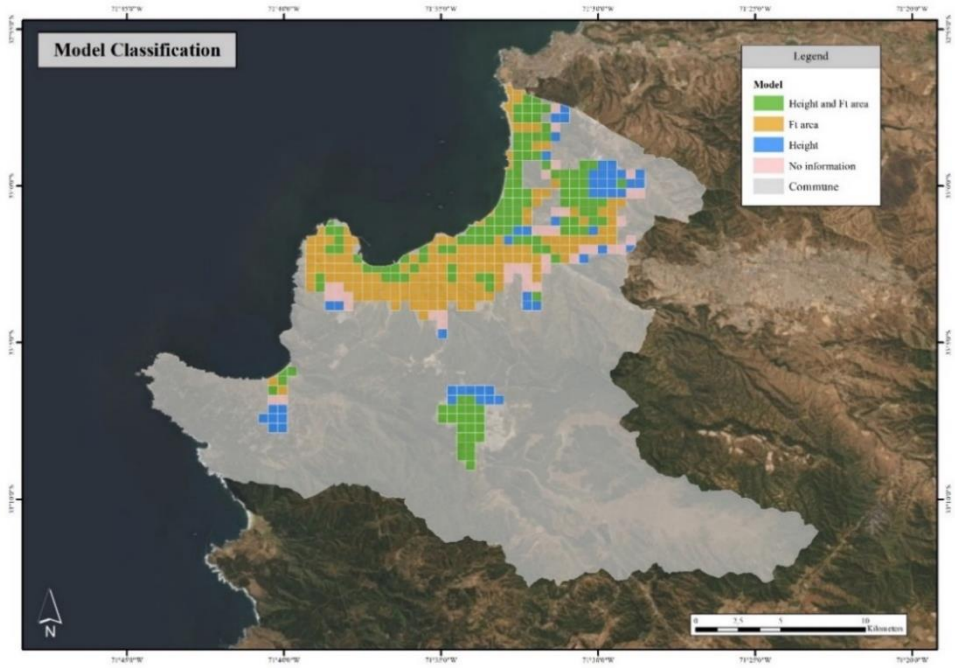

Figure 3-18. Categories according to the available input data in the study area. 136 grid cells represented by green colour have information of build-up height according to Zafrir, (2020) as well as the OSM footprint area (Sect. 3.3.2.3.1), 51 grid cells represented with blue colour have information about the build-up height and density from remote sensing data products (as studied by Zafrir, (2020)), 158 grid cells represented by orange colour have a complete information only about the footprint area from OSM, and 39 grid cells represented by pink colour have no input information. Map data: ©Google Earth 2020. Figure modified from Zafrir, (2020).

Appendix B: Assumptions followed in the preliminary model (Sect. 3.3.2.2) to obtain building counts from population and footprint areas

Pittore et al., (2020) proposes to use equation Eq. 3-1 to obtain the number of buildings belonging to every class within each geo-cell.

$$N_b = \frac{pop_{gc}}{\sum_{i=1}^{k} \theta_i * pop_{bi}} \qquad \textbf{Eq. 3-1}$$

Where pop_{gc} and N_b are the total population and the total number of buildings in the geo-cell respectively. N_{bi} , θ_i and pop_{bi} are respectively: the number of buildings per typologies *bi;* their proportion per building; and the night-time residents. N_{bi} already comprises a dwelling-to-building ratio.

Table 3-4. Procedure followed in deriving the building footprint area values for each SARA typology in Valparaíso according to the description provided in Sect. 3.3.2.1.

Taxonomy	Dwellings	Buildings	Mean # of storeys	Reference average area per dwelling (m2)	Population	construction quality	area* dwellings	floor area(m)	floor area(m) per building	Average floor area per building	Sub-categories
W+WS/H:1,2	1464.4	1464.4	1	80	5420	Low	117152	117152.1	80.00	73.24	A
ER+ETR/H:1,2	2348.8	5909.5	1.25	70	30771	Low	582001	465600.8	78.79		
MUR+ADO/H:1,2	9185.9	7472.5	1.25	70	33997	Low	643013	514410.4	68.84		
MUR+STDRE/H:1,2	5747.8	4928	1.25	70	21273	Low	402346	321876.8	65.32		
MCF/DNO/H:1,3	6841.9	876.4	1.5	70	3244	Low	61348	40898.7	46.67	65.56	B
MUR/H:1,3	2732.5	1821.7	1.5	70	10113	Low	191275	127516.7	70.00		
W+WLI/H:1,3	16254.2	10836.1	1.5	80	60157	Low	1300336	866890.7	80.00		
CR/LWAL/DNO/H:1,3	4384.3	1096.1	2	80	16226	Low	350744	175372	160.00	153.33	C
CR/LWAL/DUC/H:1,3	1461.1	365.3	2	70	5408	Low	102277	51138.5	140.00		
MCF/DUC/H:1,3	4501.3	1125.3	2	80	16659	Low	360104	180052.0	160.00		
CR+PC/LWAL/H:1,3	1016.9	203.4	2.5	80	3764	Low	81352	32540.8	160.00	153.33	D
MR/DNO/H:1,3	4652.5	930.5	2.5	80	17219	Low	372200	148880.0	160.00		
MR/DUC/H:1,3	2077.7	415.5	2.5	70	7690	Low	145439	58175.6	140.00		
CR/LWAL/DNO/H:4,7	4316	287.7	5	80	15974	Medium	345280	69056.0	240.03	225.04	E
CR/LWAL/DUC/H:4,7	2076.6	138.4	5	70	76856	Medium	145362	29072.4	210.00		
CR/LWAL/DUC/H:8,19	1656.9	34.5	12	70	6132	High	115983	9665.3	280.15	280.15	F

Appendix C: Data collection of building attributes in Valparaíso and their classification

Out of the entire sample made up of 604 buildings (Merino-Peña et al., 2021) we present in Table 3-5 some of the observed attributes values found during the survey for the building depicted in Figure 3-19. The distributions of the observed values of four selected attribute types are shown in Figure 3-20. Short descriptions of these attributes are presented in

Figure 3-19. Building façade of an inspected building, with ID=599 in Merino-Peña et al., (2021).

Table 3-5. Data collection for the building in Figure 3-19.

Attribute type	Attribute value
Material type	MCF
Material technology	CL99
Material property	MO99
Lateral load-resisting system (LLRS)	LWAL
Non-structural exterior walls	EWMA
Roof shape	RSH2
Roof coverage material	RMT6
Roof system material	RWO
Roof system type	RWO1
Floor material	FC
Floor type	FC99
Floor connections	FWCP
Number of storeys	2
Ductility of the LRRS	DU99

(a) Material type

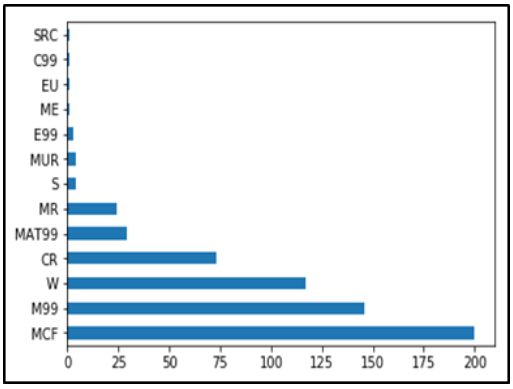

(b) Material technology

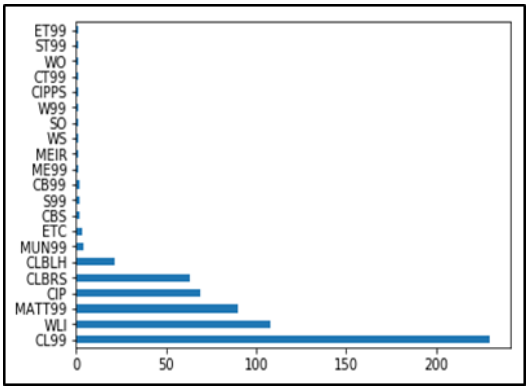

(c) Non- structural exterior walls

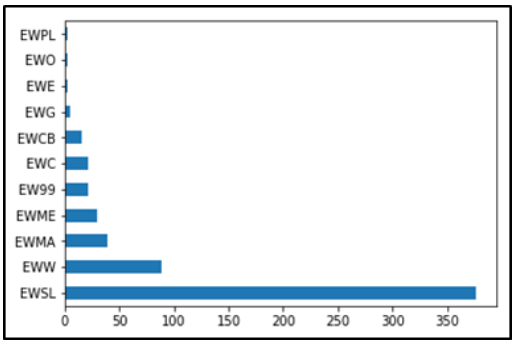

(d) Lateral load-resisting system (LLRS)

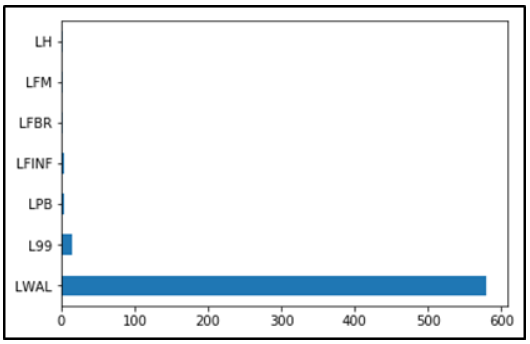

Figure 3-20. Distribution of attributes values within the GEM V.2.0 taxonomy for 604 inspected buildings in Valparaíso for: (a) material type, (b) material technology, (c) non- structural exterior walls, and (d) lateral load-resisting system.

Table 3-6. Short description of observed attribute values incorporated into the four attribute types in Figure 3-20.

(a) Material type

SRC: Concrete, composite with steel section
C99: Concrete, unknown reinforcement
EU: Earth, unreinforced
ME: Metal (except steel)
E99: Earth, unknown reinforcement
MUR: Masonry, unreinforced [MUR]
S: Steel
MR: Masonry, reinforced
MAT99: Unknown material
CR: Concrete, reinforced
W: Wood
M99: Masonry, unknown reinforcement
MCF: Masonry, confined [MCF]

(b) Material technology

ET99: Unknown earth technology
ST99: Stone, unknown technology
WO: Wood, other
WS: Solid wood
MEIR: Iron
ME99: Metal, Unknown
CB99: Concrete blocks, unknown type
S99: Steel, unknown
CBS: Concrete blocks, solid
ETC: Cob or wet construction
MUN99: Masonry unit, unknown
CLBLH: Fired clay hollow blocks or tiles
CLBRS: Fired clay solid bricks
CIP: Cast-in-place concrete
MATT99: Unknown material
WLI: Light wood members
CL99: Fired clay unit, unknown type

(c) Non- structural exterior walls

EWPL: Plastic/vinyl exterior walls, various
EWO: Material of exterior walls, other
EWE: Earthen exterior walls
EWG: Glass exterior walls
EWCB: Cement-based boards for exterior walls
EWC: Concrete exterior walls
EW99: Unknown material of exterior walls
EWME: Metal exterior walls
EWMA: Masonry exterior walls
EWW: Wooden exterior walls
EWSL: Stucco finish on light framing for exterior walls

(d) Lateral load resisting system

LH: Hybrid lateral load-resisting system
LFM: Moment frame
LFBR: Braced frame
LFINF: Infilled frame
LPB: Post and beam
L99: Unknown lateral load-resisting system
LWAL: Wall

To classify the surveyed building sample, we follow the method proposed in (Pittore et al., 2018b). v_{ik} is an attribute value belonging to the taxonomic description $\{F(b)\}_m$ of the considered building b and s_{ik}^c is the fuzzy score measuring the level of compatibility of the attribute values v_{ik} with respect to a given class T_k^A in the reference Schema A for every category value $\{v_{ik}, k = 1, \dots, m_i\}$ that the attribute type a_i can take. A set of triangular fuzzy numbers (TFN) that comprise seven increasing levels of compatibility, from "- - -", "- -", "-", "+", "+ +", "+ + +" are assigned through expert elicitation. Every a_i within the schema A has an associated weight, w_i (i.e., a crisp (non-fuzzy) number) which rank and integrate the different attribute types within the local schema.

$$\sum_{i=1}^{n} w_i \sum_{i=1}^{m_i} \delta_{ik}(b) s_{ik}^{T_k^A} \qquad \textbf{Eq. 3-2}$$

with

$$\delta_{ik}(b) = \begin{cases} 1 \; if \; v_{ik} \in T_k^A \\ 0 \; otherwise \end{cases} \qquad \textbf{Eq. 3-3}$$

The assignment of the most likely class is carried out in a post-processing stage and within a fully probabilistic framework by evaluating the level of compatibility between the observed building attributes and the classes available within the considered schema. Making use of the former method, we classified the surveyed buildings while reusing the dataset provided in Gomez-Zapata et al., (2021a) which comprises the disaggregation of the SARA scheme into the attributes comprised in the

GEM v.2.0 taxonomy along with their associated fuzzy compatibility scores with a single weighting scheme. After the evaluation of their degree of belonging, we obtained the differential compatibility levels for each building. Figure 3-21 shows the differential compatibilities of the building displayed in Figure 3-19 to be categorised as one of the 16 SARA typologies. Since its ductility was not identified (Table 3-5), the highest scores are obtained for the two types MCF-DNO-H1-3 and MCF-DUC-H1-3. Under such circumstance, the non-ductile option is chosen. After performing this classification for the entire sample, we obtain the distribution of typologies for the building sample shown in Figure 3-22. Notably, 11 building classes out of the 16 proposed were observed.

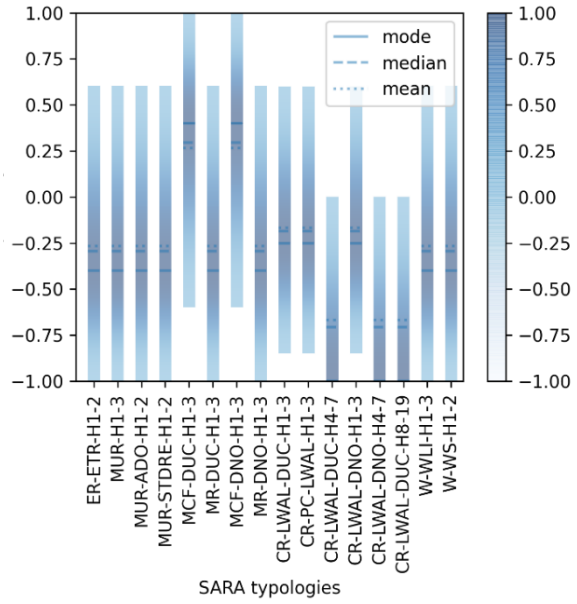

Figure 3-21. Resulting fuzzy compatibility scores for the building in Figure 3-19 with respect to the SARA typologies. The solid and dashed segment represent the equivalent defuzzified values according to the mode, median or mean value of the triangular fuzzy numbers.

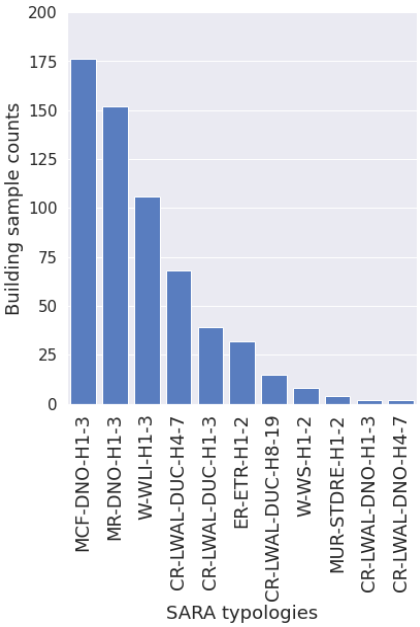

Figure 3-22. Distribution of the SARA typologies for the sample constituted by 604 surveyed buildings randomly distributed throughout Valparaíso.

Appendix D: Basic Overview of the Probabilistic Exposure Modelling Approach

In the following, we recall a Bayesian approach for exposure modelling that was initially presented in the master thesis of Zafrir, (2020). This is first performed based on the probabilistic evaluation of the likelihood of observing and classifying the set of OSM footprints as one of the six building subcategories from A to F (Table 3-1). The obtained quantities for their enclosed SARA building classes can be obtained while keeping their underlying relation.

As in any Bayesian method, we obtained a posterior distribution that represented the composition of the building stock based on the configurations of prior and likelihood distributions. The probabilistic exposure model for the residential building stock of Valparaíso based on the OSM building footprints is given by the relation in Eq. 3-4.

$$(\text{Model}|\text{buildingfootprint}) = \frac{\text{P}(\text{building footprint}|\text{Model}) * \text{P}(\text{Model})}{\text{P}(\text{building footprint})} \qquad \textbf{Eq. 3-4}$$

where $P(Model|buildingfootprint)$ is the posterior distribution of the model given by the OSM building footprints, $P(buildingfootprint|Model)$ is the likelihood function, $P(Model)$ is the prior distribution, and $P(Building\ footprint)$ is the observable data.

This formulation relies on the method initially suggested by Pittore et al. (2020) [39], which is grounded in statistical inference. A brief overview is presented below.

Let us consider $n = \{n_1, \dots, n_k\}$ and $\sum_k n_i = N$ building types are observed, where n_i is the number of buildings per typology i. The building stock can be categorised into k categories or typologies, whose frequencies are represented by a proportion $\theta = \{\theta_1, \dots, \theta_k\}, \theta_i \geq 0$ and $\sum_k \theta_k = 1$. A multinomial sampling model is assumed to represent the probability of observing n, depending on θ:

$$p(n|\theta) = Mul(n|\theta)\frac{N!}{\prod_{i=1}^{k} n_i!}\prod_{i=1}^{k}\theta_k^{n_i} \qquad \textbf{Eq. 3-5}$$

Since the true proportion is unknown, θ_i are random variables, where it is assumed that they follow a probability distribution function in the form of a Dirichlet distribution:

$$Dir(\alpha) = \frac{\Gamma(\sum_{i=1}^{k}\alpha_i)}{\prod_{i=1}^{k}\Gamma(\alpha_i)}\prod_{i=1}^{k}\theta_i^{\alpha_i - 1} \qquad \textbf{Eq. 3-6}$$

The Dirichlet distribution is parameterised by the vector α, and it has the same number of elements (k) as the multinomial parameter θ. Thus, P(θ|α) is the interpretation of the question "what is the probability distribution function in a multinomial distribution θ with a Dirichlet distribution parameter α." As a result, it can be determined how Dir(α) varies over the values of θ for a given value of α. By the Bayes theorem, and since the prior Dirichlet is the conjugate prior to the multinomial likelihood, the posterior probability distribution of θ_i is also a Dirichlet distribution that is defined by the likelihood $p(\mathbf{n}|\boldsymbol{\theta})$ and prior $p(\boldsymbol{\theta})$:

$$p(\theta|n) \propto p(n|\theta)p(\theta) \qquad \text{Eq. 3-7}$$

Since both the multinomial and Dirichlet are conjugated distributions, the prior and posterior are both Dirichlet distributions that differ only by the empirical contribution of the observed data, which corresponds to the integration of OSM footprint area values. Therefore, we assumed that the observation of the OSM building footprints could be characterised through a multinomial sampling Eq. 3-5 which, when complemented with a prior composition that followed a Dirichlet distribution (Eq. 3-6), could together characterise the posterior distribution. Since Dirichlet and multinomial are conjugated distributions, both the prior and posterior distributions followed a Dirichlet distribution. To apply Bayes' theorem, the mean footprint area in each grid-cell was used for the construction of the likelihood function P(building footprint | Model) from Eq. 3-4. We defined the function for the mean footprint model as expressed in Eq. 3-8.

$$\frac{\sum_{i=1}^{k} N_b * \theta_i * f_{bi}}{N_b} \qquad \textbf{Eq. 3-8}$$

where N_b is the total number of buildings in the geo-cells, θ_i is the proportion of buildings per typology, and f_{bi} is the footprint area per building typology. From the former expression, Eq. 3-9 can be derived:

$$\sum_{i=1}^{k} \theta_i * f_{bi} \qquad \textbf{Eq. 3-9}$$

Since θ was expected to vary from one grid cell to another, the mathematical characterisation of this variability was performed using the Dirichlet probability distribution to stochastically sample the distribution of θ in the likelihood function. Similar to what was proposed in Gómez Zapata et al., (2022b), the Dirichlet hyperparameters α (Eq. 3-6) were factorised as the product of a proportion (θ_k) and a common (constant) concentration factor α_o. This was expressed as $\alpha = \theta_k * \alpha_o$, where α_o increased the virtual counts for the category k and thus acted as a prior term. The larger the values of α_o, the more uniform the distributions are, whilst smaller values result in sparser distributions (Xing, 2014). Due to the lack of a reliable estimate about the portfolio composition, we set a low α_o value equal to 1.0. This was aligned with the decision to use uninformative priors (i.e., equal proportions for all building classes). This type of selection can be justified when there is either no particular hypothesis about the parameters that make up a given real distribution or when we have a full inventory description where all building types are equally represented (Pittore and Wieland, 2013). It is important to note that the compositions of these types of priors will be updated after the integration of the observed data within the likelihood term (e.g., Pittore et al. 2020; Gómez Zapata et al., 2022b). These data

are represented by the growing data availability of OSM footprints, their observation, and their subsequent integration into the Bayesian model.

This likelihood function was used as the joint function between the observable data and the model. It computed the probability of obtaining the mean footprint area observed in the geo-cells in the calculated mean footprint area. This was equivalent to calculating the θ that maximised Eq. 3-4, which is given by Eq. 3-10.

$$\theta = \underset{\theta}{\operatorname{argmax}}(P(\theta|obs)) = \underset{\theta}{\operatorname{argmax}}\left(\frac{P(obs|\theta)P(\theta)}{P(obs)}\right) \quad \textbf{Eq. 3-10}$$

Due to the assumption of using an uninformative prior, the posterior distribution would be proportional to a maximum likelihood estimation (Lynch, 2007). Hence, the posterior distribution of the model corresponded to the maximum likelihood estimation, which is given by:

$$\theta = \underset{\theta}{\operatorname{argmax}}(P(\theta|obs)) = \underset{\theta}{\operatorname{argmax}}\big(P(obs|\theta)\big) \quad \textbf{Eq. 3-11}$$

where argmax over θ returns the θ value that maximises the functions in Bayes' theorem. This corresponds to asking the question "how likely will it be to observe the mean footprint area (from the geo-cell) given the θ low-rise buildings model?" The process of maximizing the likelihood function defines how probable the mean footprint area is under different values of θ. Therefore, θ is a vector with values from 0 to 1. The θ value was chosen once the likelihood was maximised. Figure 3-23 presents an example of this procedure. For example, as explained by Zafrir, (2020), we can ask "what is the probability to find observed data with a mean footprint of 81m² (mean value in **Figure 3-23**) in the given model?" From **Figure 3-23**b, it is possible to observe that once the likelihood term was solved for that value, it was maximised at 94%. That area value was within the type of low-rise buildings, which was the value selected for such a category. Therefore, the chosen percentages for all of the observed buildings were the ones for which the likelihood function was maximised, as defined by Eq. 3-11.

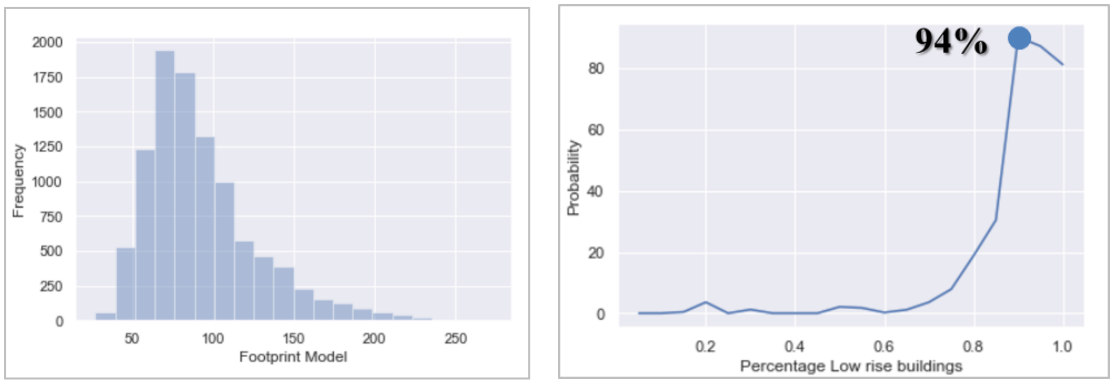

(a) **(b)**

Figure 3-23. (a) Footprint area distribution for a given grid cell, with a mean ~81 m². (b) The posterior distribution obtained for that grid cell after having maximised the likelihood function which, in this case, was for low rise buildings. Adapted from Zafrir et al., (2020).

Chapter 4

4. Variable-resolution building exposure modelling for earthquake and tsunami scenario-based risk assessment. An application case in Lima, Peru

Abstract

We propose the use of variable resolution boundaries based on Central Voronoi Tessellations (CVT) to spatially aggregate building exposure models for risk assessment to various natural hazards. Such a framework is especially beneficial when the spatial distribution of the considered hazards present intensity measures with contrasting footprints and spatial correlations, such as in coastal environments. This work avoids the incorrect assumption that a single intensity value from hazards with low spatial correlation (e.g., tsunami) can be considered to be representative within large-sized geocells for physical vulnerability assessment, without, at the same time, increasing the complexity of the overall model. We present decoupled earthquake and tsunami scenario-based risk estimates for the residential building stock of Lima (Peru). We observe that earthquake loss models for far-field subduction sources are practically insensitive to the exposure resolution. Conversely, tsunami loss models and associated uncertainties depend on the spatial correlations of the hazard intensities as well as on the resolution of the exposure models. We note that for the portfolio located in the coastal area exposed to both perils in Lima, the ground-shaking dominates the losses for lower magnitude earthquakes, whilst tsunamis cause the most damage for larger magnitude events. For the latter, two sets of existing empirical flow-depth fragility models are used, resulting in large differences in the calculated losses. This study, therefore, raises awareness about the uncertainties associated with the selection of fragility models and spatial aggregation entities for exposure modelling and loss mapping [c]

[c] published as: Gómez Zapata, J.C., Brinckmann, N., Harig, S., Zafrir, R., Pittore, M., Cotton, F., Babeyko, A., 2021. Variable-resolution building exposure modelling for earthquake and tsunami scenario-based risk assessment. An application case in Lima, Peru. Natural Hazards and Earth System Sciences 21, 3599–3628. https://doi.org/10.5194/nhess-21-3599-2021

4.1. Introduction

The spatial distribution of damage and/or losses expected to be incurred by an extensive building portfolio from a natural hazardous event can be quantified and mapped once a physical vulnerability analysis is performed. For such a purpose, a set of fragility functions per building class is conventionally used. Fragility functions describe the probability of exceeding a certain damage limit state for a given intensity measure (IM) associated with a natural hazard, such as spectral acceleration at the yield period (e.g., Fäh et al., 2001) for earthquakes, or tsunami inundation height for tsunamis (Koshimura et al., 2009). These vulnerability calculations are performed at the centroid of every aggregation unit of a building exposure model with some level of uncertainty associated with them (Bazzurro and Luco, 2005), or over weighted locations (e.g., Weatherill et al., 2015; Kappos et al., 2008). These aggregation entities can be very diverse, ranging from administrative units such as district/communes (e.g., Dunand and Gueguen, 2012), urban blocks (e.g., Papathoma and Dominey-Howes, 2003; Kappos et al., 2008; Figueiredo et al., 2018; Kohrangi et al., 2021), regular grids (e.g., Erdik and Fahjan, 2008; Figueiredo and Martina, 2016) or variable-resolution CVT (Central Voronoi Tessellation) geocells (Pittore et al., 2020). Throughout the physical vulnerability assessment, it is implicitly assumed that the intensity observed or estimated at that location (i.e., centroid or weighted points) is representative for the entire aggregation area. Depending on the considered hazard footprint and IM attenuation, this assumption might not be valid if the aggregation area is too coarse compared to the correlation length of a highly varying IM. In addition to the aggregation of the building exposure itself, the importance of these geographical aggregation entities in natural hazard risk assessment is that they are ultimately used to calculate and map the expected damage and loss metrics (e.g., building replacement/repair costs, human casualties). The diverse types of visualisation and interpretations of this kind of geospatial data define the so-called thematic uncertainties (Smith Mason et al., 2017) that can heavily impact upon the decision making processes (Viard et al., 2011). It is, therefore, important to find a compromise between the intrinsic resolution of the hazard IM, on the one hand, and the cartographic representation of the exposure models and risk metrics on the other.

When a geographically distributed hazard IM presents no significant spatial variability within distances of the order of tens of kilometres, they are said to be highly spatially correlated (e.g., Gill and Malamud, 2014; Merz et al., 2020). This is the case of hazards with relatively low attenuation and wide-spread footprints, such as ash-falls and earthquakes (de Ruiter et al., 2021). For the latter case, when seismic site conditions (e.g., soil amplification) and path effects (e.g., seismic directivity) are insignificant, seismic ground motion correlation lengths between 10 km and 25 km are typical (e.g., Esposito and Iervolino, 2012; Schiappapietra and Douglas, 2020). On the other hand, hazards are described as being low-spatially correlated if their IM are highly prone to be modified by specific features of the propagation medium. For instance, the modelling of inland IMs from a tsunami (i.e., inundation depth, flow velocity, momentum flux) are highly dependent on the nature and resolution of the bathymetry and digital elevation models (e.g., Tang et al., 2009), coastal topography (e.g., Goda et al., 2015), coastal morphology (e.g., Song and Goda, 2019), and even the nature of the built-up areas that have the potential to interact with and modify the inundation footprint and flow velocities (e.g., Kaiser et al., 2011; Lynett, 2016). Moreover, in the case of earthquake-triggered tsunamis, the maximum tsunami IMs also depend on the properties of the triggering mechanism, for example, the earthquake's magnitude (e.g., Goda et al., 2014), slip distribution (Miyashita et al., 2020), and directivity of the radiated energy (e.g., Kajiura, 1972). Thus, the spatial correlation of inland IMs from tsunamis is very low and remarkably non-linear compared to the much more uniform and highly spatially correlated seismic ground motion. Efforts to visualize uncertainties in the tsunami hazard and risk mapping that address some of the aforementioned modifiers have been reported in a few studies (e.g., Goda and Song, 2016; Goda et al., 2020).

Usually, the resolution of exposure models is constrained independently of the hazard, and to a certain extent, also independently of the exposure distribution. That might lead to poor exposure resolutions where it really matters, i.e., in areas where buildings are densely distributed and/or hazard intensities vary over short distances. Or, by contrast, to the unnecessary computation demands for loss assessment in areas with few exposed assets. If aggregation areas of the exposure model are coarser in resolution than the typical correlation lengths of low

spatially correlated hazard intensities, then local variations in these intensities would remain hidden in the vulnerability analysis, propagating the associated uncertainties up to the loss estimates. This dependency between exposure resolution and spatial correlation of hazard intensities has been usually disregarded, although some examples can be found in soil liquefaction risk assessment. Despite the hazard component can be spatially downscaled (e.g. Bozzoni et al., 2020), thematic uncertainties related to visualisation and the interpretation of risk metrics can arise if they are mapped over larger regional administrative units (e.g., Yilmaz et al., 2021) instead of being represented at more hazard-compliant resolutions (e.g., Bozzoni et al., 2021). Similarly, despite building exposure models for flood and earthquake vulnerabilities being able to be aggregated at moderate resolutions (e.g., 4x4 km grid in Dabbeek and Silva, 2019), similar thematic uncertainties can evolve due to the profound differences between both spatially correlated hazard intensities, and when the calculated losses are mapped over regional administrative units (Dabbeek et al., 2020).

To the best of the authors' knowledge, consideration of different hazard footprints and the spatial correlation of their intensity measures for the construction of aggregation entities for exposure modelling has been seldomly discussed in the literature. For instance, Chen et al. (2004) described the importance of ensuring a consistent delimitation of the resolution of exposure models along with the spatial variation of their two considered hazards, earthquakes and hailstorms, which impose damage footprints of very different extents. Meanwhile, Douglas (2007) and Ordaz et al. (2019) highlighted the importance of the geographical scale to represent the building exposure models that are affected differently, depending on variable hazard footprints. The study reported in Zuccaro et al. (2018) is perhaps the most advanced framework in the state of the art for the construction of a common aggregation entity for multi-hazard risk assessment, referred to as the minimum reference unit (MRU). This geographical unit coincides with the minimum resolution of analysis of input (i.e., hazard intensities and exposure model) and output elements (i.e., damage and loss estimates) and remarks that despite high-resolution hazard models, one would achieve neither an accurate risk assessment nor meaningful loss mapping if there is no compatibility between the cartographic representation of the building exposure model, the hazard footprints, and their IM correlation.

A denser set of geocells in the same area occupied by a coarser regular-sized cell or administrative units provides a denser arrangement of hazard intensity values (when there are local IM variations) to the set of fragility functions per considered hazard. When local IM variations are not sufficiently represented into finer aggregation entities during the vulnerability analysis, thematic uncertainties might appear in the mapping, visualisation, and interpretation of the loss estimates. Therefore, besides the conventional epistemic and aleatory uncertainties linked to the hazard, exposure, and vulnerability components, thematic uncertainties are also present in the risk chain when the loss metrics are mapped. Awareness of the thematic uncertainties as well as clear and meaningful vulnerability/loss mappings towards the most relevant hazards a community is exposed to is necessary to improve urban planning, mitigation strategies, and emergency response actions (e.g., Pang, 2008; Aguirre-Ayerbe et al., 2018).

We can distinguish two types of approaches formerly proposed in the literature to investigate the exposure aggregation for natural hazard risk applications.

(1) To independently represent the building portfolio over a series of aggregation entities such as administrative units, or equidimensional regular grids, and explore their individual contribution to the uncertainty in the losses imposed by certain hazard(s) to ultimately select a representative aggregation model. This option has been explored in Bal et al. (2010), Frolova et al. (2017), Senouci et al. (2018), and Kalakonas et al. (2020) for seismic vulnerability applications, and in Figueiredo and Martina (2016) for flood vulnerability. These studies discuss the weakness of physical vulnerability mapping at the individual building scale and over coarse aggregation areas and highlight the importance of finding an optimal resolution for building exposure modelling while minimizing the uncertainties in the loss estimates. However, these attempts did not explicitly address the spatial correlation or attenuation of the hazard intensity onto the predefined aggregation areas and focused on the vulnerability towards individual hazards rather than on multi-hazard risk applications.

(2) Aggregating the exposure models over variably resolved entities that are not necessarily administrative boundaries. This has been done in fewer studies. For instance, Muis et al. (2016) assessed the global population exposure to coastal flooding (from storm surges and extreme sea levels) through the application of a hydrodynamical model based on unstructured grids to ensure sufficient resolution in shallow coastal

areas. Scheingraber and Käser (2019) explored the uncertainty in regional building portfolio locations for seismic risk through the use of weighted irregular grids. This weighting was carried out as a function of the population density and did not use any hazard IM or footprints. Scheingraber and Käser (2020) described the advantages of the former procedure in terms of computational efficiency and the treatment and communication of uncertainties in probabilistic seismic risk assessment on a regional scale. Alternatively, aggregating the building portfolio into anisotropic CVT-based geocells (Central Voronoidal Tessellations) is suggested by Pittore et al. (2020).

In this study, we employ anisotropic CVTs to aggregate the residential building exposure models. Voronoi regions have proved to be useful in geographical partitioning (e.g., political districting, Ricca et al., 2013), as well in other hazard-related applications, such as climatological modelling (e.g., Zarzycki and Jablonowski, 2014). We present for the first time how CVT can be constructed using underlying combinations of geospatial distributions to achieve a larger resolution of spatially aggregated building portfolios where it matters for risk assessment. We adapt and customize their derivation to explicitly account for the combination of a low-correlated hazard intensity (tsunami inundation) and one exposure proxy (population density) to generate the Voronoi regions.

The aggregated building portfolios are used for earthquake and tsunami scenario-based risk applications. We have systematically investigated six megathrust subduction earthquakes and their respective tsunamis with moment magnitudes ranging between 8.5 and 9.0. We consider the residential building stock of Metropolitan Lima (Peru) classified in terms of one set of earthquake vulnerability classes and two sets of tsunami vulnerability classes. These building portfolios have been aggregated within six customized CVT models and administrative units at the highest resolution available (i.e., the block level). By using the respective set of fragility functions, we have independently calculated the direct losses from scenario-based physical vulnerability analyses (seismic ground-shaking and tsunami inundation). We show that the implementation of this approach is beneficial not only in finding a balance between accuracy and computational demand, but also in the efficient representation of the loss estimates while reducing bias generated in the loss mapping. The role of the spatial correlation of both hazard intensities in the efficiency and accuracy of the CVT-based exposure models is also discussed. Since the main scope of this work is to investigate an efficient manner to aggregate the building exposure for risk applications considering multiple hazards, we have not investigated the conditional probabilities related to cascading events (e.g., Goda et al., 2018). Instead, we have assumed that every seismic rupture produces a tsunami. Hence, we are not accounting for cumulative damage on buildings due to consecutive ground shaking and tsunami (e.g., Park et al., 2019; Negulescu et al., 2020; Goda et al., 2021) nor the risk to other seismically induced hazards (i.e., earthquake-triggered landslides, liquefaction, ground failure, etc., e.g., see Daniell et al., 2017).

4.2. Methodology

The proposed methodology is composed of the following steps:

(1) Simulation of scenario-based hazards (i.e., earthquakes and tsunamis) with the same spatially distributed intensities required by each fragility assessment.
(2) Construction of one (or a set of) representative underlying spatial distributions (i.e., focus map(s) See Sect. 4.2.2). This implies the selection and ranking (with numerical weights) of the hazard intensities or exposure proxies.
(3) Generation of CVT-based aggregation entities employing the focus map as an underlying distribution and with different numbers of seeding points.
(4) Classification of the exposed building stock of interest into vulnerability classes per considered hazard and their aggregation into the CVT-based geographical entities.
(5) Scenario-based risk assessment independently per hazard type and discussion of their associated thematic uncertainties in the loss mapping and visualisation.

The uncertainties arising from steps 3 and 5 are explored through the formulation of a condition tree.

4.2.1. Simulation of scenario-based hazards with spatially distributed intensities

We employ numerical earthquake and tsunami scenarios to replicate historical or hypothetical future events to simulate spatially distributed hazard intensities. For earthquakes, we simulate ground motions from suitable GMPE (ground motion prediction equations). Cross-correlated ground motions are generated for the spectral-periods that serve the fragility functions as intensity measures (IM). For tsunamis, we employ the physical generation and

propagation model TsunAWI (Harig et al., 2008) and simulate coastal inundation as the IM for tsunamis. The spatially distributed tsunami intensity values (inundation flow depth) are compatible with the IM of the fragility functions required in the vulnerability analysis.

4.2.2. Construction of focus maps

The focus map drives the construction of a variable-resolution exposure model for aggregating building portfolios. Focus maps were first introduced by Pittore (2015) based on the work of Dilley (2005), who proposed the spatial representation of composite indicators in hot-spots. Eq. **4-1** recalls the definition of a focus map, $S(D_i)$, that represents the probability of each location to be highlighted, given the actual values of certain indicators D_i.

$$S(D_i) = P(S|D_i) \in [0,1] \qquad \text{Eq. 4-1}$$

By using a pooling operator, a focus map highlights areas where a weighted combination of various normalized spatially distributed indicators (D_i jointly assume the larger values. We propose to obtain a focus map that drives the aggregation entities for earthquake and tsunami exposure modelling through the combination of two indicators. (1) Population density (D_0 (from aggregated data sources e.g., WorldPop; GPWv4 (Documentation for the Gridded Population of the World, Version 4 (GPWv4), Revision 11 Data Sets))). This indicator is an exposure proxy about the location of residential buildings for which their ground-shaking vulnerability should be addressed. The use of the latter can be a useful indicator when other seismic risk components such as soil amplification conditions are poorly known, come from proxies with coarse resolutions (e.g., topography-based), or when strong seismic site effects are not expected. (2) The tsunami component is constrained through the expected tsunami inundation height (D_1 obtained from a "worst-case scenario" approach (i.e., largest feasible intensities) among a series of deterministic scenarios (e.g., Omira et al., 2009; Wronna et al., 2015). For the combination of the two aforementioned normalized input layers, we use a log-linear pooling operator P_G, as outlined in Eq. **4-2**. This algorithm assigns a higher sampling probability to spatial locations where both indicators are relevant while penalizing the locations where at least one of the indicators (i.e., tsunami) is negligible.

$$lnP_G\big(P(S|D_0), P(S|D_1), .. P(S|D_n)\big) = \\ = lnZ + \sum_{i=0}^{n} w_i lnP(S|D_i) \qquad \text{Eq. 4-2}$$

where Z is a normalizing constant and w_i represents the respective weight assigned to score the relevance of each input layer, and $\sum w_i = 1, w_i > 0 \forall i$. Thus, the construction of a focus map entails the selection of the weights that rank the importance of every layer, as such carries its own epistemic uncertainties.

4.2.3. Generation of CVT-based exposure models

Selectively increasing the spatial resolution of aggregated areas is beneficial for capturing low spatially correlated hazard intensity values such as tsunami inundation heights. This is achieved by the construction of geocells with variable resolution in the form of CVT. During this construction, the focus maps are used as underlying spatial intensities and are sampled using a Poisson point process (Cox and Isham, 1980) to generate a number of seeding points. These points are used as centroids of the Voronoi geocells and through an iterative relaxation process will converge to the final CVT geocells. The number of seeding points therefore defines the number of geocells of the resulting tessellation. CVTs are computed in various iteration steps using the simple relaxation method originally proposed by Lloyd (1982) until the distance between the geometrical centroid of the geocell and the weighted mass centroid generated by the raster distribution falls below a defined threshold, or after a given maximum number of iterations. Since the relaxation process is based on the underlying focus maps as generating distribution, CVT cell sizes are inversely proportional to the intensity of the focus map. Each CVT geocell in fact becomes a minimum resolution unit, as proposed in Zuccaro et al., (2018), and the resulting tessellation sets the basis for a variable-resolution exposure model. Voronoi regions inherently fulfil spatial properties such as compactness and contiguity (without holes or isolated parts) (Ricca et al., 2008).

4.2.4. Condition tree for multi-hazard exposure modelling

Epistemic uncertainties underlying the two steps discussed above are explored by a condition tree with hierarchical levels:

I. Selection of a suitable scheme (sets of building classes and their associated fragility functions) to describe the building inventory in the study area.

II. Weight arrangement values (w_i that rank every input layer (low spatially correlated hazard intensities or spatial proxies related to the exposure component) in the focus map construction.
III. Determination of the number of seeding points sampling the Poisson Point Process driven by a focus map that drives the generation of CVT-based geocells.

The condition tree presents a summary of assumptions for uncertainty treatment (Beven et al., 2018). Through the construction of alternative multi-resolution exposure models, the impact of every level of the condition tree is systematically investigated once the vulnerability assessment is performed.

4.2.5. The classification of the building stock into vulnerability classes and aggregation

The building stock of interest is classified in terms of several sets of mutually exclusive, collectively exhaustive vulnerability classes, whose aggrupation describe a set of classes (scheme) specific to the considered hazard (i.e., earthquake and tsunami). A top-down approach is used to make use of aggregated census data and ancillary data for the seismic-oriented building classes. Subsequently, the proportions assigned to each seismic-oriented building classes are reassigned to tsunami oriented classes through the use of inter-scheme compatibility matrices as presented in Gomez-Zapata et al., (2021). Interestingly, besides the application of the taxonomic disaggregation of building types for seismic vulnerability applications (e.g.. Pittore et al., 2018b), it was suggested by Charvet et al., (2017) for the definition of tsunami-oriented building classes. Then, the classified building stocks are aggregated into every CVT model obtained in the former step.

4.2.6. Scenario-based risk assessment

The fragility of the building portfolio to the considered earthquakes and tsunami scenarios is calculated separately over every aggregation exposure model (see Sect. 4.2.1). This decision is based on the recent findings of Petrone et al., (2020) who found fundamentally different structural responses to both perils. Consequently, the authors argued that the intensity of the seismic ground motion does not play a significant role in the building's structural tsunami response unless it induces structural yield. The latter is assumed for the vulnerability analysis, considering the objective of this study of evaluating an optimal exposure model for risk assessment from the considered hazards. The scenario-based risk assessment makes use of a set fragility function associated with each building class and whose IMs are compatible with the hazard intensities modelled in Sect. 4.2.1. Every damage states has an assigned loss ratio to total replacement cost.

4.3. Application example

4.3.1. Context of the study area: Metropolitan Lima, Peru

According to Petersen et al., (2018), Peru, among all the South American countries, has the largest number of inhabitants, and considering a 10% probability of exceedance in 50 years, may experience a ground-shaking greater than VIII (modified Mercalli intensity scale, MMI). This makes Peru the country in which the largest average annual fatalities from earthquakes are expected in South America. In the same study, Lima, with nearly 10 million inhabitants, representing around 1/3 of the total country's population, has been identified as the capital city exposed to the highest seismic hazard in the region. Moreover, by 2022, nearly 58% of the Peruvian population lives in coastal communities. Løvholt et al., (2014) stated that Peru has the largest population exposed to tsunamis in the American continent. In Schelske et al., (2014), Lima was ranked as the second metropolitan area in the world in terms of the value of working days lost relative to the national economy due to earthquakes. This highlights the relevance of integrated vulnerability studies in this study area.

This city has suffered devastating disasters in the past. For instance, in 1586 and 1724 earthquakes triggered tsunami run-ups over 24 m (Kulikov et al., 2005). The 1746 earthquake, with an estimated magnitude of Mw 8.8 (Jimenez et al., 2013), produced a tsunami with local height of 15 to 20 m (Dorbath et al., 1990) and destroyed the city. In 1974, a Mw. 8.1 event produced widespread damage and caused losses of ~ 7.5 billion dollars. Since then, the city has been experiencing continuous urbanization with generally poor structural design of its residential building stock (Tarque et al., 2019) as well as of critical facilities such as hospitals (Liguori et al., 2019; Ceferino et al., 2020).

Local authorities have conducted studies for emergency management and recovery planning considering tsunami and earthquake scenarios (e.g., PREDES, 2009), including qualitative risk

estimations. The Japanese SATREPS project contributed to the improvement of the exposure model of Lima using satellite imagery and census data (Matsuoka et al., 2013). On the seismic vulnerability side, and similarly as presented in the previous chapter, the SARA project, led by the Global Earthquake Model (GEM), contributed to classifying the residential building stock of Peru (Yepes-Estrada et al., 2017). More specific models for confined masonry were reported in Lovon et al., (2018). On the tsunami vulnerability side, Adriano et al., (2014) estimated tsunami damage probabilities for two tsunami scenarios over the residential building portfolio classified into four building classes employing the empirical tsunami fragility functions developed by Suppasri et al., (2013) for other study area. Ordaz et al., (2019) developed earthquake and tsunami risk forecasts for Callao. However, that study did not describe the models used, nor the method employed to address the non-linear damage accumulation.

4.3.2. Construction of earthquake and tsunami scenarios for Lima

We have simulated six earthquakes and tsunami scenarios offshore of Peru with moment magnitudes between Mw 8.5 to 9.0. Finite fault ruptures are modelled using the OpenQuake engine (Pagani et al., 2014) emulating the historical earthquake that occurred in 1746, in line with previous studies (e.g., Mas et al., 2014; Pulido et al., 2015; Ceferino et al., 2018a). The basic parameters used in the simulations are hypocentre location (longitude = -77.93°; latitude = -12.19°; depth = 8 km), strike = 329°, dip = 20°, and rake = 90°. Spatially distributed ground motion fields (GMF) were generated using the GMPE proposed by Montalva et al. (2017). Its site term is based on the shear wave velocity in the uppermost 30 meters depth (Vs_{30}) as reported in Ceferino et al. (2018b) in which the slope-based Vs_{30} values (Allen and Wald, 2007) and seismic microzonation (Aguilar et al., 2013) were compiled and merged to the same resolution (30 arc-seconds ~ 1 km). The aleatory uncertainty in the ground motions was addressed by generating 1,000 realisations per event, as advised in Silva (2016), with uncorrelated and cross-correlated ground motion residuals. For the latter case, we used the Markhvida et al. (2018) model for PGA, and spectral acceleration for periods 0.3 s and 1.0 s. Examples considering three magnitudes (Mw 8.6, 8.8, and 9.0) and the respective tsunami scenarios are shown in Figure 4-1.

Although a sensitivity analysis on the GMPE(s) selection is outside the scope of this study, such a choice may influence the resulting cross-correlated ground motion fields. This comes from the manner in which the residuals and soil nonlinearity are accounted for in the functional form of the selected attenuation model (Weatherill et al., 2015). Although the Montalva et al. (2017) GMPE uses Vs30 as the site exploratory variable and includes nonlinear site response, the spatial resolution of the geo-dataset we have used might be too coarse to capture local variability in ground motion. These features could only be approximated through site-response analyses that account for the local geotechnical soil properties of site-specific soil profiles, as for instance performed by Aguilar et al., (2019) after applying the equivalent-linear methodology.

Tsunami simulations are based on the source parameters suggested by Jimenez et al., (2013). All earthquake parameters except for the slip value were fixed, specifying a Mw range from 8.5 to 9.0. This simplifies the simulation process and allows for a more systematic study of the contribution of the event´s magnitude and the corresponding tsunami footprint upon the loss assessment for the aggregated building exposure models. The wave propagation and tsunami inundations are obtained through numerical simulations using the finite element model TsunAWI which employs a triangular mesh with variable resolution, allowing for a flexible way to discretize the model domain with good representation of coastline and bathymetric features. The mean mesh resolution given by the triangle edge length amounts to around 20m in the coastal area of Lima and Callao. TsunAWI is based on the nonlinear shallow water equations including parameterisations for bottom friction and viscosity.

Table 4 1 summarizes some of the most important model quantities. The wetting and drying scheme is based on an extrapolation method projecting model quantities between the ocean part and the dry land part of the model domain, with the resulting simulations included in Harig and Rakowsky, (2021).

Table 4-1. Summary of TsunAWI model parameters used in the tsunami simulations.

Numerical approach	Time step/ Integration time	Resolution range (Triangle edge length)	Bottom friction parameterization	Viscosity parameterization
Finite Elements	0.1sec / 4 hrs	From 6km (deep ocean) to 7m (coastal pilot areas)	Manning (n=0.02 constant value)	Smagorinsky

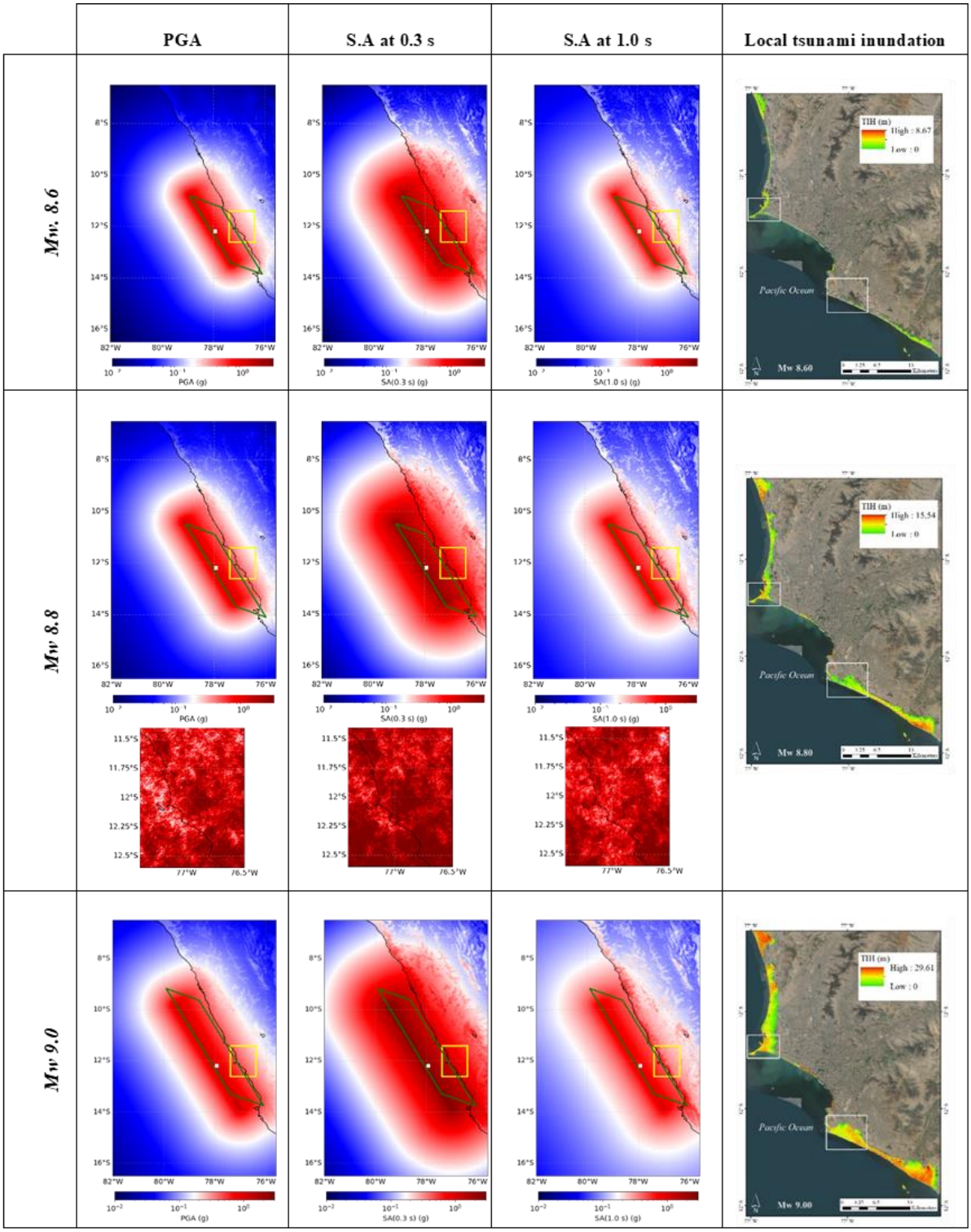

Figure 4-1. Median seismic ground motion for a single realisation using the Montalva et al., (2017) GMPE for peak ground acceleration (PGA) and spectral acceleration (SA) for periods 0.3 s and 1.0 s, and for three scenarios (Mw 8.6, 8.8 and 9.0) along the Peruvian subduction zone. Green rectangles represent the rupture planes. Hypocentres are shown by white dots. The study area (Metropolitan Lima) is enclosed within a yellow rectangle. For this area, and for the Mw 8.8 scenario, there is shown one realisation of spatially cross-correlated ground motion field per spectral acceleration. Tsunami inundation heights for the three selected scenarios are displayed for the study area. The northern "La Punta" sector (Callao district) and the southern Chorrillos district are indicated by white rectangles. Map data: ©Google Earth 2021.

Figure 4-2 displays a small section of the model domain and shows the resolution of the triangular mesh which is directly connected to the water depth and bathymetry gradient in the ocean, whereas the edge lengths are shortest in the coastal part of the study area, where tsunami inundation is expected. The model bathymetry and topography were built from several data sets. The ocean part is based on the GEBCO bathymetry (General bathymetric chart of the ocean, GEBCO_08 Grid, version 20090202, see http://www.gebco.net). The coastal topography is from the SRTM topographic model (Shuttle radar topography mission, 30m resolution, see https://www2.jpl.nasa.gov/srtm/), whereas in the study, results from the TanDEM-X mission (Krieger et al., 2007) with a spatial resolution of 12 m were used. All these data were bilinearly interpolated to the triangular mesh and slightly smoothed to allow for stable simulations. The raw model output in the triangular mesh as shown in Figure 4-2 contains all information at the model's resolution. Considering the mean resolution of the triangular mesh, a raster with grid cell dimensions of 10 x 10 m was chosen. An example of the resulting mesh and data product is shown in Figure 4-3. Details of this method are reported in Harig et al., (2020). Tsunami inundation heights from the six scenarios over the two most tsunami-prone areas in Lima city and the La Punta and Chorrillos districts (see the white square in the tsunami maps of Figure 4-1) are shown in Figure 4-4. Conversely, significant tsunami inundation is not expected in the central Lima area due to the presence of sizable cliffs.

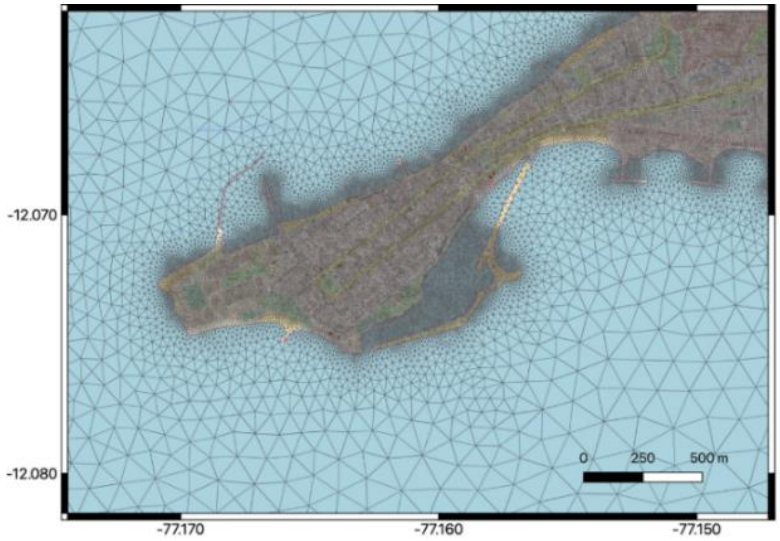

Figure 4-2. Section of the triangular mesh used for the TsunAWI simulations in the La Punta sector (Callao district). The mean resolution in the pilot area is approximately 20 m, whereas the shortest edge length measures about 7 m. The basemap and data are from © OpenStreetMap 2021. Distributed under the Open Data Commons Open Database License (ODbL) v1.0).

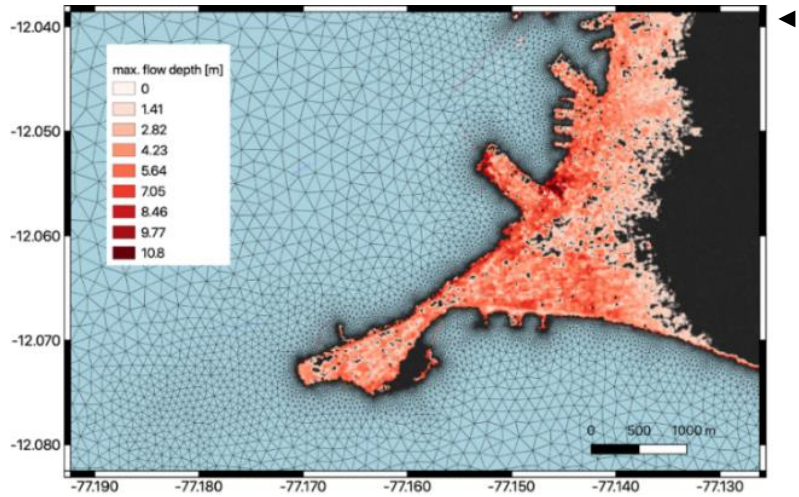

Figure 4-3. Section of the triangular mesh together with the inundation data product (10 m raster) for the tsunami scenario involving a magnitude 8.8 event in the Callao Harbour area. The basemap is from © OpenStreetMap contributors 2021. Distributed under the ODbL v1.0 License.

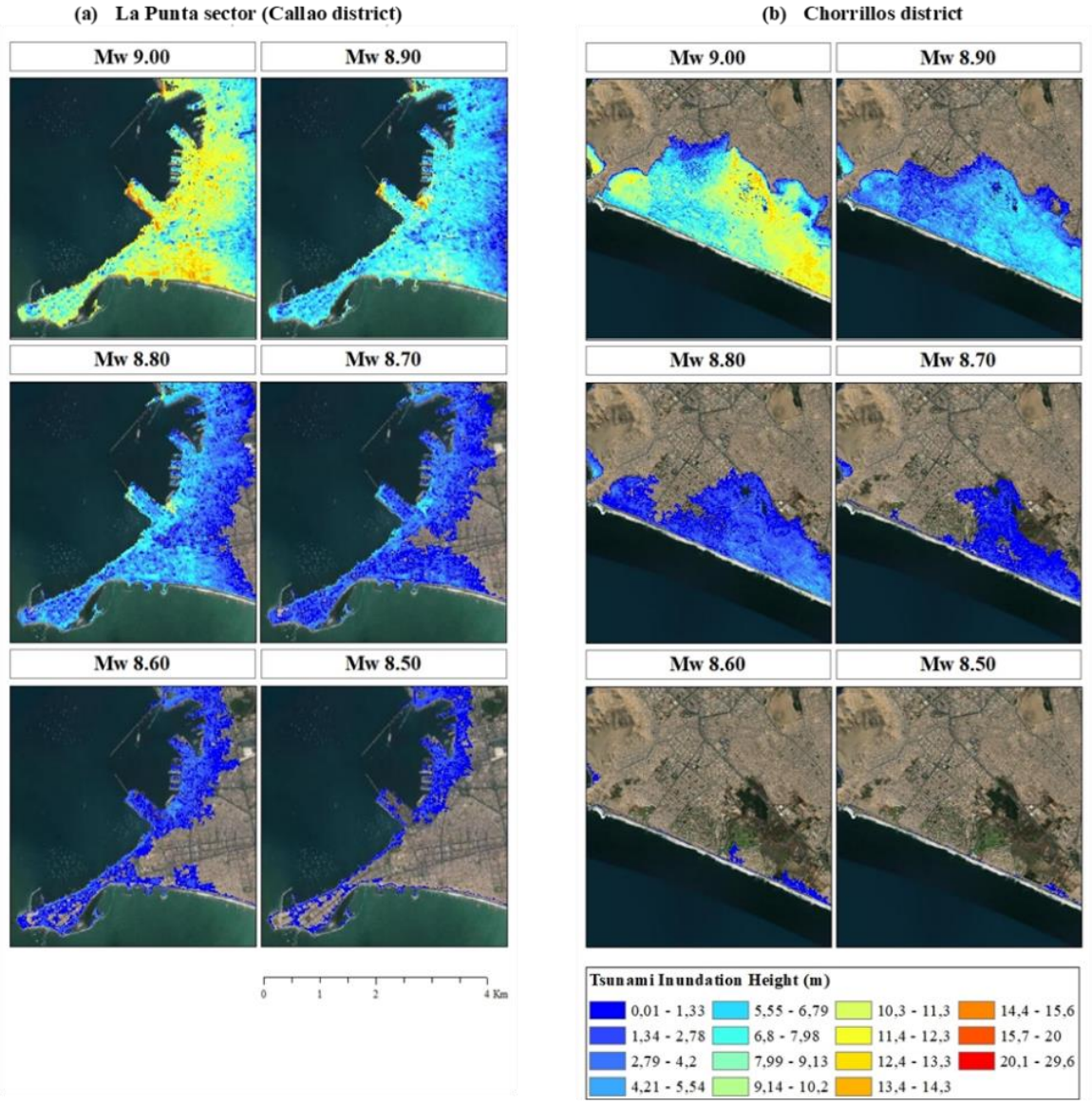

Figure 4-4. Expected tsunami inundation height (m) for two local areas within Lima for six tsunami scenarios (with locations in Figure 4-1). Map data: ©Google Earth 2021.

4.3.3. Construction of focus maps for Lima

Focus maps have been constructed as inputs to generate CVT-based aggregation boundaries for the building exposure model for seismic and tsunami risk assessment. The spatial population density (PD) in Lima at the block level (INEI, 2017) has been combined with a "worst-case" scenario of tsunami inundation height (TI) obtained from a Mw 9.0 tsunami scenario. The distribution of the GMPE-based ground motion has not been used due to the reasons outlined in Sect. 4.3.2 (i.e., absence of site-response analyses). Both map layers have been linearly normalized and combined using the log-linear pooling expressed in Eq. **4-2** in order to assign a higher probability to the spatial locations where both indicators are relevant. Two sets of weights that rank and combine the layers have been selected to perform a sensitivity analysis at this step. In both sets, tsunami intensities were ranked higher as population density due to their lower spatial correlation. The following weights were accepted for the construction of the two focus maps: set (1) PD = 30%, TI = 70% and set (2) PD = 40%, TI = 60%. The resulting focus map for the first set is shown in Figure 4-5. These models are available in Gómez Zapata et al., (2021e).

4.3.4. Generation of CVT-based exposure aggregation boundaries.

Three seeding sets have been generated by sampling the heterogeneous Poisson point processes defined by the two focus maps including 5,000, 10,000 and 50,000 initial points. We obtained six CVT aggregation entities for residential building exposure modelling by applying the Lloyd relaxation method as described in Pittore et al., (2020) and recalled in Sect. 4.2.3. As an example, the resultant CVT-based model obtained from the focus map from set (1) and the 5, 000 seeding points (model PD30_TI70_5,000) is depicted in Figure 4-5. The area jointly exposed to the earthquakes' ground motion and the largest tsunami footprint (Mw 9.0) is highlighted in pink colour. Due to the contribution of the population density layer (PD), for every Vs_{30} value at each location, there is a higher density of IM values that are computed where the exposed assets are expected to be concentrated rather than in the locations less densely populated, in contrast with what would occur using a regular grid.

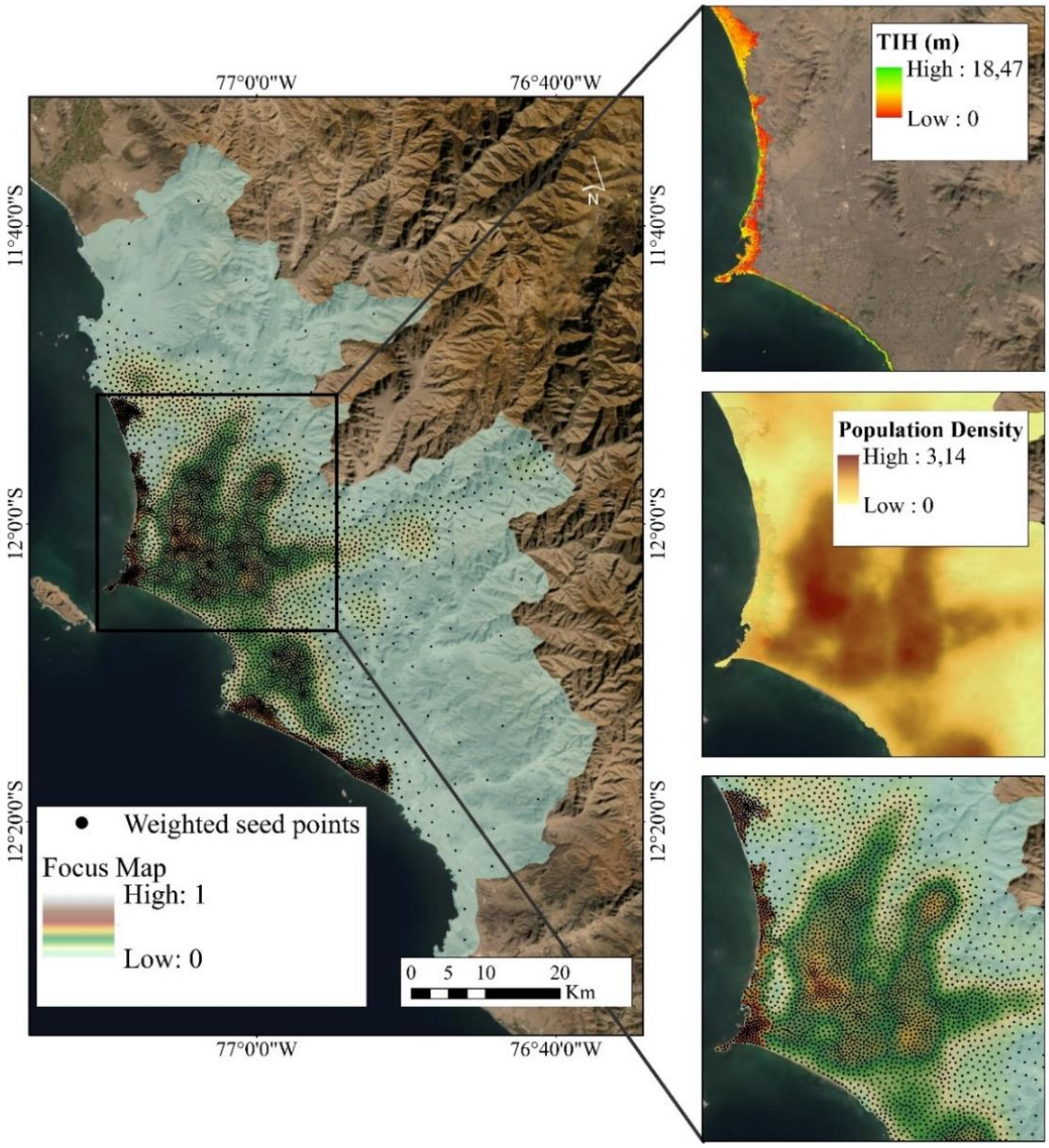

Figure 4-5. Example of the construction of focus maps for Lima. (a) 5,000 weighted seeding points sample a focus map through a Poisson point process. The normalised focus map is constructed from a log-linear pooling algorithm of the combined layers (population density (PD) and tsunami inundation height (TI) with a selection of 30% and 70% weights respectively). Map data: ©Google Earth 2021.

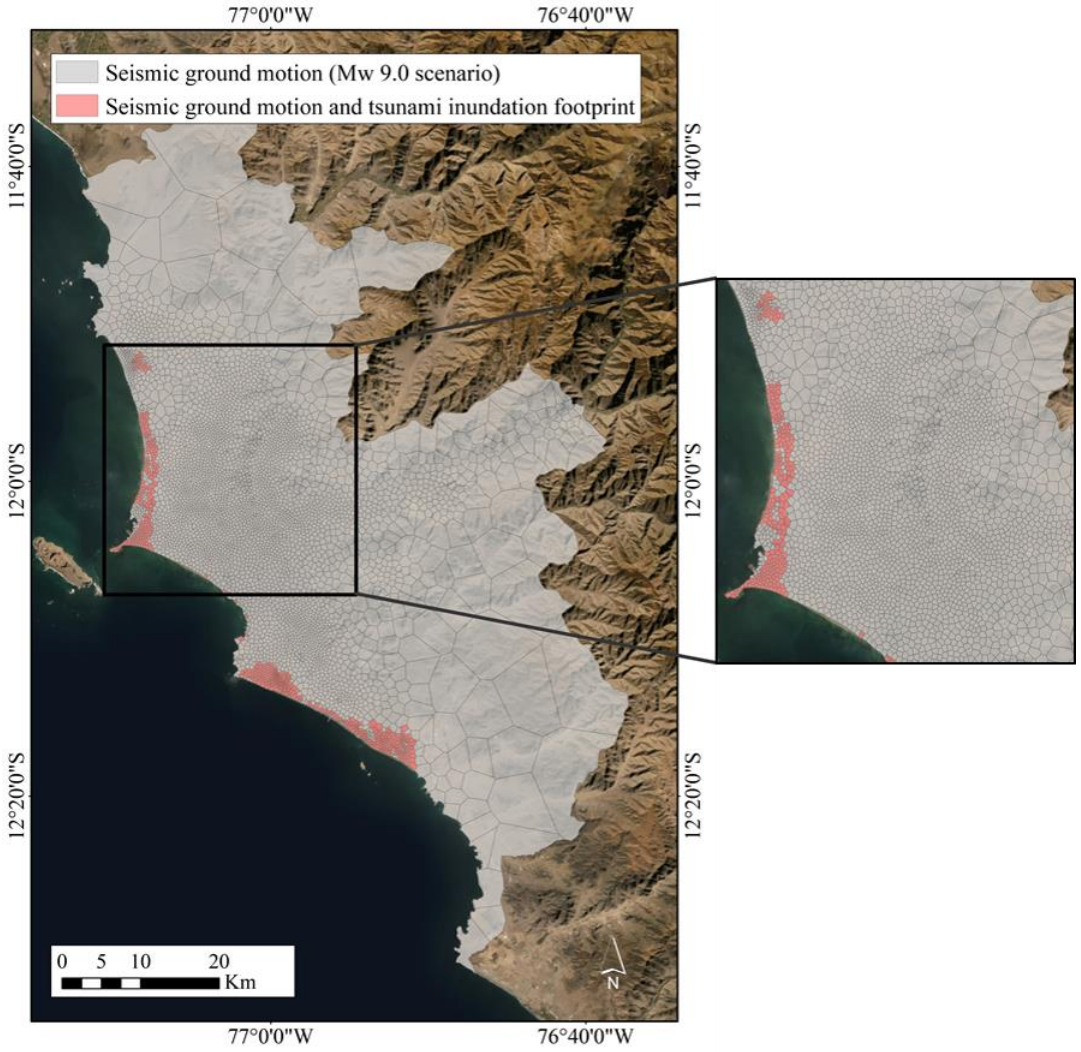

Figure 4-6. The resultant CVT geocells from the focus maps shown above. The common exposed area to a Mw 9.0 earthquake and tsunami is coloured in pink whilst the area only exposed to seismic risk is coloured in grey. Map data: ©Google Earth 2021.

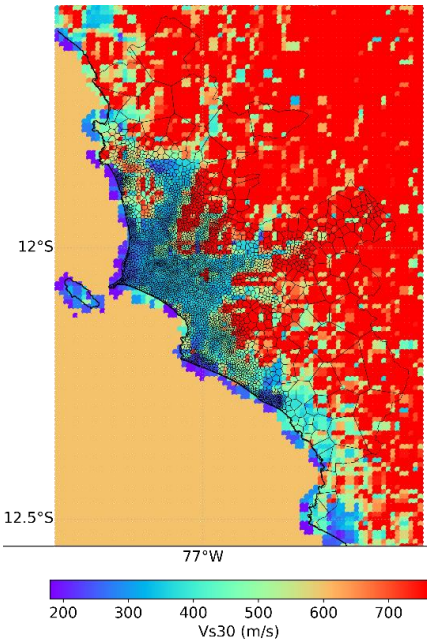

Figure 4-7. Spatial distribution of Vs_{30} values in Lima/Callao as reported by Ceferino et al. (2018b) enclosed within the CVT-based model PD30_TI70_5,000.

4.3.5. Classification of the building stock of Lima into vulnerability classes and aggregation

The residential building stock of Metropolitan Lima (Peru) has been classified in terms of one scheme oriented towards seismic vulnerability and two tsunami-related schemes with related building classes. They have been constructed following Sect. 4.2.5. The logical steps are depicted in the flowchart shown in Figure 4-8. The initial input is the official census dataset for Lima compiled by the Peruvian statistics institution (INEI, 2017) at the block level. It provides the number of buildings for each block and a few exposure attributes regarding the type of dwelling, floor, and façade predominant materials at the dwelling level. The mapping-scheme proposed through expert elicitation in the SARA project (GEM, 2014; Yepes-Estrada et al. 2017) for Peru has been used to relate the census attributes with the proportions expected for 21 building classes. Subsequently, the dwelling fractions (per building unit) proposed in the same study have been used to obtain the building counts for every urban block. The building portfolio is therefore spatially distributed into every CVT-based model through a simple disaggregation procedure addressing their mutual intersections with the block-based model.

Two tsunami reference schemes are selected to classify the building stock of Metropolitan Lima, namely Suppasri et al. (2013) and De Risi et al. (2017) to explore the epistemic uncertainty in their classification. While the first one addresses ten building classes in terms of predominant material and number of stories, the second only accounts for four classes based solely in terms of building material. Steel classes are not included since they have not been deemed representative in Lima (Yepes-Estrada et al. 2017). Thus, we retain seven and three classes, respectively. Considering SARA as the source scheme, the approach presented in Gomez-Zapata et al. (2021) was used to obtain the SARA - Suppasri et al. (2013) and SARA - De Risi et al. (2017) inter-scheme compatibility matrices shown in Figure 4-9. Through their use, the building stock is represented in terms of the building classes of the target tsunami schemes. An example of how to calculate these matrices can be consulted in Gomez-Zapata et al., (2021c).

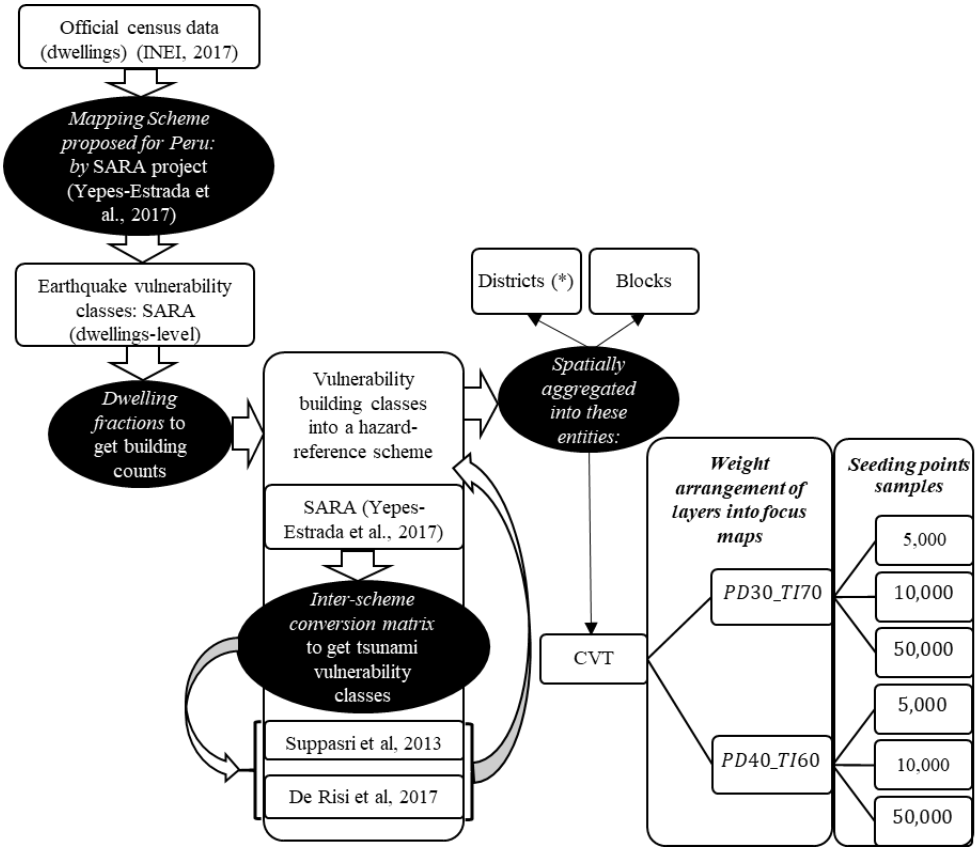

Figure 4-8. Flowchart outlining the process for constructing the building exposure model for Metropolitan Lima, including the condition tree used for the construction of CVT-based exposure models for the aggregation of earthquake and tsunami vulnerability building classes. (*District-based aggregation entities are only used for seismic risk to compare absolute loss values).

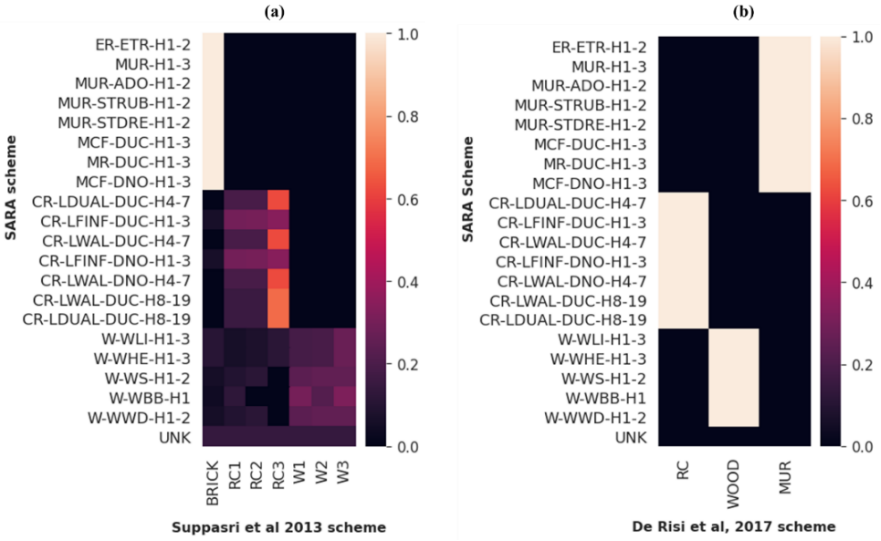

Figure 4-9. Inter-scheme compatibility matrices for Lima showing the compatibility level between the seismic-oriented reference scheme SARA and the tsunami-oriented target schemes: Left: Suppasri et al., (2013) and Right: De Risi et al., (2017).

Every building portfolio for the two considered hazards is aggregated upon the block-based aggregation entities: the six CVT-based and, for the seismic risk (using SARA), over the Peruvian third administrative level division (districts). The building class frequency distribution in the "La Punta" sector (Callao) is depicted in Figure 4-10a,b in terms of the seismic oriented- SARA scheme and in Figure 4-10c,d in terms of the two selected tsunami schemes. These models are available in Gomez-Zapata et al., (2021d).

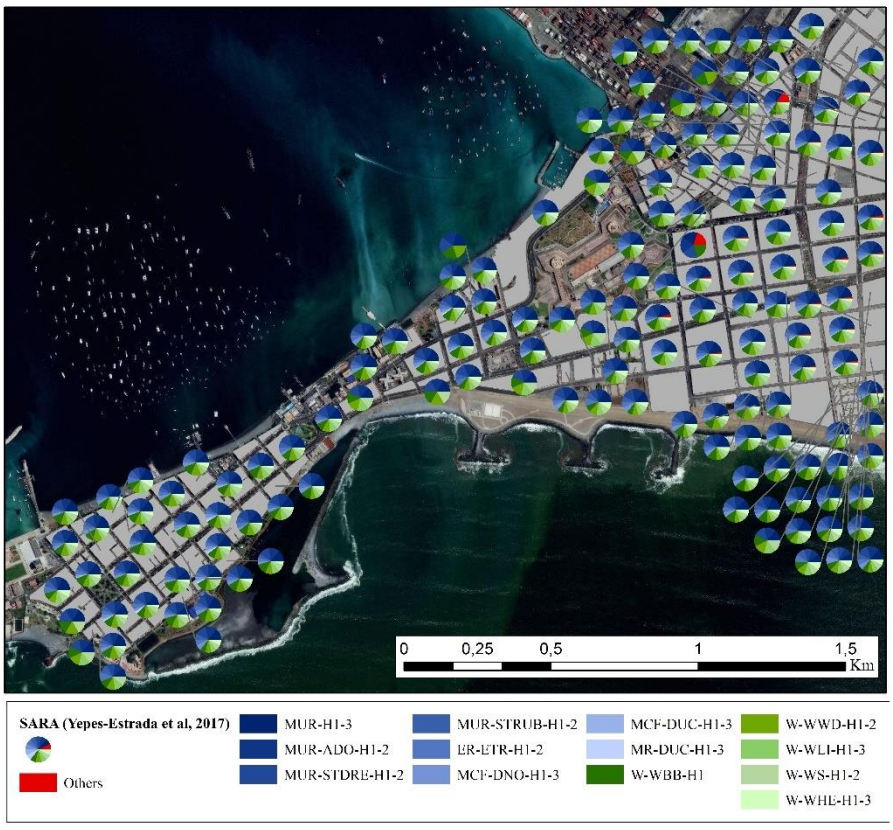

(a)

(Cont.)

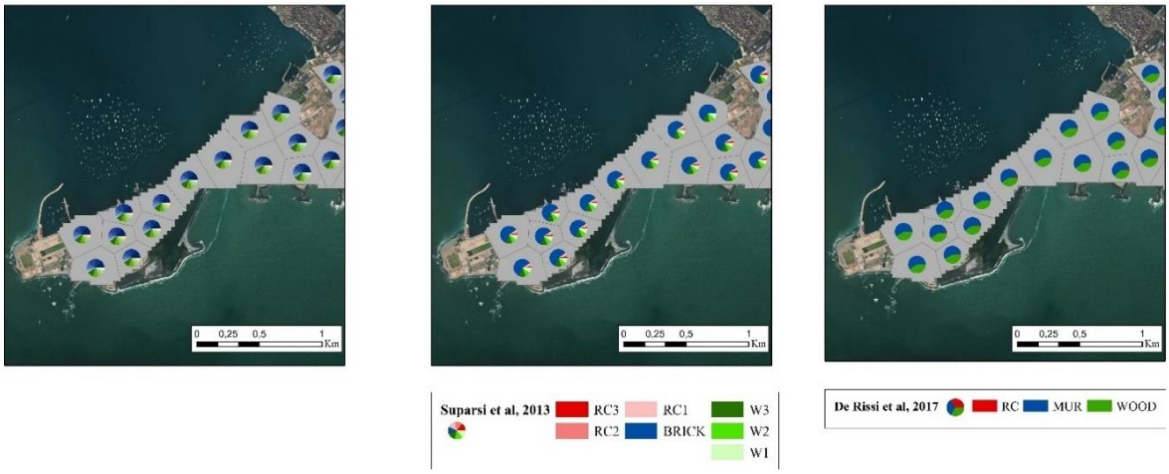

Figure 4-10. Example of the building class frequency distribution in "La Punta" (Callao) mapped using the seismic oriented-SARA scheme (Yepes-Estrada et al., 2017) (a) At the block level, (b) at the CVT based model PD30_TI70_5,000. The latter model is used to aggregate the tsunami vulnerability oriented building classes: (c) Suppasri et al. (2013) and (d) De Risi et al. (2017). Map data: ©Google Earth 2021.

4.3.6. Comparisons of the obtained aggregation areas for exposure modelling

As suggested by Petrone et al., (2020), due to the fundamentally different structural responses to both perils, the direct economic losses of the aggregated building portfolios for the six scenario earthquakes and the corresponding tsunamis have been separately estimated. The variability of the aggregation areas that form every residential building exposure model of the entire Lima/Callao is depicted in Figure 4-11 and listed in Table **4-2**a. Conversely, if we narrow down the exposed area to the largest tsunami footprint (Mw 9.0), we see that the variability in the aggregation areas differs greatly (Figure 4-11b). The CVT-based models with higher resolution geo-cells (50,000) can reach very small areas when the focus map considers the weights PD = 30%, TI = 70%, whilst the block model can reach the largest area values. The model PD30_TI70_50,000 provides a larger number of geo-cells and has a similar representation area with respect to the non-contiguous block-based model (see Table **4-2**b). Furthermore, from Table **4-2** we can see that the computational effort (in terms of file size) required to construct the various exposure models is heavily dependent upon the resolution and, hence, the number of geocells.

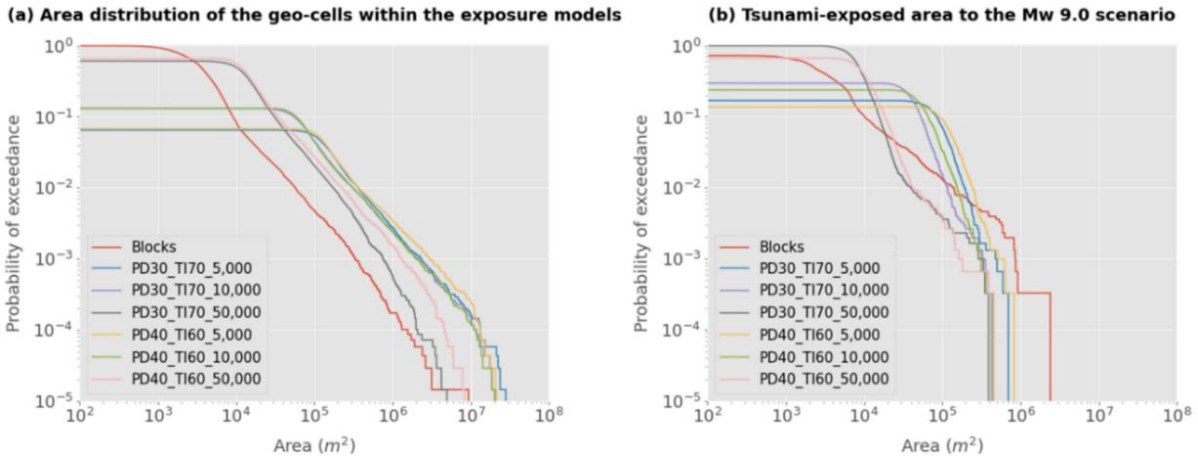

Figure 4-11. Variability in the area (in meters square) of the geocells of every aggregation area for exposure modelling, for (a) the entire urban area of Lima, and (b) for the area for which tsunami-induced loss values were obtained for the Mw 9.0 scenario. Seven models are evaluated: the administrative block-based model and six CVT. The percentages assigned to the two focus maps' components (PD= Population density, and TI= tsunami inundation height) are written, and are followed by the sampling seeding points.

Table 4-2. Variability of area (km²) and file-size (MB) across the exposure models proposed for (a) the entire urban area of Metropolitan Lima, and (b) for the area exposed to the tsunami from the Mw 9.0 scenario event. Only geocells with an urban land use are considered.

	(a) **Configuration in the entire urban area of Metropolitan Lima**			(b) **Mapped as having suffered tsunami- induced loss from the Mw 9.0 scenario**		
Exposure model	Number of geocells	~Area mapped (km²)	Input size file (MB)	Number of geocells	~Area mapped (km²)	Output size file (MB)
PD30_TI70_5,000	4,544	1,500.19	5.3	513	54.19	0.220
PD40_TI60_5,000	4,722	1,695.82	6.0	416	57.45	0.227
PD30_TI70_10,000	9,124	1,559.96	11	906	47.49	0.431
PD40_TI60_10,000	9,182	1,554.14	10.5	728	51.49	0.302
PD30_TI70_50,000	42,509	1,194.38	45.9	3,044	32.50	1.100
PD40_TI60_50,000	46,217	1,537.82	53.7	2,034	28.42	1.010
Block-based	69,786	468.88	118.6	2,203	29.66	1.700

4.3.7. Results: scenario-based risk assessment

Tsunami and seismic risk assessments on classified residential building portfolios are carried out using the software DEUS (Brinckmann et al., 2021).

4.3.7.1. Seismic risk

Seismic losses for the entire study area are initially presented for a Mw 8.8 earthquake scenario so as to discuss the implications of the resolution of the exposure model in the economic loss estimates as well as on their associated mapping and visualisation. A comparison for the other five earthquake scenarios is provided in section 0 for the commonly exposed area to ground shaking and tsunami inundation. As described, the residential building stock of Lima is classified in terms of the SARA scheme and aggregated considering eight different geographical models (six CVT-based, one block, and one district-based model). Each building class has an associated analytically derived fragility function provided in Villar-Vega et al. (2017) as well as their respective economical replacement cost reported in Yepes-Estrada et al. (2017). We have assumed loss ratios of 2%, 10%, 50%, and 100% as suggested by FEMA (2003) for each of the four damage states considered in the vulnerability model. Similar values have been recently proposed for seismic risk applications (e.g., Martins and Silva, 2020).

The seismic vulnerability analysis is performed at every geocell-centroid, where the buildings are aggregated. We consider each IM value resulting from 1,000 realisations of spatially cross-correlated and uncorrelated ground motion fields. The resultant distributions for the Mw 8.8 scenario are displayed in Figure 4-12. Uncorrelated ground motion fields led to very homogeneous distributions, except at the district level. This finding is aligned with the recent study presented by Scheingraber and Käser (2020). Moreover, the latter confirms that if the dimension of the geocells in the exposure model is larger than a typical seismic ground motion correlation length (i.e., 20 km), an artificial bias in the ground motion correlation has to be expected as described in Stafford (2012). We obtain larger median loss values from uncorrelated ground motions. We observe that for the considered scenario, the median loss values are insensitive to the aggregation of the exposure model at varying resolutions. This feature was already described in Bal et al. (2010) for a crustal earthquake damaging a building portfolio in Istanbul while neglecting the cross-correlation model. We thus confirm this finding while expanding it to when a ground motion cross-correlation model is considered.

The financial loss results that we have obtained are similar to the loss distribution estimated by Markhvida et al., (2017), investigated the possible losses of the residential building stock of Lima/Callao (aggregated into a regular grid (~ 1 km²)) expected from a similar Mw 8.8 scenario, who reported mean loss values of around 7 and maxima of around 35 billion USD. Although the authors employed a different GMPE from the one we adopted, the ground motion cross-correlation model, as well as the set of building classes and fragility functions, are the same as what we have implemented.

Despite the remarkable differences between the area distributions of the models (Figure 4-11, Table 4-2),

we do not observe significant differences in the absolute seismic-induced losses, which might be explained by the high special correlation of seismic ground motion and the resolution of the Vs_{30} geo-dataset implemented. However, large differences arise when the normalised losses are mapped. It can be noted that for the same realisation, regardless of the use of correlated or uncorrelated ground motions, the seismically vulnerable areas are still identifiable, albeit with considerable differences. The use of cross-correlated ground motion fields results in smoother mappings. However, the component which imposes the largest impact on the loss estimated from scenario earthquakes is the simulation of the seismic process, as remarked in other studies (e.g., Silva, 2016). This further highlights the importance of using quantile analysis in mapping seismic risk estimates for better visualisation and communication of the uncertainties in an inherently stochastic process (Geller, 2015).

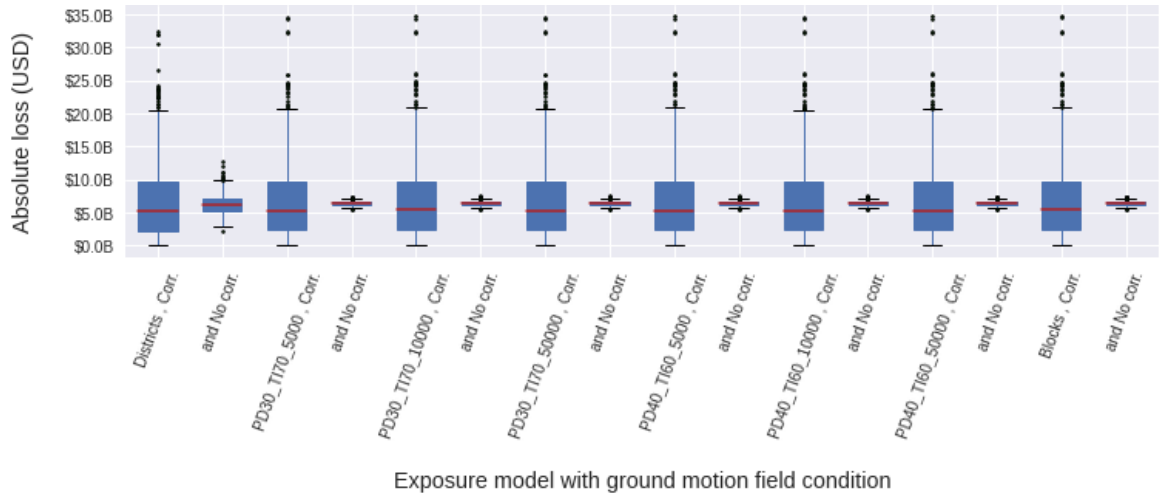

Figure 4-12. Computed loss distributions from a Mw 8.8 scenario for the residential building stock of Lima classified in terms of the SARA vulnerability classes aggregated into eight geographical entities. Two ground motion field conditions are analysed in every case, namely with the selected cross-correlation model (Corr.) and with uncorrelated ground motion fields (No Corr.).

4.3.7.2. Tsunami risk

To constrain the economical consequence model used in the tsunami risk assessment, the inter-scheme conversion matrices depicted in Figure 4-9 are used to obtain the replacement cost values per building class from the corresponding maximum scoring class in SARA. We have assumed loss ratios 5%, 15%, 45%, 65%, 85%, and 100% for each of the six damage states proposed by Suppasri et al. (2013) and similarly, but starting with 15%, for the five ones proposed in De Risi et al. (2017). A similar approach has been recently adopted by Antoncecchi et al. (2020). The impact of using more exhaustive approaches (e.g., Suppasri et al., 2019) is worth exploring, but out of the scope of this paper. Both tsunami-vulnerability schemes have been associated with a set of empirical fragility functions with tsunami inundation height in meters as the IM. They were derived from the same building damage dataset collected after the great 2011 Mw 9.1 Japan earthquake and tsunami with damage state definitions that implicitly accounted for the combined effect of both hazardous events. Thus, despite the extensive use of empirically derived fragility functions from that specific near-field event, care should be taken when using them, not only because they also account for the ground-shaking induced damage, but also because a submarine landslide could have contributed to the tsunami (Tappin et al., 2014). Nevertheless, there is a profound difference in the way the mean intensity values were obtained. Whilst in Suppasri et al. (2013) a linear least squares regression fitting was carried out, in De Risi et al. (2017), a multinomial logistic regression was performed for material-based classes. The latter found similar regression values to the case when an average simulated flow velocity of 1.84 ms^{-1} for masonry and wooden buildings classes (predominant in Lima) is integrated into a hybrid fragility model. Making use of these two schemes, we have correspondingly estimated the tsunami-induced losses for the six scenarios and for the seven exposure models. Tsunami loss estimates normalised to the losses by the block-model are presented in Figure 11. Independent of the reference scheme, the two CVT models with the largest number of geocells (50,000) show the closest similarity to the block model (normalized ratio ~1). However, for all the CVT models, this ratio dramatically drops for scenarios with lower magnitudes (8.5, 8.6, and 8.7) which can probably be explained by a smaller tsunami footprint and lower IM spatial correlation.

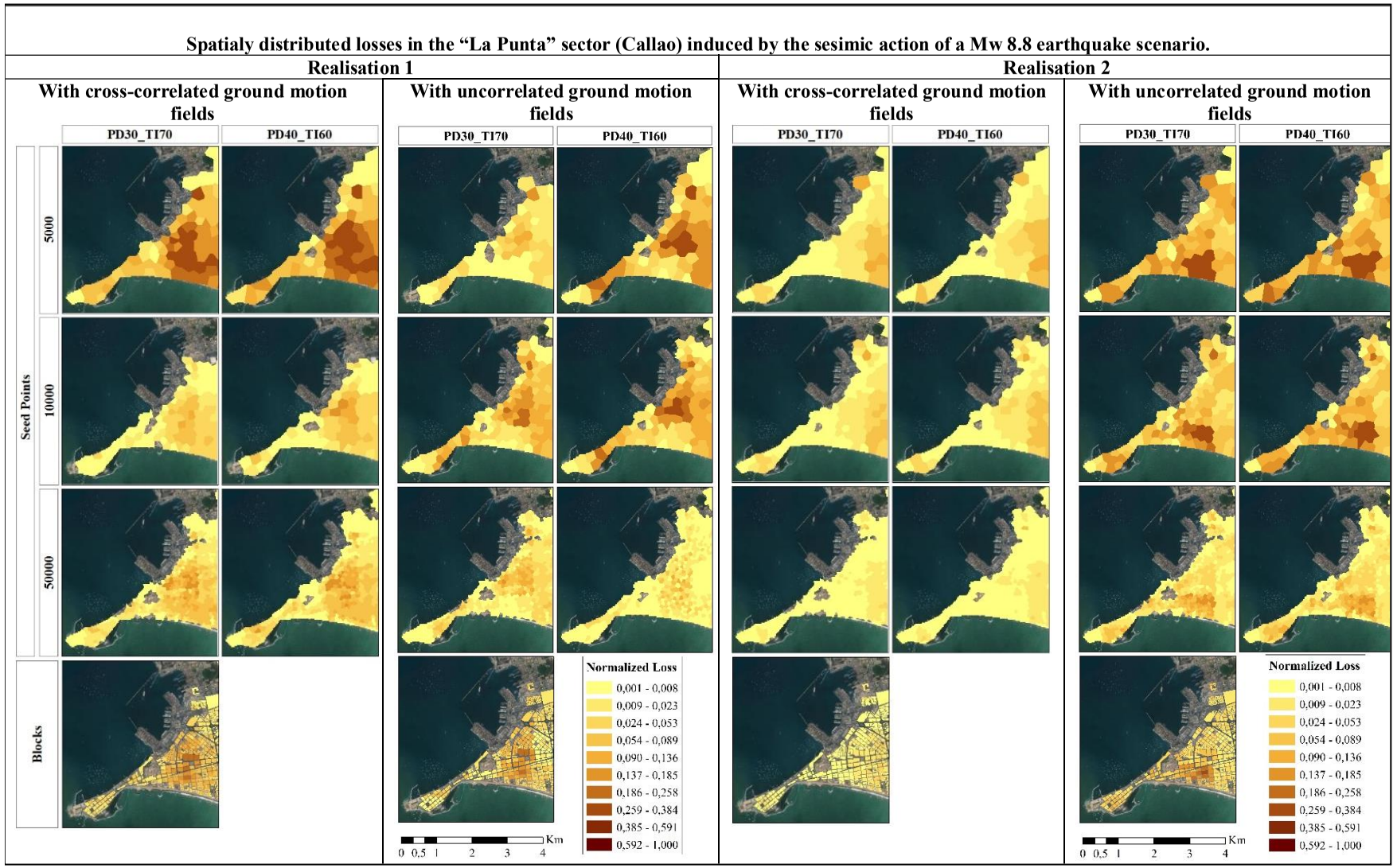

Figure 4-13. Spatially distributed losses in the "La Punta" sector (Callao) induced by seismic ground-shaking of a Mw 8.8 earthquake scenario. They are mapped over six aggregation areas of the building portfolio classified in terms of the SARA vulnerability classes. This is done for two randomly selected realisations with uncorrelated ground motion fields and cross-correlated ground motion fields using the Markhvida et al., (2018) for the periods PGA, 0.3 s and 1.0 s. Map data: ©Google Earth 2021.

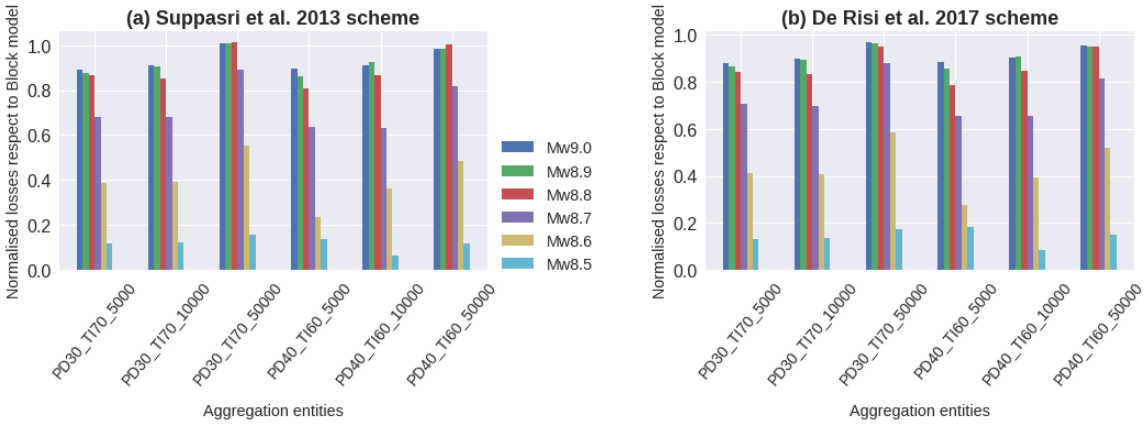

Figure 4-14. Losses induced by six tsunamis for the six CVT models normalised with respect to the ones at the block level. Tsunami vulnerability has been computed using the set of building classes proposed in (a) Suppasri et al. (2013) and (b) De Risi et al. (2017).

The absolute loss values expected after the six tsunami scenarios are reported in Figure 4-15 at the block level for the two vulnerability reference schemes. The fragility models of Suppasri et al. (2013) predict larger values with respect to the model proposed by De Risi et al. (2017) whose functional values were found within the range as if flow velocity was accounted for. These findings are in line with the observations of Park et al. (2017); and Song et al. (2017). These studies concluded that flow-depth models predict higher probabilities of complete damage for buildings than models that employed tsunami velocity in their derivation. Nevertheless, the aggregation of various building classes into less diversified schemes (e.g., only in terms of construction material in De Risi et al., 2017) might also have influenced the results due to the simplifications involved in the assigning of the financial consequence models. Crowley et al., (2005) described a similar effect for seismic risk applications.

We have computed the discrepancy in the tsunami loss estimations obtained for each CVT model with respect to the block-based model (Figure 4-16). This is minimised for the larger magnitudes and higher resolution models (50,000 geocells). This analysis shows that the Suppasri et al. (2013) fragility model leads to slightly larger differences (with respect to the block-based model) for the three lower magnitudes, whereas De Risi et al. (2017) shows larger differences for the three larger ones. These differences are minimised for the largest resolution model.

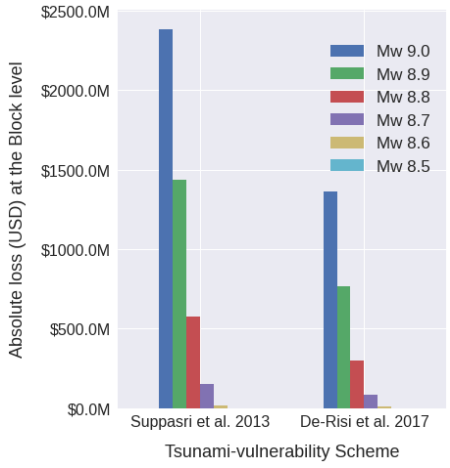

Figure 4-15. Absolute losses (USD) for six tsunami scenarios for the residential building portfolio of Lima classified in terms of two reference schemes and aggregated at the block-based model.

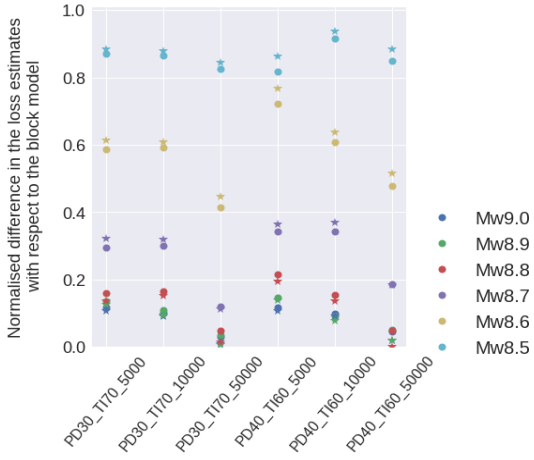

Figure 4-16. Discrepancy between the tsunami-induced losses between each CVT-based model and the block model for the six scenarios. The values obtained from the Suppasri et al., (2013) and De Risi et al., (2017) schemes are denoted by stars and circles respectively.

Tsunami loss outcomes for the Mw. 8.8 scenario are mapped and discussed hereafter for the residential building stock in "La Punta" (Figure 4-17) and Chorrillos district (Figure 4-18). Only geocells with loss values larger than zero are colour mapped. Due to the normalised metric used, no significant differences in the tsunami vulnerability mapping induced by the independent building classification schemas are noticeable. The CVT models at the coarser resolutions (first two rows in every figure) show the largest values, and hence overestimations compared to the block level and other finer CVT- models. Overestimation of losses decreases with the increase in resolution. Due to the adjacency and compactness of the highest resolution CTV model (fourth row), for "La Punta" we identify at least four zones with a comparatively higher tsunami vulnerability.

Considering Figure 4-18 it can be noted that the overall mapped area is increasingly reduced as the resolution of the CVT models increases. This is due to the lack of residential buildings within the three large parcels, namely *"Country Club de Villa", "Reserva Laguna de Villa"*, and *"Refugio de Vida Salvaje Pantanos de Villa"* that occupy most of the exposed area in the block-based model. These zones represent the largest area values in Figure 4-11b. This model assigns the largest loss values in the Chorrillos district to these three large blocks due to the assumption of using a single tsunami intensity as being representative of the entire enclosed area. Therefore, if the block polygons are too coarse compared to the hazard footprint and IM spatial correlation, biases in the loss assessment are expected. This is highlighting the importance of hazard-driven entities for exposure spatial aggregation.

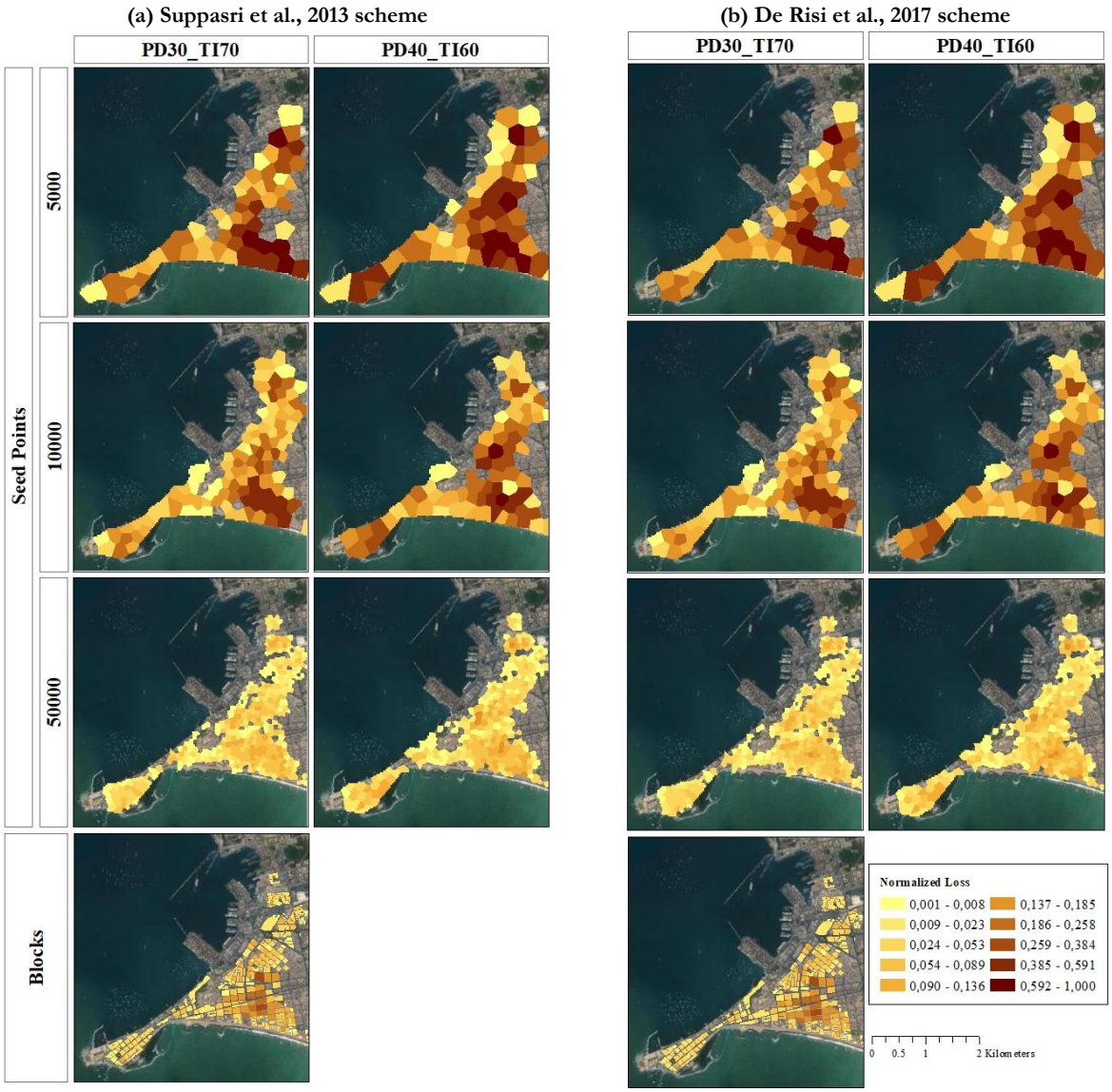

Figure 4-17. Spatial distribution of tsunami-induced normalized losses (Mw 8.8 scenario) for the La Punta sector (Callao district). Map data: ©Google Earth 2021.

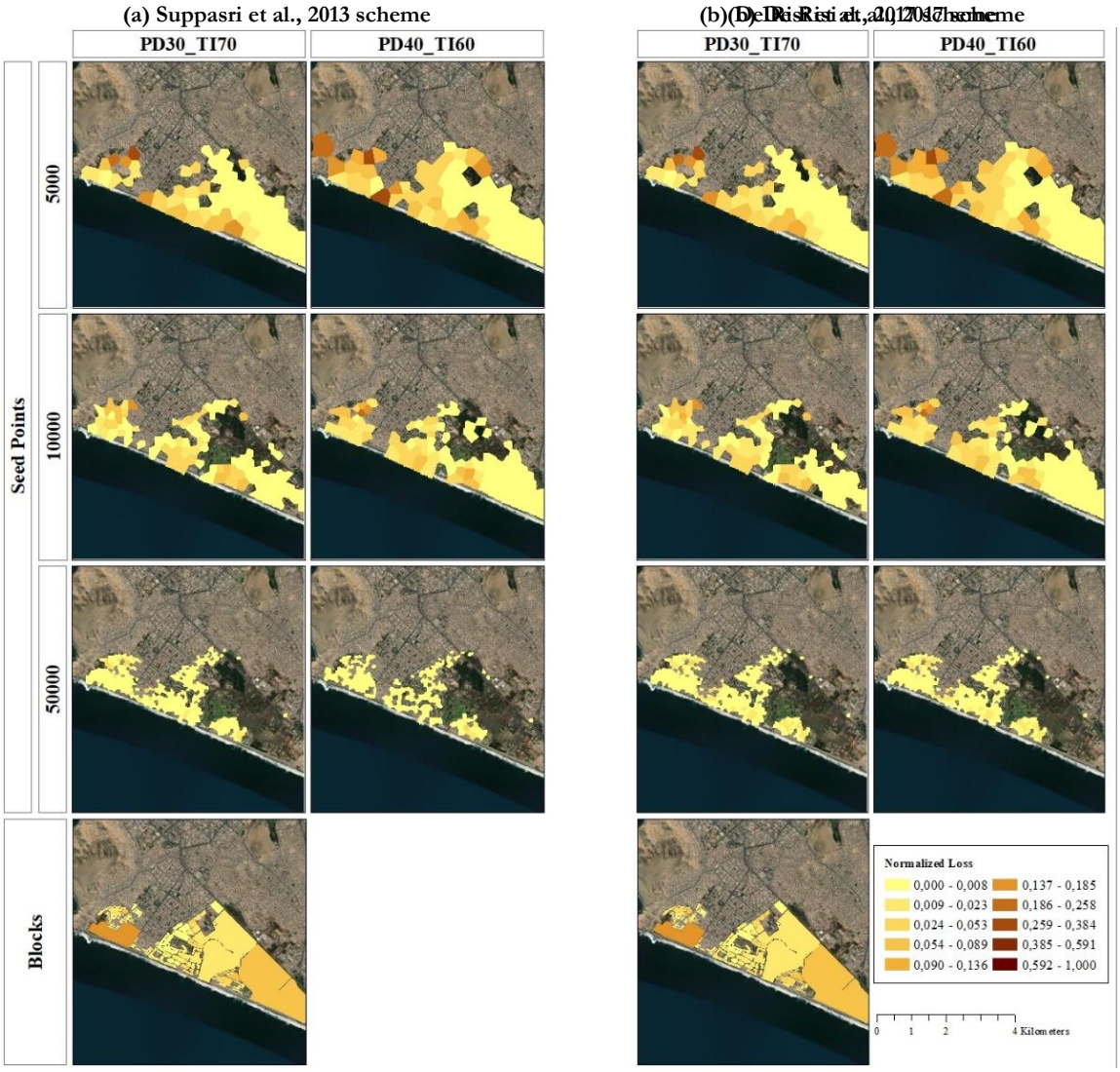

Figure 4-18. Spatial distribution of tsunami-induced normalized losses (Mw 8.8 scenario) for the Chorrillos district (Lima) using two tsunami reference schemes (a) Suppasri et al., 2013 and (b). De Risi et al., 2017. Map data: ©Google Earth 2021.

4.3.8. Comparison between earthquake and tsunami scenario-based induced losses

In Figure 4-19 we compare the absolute losses induced by each hazard scenario onto the building portfolio exposed to both perils (e.g., Mw 9.0 in Figure 4-5-b). The CVT-based PD30_TI70_5,000 is used to represent the earthquake-induced losses. The latter was compiled for the cases with and without the ground motion cross-correlation model, each sampled with 1,000 realisations. Due to the lack of stochastic realisations in the tsunami case, the respective loss distributions were constructed for both reference schemes with the seven values obtained from the various aggregation entities (6 CVT- and 1 block-based models). Even though the distributions for seismic and tsunami losses have been obtained independently, the median values are nevertheless illustrative for comparative purposes.

We observe that in our estimations for the commonly exposed area to both perils in Lima, the earthquake event dominates the median losses at lower magnitudes (Mw 8.5, 8.6) whilst the tsunami prevails in the larger ones. The tsunami-induced median losses start to be larger than the earthquake-related ones for the Mw 8.7 scenario, although the latter still present high volatility in the extreme values due to the variability in the seismic realisations. From Mw 8.8 on, the tsunami-induced losses are always larger regardless of the tsunami reference scheme implemented. Our findings regarding the role of the earthquake magnitude in the disaggregation of financial loss estimates for every hazard scenario are in line with the results of Goda and De Risi (2018) obtained for a coastal town in Japan exposed to two decoupled earthquakes and tsunamis risk scenarios (Mw 8.0, 9.0).

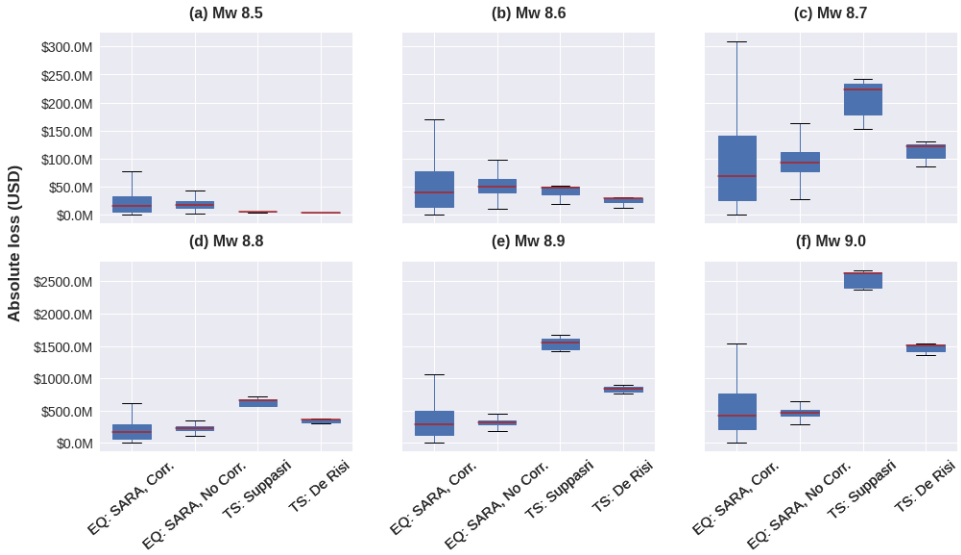

Figure 4-19. Comparison of the independent earthquake-induced losses (EQ) for two conditions (using the 1,000 GMF for each case: with a spatially cross-correlation model (Corr.) and spatially uncorrelated (No Corr.); and the tsunami-induced losses (TS) under two TS reference schemes for six magnitude scenarios over every common area exposed to both perils.

4.4. Discussion

The derivation of CVT-based aggregation entities for building exposure modelling is subject to epistemic uncertainties, namely the selection of weights for the pooling of geospatial layers into the focus map and the selection of seeding points that provide the initial seeding set and control the overall number of geocells. Through the application of a condition tree, we have selected different sets of these two components to investigate the impact of customised CVT-based geographical entities to aggregate building portfolios as well as through the reconnaissance of thematic uncertainties in the loss mapping and visualisation. Voronoi regions inherently fulfil spatial properties such as compactness and contiguity which are useful to identify areas with comparatively homogeneous physical vulnerabilities.

CVT-based aggregation entities for building exposure modelling can be further customized. For instance, the underlying focus map can be modified in order to integrate other components such as seismic microzonations with higher resolutions than the one we have employed in this work; the spatial presence of certain building taxonomic attributes that may drive the physical vulnerability towards a given hazard (e.g., soft-storey in seismic vulnerability and openings / building foundation in tsunami vulnerability (Alam et al., 2018)); high-resolution DEM (digital elevation model). However, caution should be taken not to double count their contribution if the hazard simulations have already been performed using these input data (e.g., DEM in landslide susceptibility and tsunami inundation) as well as a wise selection of their respective weights in the focus map construction. Furthermore, CVT model generation would benefit from further improvements such as outlining an iterative approach that can seek a minimum geocell size from a convergence criterion imposed by spatially correlated hazard-IM-lengths.

Several of the limitations in this study could be addressed in further studies. For instance, it is worth conducting sensitivity analyses that address the differential impact of the selection of other GMPE(s), as well as their combination in logic trees (Scherbaum et al., 2005). In addition, it is relevant to include the calculation of an exhaustive set of stochastic tsunami flood scenarios (with respect to the considered magnitudes) for the evaluation of losses. Likewise, having a higher resolution digital surface model with spatially distributed roughness values is likely to allow the generation of more accurate results. Physics-based tsunami fragility functions based on intensities more relevant to the building failure mechanisms such as momentum flux (e.g., Macabuag et al., 2016; Attary et al., 2017) would benefit future risk simulations. However, this is subject to their actual availability for typical Peruvian building classes. More comprehensive approaches to adapt such as "foreign" empirical fragility models (e.g., Suppasri et al., 2019; Paez-Ramirez et al., 2020), as well as the need of future development of analytical functions for the South American context (e.g., Medina et al., 2019) would benefit future risk assessment studies for Lima. Another area that would benefit from future research is the differential selection of loss ratios with dependencies on the building classes, as for instance recently investigated by Kalakonas et al. (2020) for seismic risk applications. This might be also relevant for tsunami-induced losses that are strongly influenced by the presence and cost of non-structural

building elements. Accordingly, more refined financial tsunami consequence models such as the one proposed by Suppasri et al. (2019) and/or Triantafyllou et al. (2019) are worth exploring when detailed information about prices and built-up areas at the individual building level are available for the study area. In the presented example case, we make use of the concept of inter-scheme conversion matrices to further prove their usefulness to derive exposure models (i.e. spatial distribution of building classes and replacement costs). This is novel because, if we can know these characteristics for a single exposure scheme (e.g. seismic vulnerability oriented), we could get the same descriptors for another vulnerability scheme (e.g. tsunami). This procedure ensures the comparability across the different schemes and this compatibility had not been considered so far in the related scientific literature for multi-hazard exposure modelling. This aspect also outlines that various exposure models existing in the literature can actually be complemented and compared in a probabilistic manner. On the one hand, the latter ensures that the exposed residential assets classified under various schemes have approximate replacement costs, and thus, the hazard-dependent risk estimates can be comparable with each other. On the other hand, caution should be taken when interpreting the presented results. Neither the damages induced by debris impacts nor scour, relevant for a clearer tsunami vulnerability assessment (Charvet et al., 2015), are included in our modelling. Moreover, it is worth mentioning that larger indirect losses can be expected from buildings with other occupancies (e.g., Chen et al., 2018) that we have not considered herein.

CVT-based models can be beneficial to define efficient, multi-hazard aggregation entities for earthquake and tsunami risk assessment, not only in Lima, but also in other coastal cities exposed to similar hazards. Furthermore, it is worth investigating the usefulness of mapping cumulative damage and losses in hazard sequences, i.e., when a first hazardous event modifies the fragility of buildings that are then affected by a successive event, e.g., an earthquake affecting and area that is then struck by a tsunami.

4.5. Conclusions

This work has introduced a novel contribution to derive spatial aggregation entities with variable resolution for large-scale building portfolios for physical risk assessment applications. To this aim, we have presented a workflow to find an adequate resolution of the exposure model where it really matters, i.e., in areas where buildings are densely distributed and/or hazard intensities vary over short distances. This contrasts with the current state of the art related to building exposure modelling (aggregation) that uses regular grids or purely administrative boundaries for exposure aggregation.

In the context of earthquake and tsunami risk, we take advantage of the focus map concept to integrate spatially correlated hazard intensity measures (IMs) with exposure proxies (i.e., population density) in order to spatially identify hot-spot areas where higher values from both spatial distributions are expected. These resultant focus maps can then be sampled by a heterogeneous Poisson point process, as proposed by Pittore et al., (2020) in order to generate variable-resolution aggregation entities in the form of Central Voronoi Tessellations (CVT). Each CVT geocell becomes a minimum resolution of risk computational analysis, handling the inputs (i.e., hazard intensities and exposure model) and output elements (i.e., damage and loss estimates).

Variable-resolution CVT-based exposure models proposed in this work have proved their efficiency in integrating large-area building portfolios for combined earthquake and tsunami loss estimations. Several advantages over conventional models based on administrative aggregation entities are:

- CVT-based models provide alternative an approach to aggregate an extensive building portfolio constructed from ancillary data (i.e., population) in the case when existing administrative aggregation areas are not suitable (either not publicly available, or too coarse in resolution) for a certain area of interest, as well as to perform scenario-based risk assessments for various hazards.
- We have observed that CVT-based models correct some bias in the spatial aggregation of buildings due to the smaller, more compact areas in high-resolution CVT geocells with respect to a coarser block-based cell. This correction is further propagated to the loss estimates due to the higher density of IM values employed by the respective fragility functions during the loss assessment. This is especially observed in areas of the largest concentration of exposed assets located within the hazard footprint area and where local spatial variations of the IM are expected, leading to more accurate estimates.
- They are computationally more efficient than the block-based models in earthquake and tsunami vulnerability assessments. This is advantageous when thousands of stochastic realisations of hazard scenarios are calculated over the

aggregation boundaries that are used to model building portfolios.

- They have shown to be beneficial for mapping loss estimates in continuous space with adjacent and compact geocells. These features allow the spatial identification of zones with similar vulnerability to the hazards considered and within the area of interest. They contribute to a more intuitive visualisation and interpretation of the loss mapping and hence contribute to raising awareness about epistemic and thematic uncertainties in the loss mapping.

For the portfolio exposed to both perils in Lima, we have found that the expected median loss values induced by seismic ground-shaking are insensitive to the representation of the exposure model over varying resolutions. Thus, we confirm the findings of Bal et al. (2010) and expand them to the case when cross-correlated ground motion fields are considered. However, this contrasts with the tsunami loss results, whose differences with respect to a high-resolution model (i.e., block-based) decrease as the resolution of the CVT geocells increases. Similarly, these differences are remarkably minimised for incrementally correlated tsunami-intensities from the large magnitude tsunami scenarios (i.e., Mw 8.8, 8.9, 9.0). According to our observations, the adopted tsunami fragility model based solely on flow-depth as the IM and linear square fitting (Suppasri et al., 2013) predicts much larger tsunami-induced losses on the residential buildings portfolios in Lima than the model of De Risi et al. (2017), which was derived through multinomial logistic regression and with similar values as if the flow velocity was accounted for. For the residential building portfolio exposed to both perils, we have found that the earthquake scenarios dominate the losses at lower magnitudes (Mw 8.5, 8.6) whilst the contribution of the tsunami is dominant for larger magnitude events.

Bearing in mind the scope of this study, but also the limitations presented in the discussion section, we are not claiming that the economic losses we have obtained for the residential building stock of Lima are exhaustive. Instead, through the adoption of the condition tree, we have drawn a branched methodological workflow to explore the differential impact of the exposure aggregation models, and the selection of building schemes on the epistemic and thematic uncertainties that are embedded in scenario-based risk applications. As described by Beven et al. (2018), condition trees facilitate the communication of the meaning of the resulting uncertainties while providing a clear audit trail for their analysis that can be reviewed and evaluated by others (e.g., local experts and stakeholders) at a later date. This study also highlights the relevance of hazard-based aggregation entities for exposure modelling, risk computations, and loss mapping. Thus, the continuous understanding of those uncertainty sources will contribute to enhancing future risk communications, mitigation, and disaster management activities by local decision-makers.

Code and data availability. The codes and data models used in this paper have been made available in open repositories (Brinckmann et al., 2021; Gómez Zapata et al., 2021e, d, b, a; Harig and Rakowsky, 2021).

Competing interests. The authors declare that they have no conflict of interest. The funders had no role in the design of the study; in the collection, analyses, or interpretation of data; in the writing of the manuscript; or in the decision to publish the results.

Acknowledgements. The authors want to express their gratitude to Glendy Linares, Waldor Arevalo, and Walter Tapia from the Peruvian Office of National Security and Defence (Ministry of Housing, Construction and Sanitation) for providing the INEI, (2017) census geo-dataset. Thanks to Catalina Yepes (GEM) for providing the SARA exposure model and mapping schemes for Lima. Thanks to Kim Knauer (EOMAP) for a unified topography and bathymetry data set for the study region. We thank Sandra Santa-Cruz and Nicola Tarque (PUCP), Miguel Estrada, Diana Calderón, Fernando Lázarez, (CISMID), Luis Ceferino, Mary Chris Suarez (YANAPAY), Alireza Mahdavi (AWI), and Omar Campos (DHN) for the fruitful discussions regarding the seismic and tsunami hazard and risk in Lima during some of the authors' visits to the city. Likewise, we thank Tiziana Rossetto, Dina D'Ayala, Ingrid Charvet, Carmine Galasso, and Juan Palomino (UCL) and Pierre Gehl (BRGM) for the feedback during the 2019 Multi-hazard EPICentre encounter in London. Thanks also goes to Heidi Kreibich (GFZ) for the invitation to the 2020-AOGS-EGU NtHazards virtual Seminar, during which we were inspired to continue this study by Anawat Suppasri (Tohoku University). Special thanks to Elisabeth Schöpfer (DLR), Cecilia Nievas, Graeme Weatherill, Henning Lilienkamp, Matthias Rüster, and Jörn Lauterjung (GFZ) for their valuable advice during the elaboration of this study. We thank Dr. Mario Salgado-Gálvez and three other anonymous reviewers for their valuable feedback. We would like to thank Kevin Fleming for the careful proofreading.

Funding. The authors disclose receipt of the financial support for the research and publication of this article from the RIESGOS project (Multi-risk analysis and information system components for the Andes region), funded by the German Federal Ministry of Education and Research (BMBF) Grant No. 03G0876, as part of the funding programme CLIENT II – International Partnerships for Sustainable Innovations.

Chapter 5

5. Scenario-based multi-risk assessment from existing single-hazard building fragility-models. An application for consecutive earthquakes and tsunamis in Lima, Peru

Abstract

Multi-hazard risk assessments for building portfolios exposed to earthquake shaking followed by a tsunami are usually based on empirical vulnerability models calibrated on post-events surveys of damaged buildings. The applicability of these models cannot easily be extrapolated to other region of larger/smaller events. Moreover, the quantitative evaluation of the damages related to each of the hazards type (disaggregation) is impossible. To investigate cumulative damage on extended building portfolios, this study proposes an alternative and modular method to probabilistically integrate sets of single-hazard vulnerability models that are being constantly developed and calibrated by experts from various research fields to be used within a multi-risk context. This method is based on the proposal of state-dependent fragility functions for the triggered hazard to account for the pre-existing damage, and the harmonisation of building classes and damage states through their taxonomic characterization, which is transversal to any hazard-dependent vulnerability. This modular assemblage also allows us to separate the economic losses expected for each scenario on building portfolios subjected to cascading hazards. We demonstrate its application by assessing the economic losses expected for the residential building stock of Lima, Peru, a megacity commonly exposed to consecutive earthquake and tsunami scenarios. We show the importance of accounting for damage accumulation on extended building portfolios while observing a dependency between the earthquake magnitude and the direct economic losses derived for each hazard scenario. For the commonly exposed residential building stock of Lima exposed to both perils, we find that classical tsunami empirical fragility functions leads to underestimations of predicted losses for lower magnitudes (Mw) and large overestimations for larger Mw events in comparison to our state-dependent models and cumulative damage method[d].

[d] published as: Gómez Zapata, J.C., Pittore, M., Brinckmann, N., Lizarazo, J.M., Medina, S., Tarque, N., Cotton, F., 2022. Scenario-based multi-risk assessment from existing single-hazard building fragility-models. An application for consecutive earthquakes and tsunamis in Lima, Peru. Natural Hazards and Earth System Sciences. Discuss. [preprint], https://doi.org/10.5194/nhess-2022-183

5.1. Introduction

Cascading natural events, commonly defined as a primary hazard triggering a secondary one, have jointly induced large disasters (Gill and Malamud, 2016). In the case of earthquakes, between 25 and 40% of economic losses and deaths have been reported to result as a consequence of secondary effects, i.e., tsunamis, landslides, liquefaction, fire, and others (Daniell et al., 2017). Well-known examples are the submarine earthquakes and the subsequent tsunamis occurred in 2004 in the Indian Ocean, in 2011 in Japan, and in 2018 in Palu Bay in Indonesia (Goda et al., 2019). These events not only induced cumulative physical damage on the exposed infrastructure, but also brought drastic socioeconomic cascading effects that are still perceptible today (de Ruiter et al., 2020; Suppasri et al., 2021). Despite the magnitude of such events, multi-hazard risk assessment remains a relatively new research field with still not unified terminologies and approaches (Pescaroli and Alexander, 2018; Tilloy et al., 2019). Nonetheless, a number of studies (e.g., Kappes et al., 2012; Komendantova et al., 2014; Gallina et al., 2016; Julià and Ferreira, 2021; De Angeli et al., 2022; Cremen et al., 2022) have unanimously agreed that more realistic multi-risk evaluations can only be conducted if both (1) multi-hazard (e.g., Marzocchi et al., 2012; Liu et al., 2016) and (2) multi-vulnerability interactions (e.g., Zuccaro et al., 2008; Gehl et al., 2013) are considered altogether. While the former comprises the study of the conditional probabilities of the occurrences of these hazards and their combination, the study of the latter involves reviewing the many classes of vulnerabilities that are associated with an exposed territory.

Therefore, this study narrows down the scope of scenario-based multi-hazard risk by assuming that a second hazardous event is always triggered after the occurrence of the first one, thus eliminating the need to quantify the probability of this occurring. Thus, we will only focus on the dynamic physical vulnerability and related cumulative damage that a building stock exposed to a close succession of hazardous events might suffer. As a premise, this study contributes to the field by proposing a modular method to probabilistically integrate sets of single-hazard vulnerability models that are being constantly developed and calibrated by experts from various research fields to be used within a multi-risk context. The rest of this introduction will discuss the state of the art in exposure modelling for large-scale building portfolios for multi-hazard risk assessment, focusing on the underlying assumptions to propose generalised building typologies with associated fragility functions used to assess their physical vulnerabilities to earthquake and tsunami. Having done that, the last part of the introduction summarises the general scope and capabilities of the original method that will be described in detail afterward.

In exposure modelling for multi-hazard risk purposes, we can distinguish between two main approaches:

1. Using a single set of building classes, each employing as many fragility/vulnerability models as the natural hazards considered, for example, the HAZUS-MH (FEMA, 2003, 2017); Dabbeek and Silva, (2020); and Dabbeek et al., (2020). They have typically associated sets of fragility functions with equivalent damage states regardless of the hazard. Aligned with this philosophy, the EMS-98 vulnerability classes (Grünthal, 1998) were used by some authors to not only describe the likely damage due to seismic action, but also to classify likely ranges of vulnerabilities to other hazards based on the building's material types (Schwarz et al., 2019; Maiwald and Schwarz, 2019).
2. Jointly applying a number of different building classifications per individual hazard to the same exposed buildings (e.g., Gómez Zapata et al., 2021e; Arrighi et al., 2022). Their associated fragility functions may have different sets of damage states (differing in number and description). Notably, these models are constantly developed and individually validated by experts of each research field.

Although the first type might be useful in the assessment of risk arising from independent hazards, their related sets of fragility models lack multi-hazard calibration and validation and, therefore, do not offer sufficient inputs for assessing the increasing damage from cascading events (Ward et al., 2020).

Moreover, the definition of the damage scale depends on the building type (Hill and Rossetto, 2008) and the likely failure mechanisms that it can experience under the action of specific hazard intensity measures (IM) (Vamvatsikos et al., 2010; Selva, 2013). Therefore, the observable damage features on individual structural or non-structural components that jointly describe a certain damage state can have contrasting descriptions across various hazard-dependent vulnerability types (Gehl and D'Ayala, 2018; Figueiredo et al., 2021) and there is often not a 1:1 relation between them, i.e., for

the case of earthquakes and tsunamis (Bonacho and Oliveira, 2018; Lahcene et al., 2021). The reasons behind such a mismatching between the definitions of damage states may arise from the absence of standard formats for damage data collection across regions and across the several vulnerability types of interest (Mas et al., 2020; Frucht et al., 2021). Notably, the study of Negulescu et al., (2020) found this aspect to be particularly significant for the multi-hazard risk context, stating that the damage states of earthquake and tsunami fragility models can have variable levels of compatibility. This assumption led to contrasting loss estimates with respect the U.S HAZUS approach, which is based on the complete equivalence between damage grades. This background portrays the need to standardise the description of the physical damage through harmonizing scales across several hazard-dependent vulnerabilities, which are inputs for unified methods in multi-hazard risk (Ward et al., 2022).

The earthquake engineering community has investigated the cumulative damage expected during seismic sequences (e.g. Papadopoulos and Bazzurro, 2021; Karapetrou et al., 2016; Trevlopoulos et al., 2020), but this concept is rarely considered in other research disciplines. For instance, the physical vulnerability of building portfolios to tsunamis has been typically evaluated through empirical fragility functions derived from post-near-field tsunami surveys. A drawback of these functions is that they have been presented solely as tsunami fragility functions in terms of the inundation depth when in reality these surveys encompassed assets that experienced cumulative damage due to the joint effect of the tsunami-generating earthquake and the tsunami itself (Charvet et al., 2017). Due to this limitation, analytical fragility functions were recently proposed for individual structures (e.g., Attary et al., 2017; Petrone et al., 2017) and for large-scale building stocks with generalised typologies (Belliazzi et al., 2021). However, as remarked by Attary et al., (2019), using these functions for loss estimation should only be valid for far-field tsunamis, and for near-field events the damage induced by shaking before the tsunami strikes must still be addressed.

To the best of the authors' knowledge, only a few studies have investigated the performance of heterogeneous and large-scale building portfolios for risk estimates subjected to consecutive ground shaking and tsunamis. Hereby, we summarize some of them. In Goda and De Risi, (2018) a rationale was proposed for adopting the larger value of the damage ratios from independent earthquake and tsunami risk computations. In Park et al., (2019) a probabilistic multi-risk approach was presented for a building stock in the USA subjected to spatially uncorrelated seismic ground motions and subsequent tsunamis. This study showed the disaggregation of losses per hazard and per material-based building type across several return periods while assuming statistical independence between their respective damage states. As a common denominator of the aforementioned studies, the cumulative damage and losses from a building portfolio were not assessed. Since these metrics cannot be obtained as the sum of the effects from each individual hazardous event (Bernal et al., 2017; Terzi et al., 2019), it is rather necessary to address the nonlinear damage accumulation on the same exposed assets during the multi-hazard sequences (Merz et al., 2020).

This study proposes a modular method to probabilistically integrate existing sets of single-hazard vulnerability models (or "reference schemes"). For this aim, this method comprises four main modules. The first two ones refer to sets of compatibilities between the vulnerability models selected for each single-hazard vulnerability (e.g., between existing seismic and tsunami building classification schemes). The first probabilistic compatibility set are obtained between (1) building classes (as presented in Sect. 5.2.1) whilst the second is obtained between (2) damage states (Sect. 5.2.2). These two conversions are done through the use of taxonomic attributes that are independent to the definition of the reference schemes. This is done with the purpose of representing the damage distribution resulting after the first hazard (i.e., earthquake) through a damage-updated exposure model whose damage scale is dependent on the classification scheme required for assessing the vulnerability to a triggered event (i.e., tsunami). The third module results from the need to perform risk assessment for the triggered hazard using the damage-updated exposure model that is now represented in terms of the second vulnerability scheme (e.g., building classes and damage states for tsunami fragility). Hence, this module comprises the proposal of (3) sets of state-dependent fragility functions for the second hazard (e.g., tsunami), as presented in Sect. 5.2.3. These three modules are valuable inputs for ultimately assessing the expected cumulative damage. They are later complemented by a last fourth module: (4) a consequence model to assess the incremental direct economic losses (Sect 5.2.4) that are expected from consecutive hazard scenarios.

In the application chapter of this paper (Sect. 5.3), we demonstrate the application of this method by

investigating the likely cumulative damage on the residential buildings of Lima (Peru) by considering this city's exposure to six mega-thrust earthquake scenarios (main shock) and subsequent tsunamis. This is done using existing vulnerability models per hazard, and addressing the probabilistic compatibilities between building classes and damage states. Complementarily, a set of tsunami state-dependent fragility functions that are obtained through the use of simple ad-hoc scaling factors are proposed. Nonetheless, as it will be discussed, these functions can and should be replaced by other sets of state-dependent tsunami fragility functions derived from more sophisticated methods when they become available. Every damage distribution is translated into direct economic losses to gain a comparative risk metric and disaggregate the contribution of each hazard scenario.

5.2. Proposed Method

To assess the cumulative damage that is expected to be experienced by a building portfolio during hazardous event sequences, we rely on the principle that its related exposure model is represented by jointly applying existing building classification schemes, one per each individual hazardous scenario of the cascading sequence. For example, one building that is expected to be affected by a first hazard intensity measure IM^A (here A refers to an IM used to model ground-shaking (e.g. PGA in g)) and a second one IM^B (B refers to an IM used to model inland tsunami inundation (e.g. inundation depth in m)) is actually classified under two exposure classification schemes (T_k^A and T_j^B), respectively, which have attached their related vulnerability models a). Each scheme contains a set of mutually exclusive, collectively exhaustive building classes $k = \{k_1, \dots, k_n\}$ and $j = \{j_1, \dots, j_n\}$ correspondingly.

To assess the expected damage state after the first hazardous event (e.g., ground-shaking), we apply their fragility function $\sum_z p(D_{kz}^A|IM^A)$, which give us the probability that a building k, typically assumed to be in an undamaged state 0, (D_{k0}^A), changes to a progressive state z due to a hazard intensity IM^A (green part in Figure 5-1b. For risk assessment, this is completed by the consequence model, $p(L|D_{kz}^A)$, which assigns a loss ratio L of the total replacement cost of building class k given the occurrence of a damage state. Thus, the expected loss given a hazard intensity IM^A is calculated considering the contributions from all possible damage states and their probabilities, as per Eq. 3.

$$p(L|IM^A) = \sum_z p(D_{kz}^A|IM^A)p(L|D_{kz}^A) \qquad \text{Eq. 3}$$

If this damaged building portfolio is subjected to the action of a second scenario with a hazard intensity IM^B, it would experience cumulative damage moving from a damage state $z, (D_{kz}^A)$ to a damage state w (but in the domain of the second vulnerability scheme: D_{jw}^B). Due to this differential scheme classification, their respective set of damage states may not have trivial equivalences because they can also have different observable damage features. Therefore, we propose integrating a set of modular components, namely:

(1) Inter-scheme compatibilities between each hazard-dependent exposure classification scheme $p(T_k^A|T_j^B)$ (i.e., purple part/ doubled line box in Figure 5-1b). Its derivation follows the method originally proposed in Gómez Zapata et al., (2022b), and it is summarised herein in Sect. 5.2.1. By reusing this approach, a building stock formerly that was initially classified for a first hazard vulnerability (i.e., earthquake-oriented typologies) can now be probabilistically represented by other predefined classes (e.g., tsunami-oriented typologies).

(2) The related compatibility levels between inter-scheme damage states $p(D_{kz}^A|D_{jy}^B)$ (i.e., red part/ dashed box in Figure 5-1b, explained in Sect. 5.2.2) that is needed when the fragility models attached to such schemes have different numbers of damage states and descriptions.

The two aforementioned conversions are represented through two sets "compatibility matrices" that are probabilistically generated. The advantage of using these matrices is that through these conversions, the damaged updated exposure model resulting from the action of IM^A can be represented in the domain of the reference scheme attached to the second vulnerability to be analysed. Once this change of reference scheme is obtained, the damage-updated exposure model can be directly used for a second risk computation (e.g. for tsunami risk, addressing cumulative when the buildings experienced previous damage due to seismic ground shaking). This second risk calculation is performed by using a third module that refers to:

(3) Generic state-dependent tsunami fragility functions (i.e. with non-zero initial damage states made of new curves that represent the permissible damage progression). Since the

resultant earthquake–induced damages are formerly expressed in the tsunami vulnerability domain (step 2), the non-zero damage limit states of this set of state-dependent tsunami fragility functions will implicitly account for such pre-existing damage. The joint ensemble of these three components can be ultimately used to calculate the cumulative expected damages after the triggered event with IM^B, while accounting for the preceding induced by IM^A (i.e., green part/ dotted box Figure 5-1b, developed in Sect. 5.2.3).

(4) For multi-risk assessment a fourth module that represents the incremental loss obtained from the economic consequence model attached to the classification scheme T_j^B (i.e., replacement costs and related loss ratios per damage state of the second scheme, D_{jy}^B) is integrated. This is represented by the last box made of continues (blue) lines in Figure 5-1b, explained in Sect. 5.2.4.

These four modules are described hereafter.

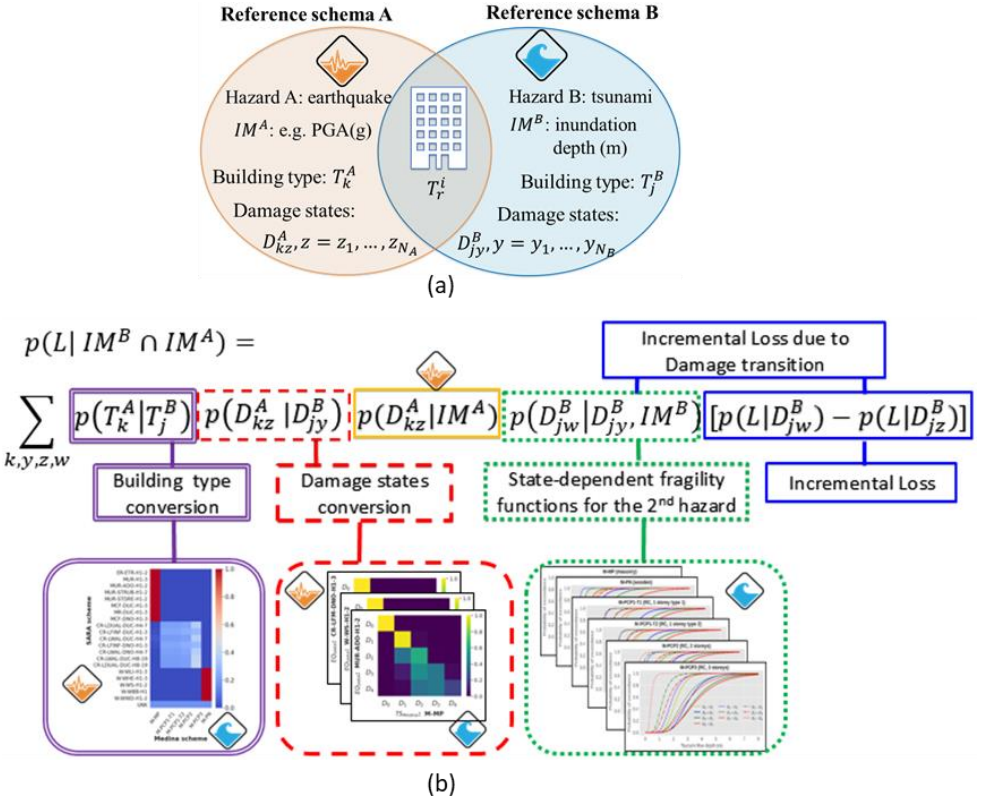

Figure 5-1. (a) Example of the principle proposed for classifying the same building class into two hazard-dependent reference schemes with associated fragility models. (b) Schematic representation of the proposed method to calculate cumulative damage from the case of earthquake-tsunami that is developed afterward.

5.2.1. Exposure modelling: taxonomic description, inter-scheme conversion and spatial aggregation of building classes

The classified building stock under the first hazard-dependent classification scheme T_k^A is spatially aggregated into a set of geocells that capture the local spatial variations of the hazards' IM of interest across the study area. For such a purpose, we recommend using variable resolution exposure models in the form of Central Voronoi Tessellations (CVT). Besides spatially representing the building portfolio, they also provide a representative IM per geocell for reliable and computationally efficient vulnerability estimations (Pittore et al., 2020b; Gómez Zapata et al., 2021f). They also implicitly serve as common minimum reference units (MRU) aggregation entities between exposure and hazard (Zuccaro et al., 2018). This is because for their derivation, one can consider the combination of local variations of the hazard intensity measures (IM) and certain exposure proxies (e.g., population density) across the same area. CVT-based models may be useful in a multi-hazard risk context where the spatial correlation of various IM can differ (e.g., ground-shaking and tsunami inundation).

As shown in Pittore et al., (2018), every building class *k* that belongs to one scheme *A* (in this case, earthquake); and every building class *j* that belongs to

one scheme B (in this case, tsunami) can be described in terms of basic observable features $\{F\}_m$ within a faceted taxonomy, that is, a building classification schema in which building classes result from the characterisation of individual attributes, or facets (Brzev et al., 2013; Silva et al., 2018, 2022). This disaggregation is the common underlying vocabulary to obtain the probability that a building class within the source scheme (T_k^A) corresponds to another class within the target scheme $\left(T_j^B\right)$. As proposed in Gómez Zapata et al., (2022b), the degree of compatibility between the buildings classes belonging to both schemes can be represented by a compatibility matrix $p\left(T_k^A|T_j^B\right)$ to account for the uncertainties when there is not a trivial (one-to-one) mapping. Knowing in advance certain exposure metrics of the source scheme $\{R\}_{T_k^A}$ (i.e., building counts), the respective values of the target scheme $\{R\}_{T_j^B}$ can be obtained by applying the dot product (Eq. 5-4).

$$\{R\}_{T_j^B} = p\left(T_k^A|T_j^B\right).\{R\}_{T_k^A} \qquad \text{Eq. 5-4}$$

5.2.2. The probabilistic description and compatibility of inter-scheme damage states

We consider how the fragility functions associated with T_k^A (earthquake) and T_j^B (tsunami) may have diverse numbers and descriptions of damage states per considered hazard-dependent vulnerability scheme ($D_{kz}^A, z = z_1, \dots, z_{N_A}$ and $D_{jy}^B, y = y_1, \dots, y_{N_B}$). To harmonise their equivalence, we propose obtaining their probabilistic inter-scheme compatibility as a set of matrices $p\left(D_{kz}^A|D_{jy}^B\right)$. This is achieved after having evaluated how the likely observable characteristics linked to each damage state within D_{kz}^A and D_{jy}^B can be expressed in terms of another one. For this aim, we first propose the use of the AeDES form *(Agibilità E Danno in Emergenza Sismica* (usability and damage in seismic emergency)) of the Italian Civil Protection (Baggio et al., 2007) as a standard scoring system to create a synthetic dataset based on the likely observable damage on individual building components. Although it was originally proposed for post-earthquake damage data collection, we propose to transversally use it to describe every damage state z and y of D_{kz}^A (due to seismic ground shaking) and D_{jy}^B (due to tsunami inundation) respectively. Expert elicitation is used on the AeDES form to create heuristics evaluating the expected damage extension per building type and each of the damage-limit-states defined within their respective fragility functions. For this aim, we make use of its implicit scale within a range of 0=L to 9=A over the building components n, (low-level taxonomic attributes) as shown in Figure 5-2. We decided to only include four out of these six components that can be found in any building type as listed in Eq. 5-5 as stairs and pre-existing damage are not always present in all buildings. The importance of such building components for assessing their physical vulnerability has been documented in previous studies to ground-shaking (e.g. Lagomarsino et al., 2021) and tsunamis (e.g. Del Zoppo et al., 2021).

$$n = \{vertical\ structure\ (VS); floor\ (FL); roof\ (RF); infills\ and\ partitions\ (IP)\} \qquad \text{Eq. 5-5}$$

Damage level - extension / Structural component Pre-existing damage		DAMAGE (1)									
		D4-D5 Very Heavy			D2-D3 Medium-Severe			D1 Light			Null
		> 2/3	1/3 - 2/3	< 1/3	> 2/3	1/3 - 2/3	< 1/3	> 2/3	1/3 - 2/3	< 1/3	
		A	B	C	D	E	F	G	H	I	L
1	Vertical structures	☐	☐	☐	☐	☐	☐	☐	☐	☐	○
2	Floors	☐	☐	☐	☐	☐	☐	☐	☐	☐	○
3	Stairs	☐	☐	☐	☐	☐	☐	☐	☐	☐	○
4	Roof	☐	☐	☐	☐	☐	☐	☐	☐	☐	○
5	Infills and partitions	☐	☐	☐	☐	☐	☐	☐	☐	☐	○
6	Pre-existing damage	☐	☐	☐	☐	☐	☐	☐	☐	☐	○

Figure 5-2. Scale to assess the damage level on buildings as proposed by the AeDES form. Reprinted from Baggio et al, (2007).

A heuristic is generated by scoring the four components in Eq. 5-5 per damage state, per fragility function, per building class of both exposure classification schemes. This is done through expert elicitation and establishes a training dataset of the possible observable damage extent $\{OD\}_n$ in a harmonized manner. For instance, one set of $\{OD\}_n$ (for a given damage state and building type) is made

up by a set of four numbers from 0 to 9, e.g., n = {1, 2, 1, 3}, meaning level I for VS and RF, level H for FL and level G for IP (Eq. 5-5). Thereafter, using the total probability theorem, the probability that the damage state z of a building class j in a scheme A corresponds to damage state y of building class j in scheme B can be calculated by Eq. 5-6.

$$p\left(D_{kz}^{A}|D_{jy}^{B}\right)=\sum_{n}p\left(D_{kz}^{A}|\{OD\}_{n}\cap D_{jy}^{B}\right)p\left(\{OD\}_{n}|D_{jy}^{B}\right) \quad \text{Eq. 5-6}$$

We assume that the representations of damage states within the two considered schemes are conditionally independent ($\perp\!\!\!\perp$). Thereby, given the information of the scored observable damage on the individual components $\{OD\}_n$, we can describe the source damage scheme D_{kz}^{A} to be modelled in terms of $\{OD\}_n$ that jointly compose the target scheme D_{jy}^{B}: $D_{jz}^{A} \perp\!\!\!\perp D_{jy}^{B}|\{OD\}_n$.Thus, Eq. 5-6 can be expressed as a product, given by Eq. 5-7.

$$p\left(D_{kz}^{A}|D_{jy}^{B}\right)=\sum_{n}p(D_{kz}^{A}|\{OD\}_{n})p\left(\{OD\}_{n}|D_{jy}^{B}\right) \quad since\ D_{kz}^{A} \perp\!\!\!\perp D_{jy}^{B}|\{OD\}_{n} \quad \text{Eq. 5-7}$$

We obtain a probabilistic compatibility degree between damage states ($D_{kz}^{A}, z=z_1,\dots,z_{N_A}$ and $D_{jy}^{B}, y=y_1,\dots,y_{N_B}$) for every pair of combination of building classes T_k^A, and T_j^B through a Bayesian formulation as presented in Eq. 5-8.

$$p\left(D_{kz}^{A}|D_{jy}^{B}\right)=\sum_{n}p(D_{kz}^{A}|\{OD\}_{n})p\left(D_{jy}^{B}|\{OD\}_{n}\right)\frac{p(\{OD\}_{n})}{p\left(D_{jy}^{B}\right)} \quad \text{Eq. 5-8}$$

The terms $p(D_{kz}^{A}|\{OD\}_{n})$ and $p\left(D_{jy}^{B}|\{OD\}_{n}\right)$ in Eq. 5-8 can be solved through supervised machine learning techniques for classification (e.g., logistic regression, naive Bayes, decision trees) to predict the probabilities between the training sets and a synthetic testing dataset. The selection of the machine learning technique, naturally, carries epistemic uncertainties (Mangalathu et al., 2020) whose investigation is beyond the scope of this study. The testing dataset is obtained after generating random numbers of all the possible combinations of the AeDES-based scores. With this dataset we express the conditional probabilities of having damage states D_{kz}^{A}, z and D_{jy}^{B}, y (for each building class within schemes A and B given $\{OD\}_n$. The term $p(\{OD\}_n)$ is a marginal probability that can be assumed to represent the proportion of one observation out of exhaustive combinations of $\{OD\}_n$. Lastly, $p\left(D_{jy}^{B}\right)$ describes the proportion of each damage state y within each building class k in the training dataset for scheme B. Once Eq. 5-8 is solved, the expression $p\left(D_{kz}^{A}|D_{jy}^{B}\right)$ is obtained, which stems from the probabilistic inter-scheme damage compatibility matrix for each possible pair of buildings within schemes A and B. Subsequently, a special set of fragility functions is needed to follow the damage progression inflicted by the second hazard. They are explained hereafter.

5.2.3. State-dependent fragility functions

The next steps of the method are carried out within the reference vulnerability scheme of the second hazard (i.e. tsunami). Let us suppose that the fragility functions $F_{T_r^i,q_{N_i}}$ (for a set of building types T_r, and composed by a set of q_{N_i} damage limite states) are assumed to be modelled by cumulative lognormal distributions. They are defined by their respective logarithmic means $\mu_{q_0}(T_r^i)$ and their logarithmic standard deviations, for which we assume that their initial damage states q_{N_i} are all represented by a zero q_0 (for a pristine, intact structure). For a set of damage states q_{N_i} in pristine structures, there is a corresponding set of values $\lambda_{q_0}=[\lambda_{q_{0_1}},\lambda_{q_y},\lambda_{q_w},\dots\lambda_{q_{0_i}}]$. With this, let us assume that the damage state w belongs to $D_{jy}^{B}, y=y_1,\dots w\dots,y_{N_B}$. Eq. 5-9 represents the conditional probability that the building j (of the scheme B) can move to a progressive state w given the action of IM^B when it already presented a damage state y due to the action of IM^A. For such a process, please note that it was already classified in terms of scheme B, thanks to the compatibilities between damage states.

$$p\left(D_{jw}^{B}|D_{jy}^{B},IM^{B}\right) \quad \text{Eq. 5-9}$$

The former expression defines a probabilistic state-dependent fragility function composed of transition probabilities between increasing damage states (for instance, for the scheme *B*, this description follows: $y_{N_B} - y_{N_B-(N_B-1)}; y_{N_B} - y_{N_B-(N_B-2)} \dots$). For a fragility model $D_{T_r^i}$ designed for a set of building types T_r, and composed of q_{N_i} damage states (for any hazard of interest *i*), the required set of transition probabilities for a given range of hazard intensities are completely defined by a triangular number G_f as expressed in Eq. 5-10.

$$G_f = \sum_{D_{T_r^i}=1}^{q_{N_i}} D_{T_r^i} = \frac{(1+q_{N_i})q_{N_i}}{2} \qquad \text{Eq. 5-10}$$

A visual example of such transition probabilities within fragility functions for several hazard-dependent models (also including $T_k^A; T_j^B$ and their respective sets of damage states $z_{N_A}; y_{N_B}$) is presented in Figure 5-3.

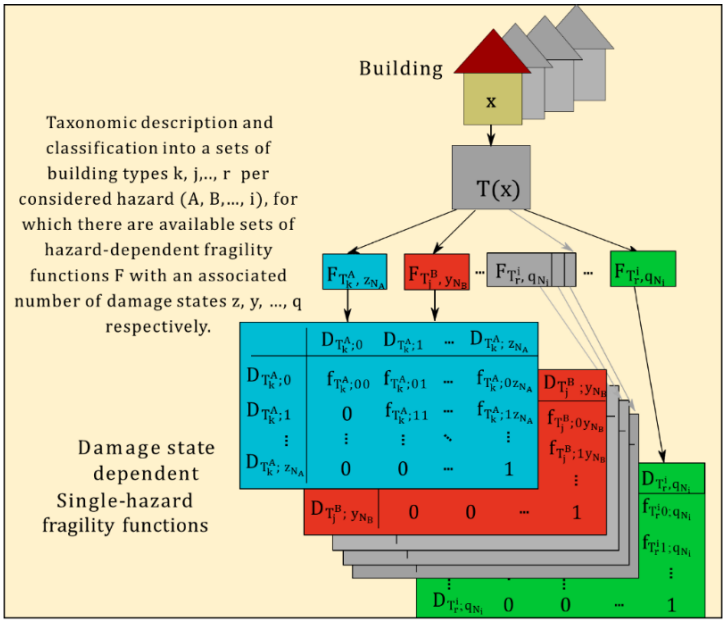

Figure 5-3. Example of a set of damage state-dependent fragility functions for several single hazard fragility functions comprising progressive transition probabilities. Figure modified from Gómez Zapata et al., (2020).

Only for the overall scope of this paper, we propose that state-dependent fragility functions can be simplified by using ad-hoc calibration parameters to modify these logarithmic mean values. For such a modification, we propose applying to them the exponential operator to obtain the physically accountable mean IM (hazard intensity measures). I.e., $\lambda_{q_0}(T_r^I)$ defines each damage state as: $\lambda_{q_0}(T_r^i) = e^{\mu_{q_0}(T_r^i)}$. Subsequently we propose to obtain their respective differences $\measuredangle\lambda_{q_0}$. For example, if a fragility function is composed of $q_{N_i} = 4$ damage states (excluding damage state 0, equivalent to no damage), there will be a set of damage states $\lambda_{q_0} = [\lambda_{q_{0_1}}, \lambda_{q_{0_2}}, \lambda_{q_{0_3}}, \dots \lambda_{q_{0_i}}]$ for which we should obtain the differences between all the possible top and bottom damage states and we must obtain six values: $\measuredangle\lambda_{q_0} = [\Delta\lambda_{q_{0_{1,2}}}, \Delta\lambda_{q_{0_{1,3}}}, \Delta\lambda_{q_{0_{1,4}}}, \Delta\lambda_{q_{0_{2,3}}}, \Delta\lambda_{q_{0_{2,4}}}, \Delta\lambda_{q_{0_{3,4}}}]$.

In this example, these six state-dependent transition values are included within the $G_f = 10$ triangular number (i.e. 4 from 0; 3 from 1; 2 from 2; 1 from 3) given by Eq. 5-10. Thereby, for each T_r^i, it is still necessary to determine the probabilistic representation (log mean and log standard deviation) of every damage state transitions $\measuredangle\lambda_{q_0}$.To do so, the $\lambda_{q_0}(T_r^i)$ values are proposed to be multiplied by the $\measuredangle\lambda_{q_0}$ factors, and reframing this quantity to a natural logarithm in order to approximate it back again to lognormal mean values. This is expressed as given by Eq. 11.

$$\delta_{w|y} = ln(\Delta\lambda_{q_0} \times \lambda_{q_0}) \qquad \text{Eq. 11}$$

The reader should note that in this approach, the $\Delta\lambda_{q_0}$ values are a set of ad-hoc calibration parameters or scaling factors that are applied directly to the λ_{q_0} for which each damage limit state was originally derived. These values form the lognormal mean of the state-dependent fragility functions. A similar approach was followed by Rao et al., (2017). The fragility functions used to constrain the state-dependent fragility functions should have been derived only for the actual second acting hazard (i.e., far-field tsunamis). Thus, the use of those derived analytically is advised over empirical ones (which had implicit the damaged induced by ground-shaking in their derivation). Further details about this approach and model assumptions to find the ad-hoc calibration parameters are provided for the example case in the data repository in Gómez Zapata et al., (2022a).

5.2.4. Loss assessment for sequences of cascading hazards scenarios

We propose a simple economical consequence model that assigns the replacement cost ratios to every damage state of the building classes T_j^B. The incremental economic loss, defined as the difference in the expected loss resultant from the initial damage state and final damage state, is calculated in terms of the reference scheme B as:

$$p\left(L|D_{jw}^B\right) - p\left(L|D_{jz}^B\right) \qquad \text{Eq. 5-12}$$

Combining the two inter-scheme compatibility matrices, ($p\left(T_k^A|T_j^B\right)$ and $\left(D_{kz}^A|D_{jy}^B\right)$, along with Eq. 5-9 and Eq. 5-12, we obtain the formulation in Eq. 5-13, which is identical to the one in Figure 5-1b. This allows us to calculate the probability of observing an incremental loss due to the cumulative damage during the sequence of hazard-scenarios. Eq. 5-13 represents the disaggregated loss caused by the triggered event upon the buildings with a pre-existing damage (due to IM^A). Finally, the likely loss for the entire sequence can be obtained by summing up Eq. 3 and Eq. 5-13.

$$p(L|IM^B \cap IM^A) = \sum_{k,y,z,w} p\left(T_k^A|T_j^B\right)p\left(D_{kz}^A|D_{jy}^B\right)p(D_{kz}^A|IM^A)p\left(D_{jw}^B|D_{jy}^B, IM^B\right)\left[p\left(L|D_{jw}^B\right) - p\left(L|D_{jz}^B\right)\right] \qquad \text{Eq. 5-13}$$

5.3. Application example

5.3.1. Context of the study area: Metropolitan Lima, Peru

In 2022, Peru had a population of around 33 million people, with nearly 58% of this living in coastal communities. In Løvholt et al., (2014) it was stated that this country has the largest population exposed to tsunamis in the American continent. Lima, its capital, with nearly 10 million inhabitants (around one third of the country's population) is home to the most important political, industrial, and economic activities of the country. Lima ranks as the capital city exposed to the highest seismic hazard in South America (Petersen et al., 2018), and as the second city in the world in terms of the value of working days lost relative to the national economy due to earthquakes (Schelske et al., 2014). This city has suffered devastating disasters in the past. For instance, in 1586 and 1724 earthquakes triggered tsunami run-ups over 24 m (Kulikov et al., 2005). The 1746 earthquake, with an estimated magnitude of M_w 8.8 (Jimenez et al., 2013), produced a tsunami with local height of 15 to 20 m (Dorbath et al., 1990) and destroyed the city. In 1974, a M_w. 8.1 event produced widespread damage and caused losses of ~ 7.5 billion dollars. Since then, the city has been experiencing continuous urbanization with generally poor structural design (Tarque et al., 2019).

The 1746 earthquake for scenario for earthquake and tsunami modelling was also used in Adriano et al., (2014) to estimate the damage probabilities of the residential building stock of Callao (part of the Metropolitan area of Lima) using the empirical tsunami fragility functions of (Suppasri et al., 2013) for four building types. More recently, Ordaz et al., (2019) developed probabilistic earthquake and tsunami risk forecasts for Callao. However, that study did not describe the vulnerability models used, nor the method employed to address the non-linear damage accumulation. To the authors' best knowledge, neither cumulative damages due to earthquake and tsunami scenarios nor the use of analytical tsunami fragility functions for Lima have been reported in the scientific literature.

5.3.2. Scenarios of earthquake and tsunami for Lima

We use the dataset compiled by Gómez Zapata et al., (2021e) which is composed of six earthquakes with moment magnitudes ranging from 8.5 to 9.0 M_w, which were made available in Gómez Zapata et al.,

2021c). In that dataset, each event is represented by an associated 1,000 realisations of cross-correlated ground motion fields (GMF) for peak ground acceleration (PGA) and spectral accelerations at 0.3 and 1.0 seconds. The selection of these spectral periods depends upon the fragility function's IM associated with the building classes of the exposure model (Sect. 5.3.1). The simulated GMF were obtained making use of the ground motion prediction equation (GMPE) proposed in Montalva et al., (2017) and the spatially cross-correlation model of Markhvida et al., (2018) employing the OpenQuake Engine (Pagani et al., 2014). For the site term of the GMPE, the dataset reported in Ceferino et al., (2018), which combined the slope-based Vs_{30} values of Allen and Wald, (2007) and a seismic microzonation (Aguilar et al., 2013) was used. On the tsunami modelling side, we reuse the data repository Harig and Rakowsky, (2021) that compiles tsunami inundations for each of the mentioned six earthquakes using the finite element model TsunAWI. Similarly as performed by Harig et al., (2020), the inundation values were interpolated to a raster file with grid cell dimensions of 10×10 m. Figure 5-4 shows three of the tsunami inundation scenarios for the study area.

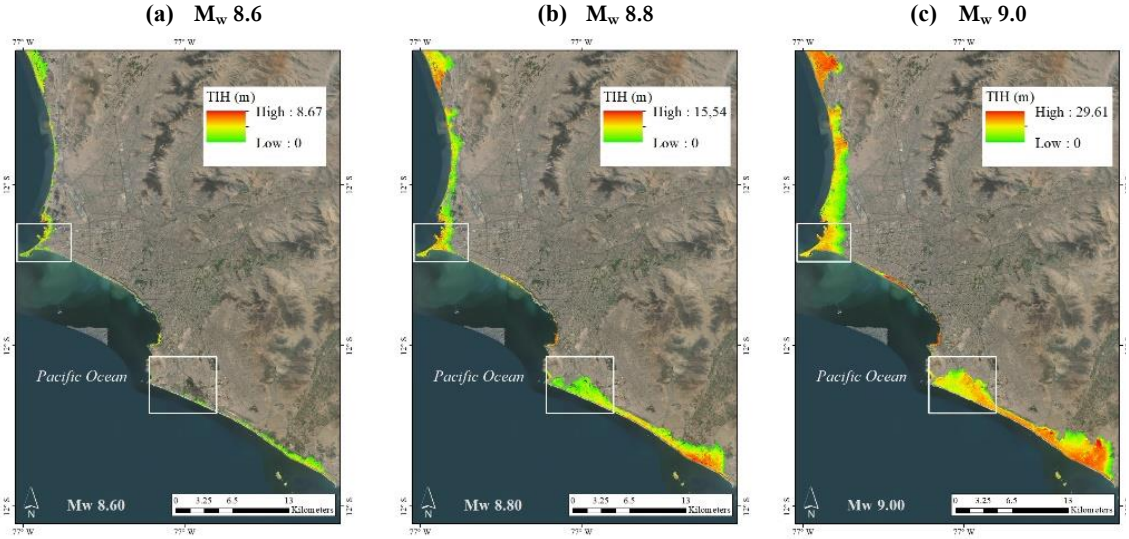

Figure 5-4. Expected tsunami inundation heights for three out of the six considered scenarios per moment magnitude (Mw). These raster products are available from Harig and Rakowsky, (2021). Two densely populated areas are depicted by white rectangles: in the north the "La Punta" (Callao) and Chorrillos in the south. Updated figure from Gómez Zapata et al., (2021e). Map data: ©Google Earth 2021.

5.3.3. Exposure modelling: taxonomic description, inter-scheme conversion and spatial aggregation of building classes for Lima

We make use of the existing building exposure models that represent the residential building stock of Metropolitan Lima for ground shaking vulnerability that were developed by Gómez Zapata et al., (2021e) and are available from Gómez Zapata et al., (2021b). Such a building classification was defined by relating some covariates included within the last official Peruvian census from 2017 (INEI, 2017) at the block-level with respect to 21 classes proposed by the South American Risk Assessment (SARA) project (Yepes-Estrada et al. 2017) through a mapping scheme proposed from expert-elicitation (GEM, 2014). Since that information was provided for dwellings, the so-called "dwelling ratios" proposed by SARA were also implemented to obtain the building counts per class. A description of these building classes is presented in Table 5-1.

It is worth noting that although these typologies are similar to those of the SARA exposure model, there are differences between the building counts reported by that project and our model. This might be due to the vintage of the input census datasets (2007 vs. 2017, respectively), the thematic detail induced by the spatial aggregation entities (districts/ blocks/ CVT), having merged some building classes in terms of similar heights, and having reduced the number of unknown (UNK) type (~91% with respect the SARA model). The resultant exposure model is made up of ~1,657,635 residential buildings, a 25% increase with respect the SAA model. However, as observed in Gómez Zapata et al., (2022b), this scheme does not properly capture the presence of high-rise buildings, underestimating their presence while overestimating the wooden types.

Table 5-1. SARA building classes proposed for the residential building stock of Metropolitan Lima and Callao, with their respective replacement costs per building unit (Repl. Cost (USD/bdg.) as reported in Yepes-Estrada et al., (2017) in the frame of the SARA model released by GEM (Global Earthquake Model) in 2015, which was based on official census data reported by INEI, (2007). The intensity measures (IM) of the associated seismic fragility functions to each building class, as reported in Villar-Vega et al., (2017), are also provided.

	Description	IM	Repl. Cost (USD/bdg.)	Building counts
MUR-H1-3	Unreinforced masonry (MUR), 1–3 stories (H1-3)	PGA	18,000	248799
MUR-ADO-H1-2	Unreinforced masonry, with adobe (ADO), 1–2 stories (H1-2)	PGA	15,000	209837
MUR-STDRE-H1-2	Unreinforced masonry, with dressed stone (STDRE), 1–2 stories	PGA	15,000	209837
W-WBB-H1	Wood (W), bamboo (WBB), 1 story (H1)	S.A at 0.3s	12,000	187355
W-WWD-H1-2	Wood, bahareque and Quincha (i.e., wattle and daub construction): WWD, 1–2 stories (H1-2)	S.A at 0.3s	15,000	149884
W-WS-H1-2	Wood, solid wood (WS), 1–2 stories	S.A at 0.3s	12,000	127401
W-WLI-H1-3	Wood, light wood (WLI), 1–3 stories	S.A at 0.3s	31,500	123654
ER-ETR-H1-2	Rammed earth (ER), reinforced earth system (ETR), 1–2 stories	PGA	15,000	89931
MUR-STRUB-H1-2	Unreinforced masonry, with rubble (field stone) or semi-dressed stone (STRUB), 1–2 stories	PGA	15,000	89931
W-WHE-H1-3	Wood (W), Heavy wood (WHE), 1–3 stories	S.A at 0.3s	12,000	82436
MCF-DNO-H1-3	Confined masonry (MCF), non-ductile (DNO), 1–3 stories	PGA	40,500	66749
MCF-DUC-H1-3	Confined masonry, ductile, 1–3 stories	PGA	126,000	66749
MR-DUC-H1-3	Reinforced masonry (MR), ductile (DUC), 1–3 stories	PGA	360,000	16745
CR-LFINF-DNO-H1-3	Reinforced concrete (CR) with infilled frame (LFINF), non-ductile, 1–3 stories	PGA	126,000	13925
UNK	Unknown	S.A at 0.3s	12,000	8432
CR-LFINF-DUC-H1-3	CR, with infilled frame, ductile, 1–3 stories	PGA	288,000	7519
CR-LDUAL-DUC-H4-7	CR, with dual wall system (LDUAL), ductile, 4–7 stories (H4-7)	S.A at 1.0s	1,080,000	125
CR-LWAL-DNO-H4-7	CR, with wall system (LWAL), non-ductile, 4–7 stories	S.A at 1.0s	472,500	76
CR-LWAL-DUC-H4-7	CR, with wall system, ductile, 4–7 stories	S.A at 1.0s	1,080,000	76
CR-LWAL-DUC-H8-19	CR, wall system, ductile, 8–19 stories (H8-19)	S.A at 1.0s	3,456,000	34
CR-LDUAL-DUC-H8-19	CR, with dual wall system, ductile, 8–19 stories	S.A at 1.0s	3,456,000	32

These SARA buildings are spatially aggregated onto Central Voronoi Tessellations (CVT) to form seismic-oriented exposure models. It is worth noting that the construction of such heterogeneous aggregation units was based on the selection of an underlying distribution that spatially combined and normalised two weighted map layers, namely: (1) a tsunami inundation depth from a Mw 9.0 scenario (70% weight), and (2) the population density at the block level (30%). The resulting model provides higher resolution cells where both conditions are maximised whilst coarser geocells occur when one can expect their absence. Further details about these models are available in Gómez Zapata et al., (2021a, b). Figure 5-5 shows the percentage of building typologies grouped by their main structural materials expected within each geocell.

The analytically derived set of seismic fragility functions by Villar-Vega et al., (2017) are assigned to every SARA class. They will be used to obtain the damage distribution for the cross-correlated ground motions per earthquake scenario (Sect. 5.3.2). For this vulnerability assessment, we use the replacement cost as given by Yepes-Estrada et al. (2017) presented in Table 5-1. For their damage states, we assumed loss ratios of 2%, 10%, 50%, and 100%, respectively.

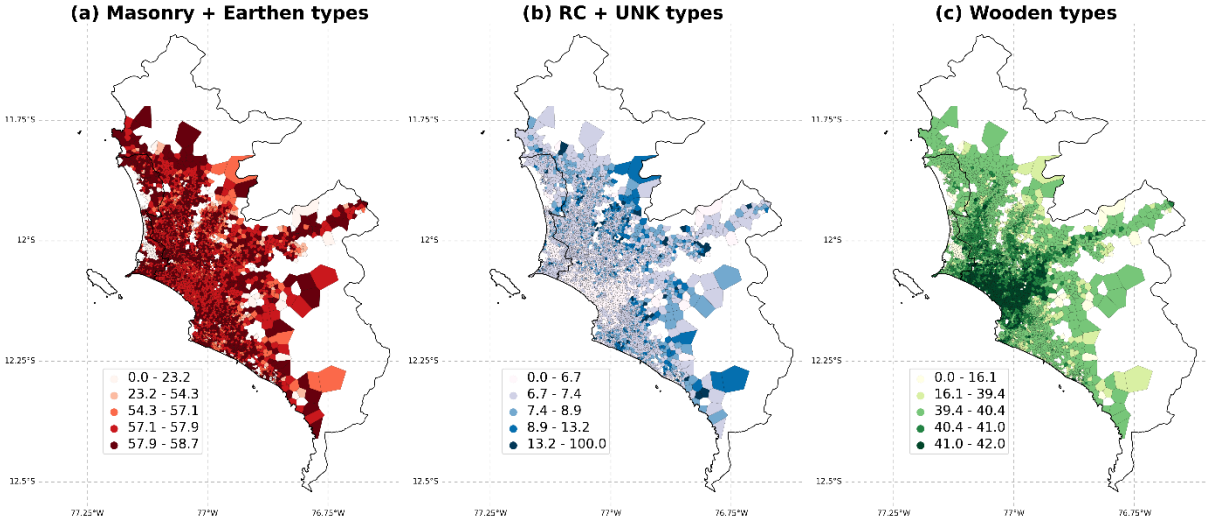

Figure 5-5. Spatial distribution of the percentage of the main structural material of the residential buildings in Metropolitan Lima in each CVT (Central Voronoi Tessellation) geocell using the dataset of Gómez Zapata et al., (2021b). The colour scale represents the material type: (a) masonry and earthen (red); (b) reinforced concrete, RC and Unknown, UNK (blue); (c) wooden types (green). Only CVT that intersected the census-based blocks **(INEI, 2017)** are shown.

On the tsunami vulnerability side, we represent the commonly exposed residential building stock to earthquakes and tsunamis in terms of two classification schemes, namely the Suppasri et al., (2013) and Medina, (2019) schemes which provide sets of empirical and analytical fragility curves, respectively. The former one was made available for Lima in Gómez Zapata et al., (2021b) and is comprised of six typologies. Notably, its corresponding set of empirical tsunami fragility functions (with six damage states) was derived by implicitly addressing the damage induced by the ground-shaking after the M_w 9.1 2011 Japan earthquake and tsunami. Due to this reason, the steps outlined in Sections 5.2.1 and 5.2.3 are not developed for the Suppasri et al. (2013) scheme. Their related direct scenario-based loss estimates were reported in Gómez Zapata et al., (2021e) from the variations obtained from seven geographical entities used to spatially aggregate the residential building portfolio of Lima, and presented in Sect. 5.4 for comparative purposes in contrast with the offered method applied to the Medina (2019) scheme. This second type of classification is to the authors' knowledge the only available model that provides analytical far-field tsunami fragility functions for the South American Pacific Coast. It includes six typical buildings located in Tumaco (Colombia) initially defined in Medina, (2019), which are generalized in this study. They are M-PN (wooden), M-MP (masonry), M-PCP1-T1 (framed RC, one storey with similar length-width ratio), M-PCP1-T2 (framed RC, one storey, with a higher length to width ratio), M-PCP2 (framed RC, 2 storeys), and M-PCP3 (framed RC, 3 or more storeys). Their associated set of fragility functions was developed following the method proposed in Medina et al., (2019) to define the structural fragility due to tsunami forces. A summary that regards the structural characteristics of these building types and the method adopted in deriving these models are provided in the data repository Gómez Zapata et al., (2022a).

As explained in Sect. 5.2.1, every building class within the three schemes of interest is disaggregated into attributes within the GEM v.2.0 faceted taxonomy. As done in Gómez Zapata et al., (2022b), fuzzy compatibility levels between the attribute values and building classes are assigned through expert elicitation. Thereby, synthetic surveys based on the possible combinations of attributes that every building class may describe are employed to solve the compatibility scores and obtain the probabilistic inter-scheme compatibility matrices in the form of $p\left(T_k^A \middle| T_j^B\right)$. Subsequently, we can obtain the building counts under the tsunami classification scheme. This is done considering the SARA classification (Figure 5-6a), as the source scheme $\{R\}_{T_k^A}$ and the inter-scheme conversion matrix (Figure 5-6b). Then, the corresponding counts under the tsunami scheme of Medina (2019) $\{R\}_{T_j^B}$ (Figure 5-6c) are obtained by applying a dot product (Eq. 5-4).

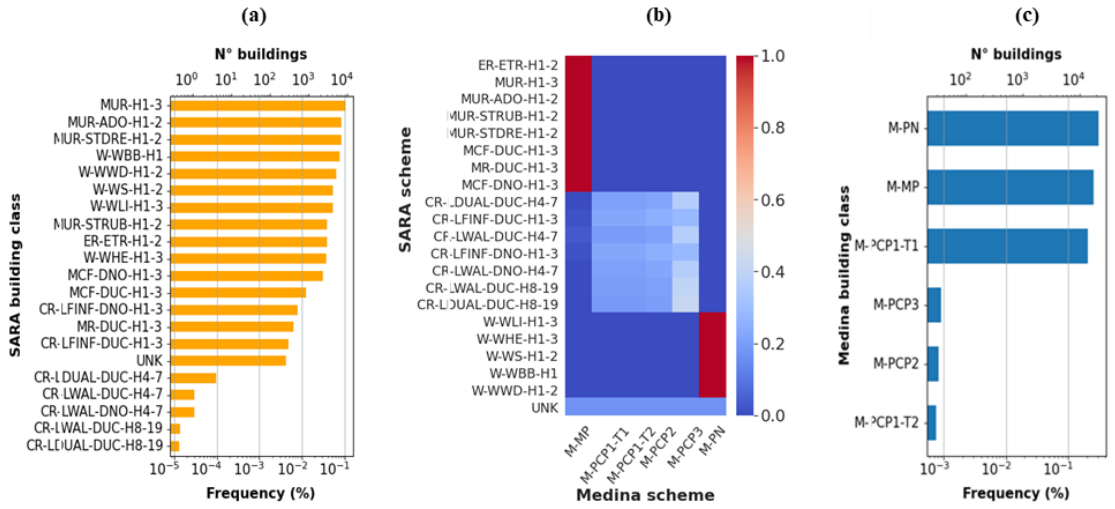

Figure 5-6. Classification of the buildings in the maximum exposed area to both perils (Mw 9.0 scenario) in terms of the (a) seismic-vulnerability oriented SARA classes (used as a source scheme) and (b) the inter-scheme conversion matrix. The former two models are used as inputs to obtain the (c) proportions for the tsunami-oriented building classes of Medina (2019).

The inter-scheme conversion between SARA and the Suppasri et al., (2013) classes for Lima was reported in Gómez Zapata et al., (2021f). The replacement costs values of the building classes within the Medina (2019) scheme are assumed to be the same as the SARA class for which the largest compatibility value was obtained from the inter-scheme compatibility matrix (Figure 5-6b). We have adopted identical loss ratios per limit damage state as the ones assumed for earthquake vulnerability. This decision is aligned with previous related studies, i.e., similar loss ratios were also adopted in Antoncecchi et al., (2020) to assess the vulnerability of buildings to tsunamis using empirical fragility functions. It is worth noting that only the commonly exposed buildings to each pair of hazard scenarios (i.e., intersection between the IM of Figure 5-4 and Figure 5-5) are considered for the assessment of cumulative damage after the cascading sequence.

5.3.4. Inter-scheme damage states for the models adopted for Lima

We obtain the inter-scheme damage compatibility matrices, $p(D_{kz}^{A}|D_{jy}^{B})$, following the method presented in Sect. to probabilistically harmonise the damage states that define the fragility functions of A (SARA) and B (Medina). It is worth noting that although A and B comprise four damage states they do not have a trivial equivalence. A defines a single damage criterion for the entire set of building classes closely following the proposal by Lagomarsino and Giovinazzi, (2006) as a function of the yielding and ultimate spectral displacements. Conversely, B uses a building class-dependent parametrization based on the HAZUS inter-storey drift ratios to define the structural damage levels on pre-code structures. First, we use the AeDES scale to score the admissible observable damage extension on individual building components (n in Eq. 5-5) through expert elicitation, which can jointly describe each building-specific damage states of every scheme's fragility functions (D_{kz}^{A}, D_{jy}^{B}). Some examples of this procedure are displayed in Figure 7. These heuristics configure the training datasets. Subsequently, we have configured the testing datasets. They are composed of a synthetic dataset of 10,000 exhaustive possible combinations of the observable AeDES score-based damage extension $\{OD\}_n$. Thereby, the likelihood terms and $p(D_{jy}^{B}|\{OD\}_n)$ in Eq. 5-8 represent the probability of classifying each damage state D_{kz}^{A} and D_{jy}^{B} given the set of scored building components $\{OD\}_n$.

To obtain the likelihood terms of in Eq. 5-8, we have decided to use the Gaussian Naïve Bayes supervised machine-learning classification-algorithm. It is available in the free software library Scikit-learn for the Python programming language (Buitinck et al., 2013). This selection is suitable for our classification problem because the observable damage heuristics can be assumed as normally distributed continuous data. This can be observed from the heuristic shown in Figure 7 where the central damage states (i.e., moderate and extensive) show wider ranges of combinations of observable damage with respect to the lowest (slight) and largest (collapse) states. For illustrative purposes, in Figure 5-8 we show one of the possible sets for the likelihood probabilities predicted for each damage state described in terms of observable damage extension with respect to the AeDES scale upon two building components (VS, IP) for two material-based

typologies in the commonly exposed area to both perils, i.e., masonry and wooden structures (see Figure 5-6a,c).

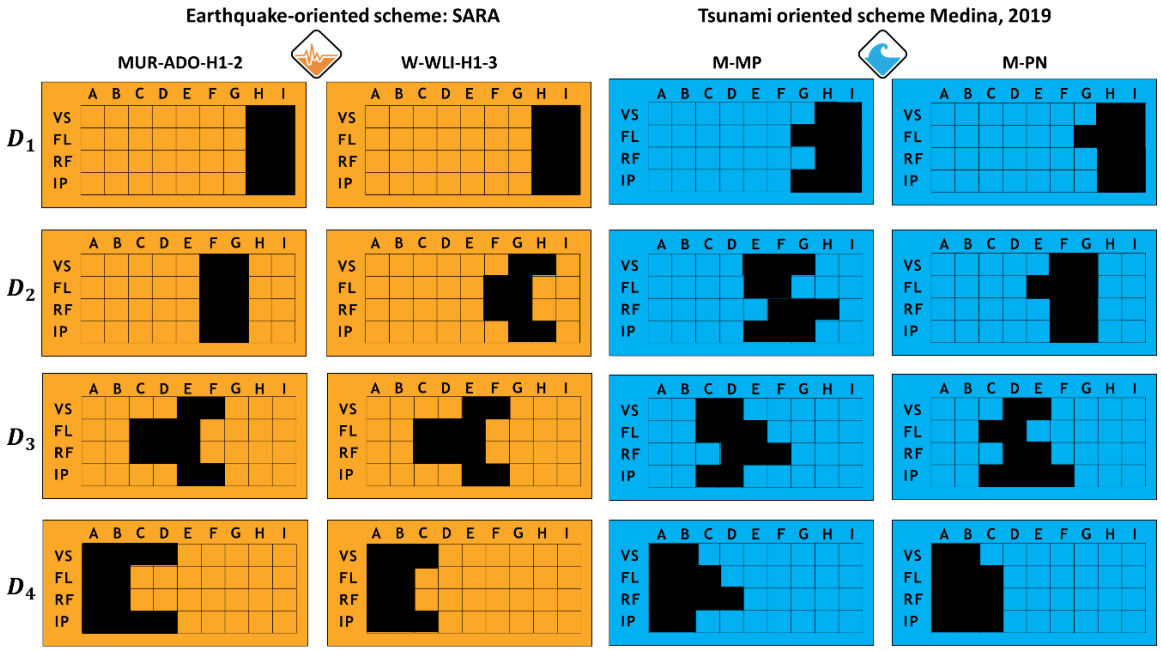

Figure 5-7. Examples of the AeDES-based heuristics (see original AeDES form (Baggio et al., (2007) on Figure 5-2)) that describe the expected observable damage onto the four selected building components listed in Eq. 5-5 (vertical structure (VS); floor (FL); roof (RF); infills and partitions (IP)) using the scale from I-A (i.e., I=0 (null) to A=9 (>2/3 extension within the "very heavy" damage level). This is done per damage state per building class within two hazard-dependent vulnerability schemes.

The marginal probability in Eq. 5-8, $p(\{OD\}_n)$, is assumed to be the proportion between one observation and the exhaustive combinations (1/10,000). Thereafter, we have obtained the probabilistic inter-scheme damage matrix $p\left(D_{kz}^{A}|D_{jy}^{B}\right)$ for each combination of building types from the two schemas (i.e., 21 SARA classes by 6 Medina classes = 126 conversion matrices). Examples of the inter-scheme damage matrices are shown in Figure 5-9 for three pairs of building types that had the highest inter-scheme compatibility values in Figure 5-6b. Each of the 126 matrices that relates the damage states for each possible combination of building classes from the two schemas is subsequently weighted by the corresponding value of $p\left(T_k^A|T_j^B\right)$, that is, by the probability of the building classes of the two schemas actually being descriptive of the same actual building (i.e., Figure 5-6b). When considered in Eq. 5-13, the damage related matrices are maximized by the most compatible pairs of inter-schema building matrices (Figure 5-6b). The scripts, heuristics, the final set of likelihoods, and the compatibility matrices are provided in Gómez Zapata et al., (2022c).

5.3.5. Tsunami state-dependent fragility functions for Lima

We have followed the method presented in section 5.2.3 to configure the state-dependent fragility functions based on Scheme B (Medina) with associated analytical far-field tsunami fragility functions. The parameters that define the lognormal cumulative distributions for the four original damage states (assuming an initial undamaged state), and well as for the set of $G_f = 10$ transitions probabilities (from Eq. 5-10) are provided in the data repository (Gómez Zapata et al., 2022a). Figure 5-10 shows the analytical tsunami fragility functions (continuous lines) and state-dependent fragility curves with their respective damage-transitions (non-continuous lines) for the six building classes.

From Figure 5-10 it is possible to observe some features of the tsunami damage-state fragility functions based on ad- hoc calibration parameters (Sect. 5.2.3). For example, the masonry buildings class is the one most fragile to tsunami forces when in an undamaged state. Consequently, their associated state-dependent fragilities are shifted towards the left side

of the plot in quite an extreme fashion (Figure 5-10a). This means that for that building type there is a higher probability for it to follow a longer damage progression after having been strongly affected by the seismic ground-shaking (dotted and dashed lines).

Conversely, for the wooden buildings (Figure 5-10-b) these are more likely to follow a damage progression than other classes if they were slightly affected by the shaking (see dashed lines). For the two one-storey RC building types assessed (M-PCP1-T1 & M-PCP1-T2) there are negligible differences between the transition probabilities D_2-D_3 and D_3-D_4, as well as between D_1-D_3 and D_2-D_4. Notably, the inter-distances between these pairs of sets (of damage states) are of a similar order as the ones comprised by one and two damage state(s) respectively. This feature is not present for the other RC buildings with increasing heights nor the wooden types. This observation is dependent on the specific analytical fragility models used and the assumptions adopted to derive them (Eq. 10) and no generalization should be done until it can be further validated through other means.

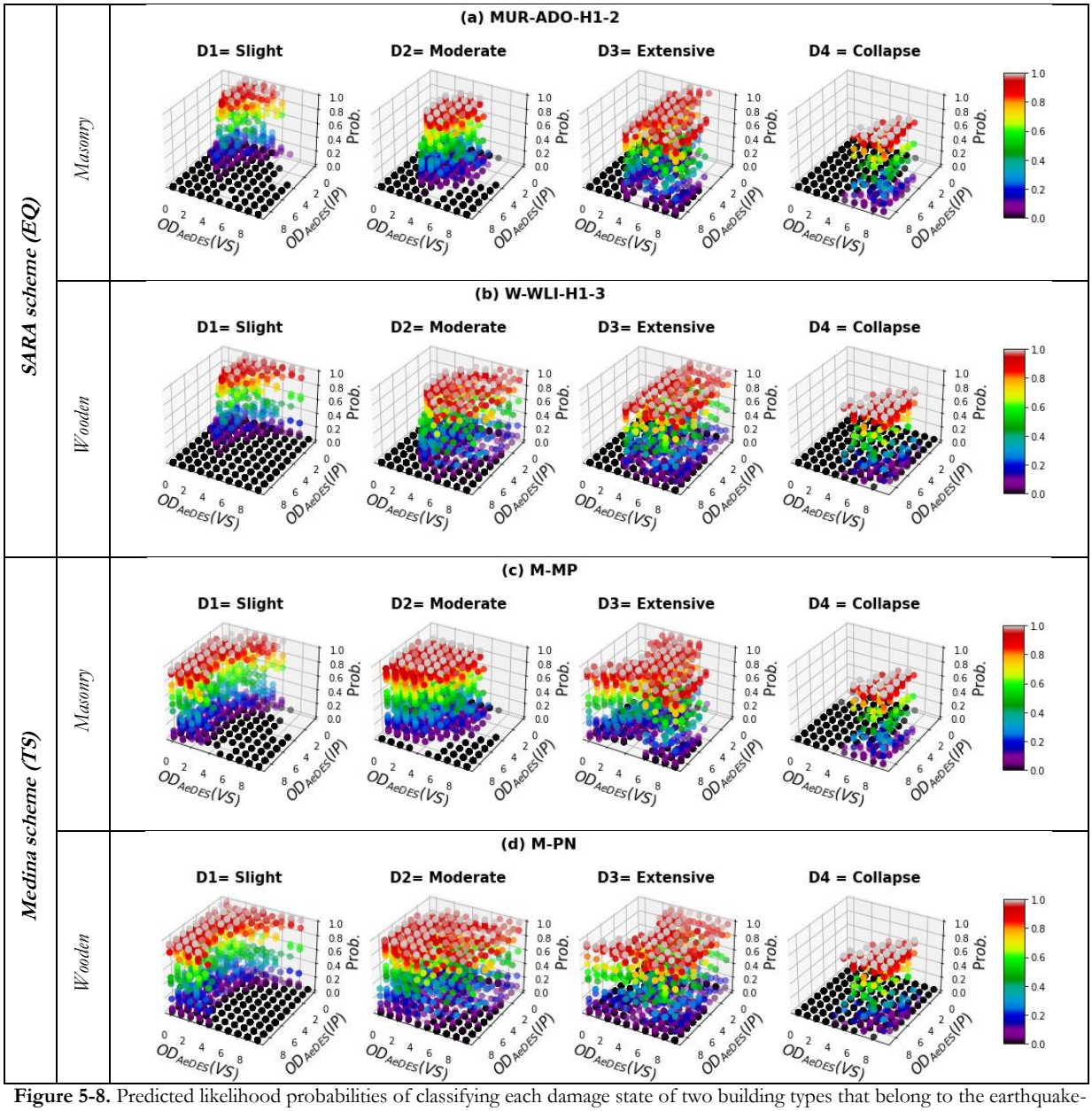

Figure 5-8. Predicted likelihood probabilities of classifying each damage state of two building types that belong to the earthquake-oriented (EQ) vulnerability scheme SARA (D_{kz}^{A} (with building types k and sets of damage states z)) and two building types that belong to the tsunami-oriented (TS) scheme Medina (D_{jy}^{B}, with building types j and sets of damage states y). These features comes from having scored the likely observable damage $\{OD\}_n$ onto the building components listed in Eq. 5-5 in terms of the AeDES scale (i.e., 0=L - 9=A (e.g., as shown in Figure 7). The predicted likelihood probabilities on the figure are only shown for the building components VS (vertical structure) and IP (infills and partitions) for masonry buildings (subplots a, c) and wooden buildings (subplots b, d).

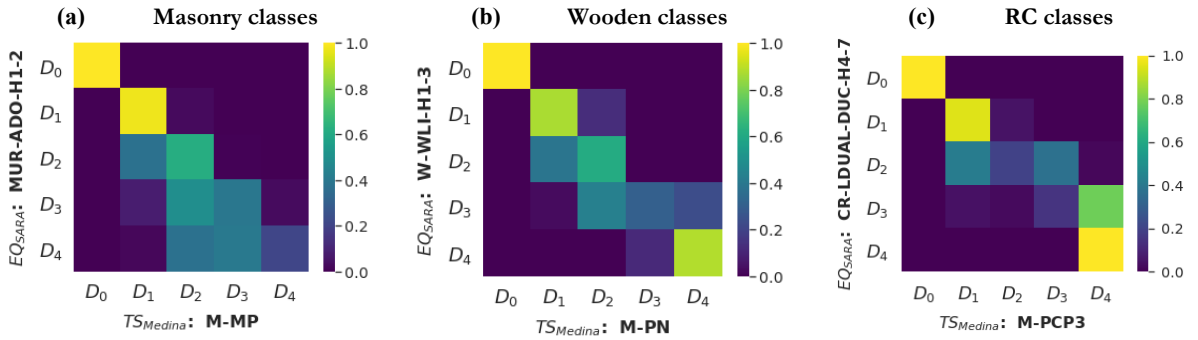

Figure 5-9. Probabilistic inter-scheme damage compatibility matrices for three pairs of building classes: (a) Masonry, (b) Wooden, and (c) Reinforced concrete (RC). The pairs of building typologies shown had the greatest compatibility in Figure 5-6b. Their respective fragility functions are comprised within the source earthquake-oriented (EQ) vulnerability scheme SARA (D^{A}_{kz}, with building types k and sets of damage states z) and the target tsunami-oriented (TS) scheme Medina (D^{B}_{jy}, with building types j and sets of damage states y).

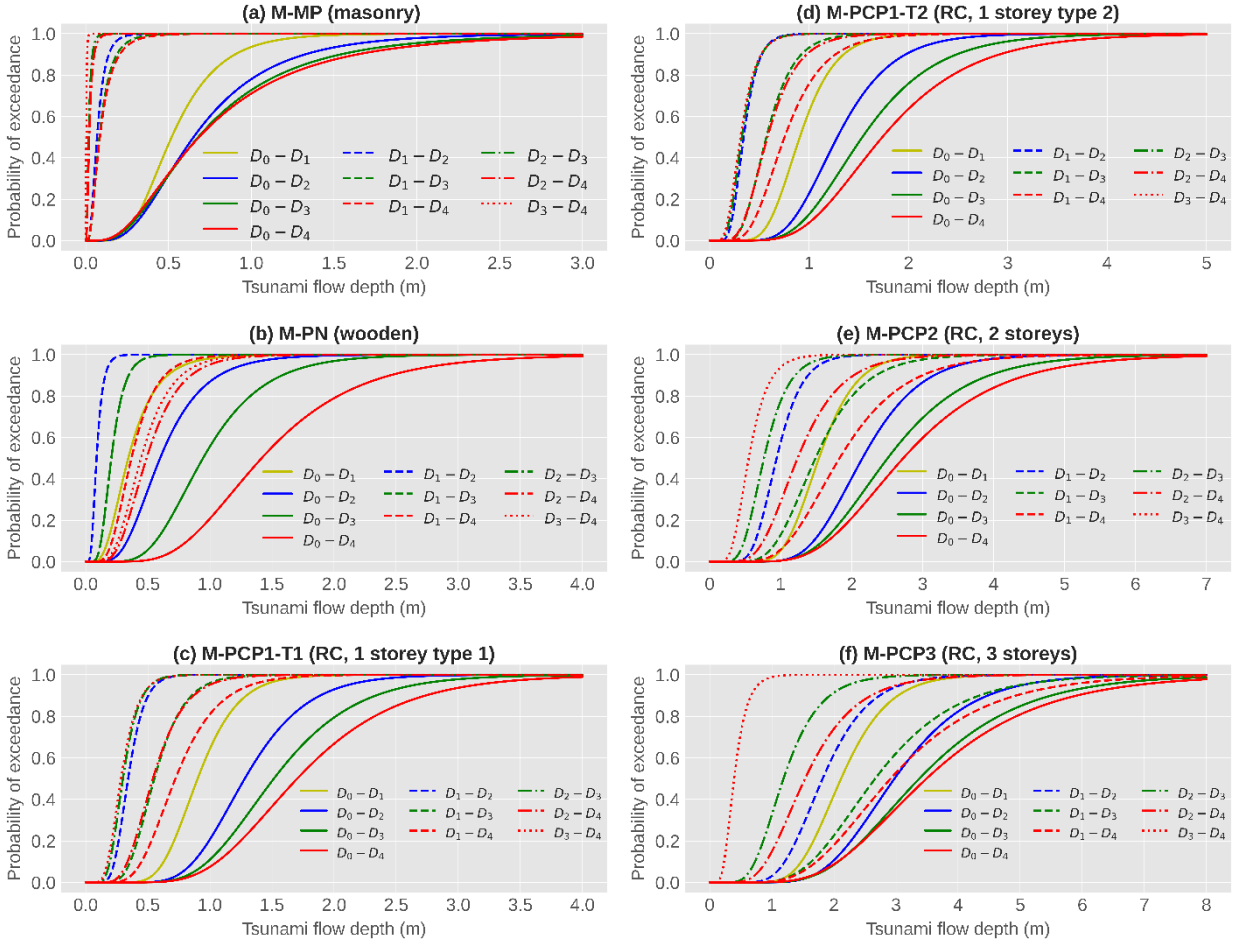

Figure 5-10. Analytical tsunami fragility functions with initial undamaged state as proposed by Medina, (2019) (continuous lines) and derived state-dependent fragility curves (non-continuous lines) in terms of flow depth (m) as IM for six building classes: (a) M-MP (masonry), (b) M-PN (wooden), (c) M-PCP1-T1 (framed reinforced concrete (RC), one storey with similar length-width ratio), (d) M-PCP1-T2 (framed RC, one storey, with a higher length to width ratio), (e) M-PCP2 (framed RC, 2 storeys, (f) M-PCP3 (framed RC, 3 or more storeys).

5.3.6. Cumulative damage from consecutive ground shaking and tsunami scenarios in Lima

The spatially cross-correlated ground motion fields (Sect. 5.3.2, Fig. 11-a, b), along with the exposure model for seismic vulnerability and their corresponding fragility functions (Sect. 5.3.1, Fig. 11-d, e) are the first set of inputs required by the engine DEUS (Brinckmann et al., 2021) to estimate the damage distribution and direct economic losses for the residential building stock of Lima after each earthquake scenario. DEUS is a software designed to compute scenario-based risk from any type of natural hazard over spatially aggregated building portfolios. This version of DEUS is an open-source Python program whose number of executions are proportional to the consecutive risk scenarios.

As shown in f, g, the resulting damaged exposure model (after ground-shaking) is used as input for a second execution to account for the cumulative damage induced by the tsunami scenarios. DEUS makes use of the two sets of inter-scheme compatibility matrices for buildings (Sect. 5.3.1) and damage states (Sect.5.3.4) to change from the source earthquake reference scheme to the target tsunami reference scheme (see Fig. 11-g). These are inputs together with the tsunami inundation heights (Sect. 5.3.2, Fig. 11--c), and state-dependent tsunami fragility functions (Sect. 5.3.5, Fig. 11-h) for the second run of DEUS. This time, the damage states are updated in the building exposure model, delivering only the disaggregated damage and losses expected from the tsunami. Finally, the cumulative distribution of losses is obtained by adding the latter disaggregated tsunami losses with the initial results derived from the earthquake ground-shaking.

5.4. Results

Since we have addressed the aleatory uncertainty in the cross-correlated ground motion fields by generating 1,000 realisations, the procedure described in Sect. 5.2.4 was carried out the same number of times. The generated results are, therefore, presented in the form of loss exceedance curves in Figure 5-12. This figure reports the probability of exceeding the selected loss metric (replacement cost in USD) for the six earthquake and tsunami scenarios that might impact the portion of the residential building stock of Lima that is commonly exposed to each pair of hazard scenarios (buildings for which the action from one of the two hazards was negligible were excluded from the comparison). This figure shows five sets of curves, described as follows:

1. Earthquake ground-shaking-induced loss (blue curves). They represent the direct losses due only to seismic ground shaking using the SARA scheme (Villar-Vega et al., 2017). They are obtained through 1,000 realisations of cross-correlated seismic ground motion fields using the models described in section 5.3.2.
2. Losses obtained from the sole use of empirical fragility functions as simulating a near field tsunami (red curves). These curves represent the losses from the cumulative effects of the shaking and the tsunami (without any possibility to separate both effects). Such losses prediction may be biased since the empirical fragility functions of (Suppasri et al., 2013) assuming an initial undamaged state (D_{k0}^{A}) has not been validated for smaller or larger events. Similarly as it was concluded in Gómez Zapata et al., (2021), we have also observed that as the earthquake magnitude increases, the differences between the two largest loss values in the curve (from the two finest resolution entities) are reduced
3. Losses obtained from the sole use of analytical fragility functions as simulating a far-field tsunami (purple curves. They represent the direct losses obtained solely through the implementation of the analytical tsunami fragility tsunami (Medina), while assuming an initial undamaged state (D_{k0}^{A}), thus, neglecting seismic ground-shaking. Similarly, as done for the former case (empirical functions), the reduced variability of these results was accounted for through computations using seven exposure models, with variable spatial resolutions obtained from a recent study (Gómez Zapata et al., 2021f). This is a result of the lack of variability in the seismogenic parameters to vary only the Mw, and not having assumed distributions for slip-rates, but single values (Gómez Zapata et al., 2021f).

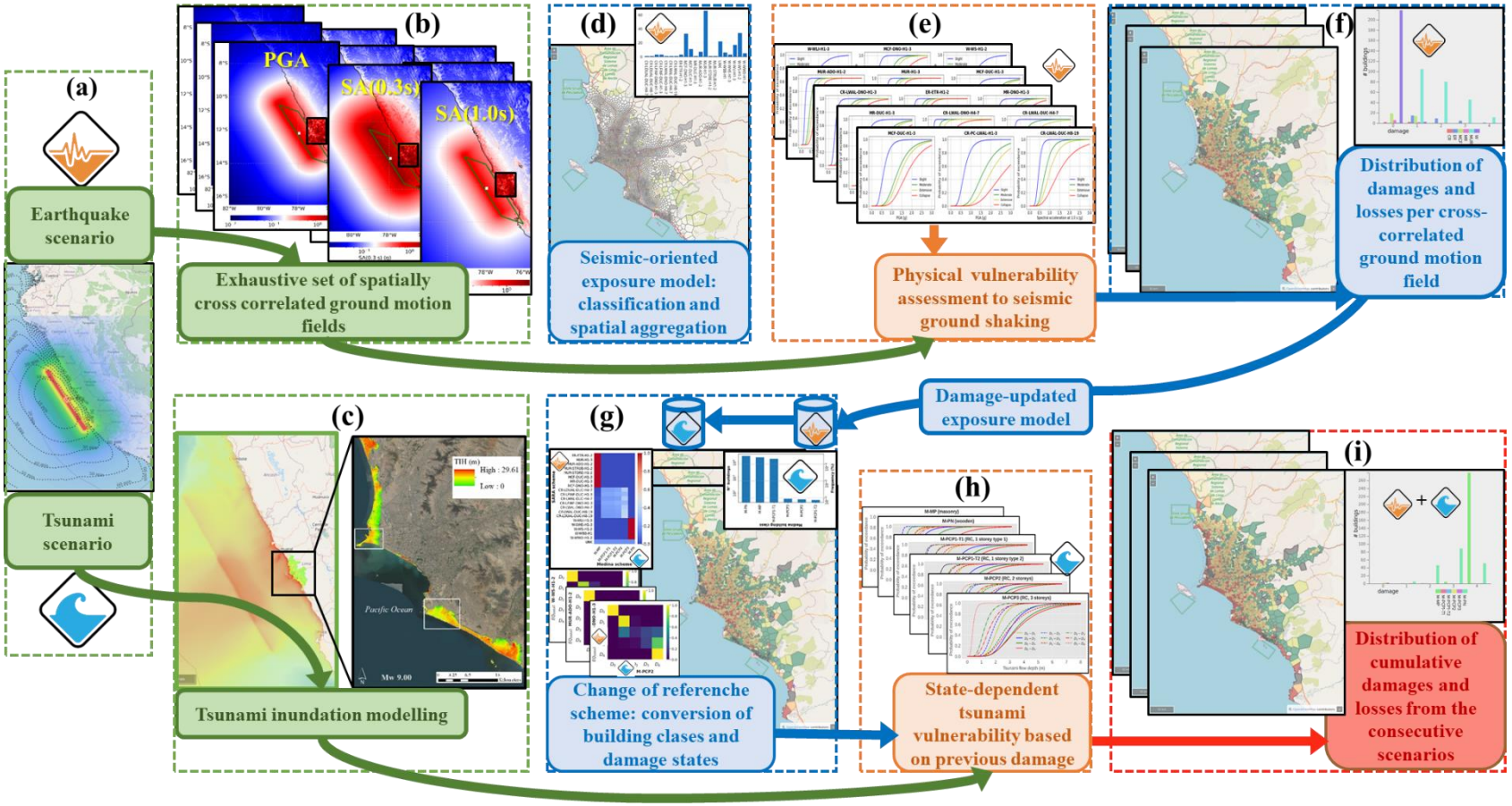

Figure 5-11. Proposed workflow for multi-risk assessment in Lima from each pair of consecutive earthquake and tsunami scenarios. A Mw 8.8 event is displayed as an example (subplot a). The processes regarding the natural hazardous events are highlighted in green. Blue and orange indicate the exposure and vulnerability processes, respectively. The spatially cross-correlated ground motion fields (subplot b) and an initial exposure model (with earthquake-oriented classes, in subplot d) are inputs for the seismic vulnerability process using analytical fragility functions for ground-shaking (subplot c), which provides the damage-updated exposure models (subplot f). The reference scheme conversion processes (building classes and damage states shown in subplot g) that generate the sets of damaged-exposure models are, together with the tsunami inundation models (subplot e) the inputs used by the state-dependent tsunami fragility functions (subplot h) to finally obtain the distribution of cumulative damages and losses (red box in subplot i)

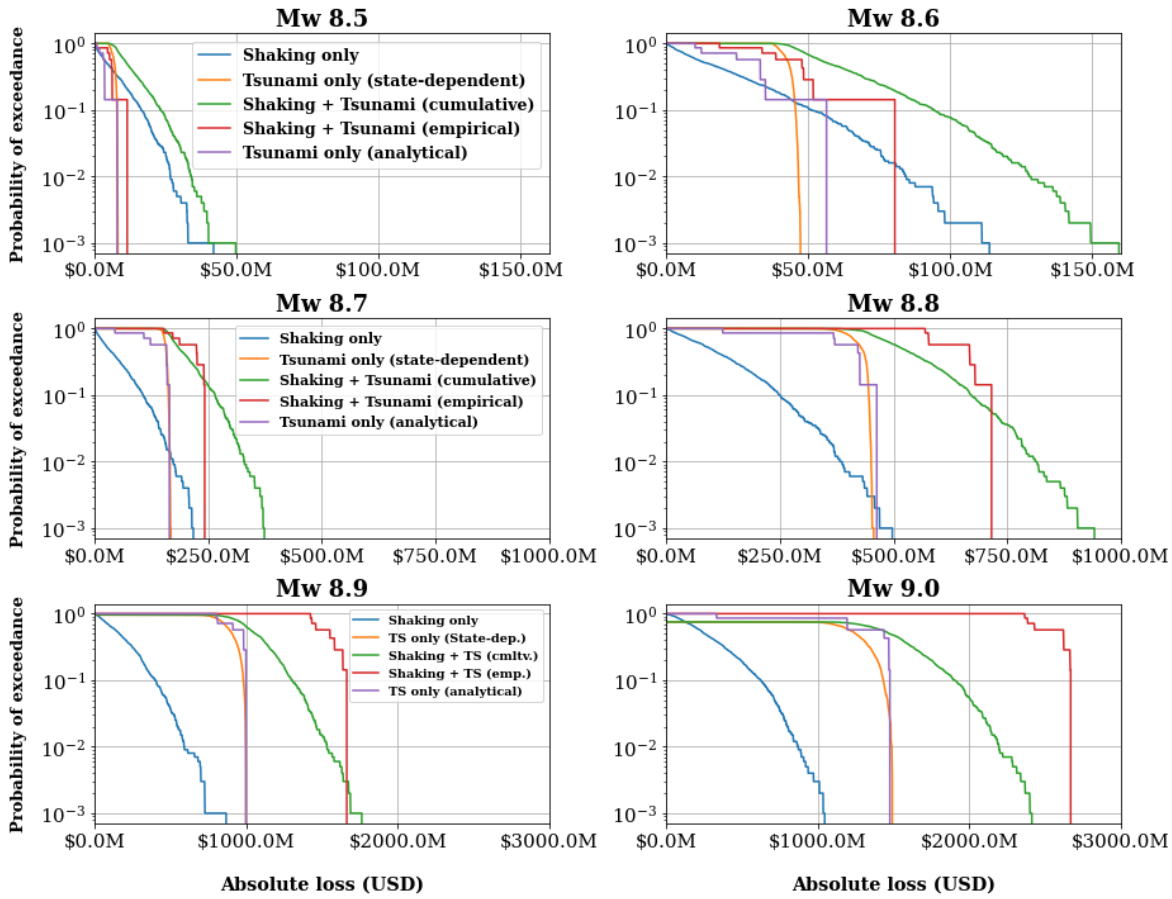

Figure 5-12. Five loss exceedance curves for the residential building portfolio of Lima are presented in six subplots per earthquake magnitude scenario (M_w (8.5-9.0). Three out of the five curves represent the disaggregated losses per hazard event: shaking-induced losses only (blue); far-field tsunami-induced losses (initial undamaged state, purple); state-dependent tsunami-induced losses (with pre-existing shaking induced damage, orange). The green curves represent the losses expected from the cascading sequence. The red ones show the losses derived solely using empirical tsunami fragility functions (implying that they have an implicit contribution by the earthquake phase)

4. Disaggregated losses of the tsunami event obtained after using state-dependent fragility functions (orange curves). They represent the direct losses which were only derived from the updated exposure model (i.e., with non-zero damage states)). This means that these curves only represent the disaggregated tsunami-induced losses for buildings that have already experienced earthquake-related damage. These loss exceedance curves are constructed using Eq. 5-13. Thus, this procedure implied the inter-scheme building conversion $p\left(T_k^A \middle| T_j^B\right)$ derived in section 5.3.1, the inter-scheme damage state conversion $p\left(D_{kz}^A \middle| D_{jy}^B\right)$ obtained in Sect. 5.3.4, as well as the state-dependent tsunami fragility functions constrained in Sect. 5.3.5.
5. Cumulative losses induced by the ground-shaking and tsunami sequence (green curves). They represent the losses obtained by adding the shaking-induced losses (blue curves) with the aforementioned disaggregated tsunami-induced losses (orange curves), that is, the outcome of the method proposed in this paper. These green curves represent, according to our approach, the likely losses that would be expected from each magnitude-dependent scenario-based cascading sequence over the considered building stock.

Hereafter we describe some observations that arise from Figure 5-12:

1. The resultant losses obtained after having used the two sets (empirical or analytical) of tsunami fragility functions (while assuming initial undamaged states) are profoundly different. As expected, the use of the empirical tsunami fragility model (red curves) is, for all the magnitudes, leads to

larger values in comparison with the values obtained from the analytically derived fragility functions (purple). These differences increase with magnitude. This feature might arise, not only from the fact that empirical fragility functions consider both earthquake and tsunami actions while the purple curves consider only the effects of the tsunami, but also because empirical fragility functions only account for flow depth as the IM. Conversely, the analytical fragility functions implemented were derived using the theoretical forces associated with the flow velocity tsunami waves as input in the generating numerical model. Similar observations regarding the reduction in the loss estimations when flow velocity is included have been drawn by other studies (e.g., Attary et al., 2019; Park et al., 2017).

2. We observe that the ground-shaking dominates the losses at lower magnitudes (Mw 8.5, 8.6), whilst the tsunami, either from analytical (emulating far-field tsunamis) or empirical fragility functions (near-field tsunamis), controls the losses for the rest of the scenarios with larger magnitudes. The former is aligned with the observations of Goda and De Risi, (2018) and (Gómez Zapata et al., 2021f) for the case of empirical tsunami models. Moreover, a similar trend is observed for the disaggregated tsunami-induced losses (assuming initial non-zero damage) whose respective loss values (orange curves) are larger than the shaking-induced losses for M_w 8.8, 8.9, and 9.0. Hence, these features highlight that as the magnitude increases, there is an increasing comparative importance of the tsunami risk within the considered sequence of hazards.
3. Expected loss values from cumulative damages based on single-hazard vulnerability models (our method, green curves) are clearly different from the one produced by classical empirical tsunami models. Classical empirical tsunami fragility functions lead to considerable lower losses estimations for the low magnitudes earthquakes and substantial larger estimations for the larger ones.
4. The differences between the loss exceedance curves derived from both sets of analytical fragility models (either from undamaged or with pre-existing damage) are larger for the lower magnitudes (M_w 8.5, 8.6) and decrease with increasing magnitude. As the magnitude increases, there is an increasing tendency of convergence between these two loss curves (M_w 8.9, 9.0).
5. Consequently, since tsunami-induced losses either from analytical fragilities (initial undamaged states) or from state-dependent and inter-scheme models converge for the larger magnitudes (M_w 8.9, 9.0), their respective summations with the shaking-induced losses would be approximately similar at the largest probabilities of exceedance. Nevertheless, this observation needs to be better investigated through more exhaustive simulations of tsunami inundation per considered scenario.
6. Conversely, considering observation 3, (i.e., as the magnitude decreases, the differences between purple curves and orange curves increases), their respective summations with the shaking-induced losses will lead to very different results. Hence, this observation suggests that, although earthquake and tsunami structural responses can be separately approximated for very large magnitudes, it is still required to address cumulative damages from the vulnerability interactions that are expected on the lower magnitudes earthquakes we have considered (i.e., M_w. 8.5, 8.6).

When we consider analytical fragility functions with D_{k0}^{A} that only emulate the damaging actions of far-field tsunamis (without any ground shaking), we observe that as the magnitude increases, their respective loss exceedance curves converge with the ones that assumed state-dependency (D_{kz}^{A}). This is because, for the larger magnitude events, the damaging actions due to seismic ground shaking will correspondingly increase. Hence, the available probabilistic damage transitions from the damage states within the earthquake (source) to tsunami (target) schemes will be consequently reduced. Therefore, we observe that if far-field analytical tsunami fragility functions are used, their corresponding results will be very much alike, regardless of whether they are considered as being undamaged (D_{k0}^{A}) or with pre-existing damage (D_{kz}^{A}). Therefore, for these larger magnitude events, regardless of which curve is summed up with the shaking-induced losses, the resulting loss distributions for the hazard sequence would lead to

quite similar results. Thus, the implementation of state-dependency on tsunami fragility may not be fully necessary to be addressed for very large earthquake magnitudes (M_w 8.9, 9.0). This observation is aligned with studies (i.e., Petrone et al., 2020; Rossetto et al., 2018) that suggest that earthquake and tsunami structural responses can be separately approximated. However, the former statement would not apply to the low magnitude earthquakes investigated in Lima for which the pre-existing damage due to earthquakes must be addressed. No generalizations should therefore be done in this regard, with sensitivity analyses needing to be carried out in the future.

5.5. Discussion

This study has proposed a modular method to disaggregate the direct losses expected for building portfolios exposed to consecutive hazardous scenarios of different natures in which their individual components could be individually improved. Therefore, future sensitivity analyses on some of the modules related to damage-state would benefit the understanding of how their embedded uncertainties would impact their corresponding results. We can mention:

1. The disaggregation of building classes into taxonomic attributes as presented in Sect. 5.2.1 is an important input to obtain the probabilistic inter-scheme compatibility matrices based on (Gómez Zapata et al., 2022b). However, it is worth noting the shortcoming described by Charvet et al., (2017) referring to the generalised poor taxonomic building characterizations of the currently available tsunami fragility models. They are, most of the time, only based on their main construction material, although sometimes they include the number of storeys, and rarely do they include other attributes such as the date of construction (e.g., Suppasri et al., (2015). When more enriched descriptions for tsunami vulnerability get available in the future, this approach will remain useful for similar purposes.
2. When/if local high quality empirical data collection and analytical models), become available, they could be used to constrain the relationships between the failure mechanisms and attribute relevance for hazard-related susceptibilities. This might contribute to enhance the construction of heuristics that characterise the likely observable damage extent (per damage limit state, building type and hazard-dependent fragility model), that could be obtained through more refined approaches such as unsupervised machine learning. Its use applied on real datasets that document observations on building components (even different from the ones presented in Eq. 5-5) could contribute to refine state-dependent tsunami fragility functions and to restrict the heuristics on the likely observable damage (Sect. 5.2.1) and thus, minimizing subjective expert judgment. In this sense, it is worth noting that the set of predicted likelihood probabilities in the probabilistic compatibility degree between damage states from different hazard fragility functions that we derived from the synthetic datasets created through the heuristics and the AeDES scoring system are not unique, as they depend on the choice of machine learning technique and on the heuristics derived through expert elicitation. In this sense, we have documented a preliminary sensitivity analysis on such parametrization in Gómez Zapata et al., (2022c). However, further investigation of the impact of such parametrization is still advised.
3. As described by Hill and Rossetto, (2008), we have observed that, when characterising damage states due to the impacts of natural hazards on buildings, there is still the need for standardisation in describing observable physical damage after any kind of hazardous event through the harmonisation of damage scales for data collection, not only on entire building units but also regarding the particular damage (and extent) experienced by certain individual components. In this regard, although we have used the AeDES scale, other damage scales could be more suitable to describe the observable damage to some building classes than for others (Hill and Rossetto, 2008; Turchi et al., 2022). Nonetheless, the choice of a standard scale to transversally describe any observable set of damage on

buildings will benefit the research in multi-hazard vulnerabilities.

4. The integration of economic consequence models for physical vulnerability based on the replacement costs as a function of the buildings' area, as for instance presented in Triantafyllou et al., (2019) for tsunami vulnerability is worth testing. This also depend on the available data and it is out of the scope of this paper, but it would be worth exploring their contribution once more refined estimations about replacement cost are available for Lima. Nevertheless, one should be aware on the uncertainties involved for large scale building exposure models.
5. The derivation of the hazard intensities could also benefit from future enhancements. For instance, the GMPE-based seismic accelerations derived on a simplified Vs_{30} site-grid of ~1 km might be too coarse to capture local site effects in the expected ground motions. However, the performance of site-response analyses that account for the local geotechnical soil properties of site-specific soil profiles, as for instance reported by Aguilar et al., (2019), is a computationally demanding task that is out of the scope of this study, but when integrated it could benefit the overall quality of seismic risk calculations for the study area. Complementary, we strongly advise the physical to generate exhaustive sets of cross-correlated-ground motion fields (at the required spectral periods by the buildings classes) to address their aleatory uncertainty. The selection of this model, among the available ones, carries epistemic uncertainties.

It is worth noting that the variability of the loss exceedance curves obtained for the cumulative damage (due to tsunamis) was derived from the damaged exposure models subjected to each realisation of cross-correlated ground motion fields (i.e., orange curves in Figure 5-12). Therefore, investigating the impact of other tsunami vulnerability and hazard data products (Behrens et al., 2021), which was beyond the scope of this paper, are nonetheless worth exploring. When such parametrisation in the tsunami data products becomes available for Lima, future studies could provide dimensionality of the contribution of the tsunami hazard upon the outlined method for scenario multi-risk estimates.

For the commonly exposed residential building stock of Lima exposed to both perils, we have observed that assuming initial undamaged states in the selected tsunami empirical fragility functions leads to large underestimations for lower magnitudes (M_w) and large overestimations for larger M_w events in comparison to when state-dependent models were used. Hence, the initial "undamaged state" assumption used to assess the tsunami vulnerability in former studies (e.g., Adriano et al., 2014; Gómez Zapata et al., 2021e) may not be completely accurate to represent the losses expected after this type of cascading sequence. This is because such an assumption misses the calculation of earthquake-related damage which is an important input needed to assess cumulative damage and losses through state-dependent analytical fragility models. On the other hand, adopting the larger value between independent earthquake and tsunami risk computations proposed by Goda and De Risi, (2018) may lead to better correspondence with our model (mostly for the lower M_w events) than the sole use of the selected non-state dependent analytical fragility functions.

To give a perspective on the importance of addressing cumulative damage and losses for building stocks, let us recall some of the findings that the available studies of Gómez Zapata et al., (2021e) and Markhvida et al., (2017) found. They investigated the likely economic losses of the entire residential building portfolio Lima and Callao solely after seismic ground motion from a M_w 8.8 scenario addressing the variability induced by the same cross-correlation model we have implemented herein. In the first study, ~1,657,635 residential buildings were considered and both studies considered the SARA building classes and fragility functions, similar to what we have done. Both studies reported mean loss values of around 7 and a maximum of around USD 35 billion (among a stochastic sample of events). It is then interesting to compare such a range of values with the mean loss values reported for a similar M_w (Fig 11-d). Notably, the forecasted losses per event (shaking and tsunami) and inferred from cumulative damage were derived from the much smaller commonly exposed building stock to each pair of hazard scenarios (see Fig 8-c), which constitute ~ 21,209 buildings. This means that the building count for the entire residential stock of Lima (Fig 6-a) is around 78 times larger than the commonly exposed to both perils (Fig 6-b). Hence, can note the important

role of tsunami-induced losses in the study area. The mean losses expected from the cascading sequence of that M_w 8.8 (i.e. value for the 50th percentile on the green curve in Fig. 11b) is ~ USD 0.75 billion and a maximum of around USD 0.94 billion. Therefore, given the difference between the size of both building portfolios, finding out that the losses for the entire city are expected to be only 9 times larger than the ones forecasted after the action of both earthquake and tsunami, tells us that the crucial importance of carefully addressing the cumulative damage due to tsunami in the study area. Moreover, this tell us that, besides all of the secondary effects of the tsunami, these types of future scenarios in Lima will constitute a huge driving source of direct economic losses for building portfolios, but also uncertainties due to the lack of data to calibrate or validate these types of risk assessment after the action of cascading hazards.

5.6. Conclusions

We have proposed a modular method that allows us to consistently re-use existing single hazard fragility models that are being developed by experts in various research fields and integrate each other for multi-hazard risk assessment for extended building portfolios. This integration aims for the probabilistic harmonisation of diverse hazard-dependent building classes and damage states which are included in their associated fragility functions. Through this integration, we aim to provide an alternative approach to conventional ones (e.g., HAZUS-MH (FEMA, 2003, 2017)) that consider a single building class with sets of fragility functions for a variety of hazards. In this sense, the method we have developed can be particularly useful to assess the cumulative damage in hazard sequences of different natures and forces that might induce various failure mechanisms upon the exposed buildings. Thereby, the presented integrative method contributes to reducing the existing gaps due to the typical lack of collective calibration and validation of multi-hazard risk methods. This is due, for instance, when triggered events act on damaged assets right after the first hazard or even simultaneously experiencing compound hazards with no time for damage reconnaissance or disaggregation of the damage features induced by the individual hazards.

We have proposed a modular method composed of the following components:

1. The selection of existing hazard-dependent vulnerability schemes to model the building portfolio under each hazard-dependent vulnerability scheme of interest. They contain sets of building classes and associated fragility functions. To model the physical vulnerability of the building portfolio towards the triggering event (in this case, earthquake), no preference on whether empirical or analytical fragility functions should be used.
2. On the other hand, to model the physical vulnerability of the building stock towards the triggered event, sets of state-dependent fragility functions must be derived for each building type within the selected scheme. For this purpose, it is important to use models that do not involve the damaging effects of the triggered event as the starting point. (i.e., avoiding empirical models and using analytical ones). This proposal overcomes the assumption of initial undamaged states for the structures exposed to the triggered event and allows to account for the differential cumulative damage between hazards.
3. The characterisation of building classes through their disaggregation into building taxonomic attributes. This description allows the harmonisation between the building classes belonging to different hazard-dependent vulnerability schemes through the probabilistic inter-scheme compatibility matrix proposed in Gómez Zapata et al., (2022b).
4. The exposure models are spatially aggregated into optimal geographic entities (i.e. CVT-based models) that account for the spatial variability of low-correlated hazard IM in their derivation (Gómez Zapata et al., 2021f). This selection was taken due to performance purposes only, but a more refined block-based model could also have been used.
5. A generalized description of the damage states based on a set of observable damage types on individual building components. This is done through a scoring system based on an underlying common scale (employing, for example, the AeDES form) that ultimately allows us to get the damage-state inter-scheme conversion. We use the total probability theorem, a Bayesian formulation, and machine learning techniques.
6. The vulnerability assessment for sequences of cascading hazards scenarios through the proposal of consistent economical consequence models across hazard-dependent vulnerability

schemes. They must define replacement cost ratios per damage state and per fragility function associated with each vulnerability scheme.

The joint combination of these components creates a method to update the damage states throughout the multi-hazard sequence while allowing us to exploit existing hazard-specific risk-oriented taxonomies (i.e., building classifications with corresponding fragility functions and defined damage states) available in the literature for a wide range of natural hazards. This is a modular method in which each one of their individual components can be separately customized when seeking future improvements.

When applying this method on the residential building stock of Lima (Peru), we have observed, on the one hand, that considering the risk metrics from tsunami vulnerability only from the selected set of empirical fragility functions (derived from near-field tsunamis) as representative of the shaking and tsunami sequences leads to underestimations for the lower magnitudes. On the other hand, we have observed overestimations for the larger magnitude scenarios in comparison with the state-dependent method that accounts for the accumulated damage due to the former earthquake solicitations. We have observed that the use of the proposed method to assess the cumulative damage is more relevant for the lower magnitude scenarios than we have considered (M_w 8.5 and 8.6). This might be due to the greater damage extension on the exposed buildings that is expected from the seismic demands in comparison with those imposed by their corresponding tsunamis, and thus, there is greater chance to obtain cumulative damage. On the contrary, for larger magnitudes, the use of state-dependent fragilities and analytical functions assuming no pre-existing damage are converging, and thus, the importance of assessing state-dependency is reduced.

Considering the limitations and simplifications assumed in this study, we are not claiming that the resulting economic losses we have calculated for the residential building stock of Lima from multi-hazard scenario-based risk computations are totally exhaustive. Thus, caution should be taken with the interpretation and extrapolation of these conclusions to other study areas and combinations of models. Nevertheless, awareness of these uncertainties for the reliable quantification of risk towards these cascading hazards is increasingly important to enhance mitigation strategies for disaster risk reduction (Imamura et al., 2019). Furthermore, it is worth recalling that the method herein proposed has been exclusively designed for spatially extended residential building buildings as a proof of concept for integrating existing fragility models. We do not provide an\ complete validation of multi-vulnerabilities approaches, but rather we offer a holistic and novel harmonising method to track such dynamics in a consistent manner. Hence, our method is not meant to replace more detailed analytical analyses required to determine the structural response of individual buildings subjected to seismic and tsunami loading (e.g., Petrone et al., 2017; Rossetto et al., 2019).

Code and data availability.

The data used in the elaboration of this study are available in open repositories. The scenario-based ground motions and tsunami inundation maps are available in Gómez Zapata et al., (2021c); Harig and Rakowsky, (2021), respectively. The first set was calculated making use of the Shakyground script (Weatherill et al., 2021) which relies on the OpenQuake Engine (Pagani et al., 2014), whilst the second set was calculated using the TsunAWI software. The exposure and fragility models for both hazard-vulnerability schemes (earthquake and tsunami) are available in Gómez Zapata et al., (2021a, b) and were adapted to fulfil the data formats required by the scripts provided by Assetmaster and Modelprop (Pittore et al., 2021). They were used as inputs for the scenario-based seismic risk assessment (Sect. 1.2.1) using the DEUS software (Brinckmann et al., 2021). The scenario-based risk estimates for earthquakes and tsunami using analytical and empirical fragility functions respectively are provided in Gómez Zapata et al., (2021d). State-dependent analytical tsunami fragility functions used in this study are available in Gómez Zapata et al., (2022a). The set of inter-scheme damage compatibility matrices used in this study are provided in Gómez Zapata et al., (2022c).

Acknowledgments.

The authors want to express their gratitude to Andrey Babeyko, Michael Haas, Michael Langbein, Giuseppe Nicodemo, Cecilia Nievas, Juan Páez-Ramírez, Juan Palomino, Matthias Rüster, and Sandra Santa-Cruz for their support during the elaboration of this study. Thanks to Sven Harig and Natalja Rakowsky for having provided us with the tsunami inundation models for Lima. We also thank Henning Lilienkamp and Graeme Weatherill for their support with the simulation of spatially correlated ground motion fields and machine learning techniques. We thank Kevin Fleming for the careful proofreading.

Funding. This research was funded by the RIESGOS and RIESGOS 2.0 projects, funded by the German Federal Ministry of Education and Research (BMBF), with Grant No. 03G0876A-J and 03G0905A-H, respectively. These projects are part of the funding programme CLIENT II – International Partnerships for Sustainable Innovations'.

Chapter 6

6. Community Perception and Communication of Volcanic Risk from the Cotopaxi Volcano in Latacunga, Ecuador

Abstract

The inhabitants of Latacunga living in the surrounding of the Cotopaxi volcano (Ecuador) are exposed to several hazards and related disasters. After the last 2015 volcanic eruption, it became evident once again how important it is for the exposed population to understand their own social, physical, and systemic vulnerability. Effective risk communication is essential before the occurrence of a volcanic crisis. This study integrates quantitative risk and semi-quantitative social risk perceptions, aiming for risk-informed communities. We present the use of the RIESGOS demonstrator for interactive exploration and visualisation of risk scenarios. The development of this demonstrator through an iterative process with the local experts and potential end-users increases both the quality of the technical tool as well as its practical applicability. Moreover, the community risk perception in a focused area was investigated through online and field surveys. Geo-located interviews are used to map the social perception of volcanic risk factors. Scenario-based outcomes from quantitative risk assessment obtained by the RIESGOS demonstrator are compared with the semi-quantitative risk perceptions. We have found that further efforts are required to provide the exposed communities with a better understanding of the concepts of hazard scenario and intensity [e]

[e] published as: Gómez Zapata, J.C; Parrado, C.; Frimberger, T.; Barragán-Ochoa, F.; Brill, F.; Büche, K.; Krautblatter, M.; Langbein, M.; Pittore, M.; Rosero-Velásquez, H.; Schoepfer, E.; Spahn, H.; Zapata-Tapia, C. 2021, Community Perception and Communication of Volcanic Risk from the Cotopaxi Volcano in Latacunga, Ecuador. Sustainability, 13, 1714. https://doi.org/10.3390/su13041714

6.1. Introduction

An active volcanic environment is prone to produce cascading and compound natural hazards. Cascading hazards comprise a primary hazard triggering a secondary one (Gill and Malamud, 2016), whilst compound hazards refer to events (not necessary interdependent) events whose spatiotemporal footprints overlap (i.e., they occur almost simultaneously and affect the same -or neighbouring- locations) (Pescaroli and Alexander, 2015). For instance, increasing volcanic activity can occur in company with seismic activity and continuous gas emissions, lightning, and ultimately trigger lava flow, pyroclastic density currents, tephra (including volcanic ash and ballistics), debris avalanches (sector collapse), tsunami (for submarine volcanoes or at the seaside), and lahars (Ward et al., 2020). Syneruptive lahars (also called primary lahars) can happen due to glacier melting during a volcanic eruption, whilst secondary lahars are commonly triggered by heavy rainfalls (Cando-Jácome and Martínez-Graña, 2019; Mothes and Vallance, 2015). The forecast of cascading and/ or compound volcanic hazards is very diverse and with time dependencies. Models are heavily tailored towards the specific volcanic system (Merz et al., 2020). To explore the possible consequences before the actual occurrence of the events, risk scenarios are instrumental for risk communication practises. A risk scenario, as stated in Li et al., (2016), is considered as a situation picture in which a hazardous event with a certain probability would occur and cause some damage. The appropriate communication of risk scenarios, can ultimately contribute to territory planning, response planning, design of evacuation routes, and enhance overall preparedness.

Consequences of volcanic events can be severe, especially when the affected community is not well prepared. One of the most widely-known examples of physical damage on assets and human losses due to a lack of effective risk communication occurred during the 1985 eruption of Nevado del Ruiz volcano in Colombia, during which 25,000 people died due to primary lahars (Lowe et al., 1986; García and Mendez-Fajury, 2018; Pierson et al., 1990). However, volcanoes do not only affect the communities in their proximities but have also generated systemic infrastructure failures and cascading effects on a large-scale. A clear example of this type of effects occurred during the eruption of the Eyjafjallajökull volcano in Iceland. During two months in 2010, about 100,000 flights between Europe and North America were cancelled due to the sustained ash emission, causing more than $1.7 billion losses in lost revenues for airlines (Bolić and Sivčev, 2011). A further example of volcanic multi-hazard risk is the 2018 eruption of the Anak Krakatau volcano in Indonesia, which induced its own flank collapse, triggering a tsunami that resulted in the death of 430 people mostly in the western area of Java Island (Walter et al., 2019). A tsunami threat from the Krakatau volcano was not unknown since a similar historical event happened in 1883. However, it was not taken up in a broader discussion on how to deal with such a risk scenario (Tsunami hazard and its challenges for preparedness).

Monitoring of volcanic activity has been significantly improved in recent years through denser and widespread networks (Poland and Anderson, 2020; Biass et al., 2014). Moreover, there have been increasing research activities on the interaction between volcanic hazards (e.g. Zuccaro et al., 2008). However, the impacts caused by volcanic hazards are rarely assessed in a comprehensive manner due to the lack of worldwide unified exposure models (Pittore et al. 2017) and the scarce damage data collection on the exposed assets needed to constrain vulnerability models (Merz et al., 2020). These difficulties are even more pronounced in a multi-risk context, where there is still a gap in the investigation of the interactions at the vulnerability level (Gallina et al., 2016). Hence, only a few examples of quantitative damage assessment have been reported in the scientific literature (e.g. Gehl et al., 2013; Zuccaro and De Gregorio, 2013). Furthermore, there is a lack of tools for simulating representative volcanic scenarios in order to analyse the extent and spatial distribution of the expected consequences, needed for decision making and planning. Therefore, scenario-based approaches for a volcanic multi-hazard risk environment are not always available or might not be effectively communicated to the exposed communities before the occurrence of a volcanic crisis (Doyle et al., 2014b). On the one hand, setting up these methods in a consistent scenario-based approach is a challenging task in its own. On the other hand, effectively communicating the potential direct damages and losses and the associated likely disruptions of critical infrastructure is also a daunting task which depends on the availability of scenario-based risk outcomes.

Rural communities of economically developing countries are particularly prone to encounter more difficulties throughout every single step of the multi-hazard risk chain (e.g. Li et al., 2020; Ran et al., 2020). The social vulnerability perception of rural inhabitants might not be always taken into consideration by the local planners, partially due to their remoteness, i.e. typical large distances from the main urban centres (Papathoma-Koehle et al., 2020), or socio-economic factors such as their alphabetization level (Parham et al., 2020), poor access to information systems or even the basic lack of knowledge of what potential hazards may impact their communities (Papathoma-Köhle et al., 2019). These characteristics are common in areas exposed to volcanic hazards. In 2015 roughly 415 million people, most of them located in rural areas, lived within a 100 km radius from the 220 active volcanoes listed in the *'NOAA Significant Volcanic Eruption Database'* (NCEI/WDS Global Significant Volcanic Eruptions Database. NOAA National Centers for Environmental Information. doi:10.7289/V5JW8BSH., 2020). Hence, rural communities worldwide are more prone to suffer damaging effects from volcanic eruptions (Pesaresi et al., 2017). These consequences are not only expected to impact individual components such as buildings (Jenkins et al., 2014) and agricultural fields (Craig et al., 2016), but also critical infrastructure (e.g. power networks, roads, and water supply systems) for which the evaluation of systemic vulnerability is also required (Wilson et al., 2017, 2014).

Cascading effects may further drastically change the health quality, as well as economic and social activities of the exposed communities (Terzi et al., 2019). For example, the continuous emissions of volcanic ashes can interrupt agro-industrial activities, which are the most typical source of income of rural communities (Thompson et al., 2017). These communities may also experience low serviceability of lifeline networks (Deligne et al., 2017) and/or suffer from physical isolation from neighbouring communities, e.g. due to damaged bridges. Only in a few cases, the cascading effects due to volcanic eruptions have been analysed in a systematic manner (Scaini et al., 2014). Therefore there is an urgent need to effectively communicate the scientific results of a volcanic risk assessment while simultaneously addressing the social perception and understandings, by the exposed communities, of different risk factors (Doyle et al., 2014a). As stated in Thomalla et al., (2018), clear risk communication in all the components of a multi-risk chain (i.e. hazards, exposure, physical and systemic vulnerabilities) with the directly exposed communities, local decision-makers and planners is fundamental to construct more resilient communities.

Although community participation is considered an essential component of effective resilience planning to natural hazard-risks (Horney et al., 2016; Kwok et al., 2018), only in recent years some studies have integrated scientific approaches with the active participation of the community, local planners, decision-makers and actors of the civil society (e.g. Lévy, 2014; Pescaroli, 2018; Heinzlef et al., 2020a; Gill et al., 2020; Fleming et al., 2020). The specific community perceptions of vulnerability and risk related to volcanic hazards have been investigated in former works (e.g. Bronfman et al., 2016; Jóhannesdóttir and Gísladóttir, 2010; Leonard et al., 2014; Paton et al., 2008) through "top-down" approaches. In Pierson et al., (2014) it was suggested that scientists should have a transversal role and a stronger presence in the communication of volcanic hazards and risks from "bottom-up" approaches. To the best authors' knowledge, these practices have been documented in a few works for rural communities (i.e. Armijos et al., 2017; Hicks et al., 2017). Hence, we can realise that there is still significant work to be carried out to strengthen the risk-informed communities exposed to volcanic hazards. With this background, we present throughout this work an integrative framework between scientific approaches that study the possible damaging effects from volcanic scenarios with the local knowledge and social risk perceptions. The study area of Latacunga, capital of the Cotopaxi province in Ecuador, with mainly rurally composed communities, and exposed to the Cotopaxi volcano has been investigated in order to enhance a risk-informed community, awareness, and contribute to increasing their resilience.

6.2. Framework and objectives

Volcanic eruptions pose an enormous risk to Ecuador because most of the exposed human settlements in the central and northern highlands are situated less than 25 km from an active volcano. Cities previously affected by volcanic eruptions include Quito, Latacunga, Salcedo, Cayambe, Ibarra-Otavalo, Ambato, Riobamba and Baños (Lupiano et al., 2020). Lahars have been among the deadliest volcanic hazards, but the emission of volcanic ash has been more frequent in the Ecuadorian Andes (Bernard et

al., 2016). Ash falls do not only have direct consequences on the inhabitants' health and on the exposed infrastructure, but also on agriculture and animal husbandry which is particularly important for the rural communities in Ecuador. Ash falls have hit the rural communities settled in the vicinity of the most active Ecuadorian volcanoes (i.e. Tungurahua, Reventador, Sangay and Cotopaxi). Moreover, poverty, marginality and high inequality of the exposed communities coexist with their physical and systemic vulnerabilities (Frontuto et al., 2020).

6.2.1. Description of the study area

The Cotopaxi volcano is an active stratovolcano (5897 m.a.s.l) located in the Cordillera Real of the Ecuadorian Andes (Figure 6-1) and is covered by an extensive, but diminishing glacier cap. Cotopaxi is one of the most dangerous volcanoes worldwide (Rodriguez et al., 2017) with average recurrence intervals for eruptions between 117-147 years (Barberi et al., 1995). It can produce syneruptive lahars triggered by explosive eruptions which can travel hundreds of kilometres (Hall and Mothes, 2008). Three drainage systems originate on Cotopaxi (Figure 6-3) which have all been inundated by lahars in prehistoric times (Sierra et al., 2019). However, only the northern and southern drainage are densely populated: The largest urban agglomeration encountered by the northern system is "El Valle de Los Chillos" (with about 400,000 inhabitants) in the vicinity of southern Quito; whilst the southern drainage system encounters the Latacunga canton (with about 300,000 inhabitants). The last major eruption of the Cotopaxi volcano in the historical records occurred in 1877. It induced syneruptive lahars that severely affected the proximal rural communities (Aguilera et al., 2004), with more than 1,000 deaths registered, and caused a severe economic crisis (Doocy et al., 2013). If a similar scenario occurred nowadays, the social and economic consequences would be far more catastrophic due to the high population density and the central importance of Latacunga and the Cotopaxi region for the economic development of the country (Rodriguez et al., 2017).

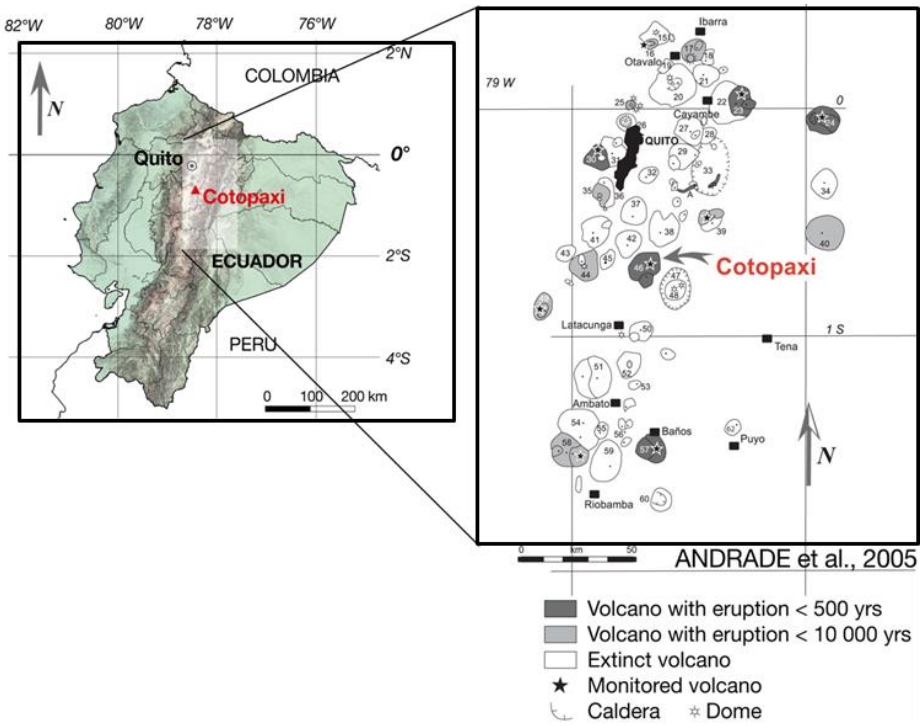

Figure 6-1. Location of the main volcanic systems in the Ecuadorian Andes highlighting the location of the Cotopaxi volcano and Latacunga. Modified after Andrade et al., (2005).

Latacunga is the largest city of the Latacunga canton (2nd Ecuadorian administrative division) and it is the capital of the Cotopaxi province (1st division). It is located at a 14 km distance from the Cotopaxi

volcano. For the year 2020, and based on the population projections of the National Institute of Statistics and Censuses (INEC, 2010), the city has an inferred population of approximately 205,600 inhabitants, with a major rural composition (59.8%). The last peak of volcanic activity of the Cotopaxi volcano occurred in mid-April 2015 and lead to a crisis in risk management in Latacunga and neighbouring municipalities (Czerny and Czerny, 2020). Firstly, an increase in the seismic activity of the volcano was accompanied by the emission of sulphur dioxide and ash fall for some weeks (Bernard et al., 2016). Subsequently, authorities and local press communicated to the inhabitants of the communities in the vicinity of the Cotopaxi volcano that it was necessary to evacuate their homes promptly due to the imminent occurrence of lahars (Czerny and Czerny, 2020). This generated social chaos due to the ignorance of the evacuation routes, the uncontrolled behaviour of the citizens (due to generalised fear of looting) as well as a very low level of trust in government representatives (Christie et al., 2015). Eventually, the 2015 activity never surpassed a magnitude VEI 2 and no large syneruptive lahar flows occurred (Mothes et al., 2019). The lesson learned from this experience was the need for adequate evacuation protocols and local authorities with an understanding of the complexity of the risk in the area. Moreover, it was realized how important it is for citizens to understand their own social, physical, and systemic vulnerability (Mothes et al., 2019).

Latacunga is settled on ancient and recent geological materials formed by volcanic material. Some of the most representative and better-exposed stratigraphic formations of ancient ashes and lahar deposits originated from the previous volcanic activity of the Cotopaxi volcano were visited (Figure 6-2) with the guidance of experts from the Geophysical Institute of the National Polytechnic School, IG-EPN) and the Decentralized Autonomous Government of the Province of Cotopaxi (GADPC, Gobierno Autónomo Descentralizado Provincial de Cotopaxi, Latacunga, Ecuador, GADPC). Some of these deposits are from pre-historical times whilst the shallower ones date from the 1877 event which destroyed Latacunga (Pistolesi et al., 2013). Official maps of the Geological and Energy Research Institute (IIGE) and IG-EPN (Mothes et al., 2016) were used during the field reconnaissance. This field trip was relevant to visualize the geological characteristics of the study area, as well as to strengthen the cooperation and idea exchanges with the local experts.

Latacunga is not only exposed to the natural hazards imposed by the Cotopaxi volcano, but also to other geodynamic (e.g. landslides and earthquakes) and hydro-climatologic hazards (e.g. frosts and droughts). As reported by Heifer Fundation, (2018), there has been an intensification in the variability of precipitations, droughts, and frosts in Latacunga. This has been evidenced in the period between the years 1981-2014, during which the average air temperature has increased about 0.8°C. These ongoing phenomena related to climate change have generated negative consequences mainly in the rural area and in agriculture areas (Heifer Fundation, 2018).

Figure 6-2. Left picture: Channel of the Cutuchi River in the city centre of Latacunga. An old textile factory is visible, which has been buried up to the fourth story by the 1877 lahar. Right picture: Thick sequence of lahar deposits, scoria flow deposits and tephra beds exposed in a quarry along the Rio Saquimala close to Mulalo. (Photos: Theresa Frimberger, 2018)

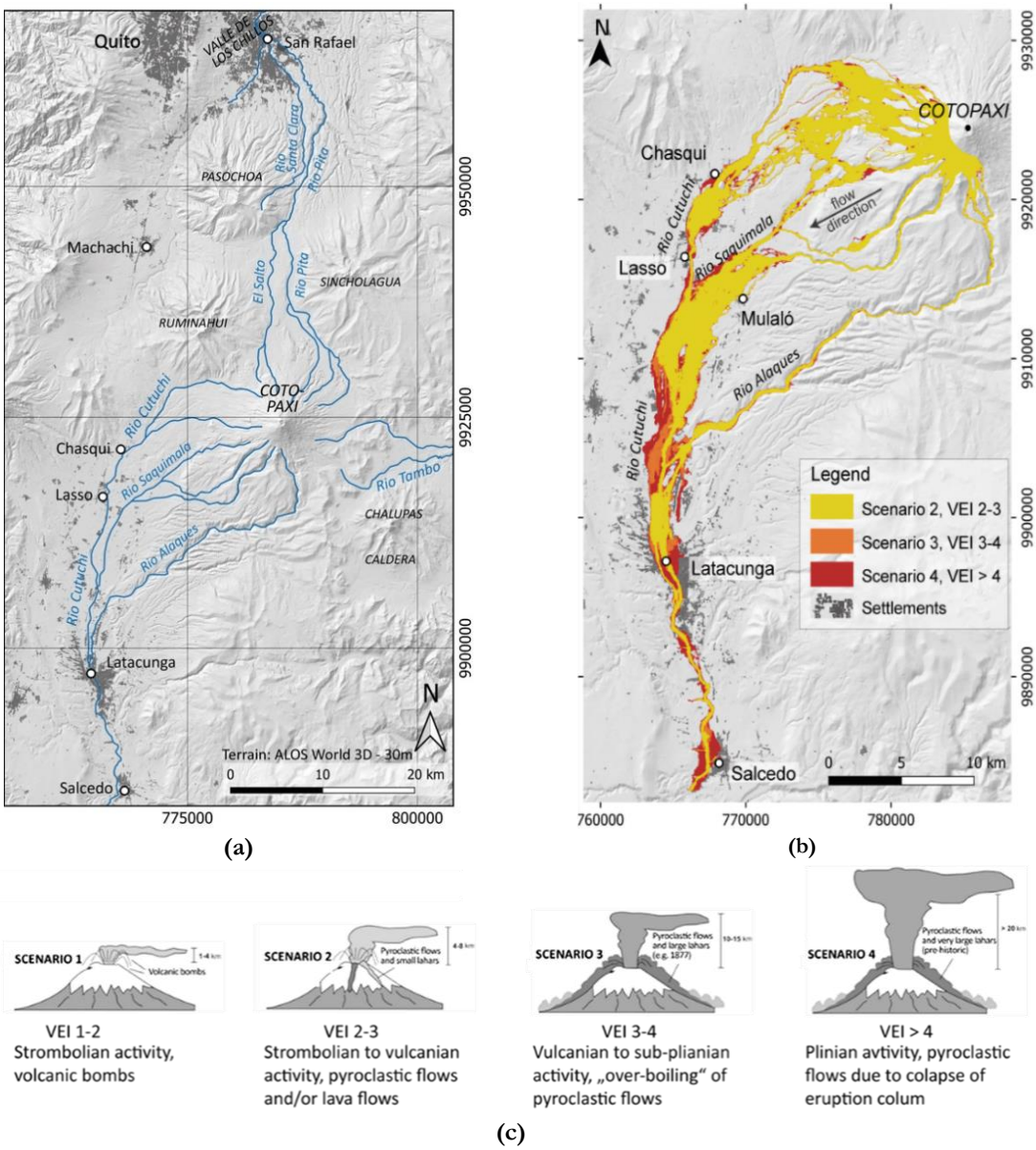

Figure 6-3. (a) Location of the Cotopaxi volcano and the main drainages and populated centres. (b) Estimated lahar footprints in the southern drainage system from three scenarios as function of the VEI (Volcanic Explosivity Index). (c) Brief description of the eruption scenarios expected at Cotopaxi in terms of the VEI. Modified after (Andrade et al., 2005; Frimberger et al., 2020).

6.2.2. Objectives

The understanding of disaster risk based on the independent investigation of their dimensions: hazards, exposure, vulnerability, guided by a multi-hazard risk approach with risk-informed decision-makers are key advice of the Sendai Framework for Disaster Risk reduction (2015-2030) (UNISDR, 2015). Having in mind the aforementioned limitations on volcanic risk assessment as well as the lack of exploration tools for risk communication, two initiatives, namely the programme *"Sustainable Intermediate Cities – CIS"*, and the research project *"Multi-Risk Analysis and Information System Components for the Andes Region – RIESGOS"* have been working in Latacunga, Ecuador with the aim of increasing awareness, preparedness, and enhance the coping capacities of the communities exposed to the Cotopaxi volcano. The particular objectives of this integrative study are:

1. To present a comprehensive risk communication process, from scenario-based volcanic risk analysis along with active participation of the exposed communities, while

also investigating the risk perception of the exposed communities.
2. Providing a recent measurement of spatially distributed risk perception in the Cotopaxi area (results from the CIS questionnaire)
3. Testing the applicability of the RIESGOS demonstrator, a decentralized web-service architecture that allows for integrating local expert knowledge and locally designed models in a scenario-based multi-risk analysis, for the purpose of interactive communication
4. Merging the results of 2 and 3 to investigate how well the simulated quantitative risk matches the subjectively perceived risk in a common area.

6.3. Materials and Methods

An integrative framework between scientific approaches and risk communication practices with the exposed society has been set up in Latacunga (Ecuador) by two different initiatives, (1) the CIS *(Sustainable Intermediate Cities)* programme and (2) the RIESGOS project *(Multi-risk analysis and information system components for the Andes region).*

6.3.1. The CIS programme: the creation of a local laboratory to evaluate the social perception of risk and resilience

"The Latacunga Laboratory: Risk management, resilience, and adaptation to climate change[1]*"* has been created within the CIS programme, as part of the joint initiatives of GIZ[2] and Grupo FARO[3]. The creation of so-called resilience observatories for exposed communities to natural hazards is a relatively new trend (Heinzlef et al., 2020a, b). Similarly, the Latacunga Laboratory seeks to contribute of the risk management to natural hazards that are likely to occur in the territory while aiming to contribute in the long-term to the development of the city embracing its urban-rural ties. With that goal, initial contributions related to social risk perceptions have been documented in Grupo FARO et al., (2020) as a joint effort between the Latacunga Laboratory, the local government, academic institutions, and local actors.

6.3.1.1. Comparative analysis of the social risk perception factors to natural hazards and the spatial distribution of volcanic-related risk factors

We conducted a survey by means of a custom-designed questionnaires, a fundamental tool for acquiring information on public knowledge of the community (Bird, 2009). It is composed of a series of multiple-choice questions in Spanish. The survey was carried out in the field and online to collect data about the individual knowledge, attitudes, and risk perceptions of the inhabitants of Latacunga. The online survey was promoted on social media and was available on the official website of the CIS Latacunga Laboratory[4] for a month. In the meantime, the field survey was carried out only in the urban agglomeration of Latacunga. The collected data is used for two main objectives: (1) As input to perform the semi-quantitative method proposed in Carreño et al., (2005) that ranks the social perception of volcanic risk factors (i.e. hazard recurrence, exposure, vulnerability, and resilience) among other natural hazards likely to occur in the study area (i.e. earthquakes, drought, frost, floods, and landslides). (2) Map the spatial distribution of volcano-related risk perception into comprehensive categories (i.e., easily understandable by the exposed communities).

A design of the field surveying site was carried out. According to the last official census available (INEC, 2010) and population projections by the survey elaboration date (September 2019), 50,442 inhabitants over the age of 18 years were considered as qualified informants. In order to get a statistically representative sample, a confidence level of 95% and a margin of error of 5% were selected. On this basis, we estimated that a sample for the field surveys not smaller than 380 inhabitants had to be selected. Considering 10% additional surveys, a final sample size of 420 people was chosen. The population density (Figure 6-4-a) was used to constrain the spatial distribution of the field surveys within the urban blocks with a residential occupancy (Figure 6-4-b). The surveys were carried out by 55 students of the ISTC (Instituto Superior Tecnológico Cotopaxi) in September 2019.

[1] Laboratorio Urbano de Latacunga: Gestión de riesgos, resiliencia y adaptación al cambio climático.
[2] "Deutsche Gesellschaft für Internationale Zusammenarbeit".
[3] Ecuadorian NGO (https://grupofaro.org/).
[4] https://latacungaresiliente.com/

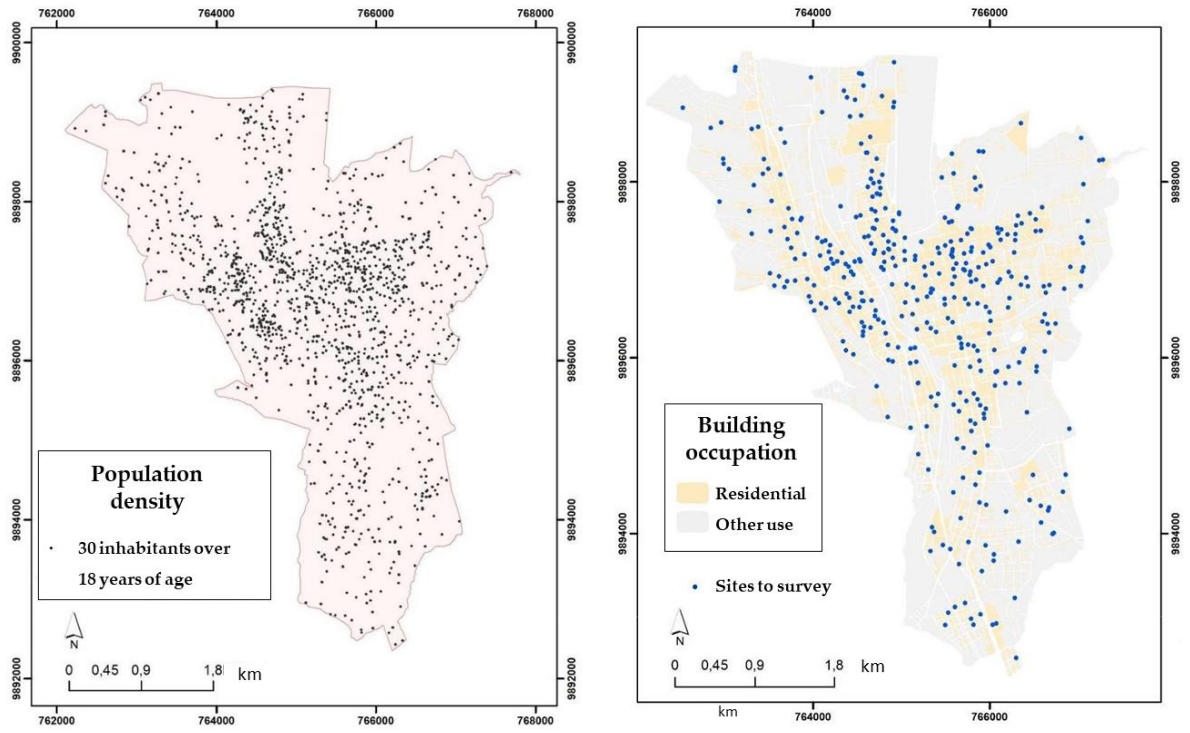

(a) (b)

Figure 6-4. (a) Population qualified for the survey to evaluate the social risk perception in the urban centre of Latacunga (b) Sites to survey within the residential buildings. Modified after (Grupo FARO et al., 2020).

It is worth to mention that, on the one hand, some drawbacks have been found when the community perception of exposure, vulnerability, and resilience are independently addressed for large-scale studies (Kelman, 2018; Shaw, 2012). On the other hand, there have been also reported benefits of this separation for mapping the social risk perception to natural hazards (e.g. Weichselgartner and Kelman, 2014; Sajjad et al., 2020) when bottom-up approaches are carried out. Therefore, we have decided to independently investigate the social perceptions towards these components through separated questions. The Likert scale is used in this context to obtain a quantifiable level of perception of each risk factor. An integer numerical score (1, 2, or 3) is assigned to every possible answer. Although the passage from a qualitative perception to an index can be questioned, several recent studies have shown the usefulness of the Likert scale (Oláh et al., 2019; Frazier et al., 2020; Wuni et al., 2020; Marín-Monroy et al., 2020; Moreno Cano et al., 2020). Notably, in Pescaroli et al., (2020) it was found to provide a good compromise between the quality of the information collected, the accessibility to respondents, while the bias in responses decreases, and there is consistency across different measurements and research domains of disaster risk reduction.

Subsequently, the average is computed for every question to obtain the perception of every component. These values are inputs to the computation of the risk perception pre-index through the use of equation 1, where P stands for "perception". An example subset of the questions is presented in Table 6-2 (Appendix). The questions and answers were validated by local risk management experts from the Association of Risk Management Professionals of Ecuador (Asociación de Profesionales de Gestión de Riesgos de Ecuador, APGR).

$$P(Risk) = \left(\frac{P(Hazard) \times P(Exposure) \times P(Vulnerability)}{P(Resilience)}\right)$$

Eq. 6-1

The numerator of equation Eq. 6-1 can have a maximum possible value of 27 whilst the minimum for the resilience term in the denominator is 1. Therefore the maximum risk perception value that this method admits is 27. The values in the range from 1-27 form a "pre-index". To obtain a more comprehensive

numerical value, a "reduced index" in the 0-3 range is obtained through the application of equation 2.

$$Reduced\ index = log_3(preindex\ value) \qquad \text{Eq. 6-2}$$

The relations between the "pre-index" and the "reduced index" is shown in Figure 6-5. For mapping purposes an "equal interval" classification for the reduced index scale is introduced with five classes of length 0.6 for finally presenting the spatialized perception of every risk factor in a compressive manner to the community. The calculated results for every answered question at each survey location (Figure 6-4-b) are used to map the spatial distribution of the perception of hazard recurrence, exposure, vulnerability and resilience, and the risk index (computed with equation 1). Subsequently, they were interpolated through the use of the *ordinary kriging* geostatistical algorithm (Issaks and Srivastava, 1989).

Pre-index value	1	2	3	4	5	6	7	8	9	10	11	12	13	14	15	16	17	18	19	20	21	22	23	24	25	26	27
Reduced index	0.00	0.63	1.00	1.26	1.46	1.63	1.77	1.89	2.00	2.10	2.18	2.26	2.33	2.40	2.46	2.52	2.58	2.63	2.68	2.73	2.77	2.81	2.85	2.89	2.93	2.97	3.00

Figure 6-5. Graphical scale and correspondence between the pre-index value and the reduced index.

6.3.2. The RIESGOS project: iterative simulation improvement and enhanced communication

The idea of constructing a web-tool, the RIESGOS demonstrator, as a decentralised and intraoperative environment for the exploration of the consequences in Latacunga from different volcanic hazard scenarios was proposed to the local stakeholders who participated in four participative workshops. Two of them were held in Latacunga (December 7th, 2018; November 25th, 2019) in the headquarters of GADPC *(Decentralized Autonomous Government of the Cotopaxi Province)* and two workshops took place in Quito on December 11th, 2018, and on November 27th, 2019, respectively. The participants ranged from research partners, representatives of the rural municipalities (parishes) of the Cotopaxi province, public authorities, environment secretaries, actors of the civil society such as local representatives of agriculture associations and urban and rural leaders. Similarly, as recently presented in Gill et al., (2020), the workshops were used as a means to implement a user-centered iterative approach seeking a continuous redesign of the RIESGOS demonstrator has been guided by the needs of potential users and practical applicability. This has been ensured by a comprehensive analysis of user requirements (e.g. open-source, user-friendly graphical user interface, and transferability).

6.3.2.1. The RIESGOS demonstrator tool for quantitative multi-risk analysis

The iteratively constructed RIESGOS demonstrator for a multi-risk information system is based on a modular and scalable concept in which the different hazards, the related exposure models and vulnerability schemas are each represented by one individual web service. These independent and distributed web-services (managed and maintained by individual research institutions) are based on the quantitative methodologies developed within the RIESGOS framework for multi-risk analysis (i.e. Frimberger et al., 2020; Rosero-Velásquez and Straub, 2019; Langbein et al., 2020; Brill et al., 2020; Gómez Zapata et al., 2020; Pittore et al., 2020a; Brinckmann et al., 2020). Therefore, their integration into the RIESGOS demonstrator simulates the multi-risk environment of Latacunga. This modular approach offers the possibility to integrate different web services into already existing system environments.

Currently, the graphical user interface of the demonstrator can be accessed from a web browser only by users with special rights. The main screen of the graphical user interface is divided into three main display areas: the central map window, the configuration wizard for the control of each web service to the left, and the results panel to the right (e.g. see Figure 6-6). The code of the graphical user

interface (RIESGOS frontend) is published on GitHub (https://github.com/riesgos/dlr-riesgos-frontend). The use of standardized web services such as geospatial web services defined by the Open Geospatial Consortium (OGC) allows users accessing open and flexible multi-risk information and data products. Web-services and exposed data resources can be accessed using a variety of means from a simple command-line tool, over a web browser, to existing graphical user interfaces of public authorities and companies which are equipped with a map user. OGC web services allow all kinds of geospatial functionality out-of-the-box including data access, data display, styling, and processing. Web services can easily be integrated into existing clients. The providers of web services define their products, display options, and configuration items. More details of this integrative process are reported in Brinckmann et al., (2020). Through the clear separation in competencies between web services and user-interface, modularity and scalability are increased.

Precomputed hazard models of ash-falls and lahars are displayed by the RIESGOS demonstrator after the selection of a scenario in terms of the expected for an eruption of the Cotopaxi volcano. Local probabilistic ashfall models for the Cotopaxi volcano generated by the IG-EPN (following the method of Tadini et al., (2020) with 20 years-observation of wind flow directions) are currently integrated as twelve explorative scenarios. They are represented by isolines (Figure 6-8). The lahar models described in Frimberger et al., (2020) are incorporated showing the maximum possible values of five physical properties (i.e. flow velocity, flow depth, pressure, erosion, and deposition (see Appendix- Figure 6-9).

The exposure model provides the input to calculate the direct losses over residential building portfolios classified in specific building classes for every hazard. An example for lahar-building classes is depicted in Figure 6-9. These models were constrained through the use of taxonomic characteristics available in the official cadastral dataset of the GADPC, such as roof and wall materials, and the proportions of the predominant building materials suggested for Latacunga in Yepes-Estrada et al. (2017). No further details are provided in the manner the building exposure models were constructed since this is out of the scope of this paper.

The vulnerability analysis of the typical residential buildings is performed using representative building exposure models with their respective fragility functions and suitable economical consequence models. Specifically, this approach is an extension of the Performance-Based Earthquake-Engineering (PBEE) method developed by Cornell and Krawinkler, (2000), which has more recently been adapted to other kinds of natural hazards. The fragility model proposed in Mavrouli et al., (2014) is used in lahar fragility, whilst the one in Torres-Corredor et al., (2017) is used in ash fall fragility for typical residential buildings that can be encountered in the study area. The demonstrator ultimately obtains the spatial distribution of damage and losses per individual hazard, plus the option of obtaining the cumulative damage and losses due to the action of both hazardous events using the novel method outlined in Langbein et al., (2020) that was based on (Gómez Zapata et al., 2020). Some examples are depicted in Figure 6-6 and Figure 6-10. No further technical details are provided because it is out of the scope of this work. Furthermore, the demonstrator enables to visualize the areas that might potentially get disconnected from different networks, and thus identify cascading effects on the economic activity. The method of implemented in the systemic vulnerability analysis applied in this case is similar to the one proposed in Crucitti et al., (2004). This information can be related with census data for estimating the population that might be affected by a blackout (Poljanšek et al., 2012). One example of this process is depicted in Figure 6-12 for the interruption probabilities of the electrical power network due to the impact of a lahar.

Figure 6-6. Example of the graphical representation of loss distribution due to ash fall scenario in the RIESGOS demonstrator (as of December 2020) from a previously selected VEI. Reddish and greenish aggregation areas representing higher and lower values respectively. On top of these results, the lahar model (with the same VEI) is displayed as input to calculate the cumulative damage over the same geo-cells exposed to both perils.

6.4. Results

6.4.1. The recognition of the Latacunga local laboratory by the local actors of the community

"The Latacunga Laboratory: Risk management, resilience, and adaptation to climate change" has strengthened its presence in the territory through several continuous participative activities that are aligned with the objectives mentioned in title 6.3.1. For instance, the Laboratory has been recently working in materialising initiatives that were proposed by local entrepreneurs. One of them is currently working on the recovery on *"Relatos de una erupcion"* (*Tales of an eruption*) which works on rescuing the historical memory of what happened in the eruption of the Cotopaxi volcano in 1877. This has been carried out through audio-visual stories that are told by direct descendants who survived this event. This initiative enhances co-responsibility and respect for historical memory. The oral transmission of this information is an important input to generate awareness. Details about these initiatives can be found in the Latacunga Laboratory website[5].

6.4.1.1. Comparative analysis of the social risk perception factors to natural hazards and the spatial distribution of volcanic-related risk factors

The method described in chapter 6.3.1.1 was applied to rank the volcanic risk perception for the most densely populated area in Latacunga conurbation. Making use of the 420 processed surveys as input data, the social perception to the recurrence of hazards, exposure, vulnerability and resilience for six natural hazards likely to occur in Latacunga (i.e. earthquakes, volcanic eruptions, droughts, frosts, landslides, floods) has been investigated. This is presented in the form of the comparative matrix shown in Table 6-1 which reports the mean values (for all the surveys) related to the perception of every component, as well as the computed risk index for every considered hazard. The higher the value, the greater the perception of risk. In the case of resilience, the interpretation is the opposite: the higher the value, the higher perception of resilience after a hazardous event.

[5] https://latacungaresiliente.com/rescate-de-la-memoria-historica-de-la-erupcion-del-volcan-cotopaxi/

Table 6-1. Hazard matrix and perception of risk factors towards natural hazards in the urban area of Latacunga.

	Risk factors	Perception of hazard recurrence	Perception of exposure	Perception of vulnerability	Perception of resilience	Perception of risk
		Scale: 0-3				Scale: 1-27
Natural Hazard	Volcanoes	2.61	2.73	2.83	1.93	10.45
	Earthquakes	2.58	2.75	2.77	1.98	9.93
	Frost	2.62	2.27	2.14	2.38	5.35
	Drought	2.33	2.27	2.23	2.32	5.08
	Floods	2.00	2.05	2.04	2.27	3.68
	Landslides	1.99	2.05	2.08	2.29	3.71

The greatest concern among the inhabitants of Latacunga is their own perceived vulnerability to volcanic hazards. Remarkably, their resilience after a volcanic event scores the lowest value. This implies the community is aware that they would have great difficulty (or impossibility) to recover from the related damages. It is worth noticing that despite that in the questionnaires there was no distinction made in terms of the type of volcanic hazards (lahar, ash fall/ tephra fall, ballistics) neither on its intensity, the collective imaginary always tended to associate the occurrence of a destructive lahar as *"the volcanic hazard"*. Most likely, the oral transmission of the experiences of the survivors from the 1877 event has permeated the mental construction of their descendants.

The mean results in terms of the percentage for the answered questionnaire that makes up the field and online surveys are depicted in Table 6-3. Contrary to the field survey, the online survey score large values in the basic knowledge and reconnaissance of their exposed environment (i.e. evacuation routes, emergency committee, the existence of initiatives for risk reduction). The field surveys express that 64% of the inhabitants consider the volcanic related hazards as events that are likely to happen in the city within their lifetimes. 86% answered that they believe an eventual eruption of the Cotopaxi volcano would cause very serious damaging effects to the city. Likewise, 75% considered they will have very serious impacts directly on their families and themselves. 25% of the population considers that *recovery* from a serious volcanic event would be *impossible* whilst 57% think it would be *difficult* to overcome. Regarding *knowledge*, 67% of the population know safe places in the event of a possible disaster, while 61% know evacuation routes. However, only 34% ensure there are emergency plans in their neighbourhood. Half of the respondents do not even know if they live in a volcanic hazard zone. 56% of the field-surveyed inhabitants and 69% of the online-respondents consider they would have rapid reaction capacities. Finally, ~42% of the population talks about *how to act in case of emergency* with their families.

Every answer of the 420 field surveys was spatially distributed onto the survey locations (Figure 6-4). Their associated numerical values of the Likert scale were interpolated through the use of the ordinary kriging geostatistical algorithm (Issaks and Srivastava, 1989). Subsequently, every numerical value is converted to the equivalent categories presented in Figure 6-5. The spatially-explicit categories represent the social perception of volcanic hazard recurrence, exposure, vulnerability, and resilience in the study area. They are respectively depicted in Figure 6-7-a, b, c, d. The former factors are integrated through equation 1 to generate Figure 6-7-e which represents the semi-quantitative volcanic risk perception index proposed in Carreño et al., (2005). In general terms, the perceptions of hazard recurrence, exposure and vulnerability are quite similar. However, in the central-easternmost and northernmost zones, there is a high perception of hazard recurrence, a very low perception of resilience, and a moderate perception of vulnerability. Whilst in the southernmost part (where the Cutuchi River flows) the four assessed factors show high and very high values that ultimately lead to a generalized "very high" category in the volcanic risk index. This is contrary to what is observed in the central-western and northern parts. Due to the increasing distances from the main drainages, there is a strong anti-correlation between the higher resilience levels (reddish areas) and the other risk factors. Hence, that despite the last volcanic crisis in 2015, there is still a generalised very low perception among the inhabitants that they cannot suffer any direct impact or damaging effect after increasing volcanic activity because they consider the occurrence of lahars (within

their lifetimes) is impossible. Clearly, the inhabitants of that sector, are not aware of the large intensities the Cotopaxi volcano can achieve (e.g. a *Plinian* activity (VEI >4) in Figure 6-3).

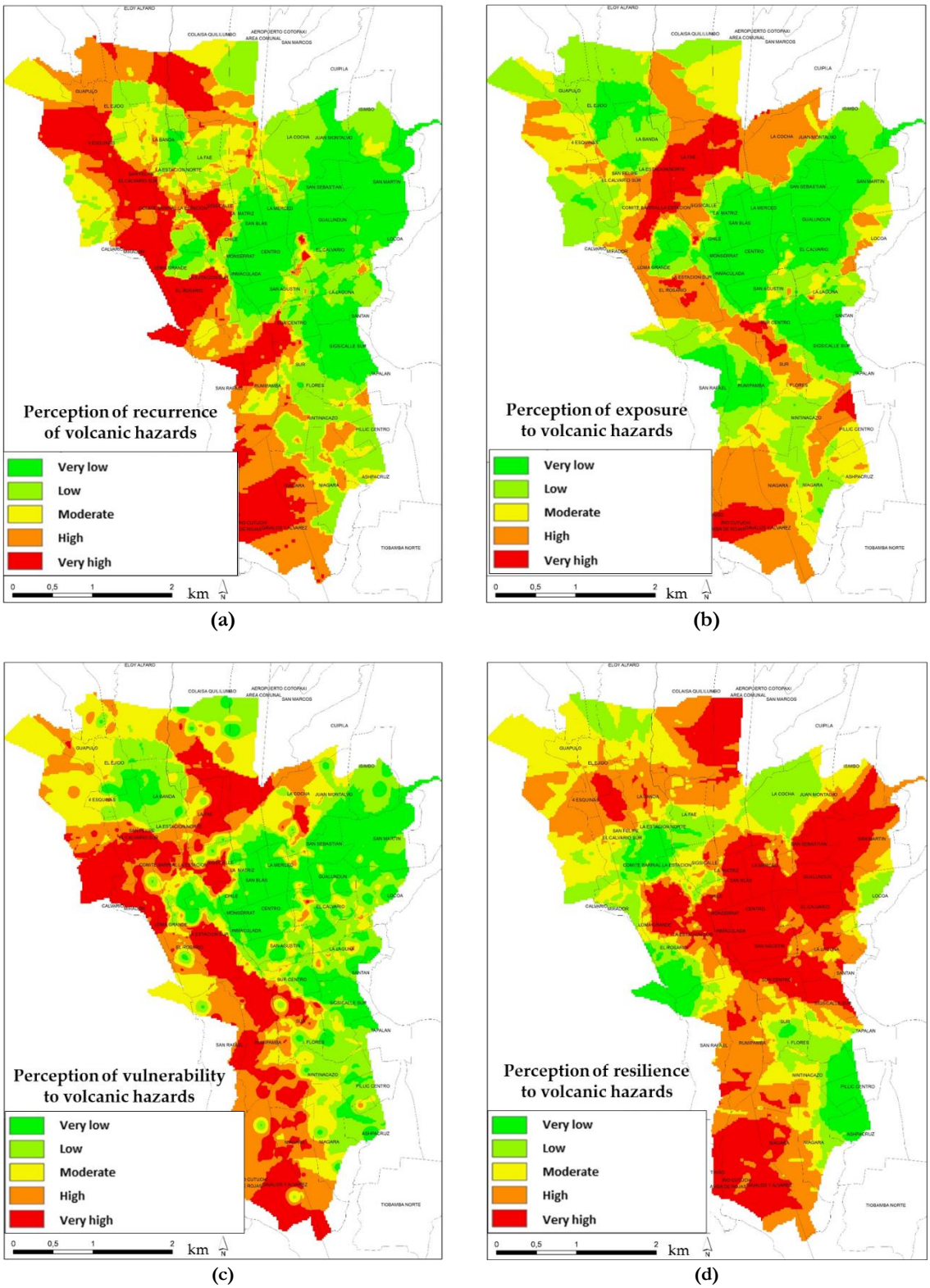

(Cont.)

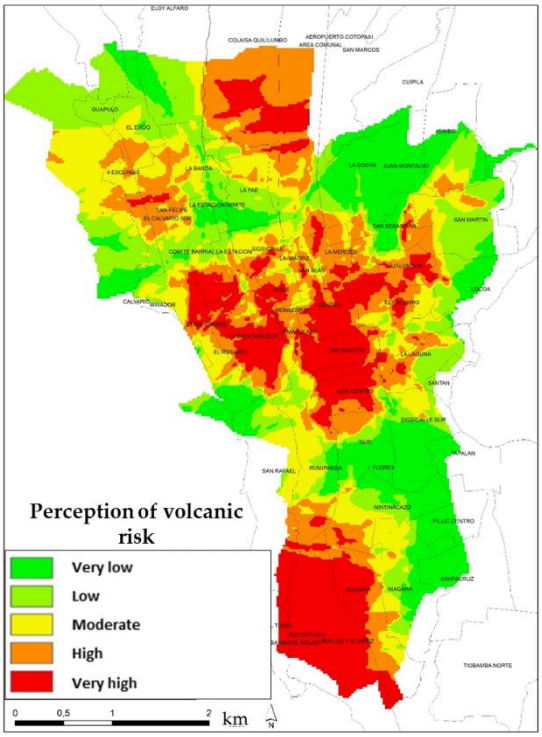

(e)

Figure 6-7. Spatial representation of the perception of volcanic hazards in the urban centre of Latacunga in terms of (a) recurrence; (b) exposure level; (c) vulnerability; (d) resilience; (e) subjective risk; (f) risk index calculated using the former components as inputs. Modified after (Grupo FARO et al., 2020).

6.4.2. The communication of the scenario-based risk assessment concept with local stakeholders

During the four RIESGOS participative workshops, the invited stakeholders expressed the interest in understanding the impacts of an extreme volcanic eruptions on the exposed elements such as buildings and critical infrastructure. Brainstorming exercises were carried out during the two first workshops. The participants were invited to imagine a future potential eruption with the emission of ash fall and occurrence of lahars. Thereafter, based on their perspectives and local knowledge, it was asked to which physical, systemic and cascading damaging effects they would expect on their built environment, infrastructure systems, and socioeconomic activities.

Some basic concepts of the probabilistic method that, as an open-source web-service assesses the vulnerability of the exposed residential buildings (see title 6.3.2.1), were presented to the local stakeholders. Due to the iterative approach used in constructing the demonstrator, some of the details that have been presented in this work as methods are actually the initial outputs of the first participative workshops. In this regard, the adaptability of "foreign" lahar vulnerability models (i.e. not developed for Ecuador) in the study area (e.g. Jenkins et al., 2014; Thouret et al., 2020; Zuccaro and De Gregorio, 2013) was initially discussed with the representatives of the scientific local institutions. Due to the absence of locally developed ash fall vulnerability models for the residential buildings in the surroundings of the Cotopaxi volcano, the use of vulnerability models for the southern Colombian Galeras volcano (Torres-Corredor et al., 2017) was perceived suitable to be implemented in the risk calculations rather than the fragility functions frequently developed for other areas (e.g. Italy (Jenkins et al., 2015)). With this feedback the web-tool was redesigned. This is an example of how the engagement of local participants can improve both the technical development of quantitative methods (by agreeing on a proper model) as well as the understanding of such methods by the community.

Possible cascading effects that would occur in the case of critical infrastructure failure were debated. For instance, the participants realised that assessing the vulnerability of electric networks to ash falls and lahars

is fundamental because of the further consequences on daily social and economic activities. However, the most debated topic was the reliability of the road system that, in the case of failure, may induce physical disruption and affect evacuation and emergency response during a volcanic crisis. Other public infrastructures that would be affected by Cotopaxi's lahars include the Army headquarters "Brigada Patria", Latacunga hospital and the new penitentiary (Rodriguez et al., 2017). The interest in relocating some of the exposed assets was discussed.

"Hands-on" sessions took place during the two last workshops. The participants could experience on their own the use of the RIESGOS demonstrator. They selected different scenarios to visually compare every hazard footprint and intensity (i.e., for ash fall and lahars) as well as their associated risk outcomes on residential buildings and electric power networks. This was done through the selection of individual and successive hazard scenarios addressing cumulative damage. During the "hands-on" session the participants recognized the potential of the demonstrator as an exploration tool for risk communication.

6.5. Discussion

The CIS and RIESGOS projects have independently addressed the domain of risk communication in Latacunga (Ecuador) at different geographical scales. The investigation and mapping of the perception of volcanic risk factors led by the Latacunga Laboratory (created by CIS) was carried out in a focused area (urban area) due to the necessity of having control points (where field-surveys were carried out) for a further geostatistical interpolation process. Whilst, in the framework of the RIESGOS project, the construction of the hazard, exposure and vulnerability approaches for scenario-based multi-risk calculations have been carried out at the canton level. Despite that, the community perceptions of the entire canton and province can be assessed in the future through field surveys for other urban centres (e.g. Pujili, Saquisili, and Salcedo), a meaningful spatially explicit perception of volcanic risk factors could only be mapped for the urban centres. This is because, due to the scattered location of the residential buildings in the rural areas, conventional geostatistical interpolation algorithms would carry significant bias in the results. For the commonly investigated area by RIESGOS and CIS, we can see that the exposed community recognise to be under a variable level of risk towards volcanic events depending on their location. These perceptions match the lahar footprints from the scenarios with higher probabilities of occurrence (VEI < 3). However for larger intensities, (e.g. lahar footprints from a VEI > 4 scenario, see Figure 6-3-b), we observe a mismatch with the spatially-explicit community perceptions of volcanic risk factors (Figure 6-7). For instance, the easternmost areas of the urban centre of Latacunga show low and very low reconnaissance of volcanic risk factors due to their increasing distance respect to the main drainages. The inhabitants of that particular sector have perceived as impossible the occurrence and to suffer consequences from lahars. The ignorance of the lahar footprints expected from these large intensity scenarios makes that the concepts of "safe place" and evacuation routes are not applicable for either. These results should not be interpreted as fixed or permanent but they rather constitute a temporal reading of the collective mental construction of the inhabitants at the time the surveys were carried out. Nevertheless, considering that the community is emplaced in ancient lahar deposits, as well as the relatively short time since the last 2015 volcanic crisis, one can realise the comparison of the respective outcomes arises the need to prioritize some zones where further divulgation activities should be made in the future regarding the possible scenarios and intensities that the Cotopaxi volcano can actually produce.

The formulated questions comprised in the survey forms are locally revised by experts from the APGR while paying attention to the use of collectively known terminology and the cultural characteristics of the community. In this work, we have implemented a simple numerical expression (equation 1) that equally ranks the risks factors of the different volcanic risk factors. This selection carries epistemic uncertainties. For instance, a customisation weighting schema to each factor, the selection of the median or mode instead of the mean value (herein adopted), together with a broader range in the Likert scale (e.g. 1 to 7 as explored in Croasmun and Ostrom, (2011)) could be alternative approaches to be compared or even integrating each other into condition trees as proposed in Beven et al., (2018). The selection of the Likert scale to rank the answers and to ultimately mapping the community perceptions implied an ordinal scale that was further converted into a nominal one based on the "equal-scale" (equation 2). This decision was made because, since the methods and results are aimed to be

divulged, the categories have been found to be comprehensive, easily understandable, and culturally accepted by the community. Although the Likert scale has been extensively and recently used to successfully assess the community perception (e.g. Oláh et al., 2019; Frazier et al., 2020; Wuni et al., 2020; Marín-Monroy et al., 2020; Moreno Cano et al., 2020), there are several limitations in its adoption. For instance, as stated in Pescaroli et al., (2020), this kind of scale, despite that maximizes the reliability of answers, it also sacrifices the level of detail. However, it should be noted that through the simple possible answers related to the vulnerability perception and the nominal categories we are only proposing a very simple categorization. More robust approaches that have addressed spatial multi-criteria analysis (as presented in Armaş and Gavriş, (2013)) have shown the impact of addressing diverse socioeconomic variables that we have not addressed in in our approach. A similar situation occurs with the resilience perception, which as discussed in Ran et al., (2020), it can be decomposed into very heterogeneous variables in economically developed countries.

Therefore, we are not claiming that our results related to the community perception of risk factors are exhaustive, but instead, they should be used as a basis for developing in future stages more complex analyses. For instance, even though we have already observed clear behaviour differences between the responses from online and field surveys, with explicitly designed survey and accounting variables such as work location, alphabetisation level, economic activity, we could in the future classify the population into different social groups, and find similarities and differences in their behaviour within a social environment to carry out more sophisticated methods as proposed in Moscato et al., (2020). Thereby, for each group, we could expect different reactions to a future volcanic crisis and then propose particular resilience practices. However, these kinds of approaches will largely depend on the data availability which is particularly difficult in the rural tropics (Frontuto et al., 2020; Li et al., 2020).

As described in recent participative experiences to assess the community perception to natural hazards (e.g. Heinzlef et al., 2020a; Fleming et al., 2020), we have also experienced that the workshops carried out allowed to go beyond a simple exchange of information. They paved the way for a better divulgation of concepts such as triggering and cascading hazards, dynamic vulnerability, cumulative damage, and cascading effects. These understandings in turn facilitated the knowledge flows and feedback acquisition to continuously design the RIESGOS demonstrator guided by increasingly risk-informed decision-makers. With this bottom-up iterative approach in the web-tool design, we are following the suggestions of the Sendai Framework for Disaster Risk reduction (2015-2030) (UNISDR, 2015). The outcomes of the demonstrator are not static hazard maps that are delivered to the exposed population from top-down approaches (e.g. Bronfman et al., 2016; Jóhannesdóttir and Gísladóttir, 2010; Paton et al., 2008), but rather, scenario-based online computations that can dynamically change based upon the continuous integration of local datasets and models.

During the "hands-on" sessions the potential users perceived the RIESGOS demonstrator to intended prompt risk communication processes. For the study area, only hazard models have been typically available and the few risk outcomes obtained in the past have been reported in tables and not in a spatially-explicit manner (Rodriguez et al., 2017). Therefore, this work is providing the community with the availability of scenario-based risk models based on the vulnerability of the exposed elements in graphical and user-friendly interphase is an added value for the local community. The integrated scenario-based lahar footprints per VEI (Frimberger et al., 2020) and the locally developed probabilistic ash falls models (Tadini et al., 2020) are themselves useful outcomes for civil protection and local-planners. They can be used to identify which human settlements and agricultural plantations might be affected or even discuss the relocation of some of the exposed components of critical infrastructure. Although we have not accounted for the conditional probabilities between triggering and cascading hazards as proposed in Zuccaro et al., (2008), we have instead presented fixed risk scenarios. For such a purpose the demonstrator is served by a novel method that calculates and disaggregates the cumulative damage when there are interactions at the vulnerability level. In the specific volcanic context, although the concept of dynamic vulnerability had been already theoretically sketched in the work of Zuccaro et al., (2018), to the best authors' knowledge, we have first presented an example case of cumulative damage for risk-informed communities exposed to compound and cascading volcanic hazards. This is an innovative approach that not only

contributes to reducing the generalized gap in the interactions at the vulnerability level (Terzi et al., 2019), but also to communicate the results to the local stakeholders. With these contributions, the potential users could identify the most vulnerable areas for further mitigation strategies. It is worth to mention that, since the RIESGOS demonstrator is currently not an operational tool, but rather shows the scientific and technological capabilities, the economic loss estimations for every exposure geo-cell (where residential buildings are aggregated) should not be used as definitive results. Therefore, due to the underlying uncertainties in these results, there is still the permanent necessity pointed out in Doyle et al., (2014); Pierson et al., (2014) of having expert local users and scientists who can analyse and effectively communicate this information.

The technology transfer of the activities included in the CIS and RIESGOS programmes is highly relevant. The modular software architecture is particularly relevant for this aspect, for which the databases and methodologies of local Ecuadorian institutions may be ultimately integrated. However, the applicability of the demonstrator in the long-term will depend on how the local authorities will "give life" to the initiative considering the local legal aspects. For future communication initiatives, due to the intrinsic interoperative sequence of inputs and outputs, the demonstrator can be a pedagogic tool to divulge multi-risk situations as similarly carried out by audio-visual approaches (e.g. Hicks et al., 2017; Mercorio et al., 2019). Nevertheless, these kinds of local actors should be the first ones to understand the aforementioned concepts of "scenario" and "intensity" within the multi-risk chain. And most importantly, that they can be further contrasted with future and continuous spatially-explicit social risk perceptions monitoring initiative.

6.6. Conclusion

We have presented an integrative framework of qualitative community risk perceptions (carried out by the CIS Latacunga Laboratory), and scenario-based quantitative multi-hazard risk assessment (developed by the RIESGOS project). These initiatives have jointly worked on comprehensive volcanic risk communication processes in Latacunga, a city with a mainly rurally composed population, exposed to volcanic hazards from the Cotopaxi volcano.

Online and field surveys were carried out to rank the volcanic risk factors to investigate the individual knowledge and attitudes in Latacunga. Only the geo-located interviews in the field were used to map the community risk perceptions and to calculate a spatially-explicit risk perception index through a semi-quantitative approach.

The participative workshops allowed the potentially affected communities to identify how their exposed assets, depending on their physical and systemic vulnerabilities would be differently affected by several volcanic hazard scenarios. The iteratively customised RIESGOS demonstrator proved to be a useful tool for the communication of quantitative risk scenarios, raising the awareness of potentially affected population for the concept of scenarios and intensity. Its outcomes facilitate discussions among the participants on topics such as relocation of critical infrastructure elements. The demonstrator is not only enhancing the awareness of the communities but also the user involvement in its development is improving the quality of the software. Although the development of the CIS and RIESGOS methodologies started independently, the respective outcomes of this collaborative work has allowed identifying areas where risk perception and scenario-based risk models are in disagreement. Thus, it is highlighted the need to continue assessing the social risk perception along with future risk communication efforts in the Cotopaxi region.

Acknowledgments: The authors want to express their gratitude to the 55 students from *Instituto Superior Tecnológico Cotopaxi* (ISTC) who carried out the field surveys. As well as to all the participants of the workshops and the inhabitants in Latacunga who replied the surveys. Thanks to Prof. Dr. Daniel Straub (TUM), Dr. Jörn Lauterjung, Prof. Dr. Heidi Kreibich and Prof. Dr. Fabrice Cotton (GFZ) for their advice during the elaboration of this work. Special thanks to Dr. Benjamin Bernard and Sebastian Averdunk (TUM) for the ash fall simulations inputs, as well as to Dr. Daniel Andrade and Dr. Patricia Mothes (IG-EPN) for the valuable feedback throughout the development of this work. Thanks, Dr. Daniela de Gregorio (UNINA), Roberto Torres-Corredor (SGC), Dr. Susanna Jenkins (EOS) and Dr. Robin Spence (Cambridge A.R) for having kindly provided sets of ash fall fragility functions. Thanks to Dr. Karl Heinz Gaudry (GIZ / CIM), Martin Cordovez Dammer, Marta Correa and Edwin León (IIGE) for the discussions about critical infrastructure and cascading effects during the former volcanic crisis in the study area during the author's visits to Ecuador. Thanks to Dr. Hugo Yepes, Dr. Pablo Palacios, Dr. Jose Marrero, and Juan Carlos Singaucho (IG-

EPN) for the feedback about exposure modelling and loss visualization. Thanks to Dorothea Kallenberger (GIZ), Ana Patricia (Grupo FARO) and Cristopher Velasco (president of the APGR), for having supported the research of the community risk perception study in Latacunga. Thanks to Luis Chasi for leading the initiative *"Relatos de una erupcion"*. Thanks to Diego Molina (GADPC) for promoting discussions about the social risk perception of the local actors of the Cotopaxi province during the workshops held in Latacunga. Thanks to all SENESCYT and SNGER for the co-organization of the workshops held in Quito. Special thanks to Nils Brinkmann and Matthias Rüster (GFZ) for having participated in the construction of some of the computer codes implemented in this work.

Conflicts of Interest The authors declare no conflict of interest. The funders had no role in the design of the study, in the collection, analyses, or interpretation of data; in the writing of the manuscript, or in the decision to publish the results.

Funding: The research and development project RIESGOS (Grant No. 03G0876) is funded by the German Federal Ministry of Education and Research (BMBF) as part of the funding programme 'CLIENT II – International Partnerships for Sustainable Innovations'. The development of the Latacunga Laboratory: Risk management, resilience and adaptation to climate change (within the program "Sustainable Intermediate Cities – CIS) is funded by the Deutsche Gesellschaft für Internationale Zusammenarbeit (GIZ) programme of the GIZ Federal Ministry for Economic Cooperation and Development of Germany (BMZ).

6.7. Appendix A

Table 6-2. Example of the procedure for calculating the risk perception pre-index.

Questions	Answer options	Quantitative score	Answer						Value transformation						Perception of risk factor		Pre-index of risk perception (in the scale 1-27)
			Earthquake	Volcanoes	Drought	Frost	Landslides	Floods	Earthquake	Volcanoes	Drought	Frost	Landslides	Floods			
Perception of hazard recurrence	Certainly yes	3	x	x	x	x		x	3	3	3	3		3	P(Hazard)	2.83	12.60
	It might occur	2					x						2				
	Impossible	1															
Perception of their impacts	Very serious	3	x	x				x	3	3				3	P(Vulnerability)	2.5	
	Moderate	2			x	x	x				2	2	2				
	No effects	1															
Perception of their effects to your family	Direct	3	x	x		x		x	3	3		3		3	P(Exposure)	2.67	
	Indirect	2			x		x				2		2				
	No effects	1															
Perception of recovery from them	Impossible	1	x	x				x	1	1				1	P(esilience)	1.5	
	Difficult	2			x	x	x				2	2	2				
	Likely	3															

Table 6-3. Questionnaire within the survey to assess the social risk perception to volcanic risk in the urban area of Latacunga. The mean values of the entire survey are reported. Adapted after Grupo FARO et al., (2020).

Questions	Possible answer	Type of survey (%)		
		Online	Field	Aggregated
% P(Hazard). Perception of volcanic hazards recurrence. Do you think a volcanic eruption (from the Cotopaxi) can occur?	Certainly yes	54.43	63.61	62.04
	It might occur	44.30	34.29	36.01
	Impossible	1.27	2.09	1.95
% P(Vulnerability). How do you consider the effects after a volcanic eruption would be?	Very serious	91.36	85.56	86.56
	Moderate	8.64	12.86	12.12
	No effects	0.00	1.57	1.30
% P(Exposure). How do you consider the effects after a volcanic eruption would impact your family and yourself?	Very serious	81.48	75.39	76.46
	Moderate	17.28	22.51	21.60
	No effects	1.23	2.09	1.94
% P(resilience). How do you consider the recovery process from the effects after a volcanic eruption?	Impossible	11.11	24.87	22.46
	Difficult	58.02	57.33	57.45
	Likely	30.86	17.80	20.09
Do you know if your home is in a volcanic hazard zone?	Yes	69.70	45.80	49.70
	No	32.1	54.2	50.3
Are there emergency plans in your neighbourhood?	Yes	19.75	36.65	33.69
	No	38.27	39.27	39.09
	Do not know	41.98	24.08	27.21
Are there safe places in the vicinity where you live? (in case of a volcanic eruption)	Yes	69.14	66.49	66.95
	No	16.05	18.85	18.36
	Do not know	14.81	14.66	14.69
Are there evacuation routes to safe sites?	Yes	70.37	60.47	62.20
	No	8.64	21.47	19.22
	Do not know	20.99	18.06	18.57
Is there an emergency committee in your neighbourhood?	Yes	9.88	32.98	28.94
	No	46.91	35.34	37.37
	Do not know	43.21	31.68	33.69
Do you know if there are initiatives, actions or works to reduce the risks from volcanic eruptions in Latacunga?	Yes	66.70	56.30	58.10
	No	33.30	43.70	41.90
Do you think you are capable of having a fast react during a volcanic eruptions?	Yes	69.10	53.10	55.90
	No	30.90	46.90	44.10
How often do you talk to your family about how to behave in the event of an emergency?	Never	0.00	17.63	14.66
	Rarely	23.38	41.05	38.07
	Sometimes	50.65	22.89	27.57
	Usually	25.97	18.42	19.69

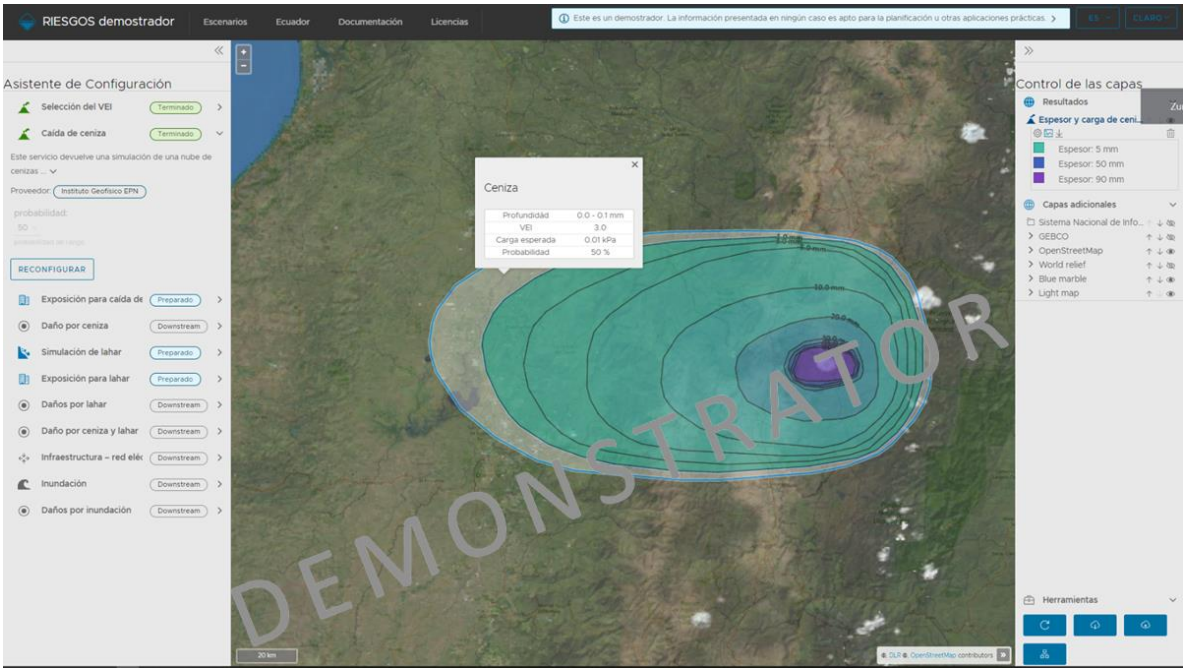

Figure 6-8. Example of the graphical representation of the spatially distributed ash fall intensities as isolines in the RIESGOS demonstrator (as of December 2020) from a previously selected VEI. The thickness values are displayed. Once a point within the isolines is clicked, the expected load (kPa) value is also shown.

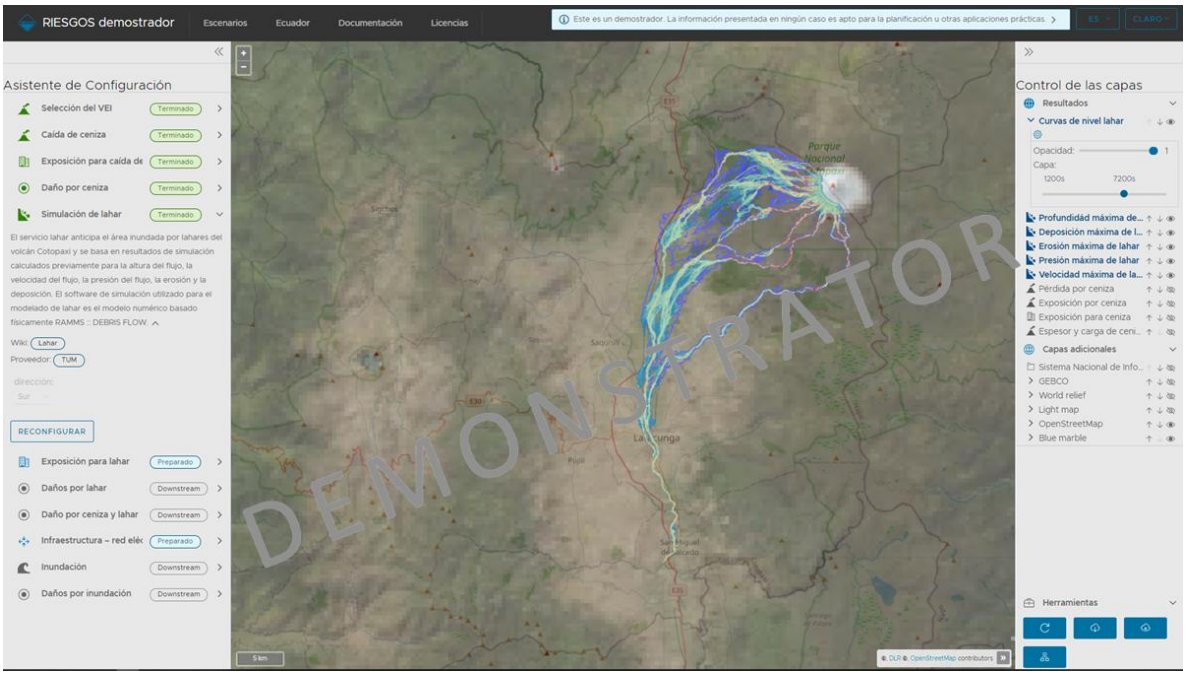

Figure 6-9. Example of the graphical representation of the footprint and intensities of the lahars in the RIESGOS demonstrator (as of December 2020) from a previously selected VEI. On the top-right side of the window, the outputs of the lahar simulation are listed (i.e. lahar flow velocity, flow depth, pressure, erosion and deposition)

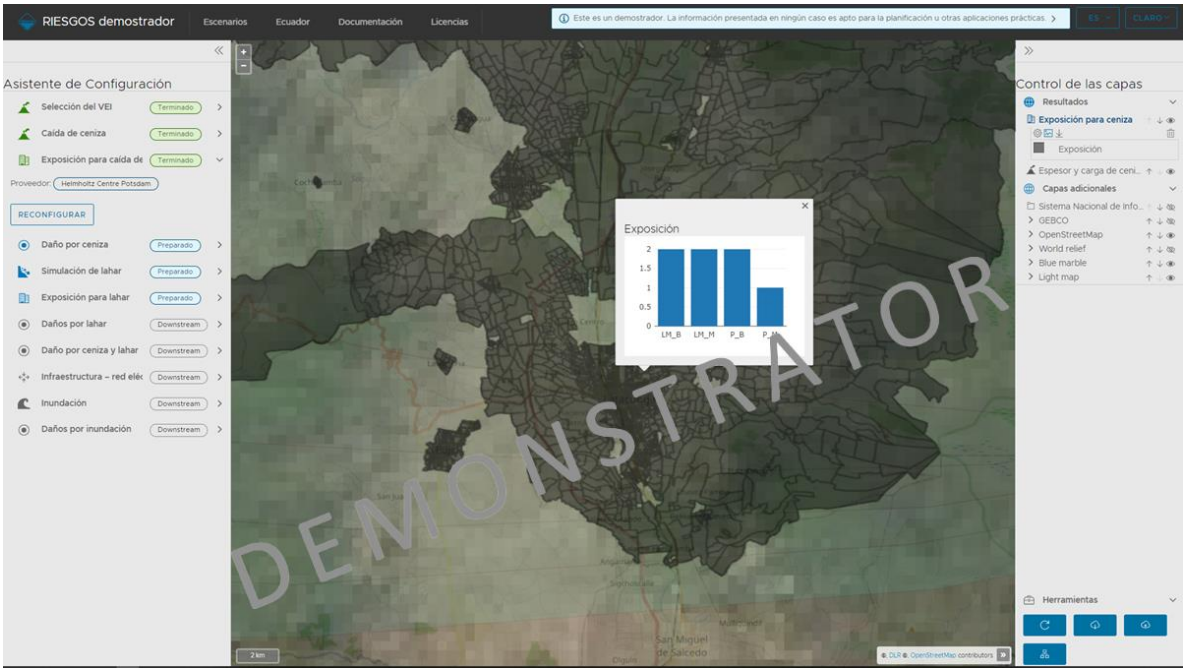

Figure 6-10. Example of the graphical representation of the residential building exposure model in the RIESGOS demonstrator (as of December 2020). It is represented into aggregation areas based on the official rural and urban administrative divisions of Latacunga. There are displayed the quantities of every ash fall risk oriented building class proposed in Torres-Corredor et al., (2017) within a selected area.

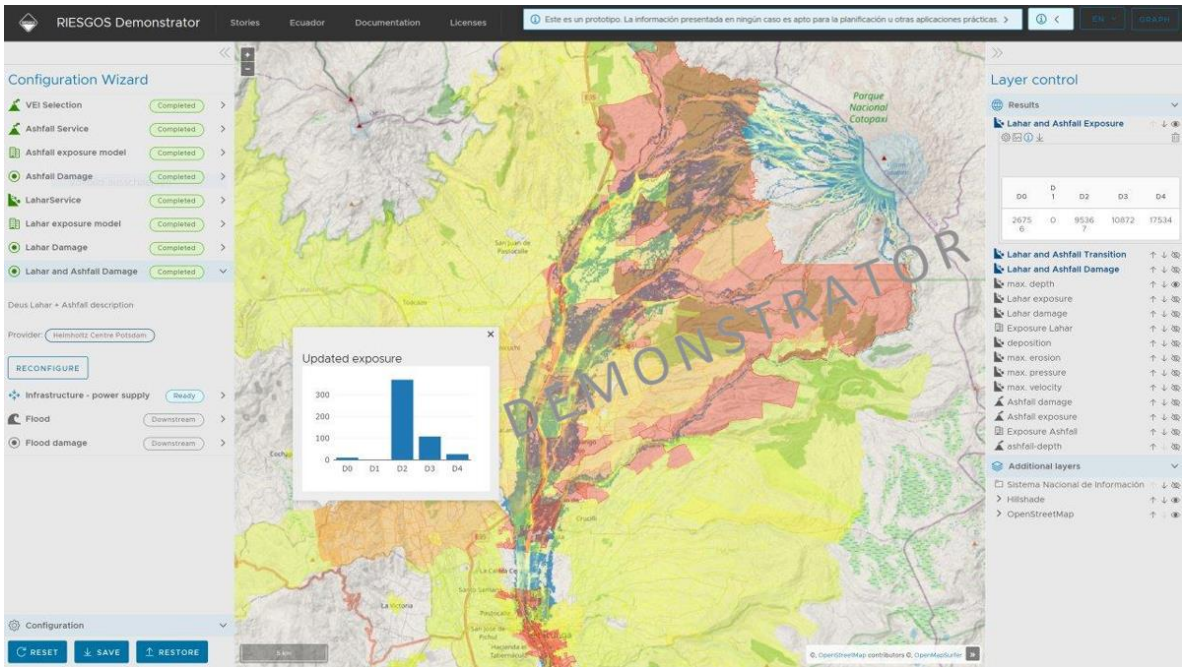

Figure 6-11. Example of the graphical representation of damage state distribution due to the combined effect of ash falls and lahar scenarios in the RIESGOS demonstrator (as of December 2020) calculated using the method proposed in Gómez Zapata et al., 2020; Langbein et al., (2020).

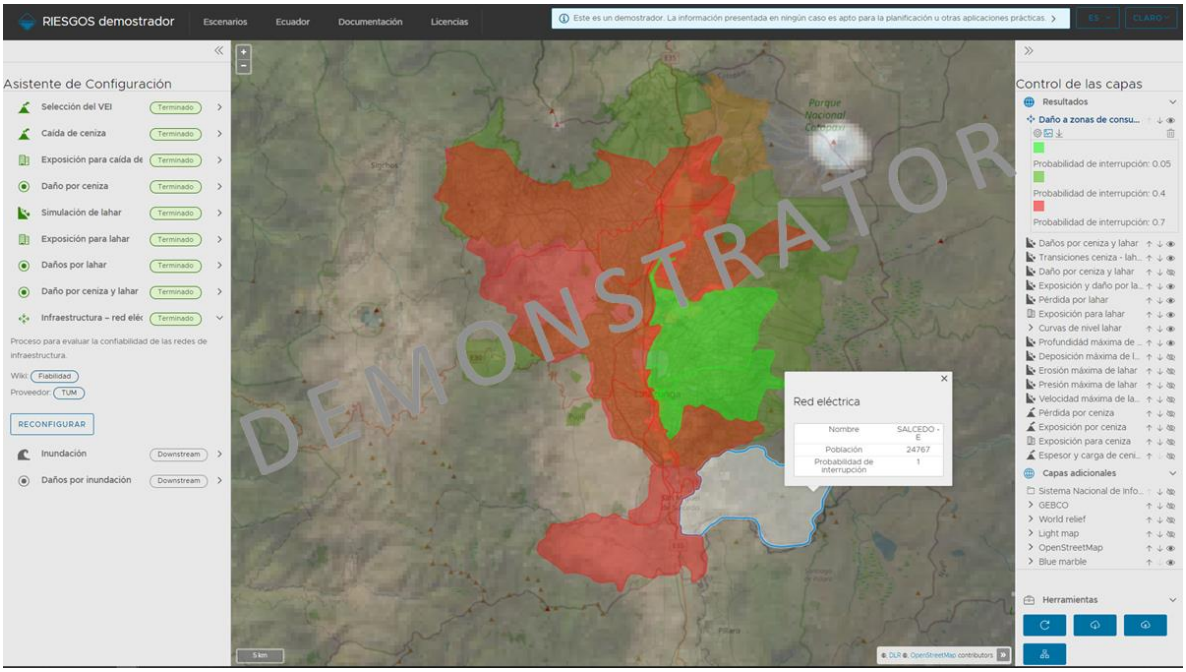

Figure 6-12. Example of the visualization of the expected interruption probabilities in the RIESGOS demonstrator (as of December 2020) of the electrical power network due to the action of a lahar scenario.

I heard one sine from above

LG & EJ

7. Synthesis

Among the three inputs required (i.e., exposure, hazard and vulnerability) to assess the physical vulnerability of city-scale building portfolios due to any natural hazard intensity, the exposure modelling process has received comparably less research attention. We, members of the scientific community, practitioners and the insurance industry do not know enough about the composition, location, pre-existing damage, or financial value of the assets contained in building exposure models. Conventional exposure models for residential building stocks that are used in risk applications have been derived from top-down approaches i.e., expert elicitation over static aggregated data sources (e.g., census-based desktop studies) without exploring the underlying uncertainties. Thus, the absolute majority of the worldwide built-up areas that have been modelled for risk assessment are implicitly assumed to have static compositions in time and no spatial evolution. Moreover, classical exposure models for residential buildings have been typically spatially aggregated onto coarse administrative areas, and no efforts had been devoted to explore manners to efficiently aggregate them onto meaningful spatial entities that are useable for multi-hazard risk applications.

Only in the last few years have some studies highlighted that exposure uncertainty is an area that would benefit from the further investigation (e.g., Silva et al. 2019). For instance, the composition of building exposure models derived from statistical projections about the population dynamics has been identified as a research area worth exploring (Calderón and Silva, 2021). Likewise, the uncertainties related to the location of some exposed assets are now being reduced due to the new increasing availability of data products, which are derived from remote sensing and volunteering geographical initiatives (e.g., Aravena Pelizari et al., 2021). Nevertheless, in most cases, only a few features (i.e., geometry, roof, and occupancy) can be successfully derived from such sources, whilst the main relevant descriptors to assess their physical vulnerability have remained hidden. Besides, only in recent times, the importance of counting with optimal geographical representations of exposure models for risk assessment has been recently discussed (e.g., Dabbeek et al., 2021). However, there has been not much research interest in addressing how the spatial variability of the hazard intensities can be used to derive new aggregation boundaries that can represent a compromise between computational efficiency and accuracy in the risk estimates. Furthermore, classical exposure models for residential building portfolios typically assume the presence of pristine or intact structures without including any pre-existing damage. This latter issue has started to be investigated by non-conventional and recent methods to account for the cumulative damage expected during seismic sequences (e.g., Papadopoulos and Bazzurro, 2021). As a general feature, all of the aforementioned shortcomings of exposure models for risk assessment have been mostly tackled in the field of earthquake loss models, and their exploration is rare for other hazard-related vulnerabilities (e.g., using openly available data for flood vulnerability in Cerri et al., 2021). Yet, in multi-hazard risk contexts, similar investigations had remained to date as open research questions.

Four main pillars have been the basis and inspiration for this stepwise arranged thesis:

(1) The first pillar is related to the study of the role and uncertainties related to the modelling of the subcomponents: composition, spatial aggregation, and pre-existing damage of residential building exposure models upon single and multi-hazard risk assessment.

(2) The second pillar is related to the development, and implementation of risk scenarios. Sensitivity analyses on the aforementioned exposure subcomponents were carried out through risk scenarios that were transversally used throughout the entire development of this thesis to forecast the direct economic losses expected from the action of single and multiple hazard intensities. The selection of scenarios naturally arises from the need to work on the understanding of the role of the aforementioned exposure subcomponents on risk due to cascading hazards. As these events are very complex to be included in a probabilistic framework, scenarios allowed up to a certain extent, to isolate their individual contributions, in such a fashion that their related uncertainties could be individually propagated up to the final loss estimates in single and multi-hazard risk contexts.

(3) The third pillar arises as a result of the necessity of harmonising newly available data together and existing fragility models. Many experts from various research fields have already generated new fragility/vulnerability models for specific regions with non-standardized metrics or scales

(i.e., local building classes; various number and descriptions of damage limit states). Thus, this third pillar constitutes a careful piece-wisely integration of the three formerly developed concepts (composition, spatial aggregation and pre-existing damage) within an original method herein proposed to assess damage accumulation on building stocks exposed to consecutive hazards (Chapter 5). This is a holistic methodology that allows the reutilisation of existing models into a consistent probabilistic approach and that relies on two levels of taxonomic building attributes:

a. "A high level": it is the result of the disaggregation of building classes (per hazard of interest) into such taxonomic attributes. This allows to obtain the probabilistic compatibility levels across hazard-dependent vulnerability schemes (sets of building classes).
b. "A low level"; it is made out of simpler set of building components that are used to score the likely observable damage (features and extension) that are expected per building type, per damage state, per vulnerability type. For this aim, an attempt to harmonise various damage scales was made. Thereby, classification machine learning and Bayesian models were used to obtain their corresponding probabilistic compatibility levels.

(4) Lastly, the fourth pillar is related to the proposal of a decentralised and interoperative web environment for the exploration of the consequences of an area exposed to various multi-hazard risk scenarios. It was constructed through an iterative process with local experts and potential end-users increasing both the quality of the technical tool as well as its practical applicability. Risk communication activities (i.e., participative workshops using this web tool) were proven to contribute to a clearer understanding of the scenario-based multi-risk chain by the exposed communities, as well as to contrast partial understandings with their own risk perception.

In the frame of the four aforementioned pillars, some contributions of this work are summarised as follows:

(1) This thesis has comprehensively discussed the limitations of the current practices in exposure modelling that rely on top-down approaches, i.e., expert elicitation over usually outdated and insufficient data sources to assess the vulnerability of the exposed structures. Thereby, it has been herein reinforced the proposal that exposure is not static but dynamic and has a probabilistic nature that can be constrained through careful data collection and statistical analyses in the form of Bayesian models (Chap. 2). Although this data collection was obtained from the visual inspection of building façade imagery, other emerging technologies (e.g., automatic façade reconnaissance) could be used in the future. It was ultimately proven the usefulness of this approach to probabilistically update the proportions assigned to building typologies while careful data collection is gathered.

(2) The integration between simple (but so far unexplored) assumptions such as representing the composition of the building portfolio through various sets of building classes, along with more refined approaches such as Bayesian exposure models that are useful to integrate observations and expert-based assumptions was proven to be useful to investigate the role and uncertainties of some exposure subcomponents through sensitivity analyses. With this, it was possible to ultimately propagate their individual contributions on scenario-based earthquake loss models through careful sensitivity analyses (Chap. 2-3).

(3) This thesis has shown the advantages of making use of freely open datasets that are continuously derived from volunteering geo-information initiatives to probabilistically update and continuously refine the composition of existing exposure models (Chap. 3). Although the lack of data formats standards is an important shortcoming that is still to be solved by these open-source initiatives, it was herein observed that the derivation of building attributes that are likely to be associated with other specific ones is a promising pathway to keep exploring in future studies through new techniques. Furthermore, it was also proved that the refinement of the spatial extent of exposure models by integrating remote sensing data products is compatible with such a probabilistic framework.

(4) This thesis has shown the importance of deriving optimal spatial aggregation entities for exposure modelling from the new integration of exposure

proxies and the spatial variability and correlation of the hazard intensities of interest. For such a purpose, geocells in the form of Central Voronoi Tessellations were proposed to accurately and efficiently estimate the physical vulnerability of large-area building stocks to various independent and cascading hazards (Chap. 4). It was proven their advantages in computation efficiency while preserving accuracy and reducing thematic uncertainties in their visualisation. Although this approach was applied for the punctual case of a coastal city exposed to seismic ground-shaking (spatially cross-correlated ground motion fields) and tsunami inundation, the proposed method could be adapted and further applied in future studies for other contexts (other areas and sets of hazards).

Subsequently, this thesis moved to a multi-hazard risk environment accounting for the interactions at the vulnerability level. Such risk scenarios were developed accounting for the damaging actions of various intensity measures on building portfolios, either due to individual hazards (i.e., earthquake ground motions, far-field tsunamis) or to include pre-existing damage in the exposure model to assess the likely cumulative damage during consecutive sequences (e.g., ground shaking followed by a tsunami in Chapter 5).

(5) This thesis has proposed a novel method to harmonise and integrate existing fragility models (that were already individually calibrated by experts) into a consistent approach for scenario-based multi-hazard risk assessment including state-dependent models. This is a modular method that allows estimating the dynamic physical vulnerability (i.e., cumulative damage and direct economic losses) of a large-city-scale residential building stock exposed to cascading hazard scenarios. With the proposal of this method, this thesis sets the precedent for the need to visualise the exposure component from a different perspective: not anymore as a fixed and pristine representation of assets, but how it can be linked to the vulnerability component to include pre-existing damage descriptions, a vital input to address cumulative damage and losses in a multi-hazard risk setting.

(6) The aforementioned method was herein exemplified by evaluating the likely damage distribution and respective direct financial losses of the residential building stock of Lima subjected to various consecutive earthquakes and tsunamis scenarios (i.e., seismic ground-shaking and tsunami inundation respectively). Having proposed scenario-based multi-risk assessment for this city is itself a particular achievement of this thesis. Lima is today an important and highly vulnerable mega-city (with nearly 10 million people) and hosts most of the important economic activities of the country. Its relevance stems from the fact that, although this city was devastated in the past by earthquakes and tsunamis, no research studies of this nature (addressing cumulative damage and losses) had not been reported in the scientific literature. The outcomes related to this original method differ from the ones obtained from classical tsunami empirical fragility functions, for which underestimation of predicted losses for lower magnitudes (Mw) and large overestimations for larger Mw events were observed.

Lastly, this thesis also documents how the developments related to exposure, risk scenarios, and their related uncertainties can be successfully integrated into a user-friendly interactive tool for the exploration of risk scenarios. The establishment of this framework has contributed to risk communication initiatives with practical societal applications. This activity has also enhanced the divulgation of results or linked with multi-risk scenarios in a transparent manner to the interested stakeholders, and to the scientific community through the creation of open source software and freely available data repositories. These aspects can be summarised as explained in the next two items.

(7) The research outcomes obtained in the former items related to exposure and multi-hazard risk investigations were designed to be ultimately integrated into a set of interoperative webservices that jointly configure a decentralised processing architecture. Such a joint integration ultimately allowed the construction of a tool for scenario exploration, which was divulgated to decision-makers and representatives of communities through risk communication activities (Chapter 6). Through such risk communication activities, it was proven how the web tool can also be used to transfer scenario-based risk outcomes to the directly exposed communities. Moreover, based on the understanding of the outcomes of risk scenarios and their uncertainties, decision-makers could in

the future advocate for local strategies for risk management and disaster risk prevention.

(8) Five open source and registered software were generated in the frame of this thesis (Sect. 1.3.3). Four of these codes can also work as inter-operable web-services. Seven data papers were created gathering the produced input and outputs for either exposure modelling or (multi) risk assessment (Sect. 1.3.4). Significant efforts were made to ensure that such products can constitute interoperable solutions. Hence, this collection of data and software is also an important and transparent outcome of this thesis, as be consulted, reused, and even improved by others.

Although several punctual pathways to improve the individual components were already examined in detail in every "discussion" section of Chapters 2 to 6, I do believe that regardless of the type of hazard-related vulnerability, there are a few cross-cutting aspects that are worth exploring in future studies.

i. The first one is grounded to the way risk modellers establish the link between fragility and the building typologies of the exposure model. Such a building categorization can be achieved in two distinctive directions:
    a) "reality -> model", i.e., through visual inspections of existing buildings or the use of co-variants to infer certain attributes contained in the predefined set of building classes).
    b) "model -> reality", i.e., when analytical models oversimplify the reality (i.e., the assets that are actually built largely differ to what was originally designed. Although the consideration of visual characteristics (taxonomic attributes) was significantly important in this thesis, it is important to consider that the increasing instrumentation of existing buildings (e.g., through seismic sensors that to measure their behaviour under the action of a variety of hazard intensities) is and will be more relevant. The shortcoming of this, is that the data obtained from such monitoring activities will be anyway dependent upon the occurrence of real hazardous events. Although this creates opportunities for the vulnerability assessment to certain hazards that are expected to occur more frequently in the future, there will be a bottleneck for very rare events (with low probabilities but likely high consequences) such as large tsunamis or high magnitude volcanic eruptions. Constraining the physical vulnerability of the exposed infrastructure to those events, will require yet undefined sophisticated approaches that should go beyond the expert-based frames. For this setting, the need of standardising damage scales across hazards will still be an important aspect for the scientific community to devote efforts.

ii. The second one is related to the improvement of two components entailed in the multi-hazard framework here proposed in Chapter 5, i.e., (1) the harmonisation of several damage scales into a transversal one; and (2) the derivation of state-dependent analytical fragility. Both components deserve more research attention to be optimised in the future through more refined approaches. Hopefully, that will involve the integration of real damage data to calibrate hybrid models (joint of empirical and analytical fragility models). This setting is likely to be compatible with other factors that also induce cumulative damage such as aging effects on existing structures.

This cumulative thesis has contributed to the advancement of the state of the art in exposure modelling for scenario-based (single and multi-hazard) risk assessment. It collects a significant amount of work in the proposal of new methodological approaches which were exemplified on real residential building stocks. For such a purpose, this thesis depicts the work devoted in the development of original, versatile and efficient computer codes, which later allowed to perform the heavy computations herein documented. Likewise, this thesis has paved the way for others to propose other research questions and manners of improving the methods herein presented within the context of risk assessment due to natural hazards for extended building portfolios.

Bibliography

Abbasnejadfard, M., Bastami, M., Fallah, A., and Garakaninezhad, A.: Analyzing the effect of anisotropic spatial correlations of earthquake intensity measures on the result of seismic risk and resilience assessment of the portfolio of buildings and infrastructure systems, Bulletin of Earthquake Engineering, 19, 5791–5817, https://doi.org/10.1007/s10518-021-01203-z, 2021.

Abrahamson, N., Gregor, N., and Addo, K.: BC Hydro Ground Motion Prediction Equations for Subduction Earthquakes, Earthquake Spectra, 32, 23–44, https://doi.org/10.1193/051712EQS188MR, 2016.

Acevedo, A. B., Jaramillo, J. D., Yepes, C., Silva, V., Osorio, F. A., and Villar, M.: Evaluation of the seismic risk of the unreinforced masonry building stock in Antioquia, Colombia, Natural Hazards, 86, 31–54, https://doi.org/10.1007/s11069-016-2647-8, 2017.

Acevedo, A. B., Yepes-Estrada, C., González, D., Silva, V., Mora, M., Arcila, M., and Posada, G.: Seismic risk assessment for the residential buildings of the major three cities in Colombia: Bogotá, Medellín, and Cali, Earthquake Spectra, 8755293020942537, https://doi.org/10.1177/8755293020942537, 2020.

Adriano, B., Mas, E., Koshimura, S., Estrada, M., and Jimenez, C.: Scenarios of Earthquake and Tsunami Damage Probability in Callao Region, Peru Using Tsunami Fragility Functions, Journal of Disaster Research, 9, 968–975, https://doi.org/10.20965/jdr.2014.p0968, 2014.

Aguilar, Z., Lazares, F., Alarcon, S., Quispe, S., Uriarte, R., and Calderon, D.: Actualización de la Microzonificación Sísmica de la ciudad de Lima, International Symposium for CISMID 25th Anniversary 17–18 August, 2012, Lima, Peru, 2013.

Aguilar, Z., Tarazona, J., Vergaray, L., Barrantes, J., Uriarte, R., and Calderon, D.: Site response analysis and its comparison with the peruvian seismic design spectrum, TECNIA, 29, n.º 2, ago. 2019, https://doi.org/10.21754/tecnia.v29i2.700, 2019.

Aguilera, E., Pareschi, M. T., Rosi, M., and Zanchetta, G.: Risk from Lahars in the Northern Valleys of Cotopaxi Volcano (Ecuador), Natural Hazards, 33, 161–189, https://doi.org/10.1023/B:NHAZ.0000037037.03155.23, 2004.

Aguirre, P., Vásquez, J., de la Llera, J. C., González, J., and González, G.: Earthquake damage assessment for deterministic scenarios in Iquique, Chile, Natural Hazards, 92, 1433–1461, https://doi.org/10.1007/s11069-018-3258-3, 2018.

Alam, M. S., Barbosa, A. R., Scott, M. H., Cox, D. T., and van de Lindt, J. W.: Development of Physics-Based Tsunami Fragility Functions Considering Structural Member Failures, Journal of Structural Engineering, 144, 04017221, https://doi.org/10.1061/(ASCE)ST.1943-541X.0001953, 2018.

Allen, T. I. and Wald, D. J.: Topographic Slope as a Proxy for Seismic Site-Conditions (VS30) and Amplification Around the Globe, https://doi.org/10.3133/ofr20071357, 2007.

Andrade, D., Hall, M., Mothes, P., Troncosco, L., Eissen, J.-P., Samaniego, P., Efred, J., Ramon, P., Rivero, D., and Yepes, H.: Los peligros volcánicos asociados con el Cotopaxi, IG-EPN, Quito, Ecuador, 2005.

Antoncecchi, I., Ciccone, F., Dialuce, G., Grandi, S., Terlizzeze, F., Di Bucci, D., Dolce, M., Argnani, A., Mercorella, A., Pellegrini, C., Rovere, M., Armigliato, A., Pagnoni, G., Paparo, M. A., Tinti, S., Zaniboni, F., Basili, R., Cavallaro, D., Coltelli, M., Firetto Carlino, M., Lipparini, L., Lorito, S., Maesano, F. E., Romano, F., Scarfì, L., Tiberti, M. M., Volpe, M., Fedorik, J., Toscani, G., Borzi, B., Faravelli, M., Bozzoni, F., Pascale, V., Quaroni, D., Germagnoli, F., Belliazzi, S., Del Zoppo, M., Di Ludovico, M., Lignola, G. P., and Prota, A.: Progetto SPOT - Sismicità Potenzialmente Innescabile Offshore e Tsunami: Report integrato di fine progetto, 1. Ministero dello Sviluppo Economico, https://doi.org/10.5281/zenodo.3732887, 2020.

Aravena Pelizari, P., Geiß, C., Aguirre, P., María, H. S., Peña, Y. M., and Taubenböck, H.: Automated building characterization for seismic risk assessment using street-level imagery and deep learning, ISPRS Journal of Photogrammetry and Remote Sensing, 180, 370–386, https://doi.org/10.1016/j.isprsjprs.2021.07.004, 2021.

Armaş, I. and Gavriş, A.: Social vulnerability assessment using spatial multi-criteria analysis (SEVI model) and the Social Vulnerability Index (SoVI model) – a case study for Bucharest, Romania, Natural Hazards and Earth System Sciences, 13, 1481–1499, https://doi.org/10.5194/nhess-13-1481-2013, 2013.

Armijos, M. T., Phillips, J., Wilkinson, E., Barclay, J., Hicks, A., Palacios, P., Mothes, P., and Stone, J.: Adapting to changes in volcanic behaviour: Formal and informal interactions for enhanced risk management at Tungurahua Volcano, Ecuador, Global Environmental Change, 45, 217–226, https://doi.org/10.1016/j.gloenvcha.2017.06.002, 2017.

Arrighi, C., Tanganelli, M., Cristofaro, M. T., Cardinali, V., Marra, A., Castelli, F., and De Stefano, M.: Multi-risk assessment in a historical city, Natural Hazards, https://doi.org/10.1007/s11069-021-05125-6, 2022.

Arroyo, O., Feliciano, D., Carrillo, J., and Hube, M. A.: Seismic performance of mid-rise thin concrete wall buildings lightly reinforced with deformed bars or welded wire mesh, Engineering Structures, 241, 112455, https://doi.org/10.1016/j.engstruct.2021.112455, 2021.

Attary, N., van de Lindt, J. W., Unnikrishnan, V. U., Barbosa, A. R., and Cox, D. T.: Methodology for Development of Physics-Based Tsunami Fragilities, Journal of Structural Engineering, 143, 04016223, https://doi.org/10.1061/(ASCE)ST.1943-541X.0001715, 2017.

Attary, N., Van De Lindt, J. W., Barbosa, A. R., Cox, D. T., and Unnikrishnan, V. U.: Performance-Based Tsunami Engineering for Risk Assessment of Structures Subjected to Multi-Hazards: Tsunami following Earthquake, null, 1–20, https://doi.org/10.1080/13632469.2019.1616335, 2019.

Baggio, C., Bernardini, A., Colozza, R., Corazza, L., Della Orsini, M., Di Pascuale, G., Dolce, M., Goretti, A., Martinelli, A., Orsini, G., Papa, F., and Zuccaro, G.: Field Manual for post-earthquake damage and safety assessment and short term countermeasures (AeDES), EUR 22868 EN – Joint Research Centre – Institute for the Protection and Security of the Citizen., : Office for Official Publications of the European Communities, Luxembourg, 100 pp. – 21.00 x 29.70 cm pp., 2007.

Bal, I. E., Bommer, J. J., Stafford, P. J., Crowley, H., and Pinho, R.: The Influence of Geographical Resolution of Urban Exposure Data in an Earthquake Loss Model for Istanbul, Earthquake Spectra, 26, 619–634, https://doi.org/10.1193/1.3459127, 2010.

Barberi, F., Coltelli, M., Frullani, A., Rosi, M., and Almeida, E.: Chronology and dispersal characteristics of recently (last 5000 years) erupted tephra of Cotopaxi (Ecuador): implications for long-term eruptive forecasting, Journal of Volcanology and Geothermal Research, 69, 217–239, https://doi.org/10.1016/0377-0273(95)00017-8, 1995.

Bazzurro, P. and Luco, N.: Accounting for uncertainty and correlation in earthquake loss estimation, in: Proceedings of the nineth international conference on safety and reliability of engineering systems and structures, ICOSSAR, Rome, Italy, 2005.

Behrens, J., Løvholt, F., Jalayer, F., Lorito, S., Salgado-Gálvez, M. A., Sørensen, M., Abadie, S., Aguirre-Ayerbe, I., Aniel-Quiroga, I., Babeyko, A., Baiguera, M., Basili, R., Belliazzi, S., Grezio, A., Johnson, K., Murphy, S., Paris, R., Rafliana, I., De Risi, R., Rossetto, T., Selva, J., Taroni, M., Del Zoppo, M., Armigliato, A., Bureš, V., Cech, P., Cecioni, C., Christodoulides, P., Davies, G., Dias, F., Bayraktar, H. B., González, M., Gritsevich, M., Guillas, S., Harbitz, C. B., Kânoğlu, U., Macías, J., Papadopoulos, G. A., Polet, J., Romano, F., Salamon, A., Scala, A., Stepinac, M., Tappin, D. R., Thio, H. K., Tonini, R., Triantafyllou, I., Ulrich, T., Varini, E., Volpe, M., and Vyhmeister, E.: Probabilistic Tsunami Hazard and Risk Analysis: A Review of Research Gaps, Frontiers in Earth Science, 9, https://doi.org/10.3389/feart.2021.628772, 2021.

Belliazzi, S., Lignola, G. P., Di Ludovico, M., and Prota, A.: Preliminary tsunami analytical fragility functions proposal for Italian coastal residential masonry buildings, Structures, 31, 68–79, https://doi.org/10.1016/j.istruc.2021.01.059, 2021.

Bernal, G. A., Salgado-Gálvez, M. A., Zuloaga, D., Tristancho, J., González, D., and Cardona, O.-D.: Integration of Probabilistic and Multi-Hazard Risk Assessment Within Urban Development Planning and Emergency Preparedness and Response: Application to Manizales, Colombia, International Journal of Disaster Risk Science, 8, 270–283, https://doi.org/10.1007/s13753-017-0135-8, 2017.

Bernard, B., Battaglia, J., Proaño, A., Hidalgo, S., Vásconez, F., Hernandez, S., and Ruiz, M.: Relationship between volcanic ash fallouts and seismic tremor: quantitative assessment of the 2015 eruptive period at Cotopaxi volcano, Ecuador, Bulletin of Volcanology, 78, 80, https://doi.org/10.1007/s00445-016-1077-5, 2016.

Beven, K. J., Aspinall, W. P., Bates, P. D., Borgomeo, E., Goda, K., Hall, J. W., Page, T., Phillips, J. C., Simpson, M., Smith, P. J., Wagener, T., and Watson, M.: Epistemic uncertainties and natural hazard risk assessment – Part 2: What should constitute good practice?, Natural Hazards and Earth System Sciences, 18, 2769–2783, https://doi.org/10.5194/nhess-18-2769-2018, 2018.

Biass, S., Scaini, C., Bonadonna, C., Folch, A., Smith, K., and Höskuldsson, A.: A multi-scale risk assessment for tephra fallout and airborne concentration from multiple Icelandic volcanoes – Part 1: Hazard assessment, Natural Hazards and Earth System Sciences, 14, 2265–2287, https://doi.org/10.5194/nhess-14-2265-2014, 2014.

Bindi, D., Mayfield, M., Parolai, S., Tyagunov, S., Begaliev, U. T., Abdrakhmatov, K., Moldobekov, B., and Zschau, J.: Towards an improved seismic risk scenario for Bishkek, Kyrgyz Republic, Soil Dynamics and Earthquake Engineering, 31, 521–525, https://doi.org/10.1016/j.soildyn.2010.08.009, 2011.

Bird, D. K.: The use of questionnaires for acquiring information on public perception of natural hazards and risk mitigation – a review of current knowledge and practice, Natural Hazards and Earth System

Sciences, 9, 1307–1325, https://doi.org/10.5194/nhess-9-1307-2009, 2009.

Bolić, T. and Sivčev, Ź.: Eruption of Eyjafjallajökull in Iceland: Experience of European Air Traffic Management, Transportation Research Record, 2214, 136–143, https://doi.org/10.3141/2214-17, 2011.

Bonacho, J. and Oliveira, C. S.: Multi-hazard analysis of earthquake shaking and tsunami impact, International Journal of Disaster Risk Reduction, 31, 275–280, https://doi.org/10.1016/j.ijdrr.2018.05.023, 2018.

Brill, F., Passuni Pineda, S., Espichán Cuya, B., and Kreibich, H.: A data-mining approach towards damage modelling for El Niño events in Peru, null, 11, 1966–1990, https://doi.org/10.1080/19475705.2020.1818636, 2020.

Brinckmann, N., Pittore, M., Rüster, M., Proß, B., and Gomez-Zapata, J. C.: Put your models in the web - less painful, in: EGU General Assembly Conference Abstracts, 8671, 2020.

Brinckmann, N., Gomez-Zapata, J. C., Pittore, M., and Rüster, M.: DEUS: Damage-Exposure-Update-Service. V. 1.0., GFZ Data Services, https://doi.org/10.5880/riesgos.2021.011, 2021.

Bronfman, N. C., Cisternas, P. C., López-Vázquez, E., and Cifuentes, L. A.: Trust and risk perception of natural hazards: implications for risk preparedness in Chile, Natural Hazards, 81, 307–327, https://doi.org/10.1007/s11069-015-2080-4, 2016.

Brzev, S., Scawthor, C., Charleson, AW., Allen, L., Greene, M., Jaiswal, K., and Silva, V.: GEM building taxonomy version 2.0, GEM Foundation, Pavia, 2013.

Buitinck, L., Louppe, G., Blondel, M., Pedregosa, F., Mueller, A., Grisel, O., Niculae, V., Prettenhofer, P., Gramfort, A., Grobler, J., Layton, R., VanderPlas, J., Joly, A., Holt, B., and Varoquaux, G.: API design for machine learning software: experiences from the scikit-learn project, in: ECML PKDD Workshop: Languages for Data Mining and Machine Learning, 108–122, 2013.

Cabrera, T., Hube, M., and Santa María, H.: Empirical fragility curves for reinforced concrete and timber houses, using different intensity measures, 17thWorld Conference on Earthquake Engineering, 17WCEE, Sendai, Japan, 2020.

Calderón, A. and Silva, V.: Exposure forecasting for seismic risk estimation: Application to Costa Rica, Earthquake Spectra, 8755293021989333, https://doi.org/10.1177/8755293021989333, 2021.

Calvi, G. M., Pinho, R., Magenes, G., Crowley, H., Bommer, J. J., and Restrepo-Velez, L. F.: Development of seismic vulnerability assessment methodologies over the past 30 years, ISET journal 483 of Earthquake Technology, 43, 75–104, 2006.

Candia, G., Poulos, A., de la Llera, J. C., Crempien, J. G. F., and Macedo, J.: Correlations of spectral accelerations in the Chilean subduction zone, Earthquake Spectra, 36, 788–805, https://doi.org/10.1177/8755293019891723, 2020.

Cando-Jácome, M. and Martínez-Graña, A.: Determination of Primary and Secondary Lahar Flow Paths of the Fuego Volcano (Guatemala) Using Morphometric Parameters, Remote Sensing, 11, https://doi.org/10.3390/rs11060727, 2019.

Carreño, M. L., Cardona, O. D., and Barbat, A. H.: Sistema de indicadores para la evaluación de riesgos, Centre Internacional de Mètodes Numèrics en Enginyeria (CIMNE), Barcelona, 2005.

Carvajal, M., Cisternas, M., and Catalán, P. A.: Source of the 1730 Chilean earthquake from historical records: Implications for the future tsunami hazard on the coast of Metropolitan Chile, Journal of Geophysical Research: Solid Earth, 122, 3648–3660, https://doi.org/10.1002/2017JB014063, 2017.

Ceferino, L., Kiremidjian, A., and Deierlein, G.: Probabilistic Model for Regional Multiseverity Casualty Estimation due to Building Damage Following an Earthquake, ASCE-ASME Journal of Risk and Uncertainty in Engineering Systems, Part A: Civil Engineering, 4, 04018023, https://doi.org/10.1061/AJRUA6.0000972, 2018a.

Ceferino, L., Kiremidjian, A., and Deierlein, G.: Regional Multiseverity Casualty Estimation Due to Building Damage following a Mw 8.8 Earthquake Scenario in Lima, Peru, Earthquake Spectra, 34, 1739–1761, https://doi.org/10.1193/080617EQS154M, 2018b.

Ceferino, L., Mitrani-Reiser, J., Kiremidjian, A., Deierlein, G., and Bambarén, C.: Effective plans for hospital system response to earthquake emergencies, Nature Communications, 11, 4325, https://doi.org/10.1038/s41467-020-18072-w, 2020.

Cerri, M., Steinhausen, M., Kreibich, H., and Schröter, K.: Are OpenStreetMap building data useful for flood vulnerability modelling?, Natural Hazards and Earth System Sciences, 21, 643–662, https://doi.org/10.5194/nhess-21-643-2021, 2021.

Charvet, I., Suppasri, A., Kimura, H., Sugawara, D., and Imamura, F.: A multivariate generalized linear tsunami fragility model for Kesennuma City based on maximum flow depths, velocities and debris impact, with evaluation of predictive accuracy, Natural Hazards, 79, 2073–2099, https://doi.org/10.1007/s11069-015-1947-8, 2015.

Charvet, I., Macabuag, J., and Rossetto, T.: Estimating Tsunami-Induced Building Damage through Fragility Functions: Critical Review and Research Needs, Frontiers in Built Environment, 3, 36, https://doi.org/10.3389/fbuil.2017.00036, 2017.

Chen, Y., Park, H., Chen, Y., Corcoran, P., Cox, D., Reimer, J. J., and Weber, B.: Integrated Engineering-Economic Model for the Assessment of Regional Economic Vulnerability to Tsunamis, Natural Hazards Review, 19, 04018018, https://doi.org/10.1061/(ASCE)NH.1527-6996.0000307, 2018.

Christie, R., Cooke, O., and Gottsmann, J.: Fearing the knock on the door: critical security studies insights into limited cooperation with disaster management regimes, Journal of Applied Volcanology, 4, 19, https://doi.org/10.1186/s13617-015-0037-7, 2015.

Documentation for the Gridded Population of theWorld, Version 4 (GPWv4), Revision 11 Data Sets,: htps://doi.org/10.7927/H45Q4T5F.

Comte, D., Eisenberg, A., Lorca, E., Pardo, M., Ponce, L., Saragoni, R., Singh, S. K., and Suarez, G.: The 1985 Central Chile Earthquake: A Repeat of Previous Great Earthquakes in the Region?, Science, 233, 449, https://doi.org/10.1126/science.233.4762.449, 1986.

Contreras, D., Wilkinson, S., and James, P.: Earthquake Reconnaissance Data Sources, a Literature Review, Earth, 2, 1006–1037, https://doi.org/10.3390/earth2040060, 2021.

Corbane, C., Hancilar, U., Ehrlich, D., and De Groeve, T.: Pan-European seismic risk assessment: a proof of concept using the Earthquake Loss Estimation Routine (ELER), Bulletin of Earthquake Engineering, 15, 1057–1083, https://doi.org/10.1007/s10518-016-9993-5, 2017.

Cornell, C. A. and Krawinkler, H.: Progress and Challenges in Seismic Performance Assessment, PEER Center News, 3(2), 1–3, 2000.

Cox, D. R. and Isham, V.: Point processes, Chapman and Hall, London, New York, 1980.

Craig, H., Wilson, T., Stewart, C., Villarosa, G., Outes, V., Cronin, S., and Jenkins, S.: Agricultural impact assessment and management after three widespread tephra falls in Patagonia, South America, Natural Hazards, 82, 1167–1229, https://doi.org/10.1007/s11069-016-2240-1, 2016.

Cremen, G., Galasso, C., and McCloskey, J.: Modelling and quantifying tomorrow's risks from natural hazards, Science of The Total Environment, 817, 152552, https://doi.org/10.1016/j.scitotenv.2021.152552, 2022.

Croasmun, J. and Ostrom, L.: Using Likert-Type Scales in the Social Sciences, Journal of Adult Education, 40, 2011.

Crowley, H.: Earthquake Risk Assessment: Present Shortcomings and Future Directions, in: Perspectives on European Earthquake Engineering and Seismology: Volume 1, edited by: Ansal, A., Springer International Publishing, Cham, 515–532, https://doi.org/10.1007/978-3-319-07118-3_16, 2014.

Crowley, H. and Bommer, J. J.: Modelling Seismic Hazard in Earthquake Loss Models with Spatially Distributed Exposure, Bulletin of Earthquake Engineering, 4, 275–275, https://doi.org/10.1007/s10518-006-9011-4, 2006.

Crowley, H. and Pinho, R.: Period-Height Relationship for Existing European Reinforced Concrete Buildings, Journal of Earthquake Engineering, 8, 93–119, https://doi.org/10.1080/13632460409350522, 2004.

Crowley, H., Bommer, J. J., Pinho, R., and Bird, J.: The impact of epistemic uncertainty on an earthquake loss model, Earthquake Engineering & Structural Dynamics, 34, 1653–1685, https://doi.org/10.1002/eqe.498, 2005.

Crowley, H., Despotaki, V., Rodrigues, D., Silva, V., Toma-Danila, D., Riga, E., Karatzetzou, A., Fotopoulou, S., Zugic, Z., Sousa, L., Ozcebe, S., and Gamba, P.: Exposure model for European seismic risk assessment, Earthquake Spectra, 8755293020919429, https://doi.org/10.1177/8755293020919429, 2020.

Crucitti, P., Latora, V., and Marchiori, M.: Model for cascading failures in complex networks, Phys. Rev. E, 69, 045104, https://doi.org/10.1103/PhysRevE.69.045104, 2004.

Czerny, M. and Czerny, A.: Urbanisation processes in zones threatened by volcanic activity: The case of Latacunga at the foot of Cotopaxi in Ecuador, Miscellanea Geographica, 24, 183–192, https://doi.org/10.2478/mgrsd-2020-0040, 2020.

Dabbeek, J. and Silva, V.: Modeling the residential building stock in the Middle East for multi-hazard risk assessment, Natural Hazards, 100, 781–810, https://doi.org/10.1007/s11069-019-03842-7, 2020.

Dabbeek, J., Silva, V., Galasso, C., and Smith, A.: Probabilistic earthquake and flood loss assessment in the Middle East, International Journal of Disaster Risk Reduction, 49, 101662, https://doi.org/10.1016/j.ijdrr.2020.101662, 2020.

Dabbeek, J., Crowley, H., Silva, V., Weatherill, G., Paul, N., and Nievas, C. I.: Impact of exposure spatial resolution on seismic loss estimates in regional

portfolios, Bulletin of Earthquake Engineering, https://doi.org/10.1007/s10518-021-01194-x, 2021.

Daniell, J. E., Schaefer, A. M., and Wenzel, F.: Losses Associated with Secondary Effects in Earthquakes, Frontiers in Built Environment, 3, 30, https://doi.org/10.3389/fbuil.2017.00030, 2017.

D'Ayala, D., Galasso, C., Nassirpour, A., Adhikari, R. K., Yamin, L., Fernandez, R., Lo, D., Garciano, L., and Oreta, A.: Resilient communities through safer schools, International Journal of Disaster Risk Reduction, 45, 101446, https://doi.org/10.1016/j.ijdrr.2019.101446, 2020.

De Angeli, S., Malamud, B. D., Rossi, L., Taylor, F. E., Trasforini, E., and Rudari, R.: A multi-hazard framework for spatial-temporal impact analysis, International Journal of Disaster Risk Reduction, 102829, https://doi.org/10.1016/j.ijdrr.2022.102829, 2022.

De Risi, R., Goda, K., Yasuda, T., and Mori, N.: Is flow velocity important in tsunami empirical fragility modeling?, Earth-Science Reviews, 166, 64–82, https://doi.org/10.1016/j.earscirev.2016.12.015, 2017.

Del Zoppo, M., Wijesundara, K., Rossetto, T., Dias, P., Baiguera, M., Ludovico, M. D., Thamboo, J., and Prota, A.: Influence of exterior infill walls on the performance of RC frames under tsunami loads: Case study of school buildings in Sri Lanka, Engineering Structures, 234, 111920, https://doi.org/10.1016/j.engstruct.2021.111920, 2021.

Deligne, N. I., Horspool, N., Canessa, S., Matcham, I., Williams, G. T., Wilson, G., and Wilson, T. M.: Evaluating the impacts of volcanic eruptions using RiskScape, Journal of Applied Volcanology, 6, 18, https://doi.org/10.1186/s13617-017-0069-2, 2017.

Dell'Acqua, F., Gamba, P., and Jaiswal, K.: Spatial aspects of building and population exposure data and their implications for global earthquake exposure modeling, Natural Hazards, 68, 1291–1309, https://doi.org/10.1007/s11069-012-0241-2, 2013.

Dilley, M.: Natural disaster hotspots a global risk analysis, Washington, D.C, World Bank, 2005.

Doocy, S., Daniels, A., Dooling, S., and Gorokhovich, Y.: The human impact of volcanoes: a historical review of events 1900-2009 and systematic literature review, PLoS Curr, 5, ecurrents.dis.841859091a706efebf8a30f4ed7a1901, https://doi.org/10.1371/currents.dis.841859091a706efebf8a30f4ed7a1901, 2013.

Dorbath, L., Cisternas, A., and Dorbath, C.: Assessment of the size of large and great historical earthquakes in Peru, Bulletin of the Seismological Society of America, 80, 551–576, 1990.

Doyle, E. E. H., McClure, J., Johnston, D. M., and Paton, D.: Communicating likelihoods and probabilities in forecasts of volcanic eruptions, Journal of Volcanology and Geothermal Research, 272, 1–15, https://doi.org/10.1016/j.jvolgeores.2013.12.006, 2014a.

Doyle, E. E. H., McClure, J., Paton, D., and Johnston, D. M.: Uncertainty and decision making: Volcanic crisis scenarios, International Journal of Disaster Risk Reduction, 10, 75–101, https://doi.org/10.1016/j.ijdrr.2014.07.006, 2014b.

ERDAS: ERDAS Imagine 2014, Hexagon Geospatial, Peachtree Corners Circle Norcross, 2014.

ESA: European Space Agency, European Space Agency, 2018.

Feldmeyer, D., Meisch, C., Sauter, H., and Birkmann, J.: Using OpenStreetMap Data and Machine Learning to Generate Socio-Economic Indicators, ISPRS International Journal of Geo-Information, 9, https://doi.org/10.3390/ijgi9090498, 2020.

FEMA: Multi-hazard loss estimation methodology, Federal Emergency Management Agency, Washington, 2003.

FEMA: Hazus mr-MH 2.1 user manual, earthquake model, 2012.

FEMA: HAZUS Tsunami Model Technical Guidance, Federal Emergency Management Agency, Washington, D.C., 2017.

FEMA 154: Rapid Visual Screening of Buildings for Potential Seismic Hazards, 2nd ed., APPLIED TECHNOLOGY COUNCIL 555 Twin Dolphin Drive, Suite 550 Redwood City, California 94065, 2002.

Figueiredo, R. and Martina, M.: Using open building data in the development of exposure data sets for catastrophe risk modelling, Natural Hazards and Earth System Sciences, 16, 417–429, https://doi.org/10.5194/nhess-16-417-2016, 2016.

Figueiredo, R., Romão, X., and Paupério, E.: Component-based flood vulnerability modelling for cultural heritage buildings, International Journal of Disaster Risk Reduction, 61, 102323, https://doi.org/10.1016/j.ijdrr.2021.102323, 2021.

Fleming, K., Abad, J., Booth, L., Schueller, L., Baills, A., Scolobig, A., Petrovic, B., Zuccaro, G., and Leone, M. F.: The use of serious games in engaging stakeholders for disaster risk reduction, management and climate change adaption information elicitation, International Journal of Disaster Risk Reduction, 49, 101669, https://doi.org/10.1016/j.ijdrr.2020.101669, 2020.

Frazier, T. G., Wood, E. X., and Peterson, A. G.: Residual risk in public health and disaster management, Applied Geography, 125, 102365, https://doi.org/10.1016/j.apgeog.2020.102365, 2020.

Frimberger, T., Andrade, D., Weber, D., and Krautblatter, M.: Modelling future lahars controlled by different volcanic eruption scenarios at Cotopaxi (Ecuador) calibrated with the massively destructive 1877 lahar, In print at Earth Surface Processes and Landforms, 2020.

Frontuto, V., Dalmazzone, S., Salcuni, F., and Pezzoli, A.: Risk Aversion, Inequality and Economic Evaluation of Flood Damages: A Case Study in Ecuador, Sustainability, 12, https://doi.org/10.3390/su122310068, 2020.

Frucht, E., Salamon, A., Rozelle, J., Levi, T., Calvo, R., Avirav, V., Burns, J. N., Zuzak, C., Gal, E., Trapper, P., Galanti, B., and Bausch, D.: Tsunami loss assessment based on Hazus approach – The Bat Galim, Israel, case study, Engineering Geology, 289, 106175, https://doi.org/10.1016/j.enggeo.2021.106175, 2021.

Gallina, V., Torresan, S., Critto, A., Sperotto, A., Glade, T., and Marcomini, A.: A review of multi-risk methodologies for natural hazards: Consequences and challenges for a climate change impact assessment, Journal of Environmental Management, 168, 123–132, https://doi.org/10.1016/j.jenvman.2015.11.011, 2016.

García, C. and Mendez-Fajury, R.: If I Understand, I Am Understood: Experiences of Volcanic Risk Communication in Colombia, in: Observing the Volcano World: Volcano Crisis Communication, edited by: Fearnley, C. J., Bird, D. K., Haynes, K., McGuire, W. J., and Jolly, G., Springer International Publishing, Cham, 335–351, https://doi.org/10.1007/11157_2016_46, 2018.

Gehl, P. and D'Ayala, D.: System loss assessment of bridge networks accounting for multi-hazard interactions, Structure and Infrastructure Engineering, 14, 1355–1371, https://doi.org/10.1080/15732479.2018.1434671, 2018.

Gehl, P., Quinet, C., Le Cozannet, G., Kouokam, E., and Thierry, P.: Potential and limitations of risk scenario tools in volcanic areas through an example at Mount Cameroon, Natural Hazards and Earth System Sciences, 13, 2409–2424, https://doi.org/10.5194/nhess-13-2409-2013, 2013.

Geiß, C., Schauß, A., Riedlinger, T., Dech, S., Zelaya, C., Guzmán, N., Hube, M. A., Arsanjani, J. J., and Taubenböck, H.: Joint use of remote sensing data and volunteered geographic information for exposure estimation: evidence from Valparaíso, Chile, Natural Hazards, 86, 81–105, https://doi.org/10.1007/s11069-016-2663-8, 2017a.

Geiß, C., Thoma, M., Pittore, M., Wieland, M., Dech, S. W., and Taubenbock, H.: Multitask Active Learning for Characterization of Built Environments With Multisensor Earth Observation Data, IEEE Journal of Selected Topics in Applied Earth Observations and Remote Sensing, 10, 5583–5597, https://doi.org/10.1109/JSTARS.2017.2748339, 2017b.

Geiß, C., Aravena Pelizari, P., Priesmeier, P., Calderon, A. R. S., Schoepfer, E., Langbein, M., Riedlinger, T., Santa María, H., Gómez Zapata, J. C., Pittore, M., and Taubenböck, H.: Earth Observation Techniques for Spatial Disaggregation of Exposure Data, in: EGU General Assembly Conference Abstracts, EGU21-8574, 2021.

Geller, R. J.: Chapter 22 - Geoethics, Risk-Communication, and Scientific Issues in Earthquake Science, in: Geoethics, edited by: Wyss, M. and Peppoloni, S., Elsevier, Oxford, 263–272, https://doi.org/10.1016/B978-0-12-799935-7.00022-8, 2015.

GEM: Report on the SARA Exposure and Vulnerability Workshop in Medellin, Colombia, 2014.

Ghofrani, H. and Atkinson, G. M.: Ground-motion prediction equations for interface earthquakes of M7 to M9 based on empirical data from Japan, Bulletin of Earthquake Engineering, 12, 549–571, https://doi.org/10.1007/s10518-013-9533-5, 2014.

Gill, J. C. and Malamud, B. D.: Hazard interactions and interaction networks (cascades) within multi-hazard methodologies, Earth System Dynamics, 7, 659–679, https://doi.org/10.5194/esd-7-659-2016, 2016.

Gill, J. C., Malamud, B. D., Barillas, E. M., and Guerra Noriega, A.: Construction of regional multi-hazard interaction frameworks, with an application to Guatemala, Natural Hazards and Earth System Sciences, 20, 149–180, https://doi.org/10.5194/nhess-20-149-2020, 2020.

Goda, K. and De Risi, R.: Multi-hazard loss estimation for shaking and tsunami using stochastic rupture sources, International Journal of Disaster Risk Reduction, 28, 539–554, https://doi.org/10.1016/j.ijdrr.2018.01.002, 2018.

Goda, K., Mori, N., Yasuda, T., Prasetyo, A., Muhammad, A., and Tsujio, D.: Cascading Geological Hazards and Risks of the 2018 Sulawesi Indonesia Earthquake and Sensitivity Analysis of Tsunami Inundation Simulations, Frontiers in Earth Science, 7, 261, https://doi.org/10.3389/feart.2019.00261, 2019.

Gómez Zapata, J. C., Pittore, M., Brinckmann, N., and Shinde, S.: Dynamic physical vulnerability: a Multi-risk Scenario approach from building- single- hazard fragility- models, in: EGU General Assembly Conference Abstracts, Online, 18379, 2020.

Gómez Zapata, J. C., Zafrir, R., Harig, S., and Pittore, M.: Customised focus maps and resultant CVT-based aggregation entities for Lima and Callao (Peru). V. 1.0., GFZ Data Services, https://doi.org/10.5880/riesgos.2021.006, 2021a.

Gómez Zapata, J. C., Zafrir, R., Brinckmann, N., and Pittore, M.: Residential building exposure and physical vulnerability models for ground-shaking and tsunami risk in Lima and Callao (Peru). V. 1.0., GFZ Data Services, https://doi.org/10.5880/riesgos.2021.007, 2021b.

Gómez Zapata, J. C., Shinde, S., Pittore, M., and Merino-Peña, Y.: Scripts to generate (1) attribute-based fuzzy scores for SARA and HAZUS building classes, and (2) probabilistic inter-scheme compatibility matrices. An application on the residential building stock of Valparaiso (Chile) for seismic risk applications, GFZ Data Services, https://doi.org/10.5880/riesgos.2021.002, 2021c.

Gómez Zapata, J. C., Brinckmann, N., Pittore, M., and Cotton, F.: Seismic ground motion fields for six deterministic earthquake scenarios (Mw 8.5-9.0) for Lima (Peru), GFZ Data Services, https://doi.org/10.5880/riesgos.2021.008, 2021d.

Gómez Zapata, J. C., Brinckmann, N., Pittore, M., and Cotton, F.: Spatial representation of direct loss estimates on the residential building stock of Lima (Peru) from decoupled earthquake and tsunami scenarios on variable resolutions exposure models., GFZ Data Services, https://doi.org/10.5880/riesgos.2021.009, 2021e.

Gómez Zapata, J. C., Brinckmann, N., Harig, S., Zafrir, R., Pittore, M., Cotton, F., and Babeyko, A.: Variable-resolution building exposure modelling for earthquake and tsunami scenario-based risk assessment. An application case in Lima, Peru, Natural Hazards and Earth System Sciences, 21, 3599–3628, https://doi.org/10.5194/nhess-21-3599-2021, 2021f.

Gómez Zapata, J. C., Medina, S., and Lizarazo-Marriaga, J.: Creation of simplified state-dependent fragility functions through ad-hoc scaling factors to account for previous damage in a multi-hazard risk context. An application to flow-depth-based analytical tsunami fragility functions for the Pacific coast of South America, GFZ Data Services, https://doi.org/10.5880/riesgos.2022.002/ Review link: https://dataservices.gfz-potsdam.de/panmetaworks/review/b1e611344f04b57fa73d31e48f5b482cda74afa8254c5685ad0fe4f97d3f8c6c/, 2022a.

Gómez Zapata, J. C., Pittore, M., Cotton, F., Lilienkamp, H., Simantini, S., Aguirre, P., and Hernan, S. M.: Epistemic uncertainty of probabilistic building exposure compositions in scenario-based earthquake loss models, Bulletin of Earthquake Engineering, https://doi.org/10.1007/s10518-021-01312-9, 2022b.

Gómez Zapata, J. C., Pittore, M., and Lizarazo, J. M.: Probabilistic inter-scheme compatibility matrices for multi-hazard exposure modeling. An application using existing vulnerability models for earthquakes and tsunami from synthetic datasets constructed using the AeDEs form through expert-based heuristics, GFZ Data Services, https://doi.org/10.5880/riesgos.2022.003 Review link https://dataservices.gfz-potsdam.de/panmetaworks/review/6355f1be60969620c71b09b4ff4595d9f3d2247b30260a49cce816c9f5f41e0d/, 2022c.

Grigoratos, I., Dabeek, J., Faravelli, M., Di Meo, A., Cerchiello, V., Borzi, B., Monteiro, R., and Ceresa, P.: Development of A Fragility and Exposure Model for Palestine – Application to The City of Nablus, Procedia Engineering, 161, 2023–2029, https://doi.org/10.1016/j.proeng.2016.08.797, 2016.

Grünthal, G.: European Macroseismic Scale 1998, Centre Européen de Géodynamique et de Séismologie., Luxembourg, 1998.

Grupo FARO, Asociación de Profesionales de Gestión de Riesgos de Ecuador, and Instituto Superior Tecnológico Cotopaxi: Percepción social del riesgo en la ciudad de Latacunga, Quito, Ecuador, 2020.

Gunasekera, R., Ishizawa, O., Aubrecht, C., Blankespoor, B., Murray, S., Pomonis, A., and Daniell, J.: Developing an adaptive global exposure model to support the generation of country disaster risk profiles, Earth-Science Reviews, 150, 594–608, https://doi.org/10.1016/j.earscirev.2015.08.012, 2015.

Haas, M.: Towards time- and state-dependent seismic risk over urban scales, PhD thesis, der Technischen Universität Berlin, Berlin, Germany, 222 pp., 2018.

DEMO: Remote Rapid Visual Screening (RRVS): https://vimeo.com/158600573.

Hall, M. and Mothes, P.: The rhyolitic–andesitic eruptive history of Cotopaxi volcano, Ecuador, Bulletin of Volcanology, 70, 675–702, https://doi.org/10.1007/s00445-007-0161-2, 2008.

Hancilar, U., Tuzun, C., Yenidogan, C., and Erdik, M.: ELER software – a new tool for urban earthquake loss assessment, Natural Hazards and Earth System Sciences, 10, 2677–2696, https://doi.org/10.5194/nhess-10-2677-2010, 2010.

Harig, S. and Rakowsky, N.: Tsunami flow depth in Lima/Callao (Peru) caused by six hypothetical simplified tsunami scenarios offshore Lima, GFZ Data Services, https://doi.org/10.5880/riesgos.2021.010, 2021.

Harig, S., Chaeroni, Pranowo, W. S., and Behrens, J.: Tsunami simulations on several scales, Ocean Dynamics, 58, 429–440, https://doi.org/10.1007/s10236-008-0162-5, 2008.

Harig, S., Immerz, A., Weniza, Griffin, J., Weber, B., Babeyko, A., Rakowsky, N., Hartanto, D., Nurokhim, A., Handayani, T., and Weber, R.: The Tsunami Scenario Database of the Indonesia Tsunami Early Warning System (InaTEWS): Evolution of the Coverage and the Involved Modeling Approaches, Pure and Applied Geophysics, 177, 1379–1401, https://doi.org/10.1007/s00024-019-02305-1, 2020.

Hastie, D. I., Liverani, S., and Richardson, S.: Sampling from Dirichlet process mixture models with unknown concentration parameter: mixing issues in large data implementations, Statistics and Computing, 25, 1023–1037, https://doi.org/10.1007/s11222-014-9471-3, 2015.

Heath, D. C., Wald, D. J., Worden, C. B., Thompson, E. M., and Smoczyk, G. M.: A global hybrid VS30 map with a topographic slope–based default and regional map insets, Earthquake Spectra, 36, 1570–1584, https://doi.org/10.1177/8755293020911137, 2020.

Hecht, R., Kunze, C., and Hahmann, S.: Measuring completeness of building footprints in OpenStreetMap over space and time, ISPRS International Journal of Geo-Information, 2, 1066–1091, 2013.

Heifer Fundation: Páramos de Cotopaxi y cambio climático. Experiencias campesinas de adaptación al cambio climático, Fundación Heifer, Quito, Ecuador, 2018.

Heinzlef, C., Robert, B., Hémond, Y., and Serre, D.: Operating urban resilience strategies to face climate change and associated risks: some advances from theory to application in Canada and France, Cities, 104, 102762, https://doi.org/10.1016/j.cities.2020.102762, 2020a.

Heinzlef, C., Barocca, B., Leone, M., Glade, T., and Serre, D.: Resilience issues and challenges into built environments: a review, Natural Hazards and Earth System Sciences Discussions, 2020, 1–35, https://doi.org/10.5194/nhess-2020-217, 2020b.

Hicks, A., Armijos, M. T., Barclay, J., Stone, J., Robertson, R., and Cortés, G. P.: Risk communication films: Process, product and potential for improving preparedness and behaviour change, International Journal of Disaster Risk Reduction, 23, 138–151, https://doi.org/10.1016/j.ijdrr.2017.04.015, 2017.

Hill, M. and Rossetto, T.: Comparison of building damage scales and damage descriptions for use in earthquake loss modelling in Europe, Bulletin of Earthquake Engineering, 6, 335–365, https://doi.org/10.1007/s10518-007-9057-y, 2008.

Horney, J., Nguyen, M., Salvesen, D., Tomasco, O., and Berke, P.: Engaging the public in planning for disaster recovery, International Journal of Disaster Risk Reduction, 17, 33–37, https://doi.org/10.1016/j.ijdrr.2016.03.011, 2016.

Hoyos, M. C. and Hernández, A. F.: Impact of vulnerability assumptions and input parameters in urban seismic risk assessment, Bulletin of Earthquake Engineering, 19, 4407–4434, https://doi.org/10.1007/s10518-021-01140-x, 2021.

Hussain, E., Elliott, J. R., Silva, V., Vilar-Vega, M., and Kane, D.: Contrasting seismic risk for Santiago, Chile, from near-field and distant earthquake sources, Natural Hazards and Earth System Sciences, 20, 1533–1555, https://doi.org/10.5194/nhess-20-1533-2020, 2020.

Imamura, F., Boret, S. P., Suppasri, A., and Muhari, A.: Recent occurrences of serious tsunami damage and the future challenges of tsunami disaster risk reduction, Progress in Disaster Science, 1, 100009, https://doi.org/10.1016/j.pdisas.2019.100009, 2019.

Indirli, M., Razafindrakoto, H., Romanelli, F., Puglisi, C., Lanzoni, L., Milani, E., Munari, M., and Apablaza, S.: Hazard Evaluation in Valparaíso: the MAR VASTO Project, Pure and Applied Geophysics, 168, 543–582, https://doi.org/10.1007/s00024-010-0164-3, 2011.

INE: Censo de Población y Vivienda 2002, Instituto Nacional de Estadística de Chile, 2002.

INE: Base cartográfica censal. Alcances y consideraciones para el usuario, Departamento de Demografía y Censos, Instituto Nacional de Estadísticas., Santiago, Chile, 2018.

INEC: Censo de Poblacion y Vivienda. Estadisticas de vivienda y hogares. Quito-Ecuador., 2010.

INEI: Censos Nacionales 2017, Instituto Nacional de Estadistica e Informatica (INEI; Institute of Statistic and Informatics), Lima, Peru, 2017.

INITN: Instituto nacional de investigaciones tecnológica y normalizaciones, cálculo antisísmico de edificios, NCh.433 Of.72. Technical report, 1972.

INN: Instituto nacional de normalización diseño sísmico de edificios, NCh.433 Of.96. Technical report, 1996.

Issaks, E. H. and Srivastava, R. M.: An Introduction to Applied Geostatistics, University Press, New York, Oxford, 413 pp., 1989.

Jaiswal, K., Wald, D., and Porter, K.: A Global Building Inventory for Earthquake Loss Estimation and Risk Management, Earthquake Spectra, 26, 731–748, https://doi.org/10.1193/1.3450316, 2010.

Jayaram, N. and Baker, J. W.: Correlation model for spatially distributed ground-motion intensities, Earthquake Engineering & Structural Dynamics, 38, 1687–1708, https://doi.org/10.1002/eqe.922, 2009.

Jenkins, S. F., Spence, R. J. S., Fonseca, J. F. B. D., Solidum, R. U., and Wilson, T. M.: Volcanic risk assessment: Quantifying physical vulnerability in the built environment, Journal of Volcanology and Geothermal Research, 276, 105–120, https://doi.org/10.1016/j.jvolgeores.2014.03.002, 2014.

Jenkins, S. F., Phillips, J. C., Price, R., Feloy, K., Baxter, P. J., Hadmoko, D. S., and de Bélizal, E.: Developing building-damage scales for lahars: application to Merapi volcano, Indonesia, Bull Volcanol, 77, 75, https://doi.org/10.1007/s00445-015-0961-8, 2015.

Jiménez, B., Pelà, L., and Hurtado, M.: Building survey forms for heterogeneous urban areas in seismically hazardous zones. Application to the historical center of Valparaíso, Chile, International Journal of Architectural Heritage, 12, 1076–1111, https://doi.org/10.1080/15583058.2018.1503370, 2018.

Jimenez, C., Moggiano, N., Mas, E., Adriano, B., Koshimura, S., Fujii, Y., and Yanagisawa, and H.: Seismic Source of 1746 Callao Earthquake from Tsunami Numerical Modeling, Journal of Disaster Research, 8, 266–273, https://doi.org/10.20965/jdr.2013.p0266, 2013.

Jiménez Martínez, M., Jiménez Martínez, M., and Romero-Jarén, R.: How resilient is the labour market against natural disaster? Evaluating the effects from the 2010 earthquake in Chile, Natural Hazards, 104, 1481–1533, https://doi.org/10.1007/s11069-020-04229-9, 2020.

Jóhannesdóttir, G. and Gísladóttir, G.: People living under threat of volcanic hazard in southern Iceland: vulnerability and risk perception, Natural Hazards and Earth System Sciences, 10, 407–420, https://doi.org/10.5194/nhess-10-407-2010, 2010.

Julià, P. B. and Ferreira, T. M.: From single- to multi-hazard vulnerability and risk in Historic Urban Areas: a literature review, Natural Hazards, 108, 93–128, https://doi.org/10.1007/s11069-021-04734-5, 2021.

Kalakonas, P., Silva, V., Mouyiannou, A., and Rao, A.: Exploring the impact of epistemic uncertainty on a regional probabilistic seismic risk assessment model, Natural Hazards, https://doi.org/10.1007/s11069-020-04201-7, 2020.

Kappes, M. S., Keiler, M., von Elverfeldt, K., and Glade, T.: Challenges of analyzing multi-hazard risk: a review, Natural Hazards, 64, 1925–1958, https://doi.org/10.1007/s11069-012-0294-2, 2012.

Karapetrou, S., Manakou, M., Bindi, D., Petrovic, B., and Pitilakis, K.: "Time-building specific" seismic vulnerability assessment of a hospital RC building using field monitoring data, Engineering Structures, 112, 114–132, https://doi.org/10.1016/j.engstruct.2016.01.009, 2016.

Kechidi, S., Castro, J. M., Monteiro, R., Marques, M., Yelles, K., Bourahla, N., and Hamdache, M.: Development of exposure datasets for earthquake damage and risk modelling: the case study of northern Algeria, Bulletin of Earthquake Engineering, https://doi.org/10.1007/s10518-021-01161-6, 2021.

Kelman, I.: Lost for Words Amongst Disaster Risk Science Vocabulary?, International Journal of Disaster Risk Science, 9, 281–291, https://doi.org/10.1007/s13753-018-0188-3, 2018.

Komendantova, N., Mrzyglocki, R., Mignan, A., Khazai, B., Wenzel, F., Patt, A., and Fleming, K.: Multi-hazard and multi-risk decision-support tools as a part of participatory risk governance: Feedback from civil protection stakeholders, International Journal of Disaster Risk Reduction, 8, 50–67, https://doi.org/10.1016/j.ijdrr.2013.12.006, 2014.

Kotha, S. R., Bazzurro, P., and Pagani, M.: Effects of Epistemic Uncertainty in Seismic Hazard Estimates on Building Portfolio Losses, Earthquake Spectra, 34, 217–236, https://doi.org/10.1193/020515EQS020M, 2018.

Kulikov, E. A., Rabinovich, A. B., and Thomson, R. E.: Estimation of Tsunami Risk for the Coasts of Peru and Northern Chile, Natural Hazards, 35, 185–209, https://doi.org/10.1007/s11069-004-4809-3, 2005.

Kwok, A. H., Paton, D., Becker, J., Hudson-Doyle, E. E., and Johnston, D.: A bottom-up approach to developing a neighbourhood-based resilience measurement framework, Disaster Prevention and Management: An International Journal, 27, 255–270, https://doi.org/10.1108/DPM-07-2017-0169, 2018.

Lagomarsino, S. and Giovinazzi, S.: Macroseismic and mechanical models for the vulnerability and damage assessment of current buildings, Bulletin of Earthquake Engineering, 4, 415–443, https://doi.org/10.1007/s10518-006-9024-z, 2006.

Lagomarsino, S., Cattari, S., and Ottonelli, D.: The heuristic vulnerability model: fragility curves for masonry buildings, Bulletin of Earthquake Engineering, 19, 3129–3163, https://doi.org/10.1007/s10518-021-01063-7, 2021.

Lahcene, E., Ioannou, I., Suppasri, A., Pakoksung, K., Paulik, R., Syamsidik, S., Bouchette, F., and Imamura, F.: Characteristics of building fragility curves for seismic and non-seismic tsunamis: case studies of the 2018 Sunda Strait, 2018 Sulawesi-Palu and 2004 Indian Ocean tsunamis, Natural Hazards and Earth System Sciences, 2020, 1–36, https://doi.org/10.5194/nhess-21-2313-2021, 2021.

Langbein, M., Gomez-Zapata, J. C., Frimberger, T., Brinckmann, N., Torres-Corredor, R., Andrade, D., Zapata-Tapia, C., Pittore, M., and Schoepfer, E.: Scenario- based multi- risk assessment on exposed buildings to volcanic cascading hazards, in: EGU General Assembly Conference Abstracts, 19861, 2020.

Tsunami hazard and its challenges for preparedness: https://www.thejakartapost.com/academia/2019/01/08/tsunami-hazard-and-its-challenges-for-preparedness.html.

Leonard, G. S., Stewart, C., Wilson, T. M., Procter, J. N., Scott, B. J., Keys, H. J., Jolly, G. E., Wardman, J. B., Cronin, S. J., and McBride, S. K.: Integrating multidisciplinary science, modelling and impact data into evolving, syn-event volcanic hazard mapping and communication: A case study from the 2012 Tongariro eruption crisis, New Zealand, Journal of Volcanology and Geothermal Research, 286, 208–232, https://doi.org/10.1016/j.jvolgeores.2014.08.018, 2014.

Lévy, J.: Science + Space + Society: urbanity and the risk of methodological communalism in social sciences of space, Geographica Helvetica, 69, 99–114, https://doi.org/10.5194/gh-69-99-2014, 2014.

Li, M., Wang, J., and Sun, X.: Scenario-based risk framework selection and assessment model development for natural disasters: a case study of typhoon storm surges, Natural Hazards, 80, 2037–2054, https://doi.org/10.1007/s11069-015-2059-1, 2016.

Li, X., Li, Z., Yang, J., Li, H., Liu, Y., Fu, B., and Yang, F.: Seismic vulnerability comparison between rural Weinan and other rural areas in Western China, International Journal of Disaster Risk Reduction, 48, 101576, https://doi.org/10.1016/j.ijdrr.2020.101576, 2020.

Liguori, N., Tarque, N., Bambarén, C., Spacone, E., Viveen, W., and Filippo, G. de: Hospital treatment capacity in case of seismic scenario in the Lima Metropolitan area, Peru, International Journal of Disaster Risk Reduction, 38, 101196, https://doi.org/10.1016/j.ijdrr.2019.101196, 2019.

Liu, B., Siu, Y. L., and Mitchell, G.: Hazard interaction analysis for multi-hazard risk assessment: a systematic classification based on hazard-forming environment, Natural Hazards and Earth System Sciences, 16, 629–642, https://doi.org/10.5194/nhess-16-629-2016, 2016.

Liuzzi, M., Aravena Pelizari, P., Geiß, C., Masi, A., Tramutoli, V., and Taubenböck, H.: A transferable remote sensing approach to classify building structural types for seismic risk analyses: the case of Val d'Agri area (Italy), Bulletin of Earthquake Engineering, 17, 4825–4853, https://doi.org/10.1007/s10518-019-00648-7, 2019.

de la Llera, J. C., Rivera, F., Mitrani-Reiser, J., Jünemann, R., Fortuño, C., Ríos, M., Hube, M., Santa María, H., and Cienfuegos, R.: Data collection after the 2010 Maule earthquake in Chile, Bulletin of Earthquake Engineering, 15, 555–588, https://doi.org/10.1007/s10518-016-9918-3, 2017.

Lloyd, S.: Least squares quantization in PCM, IEEE Transactions on Information Theory, 28, 129–137, https://doi.org/10.1109/TIT.1982.1056489, 1982.

Løvholt, F., Glimsdal, S., Harbitz, C. B., Horspool, N., Smebye, H., Bono, A. de, and Nadim, F.: Global tsunami hazard and exposure due to large co-seismic slip, International Journal of Disaster Risk Reduction, 10, 406–418, https://doi.org/10.1016/j.ijdrr.2014.04.003, 2014.

Lovon, H., Tarque, N., Silva, V., and Yepes-Estrada, C.: Development of Fragility Curves for Confined Masonry Buildings in Lima, Peru, Earthquake Spectra, 34, 1339–1361, https://doi.org/10.1193/090517EQS174M, 2018.

Lowe, D. R., Williams, S. N., Leigh, H., Connort, C. B., Gemmell, J. B., and Stoiber, R. E.: Lahars initiated by the 13 November 1985 eruption of Nevado del Ruiz, Colombia, Nature, 324, 51–53, https://doi.org/10.1038/324051a0, 1986.

Luco, N. and Cornell, C. A.: Structure-Specific Scalar Intensity Measures for Near-Source and Ordinary Earthquake Ground Motions, Earthquake Spectra, 23, 357–392, https://doi.org/10.1193/1.2723158, 2007.

Lupiano, V., Chidichimo, F., Machado, G., Catelan, P., Molina, L., Calidonna, C. R., Straface, S., Crisci, G. M., and Di Gregorio, S.: From examination of natural events to a proposal for risk mitigation of lahars by a cellular-automata methodology: a case study for Vascún valley, Ecuador, Natural Hazards and Earth System Sciences, 20, 1–20, https://doi.org/10.5194/nhess-20-1-2020, 2020.

Lynch, S. M.: Introduction to applied Bayesian statistics and estimation for social scientists, Springer, New York, 2007.

Ma, J., Rao, A., Silva, V., Liu, K., and Wang, M.: A township-level exposure model of residential buildings for mainland China, Natural Hazards,

https://doi.org/10.1007/s11069-021-04689-7, 2021.

Macabuag, J., Rossetto, T., Ioannou, I., Suppasri, A., Sugawara, D., Adriano, B., Imamura, F., Eames, I., and Koshimura, S.: A proposed methodology for deriving tsunami fragility functions for buildings using optimum intensity measures, Natural Hazards, 84, 1257–1285, https://doi.org/10.1007/s11069-016-2485-8, 2016.

Maiwald, H. and Schwarz, J.: Unified damage description and risk assessment of buildings under extreme natural hazards, Mauerwerk, 23, 95–111, https://doi.org/10.1002/dama.201910014, 2019.

Mangalathu, S., Sun, H., Nweke, C. C., Yi, Z., and Burton, H. V.: Classifying earthquake damage to buildings using machine learning, Earthquake Spectra, 36, 183–208, https://doi.org/10.1177/8755293019878137, 2020.

Marín-Monroy, E. A., Hernández Trejo, V., Ojeda Ruiz de la Pena, M. A., Avilés Polanco, G., and Barbara, N. L.: Assessment of Socio-Environmental Vulnerability Due to Tropical Cyclones in La Paz, Baja California Sur, Mexico, Sustainability, 12, https://doi.org/10.3390/su12041575, 2020.

Markhvida, M., Ceferino, L., and Baker, J. W.: Effect of ground motion correlation on regional seismic lossestimation: application to Lima, Peru using across-correlated principal component analysis model, Safety, Reliability, Risk, Resilience and Sustainability of Structures and Infrastructure. 12th Int. Conf. on Structural Safety and Reliability, Vienna, Austria, 2017.

Markhvida, M., Ceferino, L., and Baker, J. W.: Modeling spatially correlated spectral accelerations at multiple periods using principal component analysis and geostatistics, Earthquake Engineering & Structural Dynamics, 47, 1107–1123, https://doi.org/10.1002/eqe.3007, 2018.

Martínez-Cuevas, S., Benito, M. B., Cervera, J., Morillo, M. C., and Luna, M.: Urban modifiers of seismic vulnerability aimed at Urban Zoning Regulations, Bulletin of Earthquake Engineering, 15, 4719–4750, https://doi.org/10.1007/s10518-017-0162-2, 2017.

Martins, L. and Silva, V.: Development of a fragility and vulnerability model for global seismic risk analyses, Bulletin of Earthquake Engineering, https://doi.org/10.1007/s10518-020-00885-1, 2021.

Marzocchi, W., Garcia-Aristizabal, A., Gasparini, P., Mastellone, M. L., and Di Ruocco, A.: Basic principles of multi-risk assessment: a case study in Italy, Natural Hazards, 62, 551–573, https://doi.org/10.1007/s11069-012-0092-x, 2012.

Mas, E., Adriano, B., Pulido, N., Jimenez, C., and Koshimura, S.: Simulation of Tsunami Inundation in Central Peru from Future Megathrust Earthquake Scenarios, Journal of Disaster Research, 9, 961–967, https://doi.org/10.20965/jdr.2014.p0961, 2014.

Mas, E., Paulik, R., Pakoksung, K., Adriano, B., Moya, L., Suppasri, A., Muhari, A., Khomarudin, R., Yokoya, N., Matsuoka, M., and Koshimura, S.: Characteristics of Tsunami Fragility Functions Developed Using Different Sources of Damage Data from the 2018 Sulawesi Earthquake and Tsunami, Pure and Applied Geophysics, 177, 2437–2455, https://doi.org/10.1007/s00024-020-02501-4, 2020.

Matsuoka, M., Miura, H., Midorikawa, S., and Estrada, M.: Extraction of Urban Information for Seismic Hazard and Risk Assessment in Lima, Peru Using Satellite Imagery, Journal of disaster research, 8, 328–345, 2013.

Mavrouli, O., Fotopoulou, S., Pitilakis, K., Zuccaro, G., Corominas, J., Santo, A., Cacace, F., De Gregorio, D., Di Crescenzo, G., Foerster, E., and Ulrich, T.: Vulnerability assessment for reinforced concrete buildings exposed to landslides, Bulletin of Engineering Geology and the Environment, https://doi.org/10.1007/s10064-014-0573-0, 2014.

Medina, S.: Zonificación de la vulnerabilidad física para edificaciones típicas en San Andrés de Tumaco, Costa Pacífica Colombiana, Master thesis in Civil Engineering, Universidad Nacional de Colombia Facultad de Ingeniería, Departamento Ingeniería Civil y Ambiental, Bogotá, Colombia, 245 pp., 2019.

Medina, S., Lizarazo-Marriaga, J., Estrada, M., Koshimura, S., Mas, E., and Adriano, B.: Tsunami analytical fragility curves for the Colombian Pacific coast: A reinforced concrete building example, Engineering Structures, 196, 109309, https://doi.org/10.1016/j.engstruct.2019.109309, 2019.

Mendoza, L., Ayala, F., Fuentes, B., Soto, V., Sáez, E., Yañez, G., Montalva, Gonzalo., Gález, C., Sepúlveda, N., Lazo, I., and Ruiz, J.: Estimación cuantitativa de la amenaza sísmica en base a métodos geofísicos: aplicación a las localidades costeras del segmento los Vilos – San Antonio, 50 Congreso SOCHIGE., Valparaiso, Chile, 2018.

Mercorio, F., Mezzanzanica, M., Moscato, V., Picariello, A., and Sperli, G.: DICO: A Graph-DB Framework for Community Detection on Big Scholarly Data, IEEE Transactions on Emerging Topics in Computing, 1–1, https://doi.org/10.1109/TETC.2019.2952765, 2019.

Merino-Peña, Y., Pittore, M., and Gomez-Zapata, J. C.: RRVS Building survey for building exposure modelling in Valparaiso and Viña del Mar (Chile). V. 1.0., GFZ Data Services, https://doi.org/10.5880/riesgos.2021.001, 2021.

Merz, B., Kuhlicke, C., Kunz, M., Pittore, M., Babeyko, A., Bresch, D. N., Domeisen, D. I. V., Feser, F., Koszalka, I., Kreibich, H., Pantillon, F., Parolai, S., Pinto, J. G., Punge, H. J., Rivalta, E., Schröter, K., Strehlow, K., Weisse, R., and Wurpts, A.: Impact Forecasting to Support Emergency Management of Natural Hazards, Reviews of Geophysics, 58, e2020RG000704, https://doi.org/10.1029/2020RG000704, 2020.

Michel, C., Hannewald, P., Lestuzzi, P., Fäh, D., and Husen, S.: Probabilistic mechanics-based loss scenarios for school buildings in Basel (Switzerland), Bulletin of Earthquake Engineering, 15, 1471–1496, https://doi.org/10.1007/s10518-016-0025-2, 2017.

Mohammadi, A., Karimzadeh, S., Valizadeh Kamran, K., and Matsuoka, M.: Extraction of Land Information, Future Landscape Changes and Seismic Hazard Assessment: A Case Study of Tabriz, Iran, Sensors, 20, https://doi.org/10.3390/s20247010, 2020.

Montalva, G. A., Bastías, N., and Rodriguez-Marek, A.: Ground-Motion Prediction Equation for the Chilean Subduction Zone, The Bulletin of the Seismological Society of America, 107, 901–911, https://doi.org/10.1785/0120160221, 2017.

Montessus de Ballore, F.: Historia sísmica de los Andes Meridionales al sur del paralelo XVI, Cuarta parte, Imprenta Cervantes, Santiago, Chile, 1914.

Moreno Cano, A., Romón Sagredo, R., García-Carrión, R., and Garcia-Zapirain, B.: Social Impact Assessment of HealthyAIR Tool for Real-Time Detection of Pollution Risk, Sustainability, 12, https://doi.org/10.3390/su12239856, 2020.

Moscato, V., Picariello, A., and Sperli, G.: An emotional recommender system for music, IEEE Intelligent Systems, 1–1, https://doi.org/10.1109/MIS.2020.3026000, 2020.

Mothes, P., Espin, P., Hall, M., Vasconez, F., Sierra, D., and Andrade, D.: Mapa regional de amenazas volcánicas potenciales del volcán cotopaxi, zona sur. Mapa de peligros., Nacional, I.G.S.D.L.E. P.C. (ed.)., 2016.

Mothes, P. A. and Vallance, J. W.: Chapter 6 - Lahars at Cotopaxi and Tungurahua Volcanoes, Ecuador: Highlights from Stratigraphy and Observational Records and Related Downstream Hazards, in: Volcanic Hazards, Risks and Disasters, edited by: Shroder, J. F. and Papale, P., Elsevier, Boston, 141–168, https://doi.org/10.1016/B978-0-12-396453-3.00006-X, 2015.

Mothes, P. A., Ruiz, M. C., Viracucha, E. G., Ramón, P. A., Hernández, S., Hidalgo, S., Bernard, B., Gaunt, E. H., Jarrín, P., Yépez, M. A., and Espín, P. A.: Geophysical Footprints of Cotopaxi's Unrest and Minor Eruptions in 2015: An Opportunity to Test Scientific and Community Preparedness, in: Volcanic Unrest : From Science to Society, edited by: Gottsmann, J., Neuberg, J., and Scheu, B., Springer International Publishing, Cham, 241–270, https://doi.org/10.1007/11157_2017_10, 2019.

NCEI/WDS Global Significant Volcanic Eruptions Database. NOAA National Centers for Environmental Information. doi:10.7289/V5JW8BSH.: https://www.ngdc.noaa.gov/hazard/volcano.shtml, last access: 8 May 2020.

Nealy, J. L., Herman, M. W., Moore, G. L., Hayes, G. P., Benz, H. M., Bergman, E. A., and Barrientos, S. E.: 2017 Valparaíso earthquake sequence and the megathrust patchwork of central Chile, Geophysical Research Letters, 44, 8865–8872, https://doi.org/10.1002/2017GL074767, 2017.

Negulescu, C., Benaïchouche, A., Lemoine, A., Le Roy, S., and Pedreros, R.: Adjustability of exposed elements by updating their capacity for resistance after a damaging event: application to an earthquake–tsunami cascade scenario, Natural Hazards, 104, 753–793, https://doi.org/10.1007/s11069-020-04189-0, 2020.

Nicodemo, G., Pittore, M., Masi, A., and Manfredi, V.: Modelling exposure and vulnerability from post-earthquake survey data with risk-oriented taxonomies: AeDES form, GEM taxonomy and EMS-98 typologies, International Journal of Disaster Risk Reduction, 50, 101894, https://doi.org/10.1016/j.ijdrr.2020.101894, 2020.

Nievas, C. I., Pilz, M., Prehn, K., Schorlemmer, D., Weatherill, G., and Cotton, F.: Calculating earthquake damage building by building: the case of the city of Cologne, Germany, Bulletin of Earthquake Engineering, https://doi.org/10.1007/s10518-021-01303-w, 2022.

Oláh, J., Virglerova, Z., Popp, J., Kliestikova, J., and Kovács, S.: The Assessment of Non-Financial Risk Sources of SMES in the V4 Countries and Serbia, Sustainability, 11, https://doi.org/10.3390/su11174806, 2019.

Omira, R., Baptista, M. A., Matias, L., Miranda, J. M., Catita, C., Carrilho, F., and Toto, E.: Design of a Sea-level Tsunami Detection Network for the Gulf of Cadiz, Natural Hazards and Earth System Sciences, 9, 1327–1338, https://doi.org/10.5194/nhess-9-1327-2009, 2009.

Ordaz, M., Salgado-Gálvez Mario Andrés, Huerta Benjamín, Rodríguez Juan Carlos, and Avelar Carlos: Considering the impacts of simultaneous perils: The challenges of integrating earthquake and tsunamigenic risk, Disaster Prevention and Management: An International Journal, 28, 823–837, https://doi.org/10.1108/DPM-09-2019-0295, 2019.

OSM Task Manager: #502—Valparaíso, Chile Fires/Fuegos en Valparaíso, Chile, 2014a.

OSM Task Manager: #508—Valparaíso, Chile Fires 2/Fuegos en Valparaíso, Chile, 2014b.

Paez-Ramirez, J., Lizarazo-Marriaga, J., Medina, S., Estrada, M., Mas, E., and Koshimura, S.: A comparative study of empirical and analytical fragility functions for the assessment of tsunami building damage in Tumaco, Colombia, Coastal Engineering Journal, 62, 362–372, https://doi.org/10.1080/21664250.2020.1726558, 2020.

Pagani, M., Monelli, D., Weatherill, G., Danciu, L., Crowley, H., Silva, V., Henshaw, P., Butler, L., Nastasi, M., Panzeri, L., Simionato, M., and Vigano, D.: OpenQuake Engine: An Open Hazard (and Risk) Software for the Global Earthquake Model, Seismological Research Letters, 85, 692–702, https://doi.org/10.1785/0220130087, 2014.

Papadopoulos, A. N. and Bazzurro, P.: Exploring probabilistic seismic risk assessment accounting for seismicity clustering and damage accumulation: Part II. Risk analysis, Earthquake Spectra, 37, 386–408, https://doi.org/10.1177/8755293020938816, 2021.

Papathoma-Koehle, M., Maris, F., and Fuchs, S.: Remoteness and austerity: a major driver of vulnerabilities to natural hazards, in: EGU General Assembly Conference Abstracts, 1577, 2020.

Papathoma-Köhle, M., Schlögl, M., and Fuchs, S.: Vulnerability indicators for natural hazards: an innovative selection and weighting approach, Scientific Reports, 9, 15026, https://doi.org/10.1038/s41598-019-50257-2, 2019.

Parham, M., Teeuw, R., Solana, C., and Day, S.: Quantifying the impact of educational methods for disaster risk reduction: a longitudinal study assessing the impact of teaching methods on student hazard perceptions, International Journal of Disaster Risk Reduction, 101978, https://doi.org/10.1016/j.ijdrr.2020.101978, 2020.

Park, H., Cox, D. T., and Barbosa, A. R.: Comparison of inundation depth and momentum flux based fragilities for probabilistic tsunami damage assessment and uncertainty analysis, Coastal Engineering, 122, 10–26, https://doi.org/10.1016/j.coastaleng.2017.01.008, 2017.

Park, H., Alam, M. S., Cox, D. T., Barbosa, A. R., and Lindt, J. W. van de: Probabilistic seismic and tsunami damage analysis (PSTDA) of the Cascadia Subduction Zone applied to Seaside, Oregon, International Journal of Disaster Risk Reduction, 35, 101076, https://doi.org/10.1016/j.ijdrr.2019.101076, 2019.

Paton, D., Smith, L., Daly, M., and Johnston, D.: Risk perception and volcanic hazard mitigation: Individual and social perspectives, Journal of Volcanology and Geothermal Research, 172, 179–188, https://doi.org/10.1016/j.jvolgeores.2007.12.026, 2008.

Pavić, G., Hadzima-Nyarko, M., Bulajić, B., and Jurković, Ž.: Development of Seismic Vulnerability and Exposure Models—A Case Study of Croatia, Sustainability, 12, 973, https://doi.org/10.3390/su12030973, 2020.

Pesaresi, M., Ehrilich, D., Kemper, T., Siragusa, A., Florcyk, A., Freire, S., and Corbane, C.: Atlas of the human planet 2017. Global exposure to natural hazards, EUR 28556 EN., Luxembourg:, 2017.

Pescaroli, G.: Perceptions of cascading risk and interconnected failures in emergency planning: Implications for operational resilience and policy making, International Journal of Disaster Risk Reduction, 30, 269–280, https://doi.org/10.1016/j.ijdrr.2018.01.019, 2018.

Pescaroli, G. and Alexander, D.: A definition of cascading disasters and cascading effects: Going beyond the "toppling dominos" metaphor, Planet Risk, 58–67, 2015.

Pescaroli, G. and Alexander, D.: Understanding Compound, Interconnected, Interacting, and Cascading Risks: A Holistic Framework, Risk Analysis, 38, 2245–2257, https://doi.org/10.1111/risa.13128, 2018.

Pescaroli, G., Velazquez, O., Alcántara-Ayala, I., Galasso, C., Kostkova, P., and Alexander, D.: A Likert Scale-Based Model for Benchmarking Operational Capacity, Organizational Resilience, and Disaster Risk Reduction, International Journal of Disaster Risk Science, 11, 404–409, https://doi.org/10.1007/s13753-020-00276-9, 2020.

Petersen, M. D., Harmsen, S. C., Jaiswal, K. S., Rukstales, K. S., Luco, N., Haller, K. M., Mueller, C. S., and Shumway, A. M.: Seismic Hazard, Risk, and Design for South America, Bulletin of the Seismological Society of America, 108, 781–800, https://doi.org/10.1785/0120170002, 2018.

Petrone, C., Rossetto, T., and Goda, K.: Fragility assessment of a RC structure under tsunami actions via nonlinear static and dynamic analyses, Engineering Structures, 136, 36–53, https://doi.org/10.1016/j.engstruct.2017.01.013, 2017.

Petrone, C., Rossetto, T., Baiguera, M., la Barra Bustamante, C. D., and Ioannou, I.: Fragility functions for a reinforced concrete structure subjected to earthquake and tsunami in sequence, Engineering Structures, 205, 110120, https://doi.org/10.1016/j.engstruct.2019.110120, 2020.

Peyghaleh, E., Mahmoudabadi, V., Martin, J. R., Shahjouei, A., Chen, Q., Javanbarg, M., and Khoshnevisan, S.: Impact of local site conditions on portfolio earthquake loss estimation for different building types, Natural Hazards, 94, 121–150, https://doi.org/10.1007/s11069-018-3377-x, 2018.

Pierson, T. C., Janda, R. J., Thouret, J.-C., and Borrero, C. A.: Perturbation and melting of snow and ice by the 13 November 1985 eruption of Nevado del Ruiz, Colombia, and consequent mobilization, flow and deposition of lahars, Journal of Volcanology and Geothermal Research, 41, 17–66, https://doi.org/10.1016/0377-0273(90)90082-Q, 1990.

Pierson, T. C., Wood, N. J., and Driedger, C. L.: Reducing risk from lahar hazards: concepts, case studies, and roles for scientists, Journal of Applied Volcanology, 3, 16, https://doi.org/10.1186/s13617-014-0016-4, 2014.

Pilz, M. and Cotton, F.: Does the One-Dimensional Assumption Hold for Site Response Analysis? A Study of Seismic Site Responses and Implication for Ground Motion Assessment Using KiK-Net Strong-Motion Data, Earthquake Spectra, 35, 883–905, https://doi.org/10.1193/050718EQS113M, 2019.

Pilz, M., Bindi, D., Boxberger, T., Hakimov, F., Moldobekov, B., Murodkulov, S., Orunbaev, S., Pittore, M., Stankiewicz, J., Ullah, S., Verjee, F., Wieland, M., Yasunov, P., and Parolai, S.: First Steps toward a Reassessment of the Seismic Risk of the City of Dushanbe (Tajikistan), Seismological Research Letters, 84, 1026–1038, https://doi.org/10.1785/0220130040, 2013.

Pistolesi, M., Cioni, R., Rosi, M., Cashman, K. V., Rossotti, A., and Aguilera, E.: Evidence for lahar-triggering mechanisms in complex stratigraphic sequences: the post-twelfth century eruptive activity of Cotopaxi Volcano, Ecuador, Bulletin of Volcanology, 75, 698, https://doi.org/10.1007/s00445-013-0698-1, 2013.

Pittore, M.: A means of prioritizing data collection for efficient Geo-risk assessment, Annals of Geophysics, https://doi.org/10.4401/ag-6692, 2015.

Pittore, M. and Wieland, M.: Toward a rapid probabilistic seismic vulnerability assessment using satellite and ground-based remote sensing, Natural Hazards, 68, 115–145, https://doi.org/10.1007/s11069-012-0475-z, 2013.

Pittore, M., Wieland, M., Errize, M., Kariptas, C., and Güngör, I.: Improving Post-Earthquake Insurance Claim Management: A Novel Approach to Prioritize Geospatial Data Collection, ISPRS International Journal of Geo-Information, 4, 2401–2427, https://doi.org/10.3390/ijgi4042401, 2015.

Pittore, M., Wieland, M., and Fleming, K.: Perspectives on global dynamic exposure modelling for geo-risk assessment, Natural Hazards, 86, 7–30, https://doi.org/10.1007/s11069-016-2437-3, 2017.

Pittore, M., Graziani, L., Maramai, A., Haas, M., Parolai, S., and Tertulliani, A.: Bayesian Estimation of Macroseismic Intensity from Post-Earthquake Rapid Damage Mapping, Earthquake Spectra, 34, 1809–1828, https://doi.org/10.1193/112517EQS241M, 2018a.

Pittore, M., Haas, M., and Megalooikonomou, K. G.: Risk-Oriented, Bottom-Up Modeling of Building Portfolios With Faceted Taxonomies, Frontiers in Built Environment, 4, 41, https://doi.org/10.3389/fbuil.2018.00041, 2018b.

Pittore, M., Gómez Zapata, J. C., Brinckmann, N., Weatherill, G., Babeyko, A., Harig, S., Mahdavi, A., Proß, B., Rosero Velasquez, H. F., Straub, D., Krautblatter, M., Frimberger, T., Langbein, M., Geiß, C., and Schoepfer, E.: Towards an integrated framework for distributed, modular multi-risk scenario assessment, in: EGU General Assembly Conference Abstracts, 19097, 2020a.

Pittore, M., Haas, M., and Silva, V.: Variable resolution probabilistic modeling of residential exposure and vulnerability for risk applications, Earthquake Spectra, 36, 321–344, https://doi.org/10.1177/8755293020951582, 2020b.

Pittore, M., Gomez-Zapata, J. C., Brinckmann, N., and Rüster, M.: Assetmaster and Modelprop: web services to serve building exposure models and fragility functions for physical vulnerability to natural-hazards. V. 1.0, GFZ Data Services, https://doi.org/10.5880/riesgos.2021.005, 2021.

Poland, M. P. and Anderson, K. R.: Partly Cloudy With a Chance of Lava Flows: Forecasting Volcanic Eruptions in the Twenty-First Century, Journal of Geophysical Research: Solid Earth, 125, e2018JB016974, https://doi.org/10.1029/2018JB016974, 2020.

Polese, M., d'Aragona, M. G., and Prota, A.: Simplified approach for building inventory and seismic damage assessment at the territorial scale: An application for a town in southern Italy, Soil Dynamics and Earthquake Engineering, 121, 405–420, https://doi.org/10.1016/j.soildyn.2019.03.028, 2019.

Polese, M., Di Ludovico, M., Gaetani d'Aragona, M., Prota, A., and Manfredi, G.: Regional vulnerability and risk assessment accounting for local building typologies, International Journal of Disaster Risk Reduction, 43, 101400, https://doi.org/10.1016/j.ijdrr.2019.101400, 2020.

Poljanšek, K., Bono, F., and Gutiérrez, E.: Seismic risk assessment of interdependent critical infrastructure

systems: The case of European gas and electricity networks, Earthquake Engineering & Structural Dynamics, 41, 61–79, https://doi.org/10.1002/eqe.1118, 2012.

Porter, K. A., Beck, J. L., and Shaikhutdinov, R. V.: Sensitivity of Building Loss Estimates to Major Uncertain Variables, Earthquake Spectra, 18, 719–743, https://doi.org/10.1193/1.1516201, 2002.

PREDES: Diseño de escenario sobre el impacto de un sismo de gran magnitud en Lima Metropolitana y Callao". Reporte preparado para Instituto Nacional de Defensa Civil– INDECI. Agencia Suiza para el Desarrollo y la Cooperación COSUDE., 2009.

Pulido, N., Aguilar, Z., Tavera, H., Chlieh, M., Calderón, D., Sekiguchi, T., Nakai, S., and Yamazaki, F.: Scenario Source Models and Strong Ground Motion for Future Mega-earthquakes: Application to Lima, Central Peru, Bulletin of the Seismological Society of America, 105, 368–386, 2015.

Ran, J., MacGillivray, B. H., Gong, Y., and Hales, T. C.: The application of frameworks for measuring social vulnerability and resilience to geophysical hazards within developing countries: A systematic review and narrative synthesis, Science of The Total Environment, 711, 134486, https://doi.org/10.1016/j.scitotenv.2019.134486, 2020.

Rao, A., Dutta, D., Kalita, P., Ackerley, N., Silva, V., Raghunandan, M., Ghosh, J., Ghosh, S., Brzev, S., and Dasgupta, K.: Probabilistic seismic risk assessment of India, Earthquake Spectra, 36, 345–371, https://doi.org/10.1177/8755293020957374, 2020.

Rao, A. S., Lepech, M. D., and Kiremidjian, A.: Development of time-dependent fragility functions for deteriorating reinforced concrete bridge piers, null, 13, 67–83, https://doi.org/10.1080/15732479.2016.1198401, 2017.

Reszka, P. and Fuentes, A.: The Great Valparaiso Fire and Fire Safety Management in Chile, Fire Technology, 51, 753–758, https://doi.org/10.1007/s10694-014-0427-0, 2015.

Ricca, F., Scozzari, A., and Simeone, B.: Weighted Voronoi region algorithms for political districting, Mathematical and Computer Modelling, 48, 1468–1477, https://doi.org/10.1016/j.mcm.2008.05.041, 2008.

Riedel, I., Guéguen, P., Dalla Mura, M., Pathier, E., Leduc, T., and Chanussot, J.: Seismic vulnerability assessment of urban environments in moderate-to-low seismic hazard regions using association rule learning and support vector machine methods, Natural Hazards, 76, 1111–1141, https://doi.org/10.1007/s11069-014-1538-0, 2015.

Riga, E., Karatzetzou, A., Mara, A., and Pitilakis, K.: Studying the uncertainties in the seismic risk assessment at urban scale applying the Capacity Spectrum Method: The case of Thessaloniki, Soil Dynamics and Earthquake Engineering, 92, 9–24, https://doi.org/10.1016/j.soildyn.2016.09.043, 2017.

Rivera, F., Rossetto, T., and Twigg, J.: An interdisciplinary study of the seismic exposure dynamics of Santiago de Chile, International Journal of Disaster Risk Reduction, 48, 101581, https://doi.org/10.1016/j.ijdrr.2020.101581, 2020.

Rodriguez, F., Toulkeridis, T., Sandoval, W., Padilla, O., and Mato, F.: Economic risk assessment of Cotopaxi volcano, Ecuador, in case of a future lahar emplacement, Natural Hazards, 85, 605–618, https://doi.org/10.1007/s11069-016-2589-1, 2017.

Rosero-Velásquez, H. and Straub, D.: Representative Natural Hazard Scenarios for Risk Assessment of Spatially Distributed Infrastructure Systems, 29th European Safety and Reliability Conference (ESREL 2019), Hannover, Germany, https://doi.org/doi: 10.3850/978-981-11-2724-3_0821-cd, 2019.

Rossetto, T., Petrone, C., Eames, I., De La Barra, C., Foster, A., and Macabuag, J.: Advances in the Assessment of Buildings Subjected to Earthquakes and Tsunami, in: Recent Advances in Earthquake Engineering in Europe: 16th European Conference on Earthquake Engineering-Thessaloniki 2018, edited by: Pitilakis, K., Springer International Publishing, Cham, 545–562, https://doi.org/10.1007/978-3-319-75741-4_23, 2018.

Rossetto, T., De la Barra, C., Petrone, C., De la Llera, J. C., Vásquez, J., and Baiguera, M.: Comparative assessment of nonlinear static and dynamic methods for analysing building response under sequential earthquake and tsunami, Earthquake Engineering & Structural Dynamics, 48, 867–887, https://doi.org/10.1002/eqe.3167, 2019.

Rueda-Plata, D., González, D., Acevedo, A. B., Duque, J. C., and Ramos-Pollán, R.: Use of deep learning models in street-level images to classify one-story unreinforced masonry buildings based on roof diaphragms, Building and Environment, 189, 107517, https://doi.org/10.1016/j.buildenv.2020.107517, 2021.

de Ruiter, M. C., Couasnon, A., van den Homberg, M. J. C., Daniell, J. E., Gill, J. C., and Ward, P. J.: Why We Can No Longer Ignore Consecutive Disasters, Earth's Future, 8, e2019EF001425, https://doi.org/10.1029/2019EF001425, 2020.

Ruiz, S., Aden-Antoniow, F., Baez, J. C., Otarola, C., Potin, B., del Campo, F., Poli, P., Flores, C., Satriano, C., Leyton, F., Madariaga, R., and Bernard, P.: Nucleation Phase and Dynamic Inversion of the Mw

6.9 Valparaíso 2017 Earthquake in Central Chile, Geophysical Research Letters, 44, 10,290-10,297, https://doi.org/10.1002/2017GL075675, 2017.

Sajjad, M., Chan, J. C. L., and Kanwal, S.: Integrating spatial statistics tools for coastal risk management: A case-study of typhoon risk in mainland China, Ocean & Coastal Management, 184, 105018, https://doi.org/10.1016/j.ocecoaman.2019.105018, 2020.

Scaini, C., Biass, S., Galderisi, A., Bonadonna, C., Folch, A., Smith, K., and Höskuldsson, A.: A multi-scale risk assessment for tephra fallout and airborne concentration from multiple Icelandic volcanoes – Part 2: Vulnerability and impact, Natural Hazards and Earth System Sciences, 14, 2289–2312, https://doi.org/10.5194/nhess-14-2289-2014, 2014.

Scheingraber, C. and Käser, M.: Spatial seismic hazard variation and adaptive sampling of portfolio location uncertainty in probabilistic seismic risk analysis, Natural Hazards and Earth System Sciences, 20, 1903–1918, https://doi.org/10.5194/nhess-20-1903-2020, 2020.

Schelske, O., Sundermann, L., and Hausmann, P.: Mind the risk - A global ranking of cities under threat from natural disasters, 2014.

Scherbaum, F., Bommer, J. J., Bungum, H., Cotton, F., and Abrahamson, N. A.: Composite Ground-Motion Models and Logic Trees: Methodology, Sensitivities, and Uncertainties, Bulletin of the Seismological Society of America, 95, 1575–1593, https://doi.org/10.1785/0120040229, 2005.

Schiappapietra, E. and Douglas, J.: Modelling the spatial correlation of earthquake ground motion: Insights from the literature, data from the 2016–2017 Central Italy earthquake sequence and ground-motion simulations, Earth-Science Reviews, 203, 103139, https://doi.org/10.1016/j.earscirev.2020.103139, 2020.

Schorlemmer, D., Beutin, T., Cotton, F., Garcia Ospina, N., Hirata, N., Ma, K.-F., Nievas, C., Prehn, K., and Wyss, M.: Global Dynamic Exposure and the OpenBuildingMap - A Big-Data and Crowd-Sourcing Approach to Exposure Modeling, in: EGU General Assembly Conference Abstracts, 18920, 2020.

Schwarz, J., Maiwald, H., Kaufmann, C., Langhammer, T., and Beinersdorf, S.: Conceptual basics and tools to assess the multi hazard vulnerability of existing buildings, Mauerwerk, 23, 246–264, https://doi.org/10.1002/dama.201910025, 2019.

Selva, J.: Long-term multi-risk assessment: statistical treatment of interaction among risks, Natural Hazards, 67, 701–722, https://doi.org/10.1007/s11069-013-0599-9, 2013.

Senouci, A., Bard, P.-Y., Beck, E., Farsi, M. N., and Cartier, S.: Mapping seismic vulnerability at urban scale: Discussion on relevant cartography representations and smoothing for urban planning purposes on the Oran case study, Soil Dynamics and Earthquake Engineering, 115, 545–563, https://doi.org/10.1016/j.soildyn.2018.08.034, 2018.

Shaw, K.: "Reframing" Resilience: Challenges for Planning Theory and Practice, Planning Theory & Practice, 13, 299–333, 2012.

Shinde, S., Gomez-Zapata, J. C., Pittore, M., Arroyo, O., Merino-Peña, Y., Aguirre, P., and Santa María, H.: Development of multi-hazard exposure models from individual building observations for multi-risk assessment purposes, in: EGU General Assembly Conference Abstracts, 11719, 2020.

Sierra, D., Vasconez, F., Andrade, S. D., Almeida, M., and Mothes, P.: Historical Distal Lahar Deposits on the Remote Eastern-Drainage of Cotopaxi Volcano, Ecuador, Journal of South American Earth Sciences, 95, 102251, https://doi.org/10.1016/j.jsames.2019.102251, 2019.

Silva, V.: Critical Issues in Earthquake Scenario Loss Modeling, Journal of Earthquake Engineering, 20, 1322–1341, https://doi.org/10.1080/13632469.2016.1138172, 2016.

Silva, V.: Uncertainty and Correlation in Seismic Vulnerability Functions of Building Classes, Earthquake Spectra, 35, 1515–1539, https://doi.org/10.1193/013018EQS031M, 2019.

Silva, V., Yepes-Estrada, C., Dabbeek, J., Martins, L., and Brzev, S.: GED4ALL: Global exposure database for multi-hazard risk analysis. Multi-hazard exposure taxonomy, GEM Foundation, Pavia, 2018.

Silva, V., Akkar, S., Baker, J., Bazzurro, P., Castro, J. M., Crowley, H., Dolsek, M., Galasso, C., Lagomarsino, S., Monteiro, R., Perrone, D., Pitilakis, K., and Vamvatsikos, D.: Current Challenges and Future Trends in Analytical Fragility and Vulnerability Modeling, Earthquake Spectra, 35, 1927–1952, https://doi.org/10.1193/042418EQS101O, 2019.

Silva, V., Amo-Oduro, D., Calderon, A., Costa, C., Dabbeek, J., Despotaki, V., Martins, L., Pagani, M., Rao, A., Simionato, M., Viganò, D., Yepes-Estrada, C., Acevedo, A., Crowley, H., Horspool, N., Jaiswal, K., Journeay, M., and Pittore, M.: Development of a global seismic risk model, Earthquake Spectra, 8755293019899953, https://doi.org/10.1177/8755293019899953, 2020.

Silva, V., Brzev, S., Scawthorn, C., Yepes, C., Dabbeek, J., and Crowley, H.: A Building Classification System for Multi-hazard Risk Assessment, International Journal of Disaster Risk Science,

https://doi.org/10.1007/s13753-022-00400-x, 2022.

Soman, S., Beukes, A., Nederhood, C., Marchio, N., and Bettencourt, L. M. A.: Worldwide Detection of Informal Settlements via Topological Analysis of Crowdsourced Digital Maps, ISPRS International Journal of Geo-Information, 9, https://doi.org/10.3390/ijgi9110685, 2020.

Song, J., De Risi, R., and Goda, K.: Influence of Flow Velocity on Tsunami Loss Estimation, Geosciences, 7, https://doi.org/10.3390/geosciences7040114, 2017.

Sousa, L., Silva, V., and Bazzurro, P.: Using Open-Access Data in the Development of Exposure Data Sets of Industrial Buildings for Earthquake Risk Modeling, Earthquake Spectra, 33, 63–84, https://doi.org/10.1193/020316eqs027m, 2017.

Sousa, L., Silva, V., Marques, M., and Crowley, H.: On the treatment of uncertainty in seismic vulnerability and portfolio risk assessment, Earthquake Engineering & Structural Dynamics, 47, 87–104, https://doi.org/10.1002/eqe.2940, 2018.

Stafford, P. J.: Evaluation of structural performance in the immediate aftermath of an earthquake: a case study of the 2011 Christchurch earthquake, International Journal of Forensic Engineering, 1, 58–77, https://doi.org/10.1504/IJFE.2012.047447, 2012.

Suppasri, A., Mas, E., Charvet, I., Gunasekera, R., Imai, K., Fukutani, Y., Abe, Y., and Imamura, F.: Building damage characteristics based on surveyed data and fragility curves of the 2011 Great East Japan tsunami, Natural Hazards, 66, 319–341, https://doi.org/10.1007/s11069-012-0487-8, 2013.

Suppasri, A., Charvet, I., Imai, K., and Imamura, F.: Fragility Curves Based on Data from the 2011 Tohoku-Oki Tsunami in Ishinomaki City, with Discussion of Parameters Influencing Building Damage, Earthquake Spectra, 31, 841–868, https://doi.org/10.1193/053013EQS138M, 2015.

Suppasri, A., Pakoksung, K., Charvet, I., Chua, C. T., Takahashi, N., Ornthammarath, T., Latcharote, P., Leelawat, N., and Imamura, F.: Load-resistance analysis: an alternative approach to tsunami damage assessment applied to the 2011 Great East Japan tsunami, Natural Hazards and Earth System Sciences, 19, 1807–1822, https://doi.org/10.5194/nhess-19-1807-2019, 2019.

Suppasri, A., Maly, E., Kitamura, M., Syamsidik, Pescaroli, G., Alexander, D., and Imamura, F.: Cascading disasters triggered by tsunami hazards: A perspective for critical infrastructure resilience and disaster risk reduction, International Journal of Disaster Risk Reduction, 66, 102597, https://doi.org/10.1016/j.ijdrr.2021.102597, 2021.

Tadini, A., Roche, O., Samaniego, P., Guillin, A., Azzaoui, N., Gouhier, M., de' Michieli Vitturi, M., Pardini, F., Eychenne, J., Bernard, B., Hidalgo, S., and Le Pennec, J. L.: Quantifying the Uncertainty of a Coupled Plume and Tephra Dispersal Model: PLUME-MOM/HYSPLIT Simulations Applied to Andean Volcanoes, Journal of Geophysical Research: Solid Earth, 125, e2019JB018390, https://doi.org/10.1029/2019JB018390, 2020.

Tappin, D. R., Grilli, S. T., Harris, J. C., Geller, R. J., Masterlark, T., Kirby, J. T., Shi, F., Ma, G., Thingbaijam, K. K. S., and Mai, P. M.: Did a submarine landslide contribute to the 2011 Tohoku tsunami?, Marine Geology, 357, 344–361, https://doi.org/10.1016/j.margeo.2014.09.043, 2014.

Tarque, N., Salsavilca, J., Yacila, J., and Camata, G.: Multi-criteria analysis of five reinforcement options for Peruvian confined masonry walls, Earthquakes and Structures, 17, 205–219, 2019.

Terzi, S., Torresan, S., Schneiderbauer, S., Critto, A., Zebisch, M., and Marcomini, A.: Multi-risk assessment in mountain regions: A review of modelling approaches for climate change adaptation, Journal of Environmental Management, 232, 759–771, https://doi.org/10.1016/j.jenvman.2018.11.100, 2019.

Thomalla, F., Boyland, M., Johnson, K., Ensor, J., Tuhkanen, H., Gerger Swartling, Å., Han, G., Forrester, J., and Wahl, D.: Transforming Development and Disaster Risk, Sustainability, 10, https://doi.org/10.3390/su10051458, 2018.

Thompson, M. A., Lindsay, J. M., Wilson, T. M., Biass, S., and Sandri, L.: Quantifying risk to agriculture from volcanic ashfall: a case study from the Bay of Plenty, New Zealand, Natural Hazards, 86, 31–56, https://doi.org/10.1007/s11069-016-2672-7, 2017.

Thouret, J.-C., Antoine, S., Magill, C., and Ollier, C.: Lahars and debris flows: Characteristics and impacts, Earth-Science Reviews, 201, 103003, https://doi.org/10.1016/j.earscirev.2019.103003, 2020.

Tilloy, A., Malamud, B. D., Winter, H., and Joly-Laugel, A.: A review of quantification methodologies for multi-hazard interrelationships, Earth-Science Reviews, 196, 102881, https://doi.org/10.1016/j.earscirev.2019.102881, 2019.

Tocchi, G., Polese, M., Di Ludovico, M., and Prota, A.: Regional based exposure models to account for local building typologies, Bulletin of Earthquake Engineering, https://doi.org/10.1007/s10518-021-01242-6, 2021.

Torres, Y., Arranz, J. J., Gaspar-Escribano, J. M., Haghi, A., Martínez-Cuevas, S., Benito, B., and Ojeda, J. C.:

Integration of LiDAR and multispectral images for rapid exposure and earthquake vulnerability estimation. Application in Lorca, Spain, International Journal of Applied Earth Observation and Geoinformation, 81, 161–175, https://doi.org/10.1016/j.jag.2019.05.015, 2019.

Torres-Corredor, R. A., Ponde-Villarreal, P., and Gomez-Martinez, D. M.: Vulnerabilidad física de cubiertas de edificaciones de uso de ocupación normal ante caídas de ceniza en la zona de influencia del Volcán Galeras, Boletín de Geología, Vol. 39, N° 2, 2017.

Trevlopoulos, K., Guéguen, P., Helmstetter, A., and Cotton, F.: Earthquake risk in reinforced concrete buildings during aftershock sequences based on period elongation and operational earthquake forecasting, Structural Safety, 84, 101922, https://doi.org/10.1016/j.strusafe.2020.101922, 2020.

Triantafyllou, I., Novikova, T., Charalampakis, M., Fokaefs, A., and Papadopoulos, G. A.: Quantitative Tsunami Risk Assessment in Terms of Building Replacement Cost Based on Tsunami Modelling and GIS Methods: The Case of Crete Isl., Hellenic Arc, Pure and Applied Geophysics, 176, 3207–3225, https://doi.org/10.1007/s00024-018-1984-9, 2019.

Tumurbaatar, Z., Miura, H., and Tsamba, T.: Development of Building Inventory Data in Ulaanbaatar, Mongolia for Seismic Loss Estimation, ISPRS International Journal of Geo-Information, 11, https://doi.org/10.3390/ijgi11010026, 2022.

Turchi, A., Traglia, F. D., Gentile, R., Fornaciai, A., Zetti, I., and Fanti, R.: Relative seismic and tsunami risk assessment for Stromboli Island (Italy), International Journal of Disaster Risk Reduction, 76, 103002, https://doi.org/10.1016/j.ijdrr.2022.103002, 2022.

UNISDR: UNISDR terminology on disaster risk reduction, United Nations International Strategy forDisaster Reductio, Geneva, 35 pp., 2009.

UNISDR: Sendai Frameworkfor Disaster Risk Reduction2015 - 2030, 2015.

Vamvatsikos, D., Panagopoulos, G., Kappos, A. J., Nigro, E., Rossetto, T., Lloyd, T. O., and Stathopoulos, T.: Structural Vulnerability Assessment under Natural Hazards: A review, in: Urban Habitat Constructions under Catastrophic Events, CRC Press. Editor: Mazzolani, F.M, 2010.

Vásquez, J. A., Jünemann, R., de la Llera, J. C., Hube, M. A., and Chacón, M. F.: Three-dimensional nonlinear response history analyses for earthquake damage assessment: A reinforced concrete wall building case study, Earthquake Spectra, 37, 235–261, https://doi.org/10.1177/8755293020944180, 2021.

Villar-Vega, M., Silva, V., Crowley, H., Yepes, C., Tarque, N., Acevedo, A. B., Hube, M. A., Gustavo, C. D., and María, H. S.: Development of a Fragility Model for the Residential Building Stock in South America, Earthquake Spectra, 33, 581–604, https://doi.org/10.1193/010716EQS005M, 2017.

Walter, T. R., Haghshenas Haghighi, M., Schneider, F. M., Coppola, D., Motagh, M., Saul, J., Babeyko, A., Dahm, T., Troll, V. R., Tilmann, F., Heimann, S., Valade, S., Triyono, R., Khomarudin, R., Kartadinata, N., Laiolo, M., Massimetti, F., and Gaebler, P.: Complex hazard cascade culminating in the Anak Krakatau sector collapse, Nature Communications, 10, 4339, https://doi.org/10.1038/s41467-019-12284-5, 2019.

Wang, S., Zhou, Q., and Tian, Y.: Understanding Completeness and Diversity Patterns of OSM-Based Land-Use and Land-Cover Dataset in China, ISPRS International Journal of Geo-Information, 9, https://doi.org/10.3390/ijgi9090531, 2020.

Ward, P. J., Blauhut, V., Bloemendaal, N., Daniell, J. E., de Ruiter, M. C., Duncan, M. J., Emberson, R., Jenkins, S. F., Kirschbaum, D., Kunz, M., Mohr, S., Muis, S., Riddell, G. A., Schäfer, A., Stanley, T., Veldkamp, T. I. E., and Winsemius, H. C.: Review article: Natural hazard risk assessments at the global scale, Natural Hazards and Earth System Sciences, 20, 1069–1096, https://doi.org/10.5194/nhess-20-1069-2020, 2020.

Ward, P. J., Daniell, J., Duncan, M., Dunne, A., Hananel, C., Hochrainer-Stigler, S., Tijssen, A., Torresan, S., Ciurean, R., Gill, J., Sillmann, J., Couasnon, A., Koks, E., Padrón-Fumero, N., Tatman, S., Tronstad Lund, M., Adesiyun, A., Aerts, J., Alabaster, A., Butler, B., Campillo Torres, C., Critto, A., Hernández Martin, R., Machado, M., Mysiak, J., Orth, R., Palomino, I., Petrescu, E.-C., Reichstein, M., Tiggeloven, T., van Loon, A., Vuong Pham, H., and de Ruiter, M.: Invited perspectives: A research agenda towards disaster risk management pathways in multi-(hazard-)risk assessment, Natural Hazards and Earth System Sciences Discussions, 2022, 1487–1497, https://doi.org/10.5194/nhess-22-1487-2022, 2022.

Weatherill, G., Pittore, M., Haas, M., Brinckmann, N., Rüster, M., and Gomez-Zapata, J. C.: Shakyground: a web service to serve GMPE-based ground motion fields. V. 1.0., GFZ Data Services, https://doi.org/10.5880/riesgos.2021.004, 2021.

Weatherill, G. A., Silva, V., Crowley, H., and Bazzurro, P.: Exploring the impact of spatial correlations and uncertainties for portfolio analysis in probabilistic seismic loss estimation, Bulletin of Earthquake Engineering, 13, 957–981, https://doi.org/10.1007/s10518-015-9730-5, 2015.

Weichselgartner, J. and Kelman, I.: Geographies of resilience: Challenges and opportunities of a descriptive concept, Progress in Human Geography,

39, 249–267, https://doi.org/10.1177/0309132513518834, 2014.

Wesson, R. L. and Perkins, D. M.: Spatial correlation of probabilistic earthquake ground motion and loss, Bulletin of the Seismological Society of America, 91, 1498–1515, https://doi.org/10.1785/0120000284, 2001.

Wieland, M. and Pittore, M.: A Spatio-Temporal Building Exposure Database and Information Life-Cycle Management Solution, ISPRS International Journal of Geo-Information, 6, https://doi.org/10.3390/ijgi6040114, 2017.

Wieland, M., Pittore, M., Parolai, S., Zschau, J., Moldobekov, B., and Begaliev, U.: Estimating building inventory for rapid seismic vulnerability assessment: Towards an integrated approach based on multi-source imaging, Soil Dynamics and Earthquake Engineering, Complete, 70–83, https://doi.org/10.1016/j.soildyn.2012.01.003, 2012.

Wilson, G., Wilson, T. M., Deligne, N. I., Blake, D. M., and Cole, J. W.: Framework for developing volcanic fragility and vulnerability functions for critical infrastructure, Journal of Applied Volcanology, 6, 14, https://doi.org/10.1186/s13617-017-0065-6, 2017.

Wilson, T. M., Stewart, C., Wardman, J. B., Wilson, G., Johnston, D. M., Hill, D., Hampton, S. J., Villemure, M., McBride, S., Leonard, G., Daly, M., Deligne, N., and Roberts, L.: Volcanic ashfall preparedness poster series: a collaborative process for reducing the vulnerability of critical infrastructure, Journal of Applied Volcanology, 3, 10, https://doi.org/10.1186/s13617-014-0010-x, 2014.

Wronna, M., Omira, R., and Baptista, M. A.: Deterministic approach for multiple-source tsunami hazard assessment for Sines, Portugal, Natural Hazards and Earth System Sciences, 15, 2557–2568, https://doi.org/10.5194/nhess-15-2557-2015, 2015.

Wuni, I. Y., Shen, G. Q., Osei-Kyei, R., and Agyeman-Yeboah, S.: Modelling the critical risk factors for modular integrated construction projects, International Journal of Construction Management, 0, 1–14, https://doi.org/10.1080/15623599.2020.1763049, 2020.

Xin, D., Daniell, J. E., Tsang, H.-H., and Wenzel, F.: Residential building stock modelling for mainland China targeted for seismic risk assessment, Natural Hazards and Earth System Sciences, 21, 3031–3056, https://doi.org/10.5194/nhess-21-3031-2021, 2021.

Xing, E. P.: 19 : Bayesian Nonparametrics : Dirichlet Processes, Probabilistic Graphical Models 10-708, 1–8, 2014.

Yepes-Estrada, C., Silva, V., Valcárcel, J., Acevedo, A. B., Tarque, N., Hube, M. A., Coronel, G., and María, H. S.: Modeling the Residential Building Inventory in South America for Seismic Risk Assessment, Earthquake Spectra, 33, 299–322, https://doi.org/10.1193/101915eqs155dp, 2017.

Zafrir, R.: Downscaling building exposure models: a probabilistic approach using remote sensing products and open source auxiliary information, Stuttgart Technology University of Applied Sciences (Hochschule für Technik Stuttgart - HFT Stuttgart), Stuttgart, Germany, 75 pp., 2020.

Zafrir, R., Pittore, M., Gomez-Zapata, J. C., Aravena, P., and Geiß, C.: Bayesian downscaling of building exposure models with remote sensing and ancillary information, in: EGU General Assembly Conference Abstracts, 18240, 2020.

Zuccaro, G. and De Gregorio, D.: Time and space dependency in impact damage evaluation of a sub-Plinian eruption at Mount Vesuvius, Natural Hazards, 68, 1399–1423, https://doi.org/10.1007/s11069-013-0571-8, 2013.

Zuccaro, G., Cacace, F., Spence, R. J. S., and Baxter, P. J.: Impact of explosive eruption scenarios at Vesuvius, Journal of Volcanology and Geothermal Research, 178, 416–453, https://doi.org/10.1016/j.jvolgeores.2008.01.005, 2008.

Zuccaro, G., De Gregorio, D., and Leone, M. F.: Theoretical model for cascading effects analyses, International Journal of Disaster Risk Reduction, 30, 199–215, https://doi.org/10.1016/j.ijdrr.2018.04.019, 2018.